Electronic structure of open-shell Zintl clusters

Zisheng Li

St. Anne's College

University of Oxford

A thesis submitted for the degree of

Doctor of Philosophy

Trinity 2025

Declaration of Authorship

The work presented in this thesis is the original work of the author, except where references have been made to other sources. No part of this work has previously been submitted for any other degree.

Zisheng Li

Acknowledgements

As this thesis will outlast me, I hope that whenever a reader comes across its pages, they will also recognise those to whom I am deeply grateful during my DPhil journey.

I am profoundly grateful to my supervisor, Professor John E. McGrady, for his instructive and patient supervision, and for his continuous support throughout my time in Oxford. I always appreciate and cherish the opportunities he has provided me. I also thank all members of the McGrady group for their generous help and encouragement for my work. Also, for collaborators, Professor Zhong-Ming Sun and his group members, I am also grateful for their outstanding experimental work and help, without which I would not have had the chance to carry out theoretical research on these interesting clusters.

I would like to express my deepest gratitude to my parents, Huaikuan and Lisha, for their unconditional love, emotional and financial support. Without them, my DPhil experience in Oxford would not have been possible. I also wish to thank my grandparents, Liebao and Erjie, Hong and Zhimei, who have always stood firmly behind me. I have also been delighted by my partner, Yiran, who has been a patient listener and a companion I can rely on. I am grateful to all my friends for bringing me joy and inspiration, whether at home or away.

Finally, I would like to thank myself. No matter my emotional state or the obstacles in front of me, I have always managed to move forward.

List of Publications

Publications with major contributions:

1. W.-Q. Zhang, Z.-S. Li, J. E. McGrady, Z.-M. Sun. Synthesis and Characterization of $[Fe_3(As_3)_3(As_4)]^{3-}$, a Binary Fe/As Zintl Cluster with an Fe_3 Core. *Angew. Chem. Int. Ed.* 2023, **62**, e202217316.

2. W.-X. Chen, Z.-S. Li, H. W. T. Morgan, C.-C. Shu, Z.-M. Sun, J. E. McGrady. Fe-Fe Bonding in the Rhombic Fe_4 Cores of the Zintl Clusters $[Fe_4E_{18}]^{4-}$ (E = Sn, Pb). *Chem. Sci.* 2024, **15**, 4981–4988.

3. Z.-S. Li, W.-X. Chen, H. W. T. Morgan, C.-C. Shu, Z.-M. Sun, J. E. McGrady. Snapshots of Cluster Growth: Structure and Properties of a Zintl Ion with an Fe_3 Core, $[Fe_3Sn_{18}]^{4-}$. *Chem. Sci.* 2024, **15**, 1018–1026.

4. Y.-N. Yang, Z.-S. Li, S. Mondal, L. Qiao, C.-C. Wang, W.-J. Tian, Z.-M. Sun, J. E. McGrady. Metal-Metal Bonds in Zintl Clusters: Synthesis, Structure and Bonding in $[Fe_2Sn_4Bi_8]^{3-}$ and $[Cr_2Sb_{12}]^{3-}$. *Chin. Chem. Lett.* 2024, **35**, 109048.

Other publications:

5. W.-X. Chen, W.-J. Tian, Z.-S. Li, J.-J. Wang, A. Muñoz-Castro, G. Frenking, Z.-M. Sun. Capturing Aromatic Cr_5 Pentagons in Large Main-Group Molecular Cages. *Nat. Synth.* 2025, **4**, 471–478.

6. Y.-S. Huang, H.-L. Xu, W.-J. Tian, Z.-S. Li, S. Escayola, M. Solà, A. Muñoz-Castro, Z.-M. Sun. $[Co_3@Ge_6Sn_{18}]^{5-}$: A Giant σ-Aromatic Cluster Analogous to H_3^+ and Li_3^+. *J. Am. Chem. Soc.* 2025, **147**, 9407–9414.

7. W.-X. Chen, A. Manley, Z.-S. Li, J. E. McGrady, Z.-M. Sun. Synthesis, Structure, and Electronic Properties of $[Cr_6@Sn_8Sb_8(en)_2]^{3-}$: A Cr_6 Octahedron Encapsulated in a Zintl-Ion Ligand. *J. Am. Chem. Soc.* 2025, **147**, 24309–24316.

Abstract

This thesis presents a theoretical investigation of clusters composed of transition metals and main-group elements, namely Zintl clusters. The studied systems can be broadly categorised into two types: (i) endohedral clusters with core-shell architectures, and (ii) clusters in which transition metal centres are coordinated directly to inorganic or organic ligands. All clusters discussed in this work have been synthesised and structurally characterised by single-crystal X-ray diffraction. However, limited experimental data beyond crystallographic analysis underscore the importance of gaining a deeper understanding of their electronic structures through theoretical approaches. The central strategy of this thesis is to compare the target clusters with either experimentally known or hypothetical reference systems, allowing us to elucidate differences in geometry and electronic structure. Particular emphasis is placed on metal-metal bonding, which is analysed using Density Functional Theory, and where necessary, multi-configurational methods such as Density Matrix Renormalisation Group are employed to account for strong correlation effects — especially in high-spin systems or in the presence of spin contamination when using DFT. In endohedral clusters, metal-ligand interactions are explored in detail, with special attention to the role of back-bonding and its influence on stabilising intermediate cage geometries. In Fe-pnictogen systems, correlations between metal and ligand geometries are examined, originating from electron density redistribution within the clusters. Collectively, this work highlights how theoretical methods can provide essential insights into the bonding and electronic properties of Zintl chemistry.

Contents

List of Figures

List of Abbreviations

ADF Amsterdam Density Functional.

AdNDP Adaptive Natural Density Partitioning.

ANO-RCC Atomic Natural Orbital for Scalar-Relativistic Core-Correlated.

CAS Complete Active Space.

CASPT2 Complete Active Space Second-Order Perturbation Theory.

CASSCF Complete Active Space Self-Consistent Field.

CI Configuration Interaction.

CIPSI Configuration Interaction using a Perturbative Selection made Iteratively.

CIS Configuration Interaction Singles.

CISD Configuration Interaction Singles and Doubles.

CISDT Configuration Interaction Singles, Doubles, and Triples.

CISDTQ Configuration Interaction Singles, Doubles, Triples, and Quadruples.

COSMO Conductor-like Screening Model.

CSFs Configuration State Functions.

DFT Density Functional Theory.

DMRG Density Matrix Renormalisation Group.

DOS Density of States.

EBO Effective Bond Order.

EDA-NOCV Energy Decomposition Analysis with Natural Orbitals for Chemical Valence.

EDD Electron Density Difference.

EHT Extended Hückel Theory.

ELF Electron Localisation Function.

Full CI Full Configuration Interaction.

FK Frank-Kasper.

GAS Generalised Active Space.

GASSCF Generalised Active Space Self-Consistent Field.

GGA Generalised Gradient Approximation.

GTOs Gaussian-type Orbitals.

HF Hartree-Fock.

HOMO Highest Occupied Molecular Orbital.

HT Hückel Theory.

KS-DFT Kohn-Sham Density Functional Theory.

LCAO Linear Combination of Atomic Orbitals.

LDA Local Density Approximation.

LSDA Local Spin Density Approximation.

LUMO Lowest Unoccupied Molecular Orbital.

MC-PDFT Multi-Configuration Pair-Density Functional Theory.

MC-SCF Multi-Configurational Self-Consistent Field.

MP2 Møller-Plesset Second-Order Perturbation Theory.

MPO Matrix Product Operator.

MPS Matrix Product State.

MRCI Multi-Reference Configuration Interaction.

MSA Monocapped Square Antiprism.

NBO Natural Bond Orbital.

NEVPT2 n-Electron Valence State Second-Order Perturbation Theory.

ONs Occupation Numbers.

OPDOS Overlap Population Density of States.

PDOS Projected Density of States.

PES Potential Energy Surface.

PIOs Principal Interaction Orbitals.

post-HF post-Hartree-Fock.

QTAIM Quantum Theory of Atoms in Molecules.

RAS Restricted Active Space.

RASSCF Restricted Active Space Self-Consistent Field.

RHF Restricted Hartree-Fock.

RKS-DFT Restricted Kohn-Sham Density Functional Theory.

UKS-DFT Unrestricted Kohn-Sham Density Functional Theory.

RODFT Restricted Open-Shell Density Functional Theory.

ROHF Restricted Open-Shell Hartree-Fock.

SCF Self-Consistent Field.

SEPs Skeletal Electron Pairs.

STFs Slater-type Functions.

STOs Slater-type Orbitals.

SVD Singular Value Decomposition.

TTP Tricapped Trigonal Prism.

UDFT Unrestricted Density Functional Theory.

XRD X-ray Diffraction.

ZORA Zeroth-Order Regular Approximation.

Chapter 1

Introduction

Chemical bonding is a central topic in chemistry and forms the foundation for our understanding of molecular structure and chemical reactivity. The making and breaking of chemical bonds underpin the majority of chemical reactions, catalysis, biological processes, energy storage and conversion. The two-centre-two-electron bond is a cornerstone of bonding theory, but many molecules exhibit non-classical bonding types involving multiple centres (diborane is a classic example) or more or fewer than two electrons. The essence of the chemical bond is the overlap of atomic orbitals, which results in the accumulation of electron density in the vicinity of two or more nuclei. The strength of this overlap, and thus the bond, depends on both the type of orbital (s, p, d, f) and the effective nuclear charge of the atom, which determines its spatial extent. A schematic plot of the types of overlap available to s, p and d orbitals is shown in Figure 1.1. An s orbital has no angular dependence, leading to directionally non-selective σ bonds. A p orbital has a nodal plane separating its two lobes, and so a chemical bond involving p electrons is directional, giving rise to σ bonding through head-to-head and π bonding through side-to-side overlap. d orbitals show even greater angular preference and, although d-d overlap tends to be weaker than that of s or p orbitals, d orbitals can participate in σ, π and δ bonding, leading to metal-metal bond orders of up to five. The δ-symmetry interactions, achieved by face-to-face interactions of two d orbitals, are typically amongst the weakest bonding known. Perhaps the most famous example of a δ bond is one component of the Re-Re quadruple bond in $[Re_2Cl_8]^{2-}$, made up of one σ bond (from overlap of the d_{z^2} orbitals), two π bonds (from d_{xz} and d_{yz}), and one δ bond (from d_{xy}), resulting in a short Re-Re distance of 2.24 Å.[5] An even higher Cr-Cr bond order of 5 is found in $Cr_2Ar'_2$, Ar′ = 2,6-(2,6-iPr$_2-$C$_6$H$_3$)$_2$-C$_6$H$_3$), where a $\sigma^2\pi^4\delta^4$ configuration reflects the full utilisation of five d electrons on each Cr(I) to form Cr-Cr bonds.[6] The Cr-Cr distance in this compound is extremely short, reaching 1.8351(4) Å.

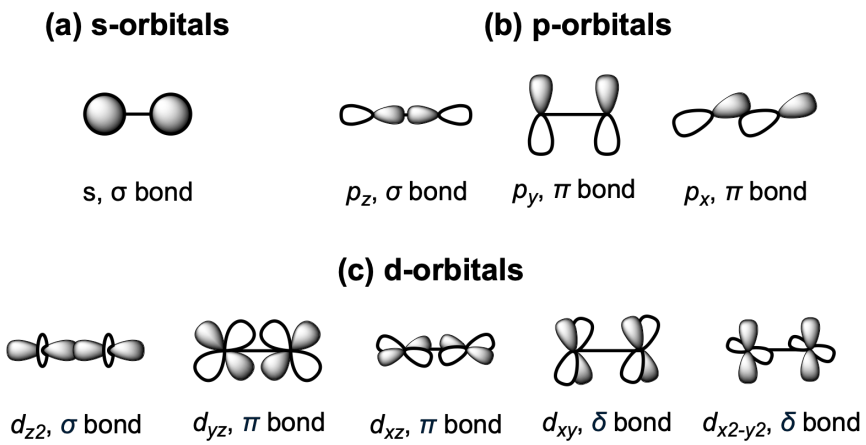

Figure 1.1: Schematic plot of bonding generated from (a) s orbitals, (b) p orbitals and (c) d orbitals.

The diversity of metal-metal bonding types in d-block element chemistry has made this class of compounds an important testing ground for new theories of chemical bonding, and the simple diatomics, M_2, have been studied using everything from Extended Hückel Theory (EHT) to Multi-Configurational Self-Consistent Field (MC-SCF) methods. However, in the realm of stable molecules that can be isolated, metal-metal bonds typically require the presence of a ligand coordination shell. These can be classical ligands (H_2O, Cl^-, NH_3, PR_3, CO, etc.) but, more recently, post-transition metal clusters have been used to stabilise metal ions and larger clusters, providing a flexible environment for generating new types of metal-metal bonds. This class of compounds, broadly termed 'Zintl clusters', is the subject of the majority of this thesis.

The field of Zintl chemistry originated from the reaction between sodium and lead in liquid ammonia.[7,8] A landmark discovery was made in 1931 when Eduard Zintl elucidated the composition of Na_4Pb_9,[9] laying the foundation for decades of subsequent research into (semi)metal clusters and solid phase frameworks. Zintl clusters are now broadly defined as polyatomic anions composed of main-group elements.[10,11] Examples are shown in Figure 1.2. Clusters containing the Group 14 elements (Si, Ge, Sn, Pb) often adopt deltahedral structures similar to the borane family, where the number of electrons is insufficient to fulfil localised two-centre-two-electron bonding for all existing bonds. Electron-deficiency is therefore an intrinsic feature of this class of cluster, and delocalised bonding dominates. The Wade-Mingos rules[12–15] can provide a preliminary understanding of the relationship between structure and electron count. Clusters containing Group 15 elements also fall into the general class of Zintl

chemistry, but here, the electron count is higher and localised models of bonding are more appropriate.

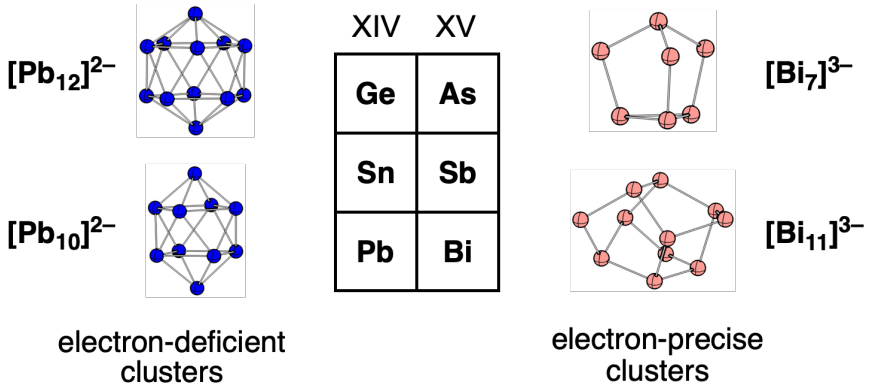

Figure 1.2: Representatives of Zintl clusters composed of Group 14 and Group 15 elements.

These polyatomic clusters, whether from Group 14 or 15, can provide a cavity that can accommodate one or more transition metal atoms, forming endohedral Zintl clusters. Encapsulation of transition metal ions can lead to expansion of the main-group cage by buffering the high negative charge, and metal-metal bonding can emerge as a result. Most known intermetallic Zintl clusters contain a late transition metal with a filled d shell: in these circumstances, the interactions between the cluster and the encapsulated atom are relatively weak. In recent years, a number of Zintl clusters with earlier transition metals have been synthesised.[16–20] The metal cores in these clusters typically have a partially filled d shell, enabling more extensive covalent bonding to the main-group shell as well as the potential for metal-metal bonding. This new class of 'open-shell' clusters gives access to a broader range of magnetic properties and versatile cluster architectures, where the structure can vary significantly from that of the corresponding empty cluster. The diversity of structures and magnetic properties opens up possibilities in the realm of single-molecule magnets and spin-based devices.

In an experimental context, single-crystal XRD has been a powerful tool, providing detailed information on atomic positions based on Bragg's law. However, XRD has limitations in distinguishing elements with similar nuclear charges (Ge and As, or Sn and Sb, for example) due to the negligible difference in their electron density, which can hinder accurate resolution of their positions in binary or ternary clusters. Additionally, the experimental yields are often rather small and the products are susceptible to oxidation, both of which limit the range of spectroscopic techniques that

can be applied. As a result, theoretical studies are playing a crucial role in helping to interpret data and in establishing a unified model for the electronic properties of these clusters.

Density Functional Theory (DFT) is the most commonly applied method due to its balance between computational efficiency and reasonable accuracy. Full details will be given in Chapter 2, but, in short, the DFT framework describes the energy of a system as a functional of the electron density, where the ground-state energy is determined by the optimal electron density. Orbital-based approaches, introduced as part of the Kohn-Sham ansatz, yield eigenvectors that can be interpreted as canonical molecular orbitals and their eigenvalues as the orbital energies. However, the exact relationship between density and energy remains unknown, and the wide choice of available functional forms presents a challenge to the field. Open-shell systems are the focus of this thesis, and here the Unrestricted Density Functional Theory (UDFT) approach is used to allow for different spatial distributions for the majority and minority spin orbitals. This often leads to a lower energy than the restricted approach, but the resulting unrestricted wavefunction is not, in general, an eigenfunction of the spin operator. This can result in spin contamination and artificial symmetry breaking. This limitation can introduce artefacts that complicate the interpretation of spectra.

An alternative approach to capturing electron correlation lies in post-Hartree-Fock (post-HF) methods based on Configuration Interaction (CI). The CI method is a straightforward way to capture electron correlation by expanding the wavefunction as a linear combination of Slater determinants or Configuration State Functions (CSFs) of the system. Further iterative optimisation of both the configuration coefficients and the active orbitals leads to the MC-SCF method, which allows for a balanced treatment of near-degenerate configurations. While MC-SCF accounts mainly for static correlation, it fails to capture most dynamic correlation, which arises from the instantaneous interactions between electrons. This deficiency can be addressed using post-MC-SCF methods such as Complete Active Space Second-Order Perturbation Theory (CASPT2),[21] n-Electron Valence State Second-Order Perturbation Theory (NEVPT2),[22] or Multi-Configuration Pair-Density Functional Theory (MC-PDFT).[23,24] MC-SCF and MC-PDFT are introduced in Chapter 2, and are used extensively in Chapters 3 and 4.

The canonical orbitals that emerge from a typical calculation (DFT or MC-SCF) are always highly delocalised, reflecting the symmetry of the molecule, and it is not always clear how they relate to simple ideas of localised chemical bonding. This link

can, however, be made using several approaches. Firstly, the canonical molecular orbitals can be localised by unitary transformations, resulting in the concentration of amplitude into a smaller subset of orbitals, providing a more intuitive picture of the bond. Natural orbitals, obtained by diagonalising the one-electron density matrix, are another orbital representation for MC-SCF calculations. The corresponding occupation numbers also provide indications of electron correlation. A similar orbital-reinterpretation method in single-reference calculations is the Natural Bond Orbital (NBO) analysis, which can identify lone pairs, two-centre bonds and even up to three-centre bonds.[25,26] The Adaptive Natural Density Partitioning (AdNDP) method extends the NBO concept by identifying multi-centre bonding patterns, which are particularly prevalent in Zintl clusters.[27] Additional orbital interaction analyses, such as Principal Interaction Orbitals (PIOs)[28,29] and Energy Decomposition Analysis with Natural Orbitals for Chemical Valence (EDA-NOCV),[30,31] help isolate and quantify the dominant bonding pairs between fragments. Bond strength and other properties can be analysed using the following methods, based on either canonical orbitals or re-interpreted orbitals. A classical method involves analysing the occupancy differences between bonding and antibonding molecular orbitals, giving rise to the concept of an Effective Bond Order (EBO). Alternatively, bond order can be quantified *via* orbital overlap. For example, the Wiberg bond index[32] is derived from the quadratic of the density matrix between atomic orbitals, while the Mayer bond order[33] incorporates the overlap matrix to provide a refined picture of bond strength. A related visualisation method is the Overlap Population Density of States (OPDOS), where the density of states is weighted by the overlap to highlight energy windows where bonding or antibonding character between orbital pairs is significant. OPDOS analysis is used extensively throughout the thesis. In addition to these overlap-based approaches, bonding can also be rationalised using topological analysis of the electron density. Quantum Theory of Atoms in Molecules (QTAIM)[34] identifies critical points in the electron density based on its gradients along three perpendicular axes, providing quantified indicators of bonding interactions. The closely related concept of the Electron Localisation Function (ELF)[35] indicates the location of lone pairs or bonding regions by determining the local maxima.

This thesis describes a series of studies on clusters that can be considered in some sense as 'Zintl clusters', in the sense that they contain transition metals surrounded by ligands based on main-group elements. In some cases (primarily with Group 14) the main-group elements form a continuous approximately spherical unit, while in others (primarily with Group 15) they are fragmented into smaller components. The

transition metals are typically from the first transition series, where the compact $3d$ orbitals lead to strong electron-electron repulsions and, hence, strongly correlated motion. The work has been done in collaboration with Professor Zhong-Ming Sun from Nankai University, whose group performed all the syntheses and characterisation. The purpose here is to extend our theoretical understanding of metal-metal bonding through the study of Zintl clusters. The thesis begins with a detailed review of the relevant computational methods employed across the thesis, ranging from single-reference methods such as Hartree-Fock (HF) approximation, DFT, and EHT, to multi-reference approaches including Complete Active Space Self-Consistent Field (CASSCF), Density Matrix Renormalisation Group (DMRG), and MC-PDFT. The appropriate choice of computational method is essential for obtaining reasonable results at moderate computational cost. EHT is a semi-empirical approach which accounts for electron repulsion only through the parametrisation of orbital energies and sizes. It is a highly approximate but computationally efficient method, and is used primarily for plotting Walsh diagrams to describe changes in geometry. Qualitative trends in orbital energy as a function of geometry change can be captured through a series of single-point calculations. DFT introduces electron correlation *via* exchange-correlation functionals, and generally provides reliable results for both closed-shell and open-shell clusters. However, the performance of DFT depends strongly on the choice of functional, which can lead to inconsistent predictions, highlighting the need for careful benchmarking, especially in systems with strongly correlated electrons, such as the high-spin open-shell clusters that are the subject of most of this thesis. In such circumstances, a more explicit treatment of electron correlation offered by post-HF methods is required. Static correlation is treated using CASSCF and DMRG, while dynamic correlation is incorporated using MC-PDFT. The computational methods selected in the following chapters reflect the physics of the systems, and also the nature of the question that I am trying to address.

The results are collected into two chapters, which are loosely organised on the basis of the content of the main-group shell: Chapter 3 deals with clusters containing Group 14 elements in a core-shell structure, while Chapter 4 documents studies on clusters composed of Group 15 elements. This distinction is not exact, as some clusters contain both ($[Fe_2Sn_4Bi_8]^{3-}$, for example). In Chapter 3, I present a more detailed introduction to cluster chemistry, and then set out three distinct studies, all of which have been published in separate articles. The work is arranged in such a way that I progress from clusters containing two transition metal ions, to three and then four. In all cases, the main-group cage serves as a geometric constraint, confining

the metals in a small volume. This unique setup allows us to theoretically explore multi-centre metal-metal bonding in depth. Furthermore, we examine how core-shell interactions influence the overall cage geometry. Comparisons with closed-shell analogues offer critical insights into these effects. The structural evolution leading to the formation of complex cage architectures is also discussed. These open-shell clusters can exhibit a multi-configurational electronic structure, making accurate treatment of electron correlation essential for identifying the true ground state. This is addressed through multi-reference methods, including CASSCF, DMRG and MC-PDFT, as a complement to DFT. In Chapter 4, I turn to Zintl clusters coordinated by Group 15 elements, in this case with either two or three transition metal ions. The higher electron count of the Group 15 elements leads to more open structures where the metals are not fully encapsulated. Nevertheless, the main-group component serves to hold the metals in close proximity, allowing metal-metal bonding to develop. Here, the analysis of metal-metal bonding begins with a Linear Combination of Atomic Orbitals (LCAO)-based approach to understand bonding interactions. MC-SCF calculations are again used as a complementary method to carefully explore the change in electronic configuration as the metal-metal bond length varies. By applying these different levels of theoretical treatment, I hope to generate a more coherent interpretation of metal-metal bonding in these systems. The geometric correlation between the transition metal and the ligand is also discussed from the view of electronic structure variations. Finally, we conclude the thesis with a brief summary and outlook on the future of computational Zintl chemistry.

Chapter 2

Theoretical Background

This chapter introduces fundamental concepts and theorems of quantum chemistry that underpin the computational methods used throughout this thesis. The time-independent Schrödinger equation will first be introduced, followed by a discussion of the physical meaning of its eigenvalues and eigenfunctions. In order to solve this fundamental equation from first principles, the nature of the interaction between electrons needs to be considered, as does the mathematical treatment of the atomic orbitals. The first aspect leads to the development of *ab initio* methods for solving the Schrödinger equation, ranging from the Hartree-Fock approximation to Density Functional Theory and Configuration Interaction. In the second aspect, the mathematical representation of the atomic orbitals takes us to a discussion of basis sets.

2.1 Foundations of quantum chemistry

Unlike classical Newtonian systems, microscopic particles like nuclei and particularly electrons exhibit both wave-like and particle-like characteristics, and hence the position and momentum of such particles cannot be measured simultaneously. Therefore, these particles can only be described within the framework of quantum mechanics, the centrepiece of which is the solution to the time-independent Schrödinger equation

$$\hat{H}\Psi = E\Psi \tag{2.1.1}$$

Here, the Hamiltonian $\hat{H}$ is an operator, whose eigenvalues are the total energies (E) of states of the system. Ψ, also called the wavefunction, is the corresponding eigenfunction of the Schrödinger equation. The Hamiltonian can be decomposed into a series of kinetic and potential energy terms as follows:

$$\hat{H} = \hat{T}_n + \hat{T}_e + \hat{V}_{nn} + \hat{V}_{ne} + \hat{V}_{ee} \tag{2.1.2}$$

$\hat{T}_n$ and $\hat{T}_e$ represent the kinetic energy of the nuclei and electrons, and $\hat{V}_{nn}$, $\hat{V}_{ne}$ and $\hat{V}_{ee}$ terms describe the nucleus-nucleus, nucleus-electron, and electron-electron interactions, respectively. As the nuclear mass is at least three orders of magnitude larger than that of the electron, the nuclei can be considered to be static on the timescale of electron motion. This is called the Born-Oppenheimer approximation, which decouples the motion of electrons and nuclei and eliminates the kinetic energy of nuclei from the Hamiltonian. The repulsion between nuclei, $\hat{V}_{nn}$, is then a constant term (for a fixed arrangement of nuclei) that can be calculated using classical electrostatics, and the total wavefunction can be separated into a product of nuclear (Ψ_n) and electronic parts (Ψ_e). We can therefore focus only on the electronic part of the time-independent Schrödinger equation where the electronic part of the Hamiltonian $\hat{H}_e$ can be expressed as

$$\hat{H}_e \Psi_e = E_e \Psi_e \tag{2.1.3}$$

$$\hat{H}_e = \hat{T}_e + \hat{V}_{ne} + \hat{V}_{ee} \tag{2.1.4}$$

The wavefunction is a complex mathematical description of the quantum state of the electronic system, but it can be connected to experiment through the Born interpretation, which states that its square (or more precisely the product of the wavefunction and its complex conjugate) at a point in space is proportional to the probability of finding an electron within a finite volume element surrounding this point. The expectation value of observable properties (λ) such as energy can be obtained by calculating the wavefunction with an appropriate Hermitian operator ($\hat{Q}$):

$$\lambda = \frac{\int \Psi^* \hat{Q} \Psi d\tau}{\int \Psi^* \Psi d\tau} = \frac{\langle \Psi | \hat{Q} | \Psi \rangle}{\langle \Psi | \Psi \rangle} \tag{2.1.5}$$

As the electron motions are correlated with each other, it is not possible to solve for the exact energy and wavefunction analytically in systems with more than one electron. However, the variational principle provides an upper bound to the exact ground-state energy of the system: it states that the energy generated from any trial wavefunction must be greater than or equal to the true ground-state energy. This principle provides a basis for many approximate methods, as it enables a strategy to approach the ground-state energy (E_0, defined by the ground-state wavefunction Ψ_0) by optimising the trial wavefunction (Ψ') to minimise the total energy.

$$E = \frac{\langle \Psi' | \hat{H} | \Psi' \rangle}{\langle \Psi' | \Psi' \rangle} \geq \frac{\langle \Psi_0 | \hat{H} | \Psi_0 \rangle}{\langle \Psi_0 | \Psi_0 \rangle} = E_0 \tag{2.1.6}$$

2.2 Single-determinant methods

2.2.1 Hartree-Fock approximation

As stated above, the exact solution of the Schrödinger equation is only available in analytical form for simple one-electron systems. For systems with more than one electron, strategies have to be introduced to reach an approximate solution of sufficient accuracy. The starting point here is the Hartree-Fock approximation,[36,37] where each electron is assumed to move independently in an external mean-field created by all other particles (electrons and nuclei). A second constraint is imposed by the Pauli exclusion principle, which requires the wavefunction to be antisymmetric under the exchange of two identical fermions. The total wavefunction of an n-electron system in the Hartree-Fock approximation can then be expressed as a single determinant composed of spin orbitals χ_i as

$$|\Psi\rangle = |\chi_1\chi_2 \cdots \chi_i\chi_j\chi_a\chi_b \cdots \chi_N\rangle = \frac{1}{\sqrt{N!}} \begin{vmatrix} \chi_1(1) & \chi_1(2) & ... & \chi_1(N) \\ \chi_2(1) & \chi_2(2) & ... & \chi_2(N) \\ ... & ... & ... & ... \\ \chi_N(1) & \chi_N(2) & ... & \chi_N(N) \end{vmatrix} \tag{2.2.1}$$

The spin orbitals are orthogonal to each other as $\langle\chi_i|\chi_j\rangle = \delta_{ij}$. The spatial part of any spin orbital (ψ_j) is expressed using the LCAO approximation

$$\psi_j = \sum_{\mu} c_{\mu j}\phi_{\mu} \tag{2.2.2}$$

The atomic orbital and its expansion coefficient are represented as ϕ_μ and $c_{\mu j}$, respectively. In order to obtain the energy and the composition of a spin orbital, the Fock operator $\hat{f}_1$ acting on electron 1 can be introduced as:

$$\hat{f}_1\chi_1(1) = \epsilon_1\chi_1(1) \tag{2.2.3}$$

The orbital energy, ϵ_1, can be optimised variationally with respect to the coefficient vector of the spin orbitals. The orbital energy and wavefunction correspond to the eigenvalue and eigenvector of this equation. The Fock operator defining the effective one-electron Hamiltonian can be expanded as:

$$\hat{f}_a = -\frac{1}{2}\nabla^2 - \sum_A \frac{Z_A}{r_{1A}} + \sum_{b\neq a} \hat{J}_b - \sum_{b\neq a} \hat{K}_b \tag{2.2.4}$$

The first two terms are from one-electron contributions: the kinetic energy ($-\frac{1}{2}\nabla^2$) and the electron-nuclear attractions ($-\sum_A \frac{Z_A}{r_{1A}}$) between electron 1 and nucleus A

with the nuclear charge as Z_A. The remaining terms arise from two-electron interactions. The Coulomb operator, $\hat{J}_b$, captures the classical electrostatic interactions between an electron in χ_a and another in χ_b. There is no simple physical explanation for the exchange operator $\hat{K}_b$ other than it emerges from the requirement for antisymmetry to electron exchange on the wavefunction. In the equation, the exchange operator 'exchanges' the orbital location of electron 1 and 2 on its right side. The effect of $\hat{J}_b$ and $\hat{K}_b$ operating on an electron located in χ_a can be expressed as:

$$\hat{J}_b(1)\chi_a(1) = \left[\int dx_2 \chi_b^*(2)\frac{1}{r_{12}}\chi_b(2)\right]\chi_a(1) \tag{2.2.5}$$

$$\hat{K}_b(1)\chi_a(1) = \left[\int dx_2 \chi_b^*(2)\frac{1}{r_{12}}\chi_a(2)\right]\chi_b(1) \tag{2.2.6}$$

Decomposing the spin orbitals into separate spatial and spin components allows further simplification. In a closed-shell system, each orbital is doubly occupied by two electrons with identical spatial distribution but opposite spins (α or β). The Coulomb operator acts on each electron by considering its interaction with all other electrons, regardless of their spin. Since two electrons occupying the same orbital have identical spatial distributions, the Coulomb repulsion operating on both electrons is the same. In contrast, the exchange interactions show a dependency on spin, where the exchange term vanishes when acting on electrons possessing an opposite spin due to spin orthogonality. In other words, in the Hartree-Fock approximation, exchange interactions occur only between electrons with the same spin. After integrating over spin coordinates, the Fock operator operating on closed-shell spatial orbital $\psi_j(r_1)$ for a system in terms of orbital c can be written as:

$$\begin{aligned}\hat{f}(r_1)\psi_j(r_1) = (-\frac{1}{2}\nabla^2 - \sum_A \frac{Z_A}{r_{1A}})\psi_j(r_1) + \left[2\sum_c^{N/2}\int dr_2 \psi_c^*(r_2)\frac{1}{r_{12}}\psi_c(r_2)\right]\psi_j(r_1) \\ - \left[\sum_c^{N/2}\int dr_2 \psi_c^*(r_2)\frac{1}{r_{12}}\psi_j(r_2)\right]\psi_c(r_1)\end{aligned} \tag{2.2.7}$$

The molecular orbitals can be represented in terms of the LCAO approximation using basis functions. If we multiply ϕ_μ^* on the left, followed by integration, the HF equations can then be converted into a matrix problem, the so-called Roothaan-Hall equations.[38,39]

$$\sum_\nu C_{\nu i}\int dr_1 \phi_\mu^*(1)\hat{f}(1)\phi_\nu(1) = \varepsilon_i \sum_\nu C_{\nu i}\int dr_1 \phi_\mu^*(1)\phi_\nu(1) \tag{2.2.8}$$

$$FC = \epsilon SC \tag{2.2.9}$$

The complete Fock matrix, F, can be constructed from the integration of Fock operators over all basis functions. The orbital energies in this equation are denoted by ϵ. The coefficient vectors, C, represent the LCAO expansion of the molecular orbitals and S is the matrix of overlap integrals between basis functions.

$$F_{\mu\nu} = \int dr_1 \phi_\mu^*(1)\hat{h}(1)\phi_\nu(1) + \sum_c^{N/2} \int dr_1 \phi_\mu^*(1)(2\hat{J}_c(1) - \hat{K}_c(1))\phi_\nu(1) \tag{2.2.10}$$

where the one-electron operator is

$$\hat{h}(1) = -\frac{1}{2}\nabla^2 - \sum_A \frac{Z_A}{r_{1A}} \tag{2.2.11}$$

The product of the coefficient matrix can be simplified through the introduction of the density matrix $P_{\mu\nu}$:

$$P_{\mu\nu} = \sum_c^{N/2} C_{\mu c} C_{\nu c} \tag{2.2.12}$$

If the overlap matrix can be converted to a unit matrix, the Roothaan-Hall equations can be converted to an eigenvalue problem. This diagonalisation procedure can be performed by $U^\dagger S U = s$ with a unitary matrix, whose inverse equals its conjugate transpose. An appropriate choice is $S^{-1/2}$, which is a Hermitian matrix as $S^{-1/2} = S^{-1/2\dagger}$. The equation can be translated as an eigenvalue problem with a derived coefficient matrix from $C = S^{-1/2}C'$.

$$S^{-1/2} S S^{-1/2} = S^{-1/2} S^{1/2} = I \tag{2.2.13}$$

$$(S^{-1/2} F S^{-1/2}) C = (S^{-1/2} S S^{-1/2}) C\varepsilon \tag{2.2.14}$$

$$F'C' = C'\varepsilon \tag{2.2.15}$$

By solving the equation, the orbital energies are obtained as the eigenvalues and the composition of the molecular orbitals can be extracted from the coefficient matrix converted from the eigenvectors. The equation must be solved iteratively using the Self-Consistent Field (SCF) method, due to the mutual dependency between the charge density and the elements of the Fock matrix (the Coulomb and exchange operators both depend on the coefficient matrix). The SCF procedure can be carried out in the following steps:

- Initialise the one-electron Hamiltonian, one-electron and two-electron integrals.

- Diagonalise the overlap matrix and obtain the transformation matrix $S^{-1/2}$.
- Generate an initial guess for the density matrix.
- Calculate the Coulomb and exchange integrals.
- Construct the Fock matrix and convert it into F'.
- Diagonalise F' to obtain C' and the orbital energies.
- Convert the C' back into the coefficient matrix and form the density matrix for the next iteration.
- Determine the convergence of the SCF cycle, by comparing the energy and density matrix between the previous and current cycle. If not converged (*i.e.* the current and previous values differ by more than a specified tolerance), use the F', C' and density matrix $P_{\mu\nu}$ in the next iteration of the SCF.

The variational principle guarantees that the SCF procedure yields the lowest energy within the chosen single-determinant ansatz, as well as its corresponding orbital set.

The Hartree-Fock approximation provides an elementary approach for solving the Schrödinger equation. Even though an exact description of the exchange interactions between parallel spins is provided in the Hartree-Fock equation, the model is limited by the choice of wavefunction, a single determinant. This is chosen because it ensures that the antisymmetry requirements are met, but it is by no means the only conceivable wavefunction that would achieve this. Any linear combination of determinants also has this property. Thus the single-determinant description that is the basis of Hartree-Fock theory can be seen as the minimal acceptable form of the wavefunction. The limitations of this choice are, however, clear: if two electrons with opposite spin (α and β) are described by the same spatial wavefunction then the most probable outcome of a (hypothetical) experiment that would measure their position simultaneously would be that they would be in the same place. This is clearly unphysical — we say that the motion of the two electrons is uncorrelated. An electron only feels the average repulsion generated by all other electrons, but does not respond to the specific position of another electron at any instant in time. Therefore, the Hartree-Fock approximation tends to overestimate the repulsion between electrons. The ability of electrons to avoid each other in a way that is not captured by the Hartree-Fock theory is called correlation, which can be captured with post-Hartree-Fock methods.

2.2.2 Extended Hückel theory

Unlike Hartree-Fock theory, which solves the Schrödinger equation using SCF techniques, a more computationally feasible approach is to incorporate experimentally fitted parameters to develop a semi-empirical method at the cost of accuracy and universality. Extended Hückel Theory is a semi-empirical method,[40] closely related to Hückel Theory (HT) which has been used extensively to describe molecules like benzene with conjugated bonds. EHT considers only valence atomic orbitals, and the elements of the Fock matrix are obtained using empirical parameters (specifically, the experimentally measured ionisation energies). The use of parameters and the neglect of core orbitals mean that the total energy is not calculated by EHT, and so properties that derive from the total energy, such as the optimal geometry, are not accessible. EHT is, however, very useful as a means of quickly computing orbital energies, and particularly in exploring how they vary over a reaction coordinate.

The molecular orbitals ψ_i in EHT are also constructed using the LCAO approximation, and Slater-type basis functions are typically used (see later discussion).

$$\psi_i = \sum_{\mu} c_{i\mu}\phi_{\mu} \tag{2.2.16}$$

The orbital energy can be obtained by solving a one-electron effective Hamiltonian $\hat{h}_{eff}$ eigenvalue problem. Its expectation value as energy, ε_j, can be expressed by Eq. 2.2.18.

$$\hat{h}_{eff}\psi_j = \varepsilon_j\psi_j \tag{2.2.17}$$

$$\varepsilon_j = \frac{\langle\psi_j|\hat{h}_{eff}|\psi_j\rangle}{\langle\psi_j|\psi_j\rangle} \tag{2.2.18}$$

The LCAO method applied here again introduces a coefficient matrix into the equations. The elements of the overlap matrix, S, are computed analytically, in much the same way as in HF theory. The elements of the Hamiltonian matrix, in contrast, are calculated using parameters and a set of empirical rules devised by Hoffmann and others.

The diagonal elements,

$$H_{ii} = \int \psi_i^* \hat{H} \psi_i d\tau \tag{2.2.19}$$

are approximated as the ionisation energies of the element in question. The off-diagonal elements are then constructed using the so-called Wolfsberg-Helmholtz formula:

$$H_{ij} = \frac{1}{2}K[H_{ii} + H_{jj}]S_{ij} \tag{2.2.20}$$

The best value of K has been debated, but 1.75 is used in most implementations, including the calculations in this thesis. The orbital energies are then given by coefficients c_r, elements in the Hamiltonian H_{rs} and in the overlap matrix S_{rs}:

$$\varepsilon_j = \frac{\sum_{r=1}^{N}\sum_{s=1}^{N} c_{rj}^* c_{sj} H_{rs}}{\sum_{r=1}^{N}\sum_{s=1}^{N} c_{rj}^* c_{sj} S_{rs}} \tag{2.2.21}$$

In this thesis, EHT is employed to compute the orbital arrangements of interpolated structures between stationary ones, facilitating the construction of Walsh diagrams. Since these structures exist in different charge states, SCF methods such as DFT will lead to discontinuities associated with changes in the total number of electrons. This problem is avoided in EHT (as long as the parameters are treated as fixed) and this aids in interpretation. The calculations can be efficiently performed using a Python interface on a laptop. Compared with DFT results, EHT provides qualitatively reasonable orbital energies and frontier orbital compositions as a function of structural distortions at a much lower computational cost.

2.2.3 Density functional theory

2.2.3.1 Hohenberg-Kohn theorem

The limitations of the Hartree-Fock approximation to the Schrödinger equation were previously discussed in Chapter 2.2.1, which neglects electron correlation. It does, however, provide a convenient starting point for further theoretical improvement. Approaches include developing wavefunction-based methods, and re-formulating the expression for the exchange-correlation energy which is the key idea in density functional theory.

The earliest form of density functional theory, a density-based equation to calculate the energy, was provided by Thomas and Fermi in 1927.[41,42]

$$E = \frac{3}{10}(3\pi^2)^{2/3}\int[\rho(r)]^{5/3}dr + Z\int\frac{\rho(r)}{r}dr + \frac{1}{2}\int\frac{\rho(r)\rho(r')}{|r-r'|}drdr' \tag{2.2.22}$$

In the Thomas-Fermi equation, the kinetic energy, electron-nuclear attraction and electron-electron repulsion are all expressed as a functional of electron density $\rho(r)$. The direct connection between the energy and density greatly simplifies the number of variables involved from $4N$ (N is the number of particles) to 3 (the three orthogonal directions in which the density, $\rho(x, y, z)$, can vary). The significance of this equation lies in its ability to relate the total energy of a system directly to its electron density. The major drawback of this method, however, is its poor accuracy in estimating the

electron kinetic energy and the absence of explicit terms for exchange and correlation. Since this equation relies only on the electron density, with no reference to orbitals, it is regarded as a representative of 'orbital-free' density functional theory.

In 1965, Hohenberg and Kohn first proposed that the external potential is uniquely determined by the ground state electron density for any system of interacting electrons.[43] The external potential V_{ext} can be a medium, which establishes the unique relationship between the ground state electron density with the Hamiltonian. With this connection, all properties including the wavefunction can, in principle, be generated from the ground-state electron density. The energy can then be expressed as:

$$E[\rho] = T[\rho] + V_{ee}[\rho] + \int \rho(r) V_{ext}[\rho] dr \tag{2.2.23}$$

The second Hohenberg-Kohn theorem deals with the variational principle. It states that the ground-state energy is lower than or equal to the energy derived from any trial density $\widetilde{\rho}$.

$$\langle \widetilde{\Psi} | \hat{H} | \widetilde{\Psi} \rangle = T[\widetilde{\rho}] + V_{ee}[\widetilde{\rho}] + \int \widetilde{\rho}(r) V_{ext} dr = E[\widetilde{\rho}] \geq E_0[\rho_0] = \langle \Psi | \hat{H} | \Psi \rangle \tag{2.2.24}$$

2.2.3.2 Kohn-Sham formalism

The Hohenberg-Kohn theorem provides the foundation for a further evolution to the Kohn-Sham formalism by highlighting the importance of the ground state density. However, the challenge in calculating the kinetic energy in the Thomas-Fermi equation remained to be solved. Kohn and Sham realised that this term could be calculated more accurately using a wavefunction and an orbital basis, from which the density could be easily generated as the sum of the squares of the wavefunctions of the occupied orbitals φ_i.[44]

$$\rho(r) = \sum_{i}^{N} |\varphi_i|^2 \tag{2.2.25}$$

The Hamiltonian in the Kohn-Sham equation ($\hat{f}^{KS}$) is written as a kinetic energy term plus an effective potential term. The orbital energies and wavefunctions are obtained as the eigenvalues and eigenfunctions. Each φ_i is referred to as a 'Kohn-Sham orbital'. The total wavefunction is constructed by a single Slater determinant composed of these orbitals, as in the Hartree-Fock ansatz.

$$\hat{f}^{KS} \varphi_i = \epsilon_i \varphi_i \tag{2.2.26}$$

$$\hat{f}^{KS} = -\frac{1}{2}\nabla^2 + \hat{V}_{eff} \tag{2.2.27}$$

The kinetic energy T_S is computed as in the Hartree-Fock framework as follows:

$$T_S = -\frac{1}{2}\langle\varphi_i|\nabla^2|\varphi_i\rangle \tag{2.2.28}$$

The effective potential operator is the sum of the nucleus-electron attraction $\hat{V}_{ne}[\rho(r)]$, classical Coulomb repulsion $\hat{J}[\rho(r)]$ and exchange-correlation interactions $\hat{V}_{xc}[\rho(r)]$.

$$\begin{aligned}\hat{V}_{eff}(r) &= \hat{V}_{ne}[\rho(r)] + \hat{J}[\rho(r)] + \hat{V}_{xc}[\rho(r)] \\ &= -\sum_A \frac{Z_A}{|r - R_A|} + \int \frac{\rho(r')}{|r - r'|}dr' + \hat{V}_{xc}\end{aligned} \tag{2.2.29}$$

The exchange-correlation term that emerges in the equation is a complex one: it contains the exchange energy as well as the difference in kinetic energy between the interacting (as $T[\rho]$) and non-interacting system (as $T_S[\rho]$), the corrections to the self-interaction error, and also correlation between electrons. Nevertheless, the Hohenberg-Kohn theorem states that, if an exact form of V_{xc} were known, the equation would yield the exact energy of the system without any approximation. Unfortunately, the exact form of V_{xc} is unknown, and we can only approximate it. A detailed discussion of common exchange-correlation functionals is reserved for Section 2.2.3.4.

$$V_{xc} = \frac{\delta E_{xc}}{\delta \rho} \tag{2.2.30}$$

$$E_{xc}[\rho(r)] = (T[\rho] - T_S[\rho]) + (E_{ee}[\rho] - J[\rho]) \tag{2.2.31}$$

The Kohn-Sham equations are, like the Roothaan-Hall equations, non-linear, and iterative techniques are required. The trial electron density can be optimised, the variational principle guarantees that the process approaches the ground state.

The chemical significance of the Kohn-Sham orbitals still remains controversial: in principle, the orbitals exist only as a means to generate the density. Nevertheless, Hoffmann has argued that they are very similar to Hartree-Fock orbitals, and they are usually interpreted in the same way.[45] In the following chapters, I will make extensive use of the Kohn-Sham orbitals to analyse the chemical bonding in molecular systems.

2.2.3.3 Unrestricted framework

In the discussion above, it is assumed that orbitals of both spin-α and spin-β sets share the same spatial part — this is called Restricted Kohn-Sham Density Functional Theory (RKS-DFT) or Restricted Hartree-Fock (RHF). However, a restricted calculation cannot accommodate dissociated H_2, where one electron (α or β) necessarily

ends up on one H atom and the other electron on the other. If we lift the restriction of identical spatial distributions for both spins, an Unrestricted Kohn-Sham Density Functional Theory (UKS-DFT) formalism is reached. In this ansatz, the majority and minority orbital arrays are optimised separately in the SCF cycle by solving two sets of Roothaan equations, which doubles the computational cost. In the H_2 case, the unrestricted method can correctly describe the dissociation limit as a combination of two hydrogen atoms, where the spin-α density locates on one H and spin-β on the other. Even though it corrects the density distribution, the unrestricted approach breaks the symmetry of the wavefunction, as the α and β spin density may localise on different parts of the molecule, a so-called 'broken-symmetry' state. The wavefunction is then not an eigenfunction of the spin operator, $\hat{S}^2$, which is called spin contamination. As a result, an unrestricted DFT/HF wavefunction can be regarded as the wavefunction of the corresponding spin state mixed with some higher spin state wavefunctions. For example, the unrestricted wavefunction for H_2 at its dissociation limit is a 50:50 mixture of singlet and triplet states. More generally, an unrestricted 'doublet' ($^2\Psi_{unrestricted}$) can be considered as a combination of wavefunctions of higher spin states such as quartet, sextet, octet and so on.

$$^2\Psi_{unrestricted} = c_1{}^2\Psi_{res} + c_2{}^4\Psi_{res} + c_3{}^6\Psi_{res} + ... \tag{2.2.32}$$

In order to obtain a wavefunction as an eigenstate of the spin operator, it is possible to treat the doubly occupied orbitals in a restricted way and the singly-occupied orbitals as unrestricted — a so-called restricted open-shell calculation (Restricted Open-Shell Hartree-Fock (ROHF) or Restricted Open-Shell Density Functional Theory (RODFT)). It can compensate for the drawback that the unrestricted Hamiltonian does not necessarily commute with the spin operator, but still fails for dissociated H_2 due to its lack of spatial flexibility. If we wish to retain both spin and spatial symmetry of the wavefunction, it is necessary to use more than one Slater determinant to represent the wavefunction, as CSFs in CASSCF. These methods will be introduced in the next section.

2.2.3.4 Functionals

The exchange-correlation energy in DFT constitutes a relatively small but essential component of the total energy. If the exact exchange-correlation functional were known, DFT would yield the exact ground-state energy for the Schrödinger equation. However, this exact functional remains unknown and is, in practice, unattainable.

Therefore, one of the main topics in DFT is the development of suitable approximations for the exchange-correlation functional. Since the central idea of DFT is to construct the total energy as a functional of the electron density, a natural starting point is to approximate the exchange-correlation energy directly using the local value of the electron density. This leads to the Local Density Approximation (LDA). For spin-unrestricted systems, the method can be extended to treat the spin-up and spin-down electron densities separately, resulting in the Local Spin Density Approximation (LSDA). The LDA gives accurate predictions for the model homogeneous electron gas system, where the constant electron density assures an exact exchange energy. It can also be extended to inhomogeneous systems like molecules by dividing the system into grids inside which the density can be considered as locally homogeneous.

$$E_{xc}^{LDA}[\rho] = \int \rho(r)\epsilon_{xc}(\rho(r))dr \tag{2.2.33}$$

The exchange-correlation energy can be further decomposed into the exchange part ϵ_x and correlation part ϵ_c. The success of LDA for systems with inhomogeneous electron densities is often attributed to a fortuitous error cancellation of the underestimated exchange energy and the overestimated correlation energy, as well as the good prediction of the spherical average of the pair density. The most commonly used LDA functionals include VWN (Vosko, Wilk and Nusair),[46] which is named after the developers.

The LDA serves as a foundational reference for the development of more sophisticated exchange-correlation functionals. An improved method is the Generalised Gradient Approximation (GGA), in which the functional depends not only on the local electron density but also on its first derivatives (gradients). Both exchange and correlation parts in GGA are based on the LDA approximation with an additional correction term comprising the gradient of the density. The empirical parameters in GGA functionals can be constructed either by fitting to experimental data or high-level theoretical results, or based on fundamental conditions that the correct functional should meet. The extensively used PBE (Perdew-Burke-Ernzerhof) functional[47] in this thesis is based on this second approach. Other common GGA functionals include BP86 (Becke for exchange, Perdew for correlation, 1986),[48,49] PW91 (Perdew-Wang 1991)[50] and BLYP (Becke for exchange, Lee-Yang-Parr for correlation).[48,51] In practical terms, the GGA often performs better than LDA in calculations of transition energy barriers, structural properties and dissociation energies.

$$E_{xc}^{GGA}[\rho_\sigma] = \int f[\rho_\sigma(r), \nabla\rho_\sigma(r)]dr \tag{2.2.34}$$

A natural extension to GGA is to add the Laplacian of the electron density (its second derivative) or the kinetic-energy density as a variable in the approximation alongside the local density and its gradient — so-called meta-GGA functionals. Specific examples include TPSS (Tao-Perdew-Staroverov-Scuseria)[52] and M06-L (Minnesota 06 - local)[53,54] which incorporate the kinetic-energy density.

$$E_{xc}^{meta\text{-}GGA}[\rho_\sigma] = \int f[\rho_\sigma, \nabla\rho_\sigma(r), \nabla^2\rho_\sigma(r)]dr \tag{2.2.35}$$

$$E_{xc}^{meta\text{-}GGA}[\rho_\sigma] = \int f[\rho_\sigma, \nabla\rho_\sigma(r), \tau]dr \tag{2.2.36}$$

Even though Hartree-Fock theory does not capture the correlation energy, the exact expression for the exchange term can also be incorporated into the DFT framework to improve its performance. The so-called hybrid functionals achieve this by replacing a portion of the DFT exchange energy with the Hartree-Fock description, while keeping the correlation term from the DFT approximation. The mixing parameter can be determined by fitting to experiment — 20% in B3LYP (Becke, 3-parameter, Lee-Yang-Parr)[55] or from theoretical foundations, as in the 25% used for PBE0 (Perdew-Burke-Ernzerhof Hybrid).[56,57] Hybrid functionals require an additional overhead compared to pure DFT because the Hartree-Fock exchange part has to be calculated. As a result of the addition of a fraction of exact exchange energy, increasing the fraction of exact exchange often stabilises high-spin states relative to low-spin states, particularly in transition-metal systems. Indeed, the energy gap between high-spin and low-spin states often varies linearly with the amount of exact exchange included. Moreover, hybrid functionals help reduce self-interaction error and often yield more accurate estimates for some properties such as the HOMO-LUMO gap.

$$E_{xc}^{hybrid} = \alpha E_x^{HF} + (1-\alpha)E_x^{GGA} + E_c^{GGA} \tag{2.2.37}$$

All the functionals mentioned above represent different strategies for approximating the exchange-correlation energy, but none is guaranteed to reproduce the true ground-state energy. It is, therefore, critical to choose an appropriate functional for a particular research problem. I will discuss the choice of functionals and the impact of the choice at various points in the following chapters.

2.3 Post-Hartree-Fock methods

2.3.1 Configuration interaction

DFT provides an efficient pathway for solving the Schrödinger equation by approximating an interacting electron system through a non-interacting model, utilising approximate exchange-correlation functionals. In contrast, wavefunction-based methods derived from HF theory aim to enhance the description of electron correlation by explicitly refining the electronic wavefunction. The HF approximation employs a single Slater determinant, inherently capturing exchange interactions but omitting correlation energy entirely. To overcome this limitation, advanced wavefunction-based methods can be introduced. One fundamental method in this category is the Configuration Interaction approach. In the CI framework, the wavefunction is expressed as a linear combination of Slater determinants, each corresponding to distinct electronic configurations based on HF orbitals. To achieve spin adaptation — wavefunction as eigenfunctions of spin operators $\hat{S}^2$ and $\hat{S}_z$ — CSFs can be employed to replace Slater determinants to represent the wavefunction. These CSFs, which themselves are linear combinations of Slater determinants, guarantee the proper spin symmetry of the total wavefunction. If a CI calculation incorporates every possible Slater determinant or CSFs within a given basis set, it is termed a Full Configuration Interaction (Full CI) calculation. Full CI provides the exact correlation energy achievable within the chosen basis set. Thus, the exact correlation energy within the given basis set at the HF level of approximation can be precisely quantified as the energy difference between the Full CI and the corresponding HF calculation.

$$E_{corr} = E_{FCI} - E_{HF} \tag{2.3.1}$$

However, in practical quantum chemical calculations, reaching the Full CI limit is generally infeasible due to the exponential scaling with system size. Therefore, truncations are necessary to balance computational cost and accuracy. These truncations are typically made by classifying Slater determinants or CSFs according to the number of excited electrons relative to the HF reference. For example, Configuration Interaction Singles (CIS), Configuration Interaction Singles and Doubles (CISD), and Configuration Interaction Singles, Doubles, and Triples (CISDT) include single, single-double, and single-double-triple excitations, respectively.

$$\Psi_{CI} = c_0\Psi_{HF} + \sum c_S\Psi_S + \sum c_D\Psi_D + \sum c_T\Psi_T + \sum c_Q\Psi_Q + ... \tag{2.3.2}$$

This excitation-based truncation is convenient and widely used. However, for ground-state calculations, Brillouin's theorem implies that singly excited determinants do not directly interact with the ground state and thus do not contribute straightforwardly to the correlation energy. As a result, CISD is often the minimal meaningful level for capturing electron correlation, where doubly excited determinants provide the dominant contribution, while singly excited configurations contribute indirectly through interaction with double excitations. Higher-level truncations such as Configuration Interaction Singles, Doubles, Triples, and Quadruples (CISDTQ) include triple (T) and quadruple (Q) excitations. Because the electronic Hamiltonian contains at most two-body operators, determinants differing by more than two spin orbitals do not couple directly. Therefore, triple excitations do not couple directly to the reference determinant, but may do so weakly through the doubly-excited states. Quadruple excitations, on the other hand, can interact more strongly with double excitations, enhancing their contribution to the correlation energy. In many cases, D and Q excitations dominate the correlation energy, while S and T contributions remain relatively small. Although these truncated CI methods can recover a large portion of the correlation energy for small molecules, their performance degrades with increasing molecular size. A major drawback is their lack of size-consistency, meaning that the energy of two non-interacting subsystems is not equal to the sum of their individual energies. This inconsistency arises from the improper factorisation of wavefunctions in truncated CI, which can lead to errors in computing dissociation or binding energies. In contrast, Full CI is size-consistent by construction. Nonetheless, both full and truncated CI methods obey the variational principle, guaranteeing that the computed ground-state energy is an upper bound to the exact energy and is approached from above.

2.3.2 Complete active space self-consistent field

In molecular systems, chemical behaviour is often dominated by the valence shell electrons. To make a Full CI calculation more computationally affordable, one can restrict the CI expansion to a selected set of electrons and orbitals, treating the remaining ones at the Hartree-Fock level. This forms the basis of the Complete Active Space Self-Consistent Field method.[58] A CASSCF calculation involving m active electrons distributed among n active orbitals is denoted as CAS(m, n). Within the active space, orbitals can exhibit fractional occupation numbers, typically ranging between 0 and 2. In contrast, core orbitals remain fully occupied, and secondary orbitals remain unoccupied. For active orbitals, a typical range of occupation numbers lies

between 0.02 and 1.98, reflecting their involvement in electron correlation. Active orbitals are usually included as pairs, such as bonding and antibonding orbitals, to effectively describe static correlation. The active space can also be constructed by explicitly including the designated valence orbital shell, ensuring all related valence electrons and orbitals are treated at the multi-configurational level. An initial guess for the active space can be obtained using Møller-Plesset Second-Order Perturbation Theory (MP2).[59] Orbitals with natural occupation numbers between 0.05 and 1.95 in MP2 are often good candidates for the active space. Due to the exponential growth of CSFs with the number of electrons and orbitals, current computational capabilities limit CASSCF to roughly CAS(20e, 20o) in systems without symmetry. Approximations or truncations are required when calculating a larger active space. Variants of CASSCF include the Restricted Active Space (RAS)[60] and Generalised Active Space (GAS) methods,[61] both of which aim to reduce the number of CSFs while retaining the essential correlation effects. A schematic illustration is exhibited in Figure 2.1 (a). RAS partitions the active space into three subspaces: RAS1, RAS2, and RAS3. A limited number of electrons are allowed to excite from RAS1 and into RAS3, while RAS2 is treated as a full Complete Active Space (CAS). Typically, orbitals in RAS1 have occupation numbers close to 2, and those in RAS3 have occupations close to 0. GAS, on the other hand, divides the active space into groups where electron excitations are only allowed within each subspace, while inter-group excitations are forbidden. This block-wise structure is commonly employed as a selective treatment of electron correlation, allowing the separation of excitations associated with different bonding characters. Both RAS and GAS approaches effectively reduce the number of configurations in the wavefunction, allowing the treatment of larger systems while preserving the dominant correlation effects essential for accurate electronic structure calculations.

As mentioned above, CI calculations are typically performed using a fixed set of orbitals to solve the multi-determinant problem. However, in the CASSCF method, the orbitals within the active space are not kept fixed but are optimised self-consistently along with the CI coefficients to minimise the total energy. This is achieved by introducing orbital rotations in addition to the standard CI coefficient updates, forming an SCF procedure. The energy is minimised variationally under the constraints of orbital orthonormality and normalised wavefunction coefficients, forming the mathematical foundation of CASSCF. By allowing both the orbitals and the configuration mixing to adapt, CASSCF can effectively capture static correlation.

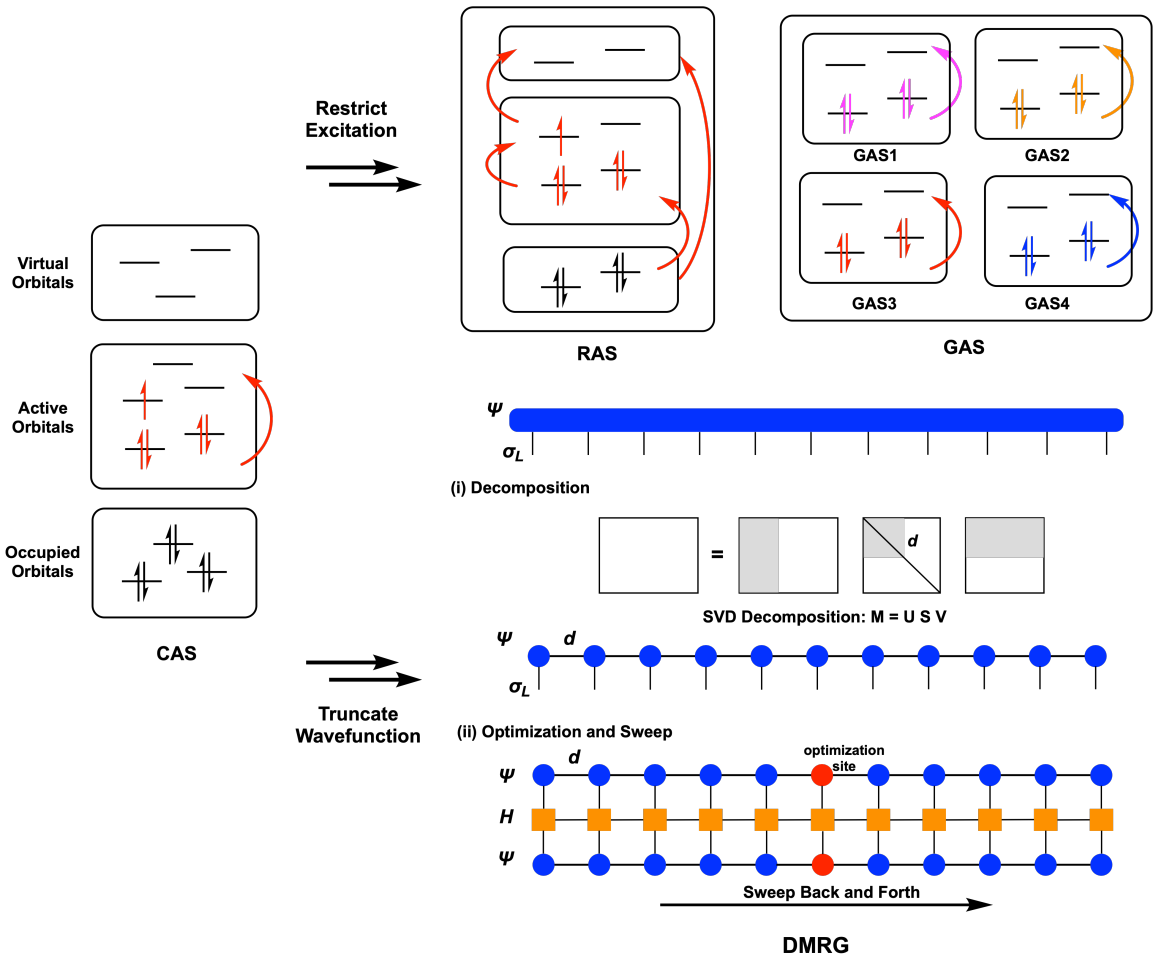

Figure 2.1: Schematic illustration of CASSCF and related approximate approaches: RASSCF and GASSCF restrict electron excitations within the active space, while DMRG compresses the wavefunction using tensor decomposition.

2.3.3 Density matrix renormalisation group theory

Full CI within the active space of a CASSCF calculation limits the size of the active space due to its exponential growth of the computational cost. For systems containing more than two transition metals, it often becomes computationally prohibitive to include all valence d orbitals without approximation. To address these limitations, methods based on restricting electron excitations, such as the RAS and GAS approaches, have been developed and mentioned above. In this section, an alternative CI solver based on density matrix truncation will be introduced, known as the Density Matrix Renormalisation Group method, which enables the treatment of an active space as large as 100 electrons in 100 orbitals, while maintaining accurate correlation effects. DMRG was first proposed by Steven White for strongly correlated one-dimensional systems, such as Heisenberg spin chains.[62,63] Its applicability

was later extended to quantum chemistry by combining the formalism with Matrix Product State (MPS) and Matrix Product Operator (MPO) forming the basis of modern DMRG implementations.[64,65] In this framework, orbitals in the active space are regarded as aligned in a one-dimensional chain. The wavefunction is decomposed into a product of local wavefunctions, one for each orbital (called a site), in the style of MPS. This allows the replacement of the prohibitively large Full CI wavefunction with a sequence of localised tensors with a restricted bond dimension, significantly reducing the computational complexity. Each site (n_i), corresponding to an orbital in the active space, can exist in four possible occupation states: (1) doubly occupied, (2) singly occupied with spin-up, (3) singly occupied with spin-down, and (4) unoccupied.

$$|n_i\rangle = \{|\uparrow\downarrow\rangle; |\uparrow\rangle; |\downarrow\rangle; |\ \rangle\} \tag{2.3.3}$$

A Full CI wavefunction, which is a linear combination of CSFs, can be re-written in the following form

$$|\Psi\rangle = \sum_{n_1 n_2 n_3 \ldots n_L} c^{n_1 n_2 n_3 \ldots n_L} |n_1 n_2 n_3 \ldots n_L\rangle \tag{2.3.4}$$

Here, $|n_1 n_2 \ldots n_L\rangle$ denotes the basis states representing all possible occupations of L spatial orbitals in the active space, where each n_i corresponds to one of the four possible local states. The coefficients $c^{n_1 n_2 \ldots n_L}$ represent the amplitudes of the respective configurations. The total number of such basis states grows exponentially as 4^L. Since the CSFs form an orthonormal basis in the Full CI space, the wavefunction $|\Psi\rangle$ can be interpreted as a high-dimensional tensor (or vector) composed of the CI coefficients. To reduce the computational complexity, Singular Value Decomposition (SVD) is applied to factorise the Full CI coefficient tensor into a product of lower-rank tensors. At each step in the decomposition, the tensor is reshaped into a matrix and factorised as $M = USV^\dagger$, where S is a diagonal matrix containing singular values sorted in decreasing order. To make this method feasible for larger active spaces, only the largest m singular values in S can be retained, truncating the less significant contributions. In a DMRG calculation, m is defined as the bond dimension and a critical parameter that determines the accuracy of the calculation. The larger the value of m is, the more accurate the DMRG calculation can be, and the more entanglement can be retained between the neighbouring sites. If m becomes infinite, DMRG approaches Full CI within the chosen basis. Correspondingly, the unitary matrices U and $V^\dagger$ are also truncated to match this reduced dimensionality. This approximation preserves the most important information of the system while significantly reducing the computational cost. The matrix U is then reshaped into a site-local renormalised

tensor A that connects to neighbouring sites through a defined bond dimension m. By applying this decomposition sequentially from the left end of the orbital chain to the right, the wavefunction is ultimately expressed in the left-canonical MPS form

$$|\Psi\rangle = \sum_{n} \sum_{a_1 a_2 \ldots a_{L-1}} A^{n_1}_{1 a_1} A^{n_2}_{a_1 a_2} \ldots A^{n_{L-1}}_{a_{L-2} a_{L-1}} A^{n_L}_{a_{L-1} 1} |n\rangle \tag{2.3.5}$$

where $A^{n_i}_{a_{i-1} a_i}$ represents the local rank-3 MPS tensor associated with orbital i, decomposed from the coefficient vector. The superscript n_i denotes the local occupation state of the orbital, while the subscripts a_{i-1} and a_i are the auxiliary bond indices that encode entanglement between orbital i and its connecting orbitals. To maintain consistency at the boundaries of the MPS chain, the first and last tensors are treated specially by setting $a_0 = a_L = 1$. The MPS decomposition can also be performed from right to left, resulting in a right-canonical form. By combining both left- and right-normalised decompositions and meeting at a site in the middle of the tensor chain, one obtains the mixed-canonical form, which is essential for efficiently optimising the wavefunction at a specific site. The Hamiltonian can similarly be decomposed into an MPO form, where the site-local tensors can be contracted with the MPS tensors on the corresponding sites. During optimisation of the wavefunction, all MPS and MPO tensors except MPS at the site(s) being optimised are contracted along both the auxiliary indices and the physical indices. The tensor at the target site remains the variational degrees of freedom, which are updated through solving an eigenvalue equation constructed from the Lagrange multiplier. This optimisation and update process can be repeated for each localised site in forward and backward sweeps until convergence criteria are reached. This process is called 'sweeping' in DMRG. The total wavefunction is optimised as a combination of the improved site-based MPS. The schematic plot of the DMRG procedure is shown in Figure 2.1 (b).

2.3.4 Multi-configuration pair-density functional theory

CASSCF calculations use a full configuration expansion within the chosen active space to provide a balanced description of near-degenerate electronic states, which is essential for capturing static correlation. However, dynamic correlation, which arises from the instantaneous repulsion between electrons, is not effectively accounted for within the limited active space. This type of correlation is especially significant in electron-dense regions, such as the $3d$ orbitals of transition metal centres. This correlation needs to be captured by some post-MC-SCF strategies focusing on electron excitations or on capturing the instantaneous density distribution. These include

perturbation theories such as CASPT2,[21] Multi-Reference Configuration Interaction (MRCI), and MC-PDFT.[23,24] While CASPT2 and MRCI are widely used, they suffer from certain limitations. In perturbation theory, a notorious issue is the appearance of intruder states, which can lead to spuriously large dynamic correlation energies. Remedies such as level shifting are often applied to address this, but these shifts can result in unphysical problems when energy levels are artificially overlapped. Furthermore, perturbation theory can suffer from double-counting of electron correlation, when combined with MC-SCF. The method also relies on the computation of three- and four-body reduced density matrices, which are computationally demanding, even with available approximations. In contrast, MC-PDFT provides a more efficient alternative by combining the multi-configurational wavefunction from CASSCF with DFT concepts through the on-top pair density. It avoids both intruder-state problems and double-counting errors, making it a computationally attractive and conceptually consistent approach for treating dynamic correlation on top of a multi-configurational wavefunction.

The fundamental idea of MC-PDFT is to use an on-top density functional to calculate the exchange-correlation energy based on the MC-SCF density. The one- and two-electron reduced density matrices ($\rho(r_1)$ and $P(r_1, r_2)$) and the on-top pair density ($\Pi(r)$) can be represented as

$$\rho(r_1) = N \int \Psi^*(x_1, x_2, ..., x_N)\Psi(x_1, x_2, ..., x_N)d\sigma_1 dx_2 dx_3 ... dx_N \tag{2.3.6}$$

$$P(r_1, r_2) = \frac{N(N-1)}{2} \int \Psi^*(x_1, x_2, ..., x_N)\Psi(x_1, x_2, ..., x_N)d\sigma_1 d\sigma_2 dx_3 ... dx_N \tag{2.3.7}$$

$$\Pi(r) = P(r_1, r_2)|_{r_1=r_2=r} \tag{2.3.8}$$

The one-electron density refers to the probability of finding an electron at r_1, therefore the integration is carried out only over the spin (σ_1), not the spatial coordinate (r_1) of electron 1. The pair density shows the probability of simultaneously finding an electron at r_1 and another at r_2. The on-top pair density represents the probability of finding two electrons at the same place, r.

The MC-PDFT energy can be calculated following the equation as

$$E = V_{NN} + T_e + V_{Ne} + V_{ee} + E_{on\text{-}top}[\rho, \Pi] \tag{2.3.9}$$

The energy is composed of classical interactions between all nuclei and electrons, the electron kinetic energy, and an on-top exchange-correlation energy ($E_{on\text{-}top}[\rho, \Pi]$) that depends on the electron density and on-top pair density. The kinetic energy, electron

density and on-top density are all obtained from the preceding MC-SCF calculation. V_{NN} and V_{Ne} can be evaluated using the electron density in conjunction with the known nuclear positions. The electron-electron repulsion term already incorporates the static correlation by the MC-SCF density. The electron correlation in the on-top functional accounts only for the correlation ignored in the active space, which mostly corresponds to the dynamic correlation. To incorporate the on-top pair density into functionals, the standard Kohn-Sham Density Functional Theory (KS-DFT) functionals need to be translated into the MC-PDFT formalism. This is achieved by introducing the spin density m as an auxiliary variable, allowing the exchange-correlation energy to be expressed in the form $E_{xc}(\rho, m)$. The spin density can be rewritten as a function of the total electron density $\rho(r)$ and the on-top pair density $\Pi(r)$, providing a bridge between standard DFT and MC-PDFT as

$$R(r) = \frac{4\Pi(r)}{\rho(r)^2} \tag{2.3.10}$$

$$m(r) = \rho(r)[1 - R(r)]^{1/2} \tag{2.3.11}$$

where $R(r) \leq 1$ as a consequence of the Pauli principle in the single-determinant framework. However, in a multi-determinant calculation, $R(r)$ can be greater than 1. The translated functional in the MC-PDFT concept proposed a categorised format for different ranges of R.

$$\begin{aligned} E_{ot}[\rho, \Pi] = E_{xc}\Bigg(& \rho(r), \begin{cases} \rho(r)(1 - R(r))^{1/2} & \text{if } R \leq 1 \\ 0 & \text{if } R > 1 \end{cases}, \\ & \rho'(r), \begin{cases} \rho'(r)(1 - R(r))^{1/2} & \text{if } R \leq 1 \\ 0 & \text{if } R > 1 \end{cases} \Bigg) \end{aligned} \tag{2.3.12}$$

This equation corresponds to a translated functional derived from a GGA functional in KS-DFT, in which the gradients of both the electron density and the spin density are incorporated. However, a known drawback of this approach is its potential discontinuity in the spin-density-dependent terms at $R(r) = 1$. Specifically, the term $\rho(r)(1 - R(r))^{1/2}$ is forced to vanish when $R(r)$ is greater than 1, resulting in unphysical behaviour and non-smooth transitions in regions of strong correlation. To resolve this issue, a fully-translated functional was developed.[24] This refined functional introduces a smooth polynomial interpolation between two threshold values, $R = R_0$ and $R = R_1$, to eliminate the discontinuity in the spin density and its gradient at $R = 1$. In addition to improved numerical stability and physical continuity,

the fully-translated functional enables the explicit inclusion of the gradient of the on-top pair density, and allows for the analytical evaluation of first and second energy derivatives, facilitating geometry optimisations and vibrational analyses within the MC-PDFT framework.

$$
\begin{aligned}
E_{ot}[\rho(r), \Pi(r)] = E_{xc}\Bigg(& \rho(r), \begin{cases} \rho(r)\,\chi_t(R) & \text{for } R < R_0 \\ \rho(r)\,\chi_{ft}(R) & \text{for } R_0 \le R \le R_1 \\ 0 & \text{for } R > R_1 \end{cases}, \\
& \rho'(r), \begin{cases} \rho'(r)\,\chi_t(R) + \rho(r)\,\chi'_t(R) & \text{for } R < R_0 \\ \rho'(r)\,\chi_{ft}(R) + \rho(r)\,\chi'_{ft}(R) & \text{for } R_0 \le R \le R_1 \\ 0 & \text{for } R > R_1 \end{cases} \Bigg)
\end{aligned}
\tag{2.3.13}
$$

$$
\chi_t(R) = (1 - R)^{1/2} \tag{2.3.14}
$$

$$
\chi_{ft}(R) = A(R - R_1)^5 + B(R - R_1)^4 + C(R - R_1)^3 \tag{2.3.15}
$$

The function $\chi_t(R)$ in the equation corresponds to the form used in the translated functional, while $\chi_{ft}(R)$ is a higher-order polynomial that ensures a smooth decay to zero at R_1. The parameters R_0 and R_1 define the interpolation range, and the coefficients A, B and C in the expression for $\chi_{ft}(R)$ are determined by enforcing continuity and differentiability conditions at the boundaries.

2.4 Basis sets

Another aspect we need to address to achieve an accurate solution to the Schrödinger Equation is how to accurately describe the atomic orbitals. The mathematical expression for atomic orbitals can be decomposed into the radial and the angular part as:

$$\psi_{n,l,m}(r,\theta,\phi) = R_{nl}(r)Y_m^l(\theta,\phi) \tag{2.4.1}$$

The radial part of an atomic orbital is described by $R_{nl}(r)$, and the angular part is given by the spherical harmonic function $Y_m^l(\theta,\phi)$. In atomic systems, the radial distribution of the wavefunction decays exponentially with increasing distance from the nucleus, whereas the angular part depends on both the angular quantum number l and the magnetic quantum number m, typically involving trigonometric functions. To represent atomic orbitals in quantum chemical calculations, mathematical basis functions are employed. A straightforward approach is to mimic the radial behaviour of atomic orbitals using an exponential form. This can be expressed as:

$$\psi_{n,l,m}(r,\theta,\phi) \propto r^{n-1}exp(-\zeta r)Y_m^l(\theta,\phi) \tag{2.4.2}$$

The radial distribution incorporates both the principal quantum number to produce nodes and an orbital exponent as ζ to describe the degree of radial diffuseness of the wavefunction. Such functions to depict the atomic orbitals are called Slater-type Functions (STFs) or Slater-type Orbitals (STOs).[66] The larger the value of ζ, the more contracted the wavefunction is. The energy of the atomic orbital can be minimised with respect to the value of ζ in a variational way in order to obtain the best description of a single atomic orbital. However, the drawback of the STOs is that the integrals involving the wavefunction are difficult — specifically, the many two-electron integrals that make up the Coulomb and exchange terms are extremely challenging with a Slater-type basis. A solution to this problem is to replace STOs with so-called Gaussian-type Orbitals (GTOs):[67]

$$\psi(x,y,z) \propto x^i y^j z^k exp(-\alpha r^2) \tag{2.4.3}$$

Here, i, j, and k are non-negative integers, and α is the orbital exponent that controls the width of the Gaussian function. The sum $i+j+k$ corresponds to the angular quantum number l, thereby determining the orbital's angular characteristics. The key difference between STOs and GTOs is in the exponent, which varies as r in the former but as r^2 in the latter. This subtle difference renders the integrations necessary for the two-electron terms much simpler, and Gaussian basis functions are

used in the majority of electronic structure calculations. One notable disadvantage of GTOs, however, is their inability to accurately reproduce the shape of atomic orbitals compared to STOs. Specifically, GTOs exhibit a gradient that is too flat near the nucleus and decay too rapidly at long distances. This discrepancy limits the accuracy of GTOs when used individually to model real electron distributions. To address this limitation, a method known as 'contracted Gaussian-type orbitals' was developed, in which a linear combination of multiple GTOs is applied to approximate a single STO. This approach is referred to as STO-nG, where n denotes the number of primitive Gaussians used in the contraction.[68] For example, the minimal basis set STO-3G uses a linear combination of three Gaussian primitives to approximate one STO. It can be written as

$$\psi_{STO-3G} = c_1\psi_1^{GTO} + c_2\psi_2^{GTO} + c_3\psi_3^{GTO} \tag{2.4.4}$$

The radial distribution comparison between a single-zeta H $1s$ STO and its STO-3G Gaussian approximation is shown in Figure 2.2: the behaviour of STO-3G is very similar to the STO that it is representing.

In molecular systems, the atomic orbitals have different radial distributions depending on the chemical environment, oxidation state, *etc.* Basis sets with a single ζ value do not have the flexibility to describe atomic orbitals with different radial extents, and so multiple basis functions with different ζ values are needed to describe an atomic orbital in all the possible chemical environments that it might be found. For instance, if we are using two ζ values, the basis sets can be expressed as

$$\psi_{n,l,m}(r,\theta,\phi) \propto r^{n-1}[c_1 exp(-\zeta_1 r) + c_2 exp(-\zeta_2 r)]Y_m^l(\theta,\phi) \tag{2.4.5}$$

which is called a double-zeta basis set. Triple-zeta and quadruple-zeta basis sets can be built up in a similar manner. The parameters of ζ still need to be optimised also in a variational manner until reaching the energy minimum.

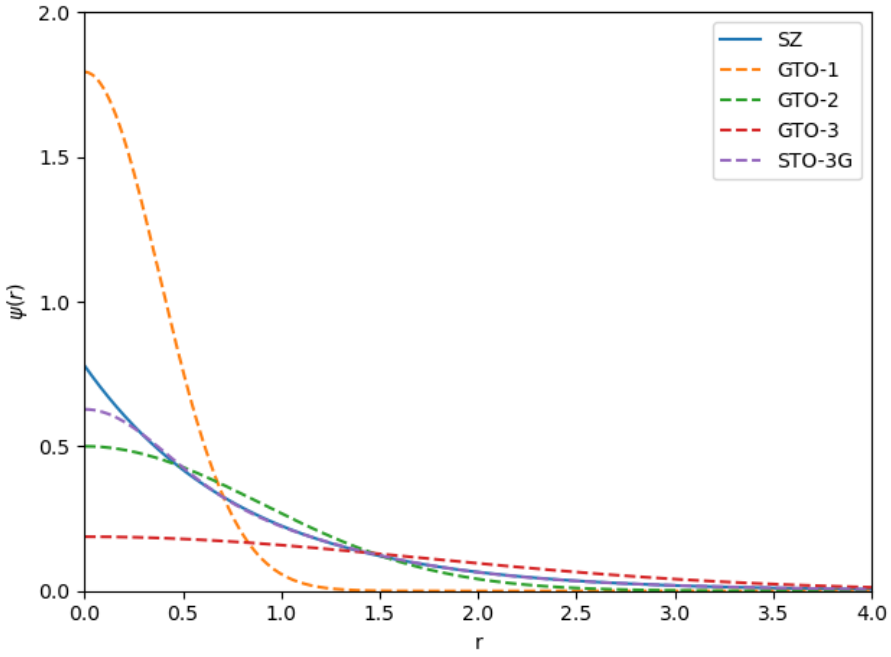

Figure 2.2: Comparison of the radial distributions of a single-zeta H 1s STO (blue solid line) and its STO-3G Gaussian approximation (purple dashed line). Three components of the STO-3G are plotted as GTO1 (orange dashed line), GTO2 (green dashed line) and GTO3 (red dashed line).

In addition to improving the radial distribution by including multiple Gaussian functions, it is also essential to enhance the angular flexibility of basis functions. This is achieved by incorporating basis functions with higher angular momentum than those required to describe the occupied atomic orbitals. These additional functions allow for orbital relaxation in response to bonding and are crucial for accurately modelling anisotropic electron distributions. For instance, p-type orbitals are added as polarisation functions when describing valence s orbitals, enabling a more flexible angular representation. In general, the inclusion of polarisation functions in an n-zeta basis set is denoted as an nZP basis set. Multiple sets of polarisation functions can be included to further increase angular flexibility; however, excessive polarisation may lead to artificial electron delocalisation and overestimation of bond strengths. Another important complement to standard basis sets is the addition of diffuse functions, which describe the long-range character of atomic orbitals. Diffuse functions are characterised by small orbital exponents, allowing electrons to extend further from the nucleus. These functions are particularly important in systems where long-range interactions or weak non-covalent interactions are significant. They are also essential for accurately describing anions, where the extra electron is more loosely bound and

resides in a spatially more diffuse region.

In this thesis, different types of basis functions are used for different purposes. For the MC-SCF calculations, basis sets are always of the GTO type — the very large number of two-electron integrals that are required make this the only practical choice. The majority of the DFT calculations in this thesis were performed with the Amsterdam Density Functional (ADF) software package,[69] which uses Slater-type basis functions (other packages such as Gaussian and ORCA use GTOs for DFT). The reason for this choice in ADF is that the two-electron integrals that are so problematic with STOs are not required for pure DFT, which has been the core functionality of ADF (although they are for hybrid functionals). There is, therefore, no particular benefit to using GTOs, and it is then practical to use STOs, fewer of which are needed to give an accurate representation of an atomic orbital. The EHT calculations also use STOs, again because two-electron integrals are not required (they are included implicitly through the parametrisation of the orbital energies and exponents). Indeed, the only integration required is the overlap integral, which is only marginally more difficult with STOs than GTOs.

Chapter 3

Electronic Structures of Open-Shell Endohedral Zintl Clusters

3.1 Introduction

3.1.1 Introduction to endohedral clusters

Endohedral clusters containing one or more transition metal atoms inside a shell of main-group atoms represent an increasingly diverse family of molecules that exhibit remarkable electronic properties.[70] The notation '@' is commonly used to denote encapsulation. The nature of the interactions between the encapsulated metal and the surrounding cage is extremely flexible, varying from strongly covalent through to much weaker London-type forces. In the latter scenario, the metal is trapped inside the cluster only by the high barrier to passing through the wall of the cage. Investigations into endohedral clusters originated with fullerenes, and LaC_{60} was synthesised *via* laser vapourisation of graphite and La_2O_3 in 1985.[71] Like many clusters of this type, it was identified using mass spectrometry and recognised as the first observed endohedral metallofullerene. Since then, the family of endohedral metallofullerenes has expanded to include a variety of encapsulated species, including di-metal, tri-metal fragments as well as metal-nitride and metal-carbide units.[72,73] Examples are shown in Figure 3.1 (a).[74–76] The encapsulated species are mostly metals from the lanthanide and actinide series, which interact with the shell primarily *via* charge transfer.

Moving beyond carbon-based metallofullerenes, the *p*-block elements from the third period including aluminium and silicon can also form endohedral clusters, with aluminium species typically encapsulating other main-group elements (Figure 3.1 (b)),[77] while silicon has been shown to encapsulate many transition metals (Figure 3.1 (c)).[78,79] The $[AlAl_{12}]^-$ cluster was the first confirmed example of a 'superatom', so-named because its 40-electron configuration generates a closed electronic shell,

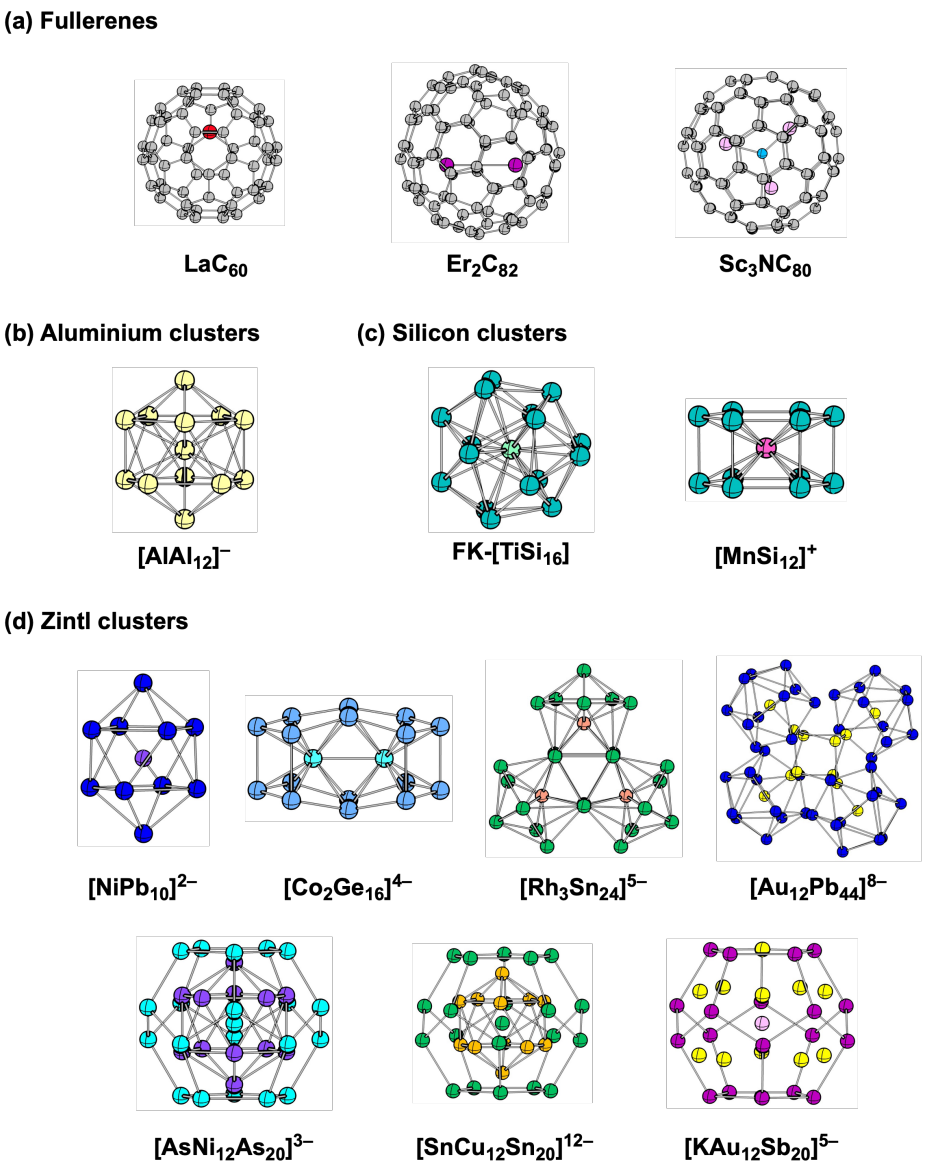

Figure 3.1: Geometries of representative endohedral clusters, including (a) endohedral metallofullerene and endohedral cluster fullerene; (b) aluminium cluster; (c) FK-type and three-connected silicon clusters; (d) endohedral Zintl clusters from single metal doped to giant Matryoshka clusters.

and in that sense it mimics the properties of a noble gas element.[77] By tuning the dopant, superhalogen and superchalcogen clusters can be created by shifting the electron count relative to $[AlAl_{12}]^-$.[80,81] Unlike carbon, silicon shows a reduced tendency to undergo s/p hybridisation and also a reduced inclination to form π bonds, both of which destabilise fullerene-like electron delocalisation. Silicon clusters can adopt either electron-deficient deltahedral Frank-Kasper (FK) structures, or three-connected networks resembling fullerenes.[70,78,82] Cluster size ranges from MSi_{10} to MSi_{20}, where

the dopant plays a key role in determining the cage size and conformation. However, experimental characterisation of these gas-phase clusters still relies heavily on spectroscopic techniques (primarily infrared), and theory has a vital role to play in aiding the interpretation of this data.

Clusters of the heavier Group 14 elements, such as Ge, Sn and Pb (Zintl clusters), are the main focus of this chapter. Examples are shown in Figure 3.1 (d).[83–89] In contrast to electron-rich metallofullerenes, the heavier analogues adopt frameworks with highly connected vertices, much like the boranes, and this structural category is with very typical of electron-deficient bonding. Typical sizes are also very different: fullerenes like C_{60} have a diameter of ∼7 Å whereas simple Zintl clusters such as $[Pb_{12}]^{2-}$[90] and $[Pb_{10}]^{2-}$[91] are smaller by about 1 Å and can usually accommodate only a single transition metal. The first example of endohedral Zintl clusters, $[PtPb_{12}]^{2-}$, was synthesised by Esenturk and co-workers, swiftly followed by $[MPb_{12}]^{2-}$ and $[MPb_{10}]^{2-}$ (M = Ni, Pd, Pt).[92] The endohedral metals in these clusters have an inert d^{10} configuration, and the remaining valence electrons make up the skeletal electron count for the cage, following the Wade-Mingos rules.[12–15] For example, the 60 valence electrons in $[PtPb_{12}]^{2-}$ can be partitioned into a d^{10} configuration at the metal and $50 = 4n+2$, the typical count for a *closo* cluster, on the cage (where n is the number of vertices, here $n = 12$). The details of the electron-counting rules will be introduced in the following paragraph.

Endohedral Zintl clusters are now known with 9 to 14 vertices, and their structures can be classified based on their topology according to the Wade-Mingos rules. For example, 10-vertex $[RhSn_{10}]^{3-}$ and 12-vertex $[RhSn_{12}]^{3-}$,[85] and $[MPb_{12}]^{3-}$ (M = Co,[93] Rh,[85] Ir[94]) can be classified as *closo*-type. *Nido*-type clusters are less common, but include 9-vertex $[CoGe_9]^{5-}$,[95] $[NiSn_9]^{4-}$,[96] $[CuE_9]^{3-}$ (E = Sn, Pb),[97] $[CoSn_9]^{5-}$,[98] and 11-vertex $[AgPb_{11}]^{3-}$.[86] Larger Zintl clusters can form by expanding or fusing individual cages. Examples of vertex-sharing clusters that accommodate multiple transition metals include $[Ni_2Sn_{17}]^{4-}$,[99] $[Pt_2Sn_{17}]^{4-}$,[100] $[Co_2Sn_{17}]^{5-}$,[101] and $[Rh_2Sn_{17}]^{6-}$.[85] Transition metals can also occupy the bridging vertex, as for example in $[Cd(NiSn_9)_2]^{6-}$,[102] $[In(NiGe_9)_2]^{5-}$,[103] $[Au_8Pb_{33}]^{6-}$ and $[Au_{12}Pb_{44}]^{8-}$.[104] Alternatively, clusters can form through face-sharing or fusion, leading to an integrated cage that encapsulates multiple transition metals within a single cage structure. Examples include $[Ni_2Bi_{12}]^{4+}$,[105] $[Ni_2E_7Pn_5]^{3-}$ (E = Sn, Pn = Sb, Bi; E = Pb, Pn = Bi),[106–108] $[Co_2Sn_5Sb_7]^{3-}$,[106] $[Co_2Ge_{16}]^{4-}$,[84] $[Cu_4E_{18}]^{4-}$ (E = Sn, Pb),[109] $[Pd_2E_{18}]^{4-}$ (E = Ge,[110] Sn[111]), $[Ni_3Ge_{18}]^{4-}$,[112] $[Rh_3Sn_{24}]^{5-}$.[85] This latter class is particularly relevant to this

thesis, as the presence of multiple metals inside a continuous cage admits the possibility of metal-metal bonding. At the extreme of structural complexity, onion-like Matryoshka clusters such as $[SnCu_{12}Sn_{20}]^{12-}$ [88] and $[AsNi_{12}As_{20}]^{3-}$ [87] represent the highest level of hierarchical encapsulation. These multi-layered clusters offer unique opportunities for superatom investigations.

Endohedral clusters with closed electronic shells (d^{10}) typically adopt a highly symmetric, almost spherical structure, but open-shell analogues are often distorted. The distortion reflects the increasingly active role of the d orbitals, which can transfer electron density to the cage, driving distortion. For example, the 10-vertex $[FeSn_{10}]^{3-}$ adopts a distorted C_{2v} geometry in contrast to the D_{4d} structure of the $[NiPb_{10}]^{2-}$.[17] An even more pronounced structural change is observed in $[FeGe_{10}]^{3-}$, which is a pentagonal prismatic cage with D_{5h} symmetry.[18] Similar patterns can be discerned in the 12-vertex family, where the D_{2h}-symmetric $[MnPb_{12}]^{3-}$ represents a slightly distorted form of the icosahedron adopted by $[NiPb_{12}]^{2-}$,[16] while $[RuGe_{12}]^{3-}$ has a D_{2d}-symmetric fullerene-like structure.[19] The open-shell clusters noted here have formal d-electron counts of less than 10, but geometric distortion can also be triggered by excess electrons, for example in D_{5d}-symmetric $[AuPb_{12}]^{3-}$, which can be formulated as $(Au)^{+}@(Pb_{12})^{4-}$.[104] The presence of two additional electrons on the cage, over and above the 50 electrons needed to fill the bonding orbitals of a perfect icosahedron, drives the distortion from I_h symmetry.

Even though various larger Zintl clusters have been synthesised, the cluster growth pathways have not been extensively studied. It is appealing to think of modular pathways where larger clusters can be constructed by the fusion of smaller pre-formed fragments, but it is difficult to find experimental evidence to support or refute this idea. A comprehensive study has been performed for $[Au_{12}Pb_{44}]^{8-}$, where coinage metals doped on the cage act as electron acceptors, accepting electron density from the main-group elements and stabilising the cage expansion. A well-defined growth sequence has been proposed based on structural similarities between $[AgPb_{11}]^{3-}$,[86] $[Cu_4Pb_{22}]^{4-}$,[113] and $[Au_8Pb_{33}]^{6-}$,[86] all of which have been characterised using X-ray crystallography.

3.1.2 Stability of clusters

The stability of encapsulated clusters, particularly their cage structures, is intrinsically linked to the encapsulated fragment, which can influence the electron count of the cage through charge transfer. For spherical π-systems, such as fullerenes, cage stability can be explained *via* the concept of spherical aromaticity proposed by

Hirsch.[114] An aromatic electron count is given by the formula $2(N+1)^2$, where N refers to a positive integer, and some Zintl clusters, often composed of Group 15 elements, possess electron counts that allow their stability to be rationalised more straightforwardly using the octet rule. For electron-deficient clusters, the traditional two-centre-two-electron bonding model is insufficient to explain their skeletal structures, simply because there are insufficient electrons to assign a pair to each short interatomic contact. This limitation is particularly evident in boron clusters, where multi-centre bonding plays a crucial role in stabilising the framework. The presence of such delocalised bonds necessitates the development of a systematic correlation between the architecture of the cluster and its valence electron count. The isolobal relationship between a BH fragment and a tetrel atom suggests that the framework developed to understand borane cluster chemistry should be applicable to the Zintl cluster family. The Wade-Mingos rules, which are widely used to interpret the structural chemistry of electron-deficient compounds, specifically predict the electron count required for different cluster structures based on their vertex count, n, for the deltahedral cluster family. The prototype structures and electron counts predicted by the Wade-Mingos rules are shown in Figure 3.2 (a). For a *closo* cluster, which is a fully closed deltahedral structure, the closed-shell electron count is $4n+2$, where n is the number of vertices. This corresponds to the occupation of all the s orbitals ($2n$), one in-phase combination of inwardly-directed radial p orbitals (2), and the bonding combinations of the tangential p orbitals ($2n$). If one vertex is removed from the *closo* structure, a *nido* structure forms, with an electron count of $4n+4$, and further vertex removal leads to an *arachno* cluster, which requires $4n+6$ electrons. The *hypho* structure, which has three fewer vertices than the *closo*, requires $4n+8$ electrons.

To illustrate this framework from the orbital perspective, we can consider $[Pb_{12}]^{2-}$, a 12-vertex deltahedral cluster, as an example. Its occupied frontier orbitals, 13 in total, span the $a_g + g_u + h_g + t_{1u}$ representations. These constitute the in-phase combination of inwardly-directed p orbitals (a_g) and in-phase combinations of tangential orbitals ($g_u + h_g + t_{1u}$) alluded to in the previous paragraph — the 12 linear combinations of Pb $6s$ orbitals are at lower energy and are not shown. The electron count to fill all orbitals shown in Figure 3.2 is therefore 26, supplemented by 24 in the doubly-occupied Pb $6s$ orbitals, giving 50 ($4 \times 12 + 2 = 50$) in total. If the electron count is reduced to $4n$, the degeneracy of the Highest Occupied Molecular Orbital (HOMO), t_{1u}, will drive a Jahn-Teller distortion. Similarly, if the electron count increases by 2 to $4n+4$, the degeneracy of the Lowest Unoccupied Molecular Orbital (LUMO), g_g, will drive a distortion. The Wade-Mingos rules are not a panacea for all

clusters, and exceptions are known, but they suggest that cluster stability is associated with the occupation of high-degeneracy frontier orbitals that maximise bonding character. Jemmis has extended the Wade-Mingos rules to a more general '*mno*' rule that can accommodate larger clusters based on fused polyhedral fragments.[115] In this concept, m is the number of polyhedra used to construct the cluster, n is the number of vertices, o is the number of single-vertices connecting the monomers, p is the number of missing capping atoms associated with open faces and q refers to the number of capping atoms. The required number of Skeletal Electron Pairs (SEPs) is $m+n+o+p-q$. As all clusters investigated in this chapter are composed of a fused cage, we will heavily use this method to pre-analyse the SEP of the structures.

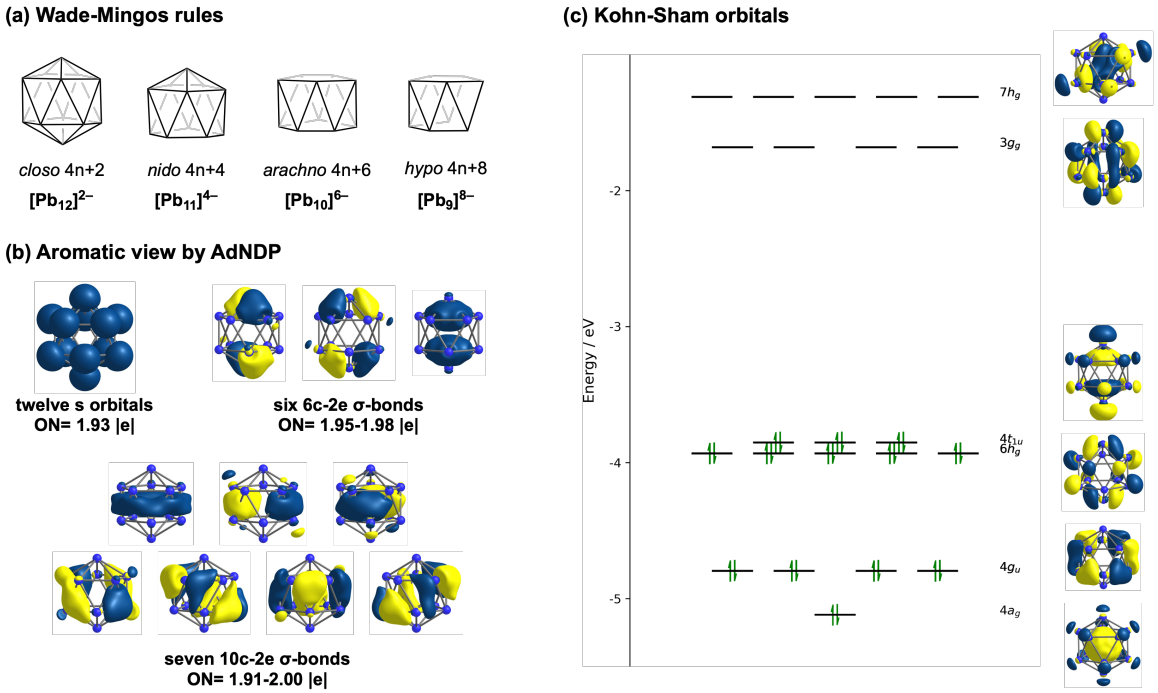

Figure 3.2: Methods used to explain the stability of $[Pb_{12}]^{2-}$, including (a) Wade-Mingos rules, (b) aromaticity analysed by AdNDP, and (c) Kohn-Sham orbitals.

The Wade-Mingos framework and its extensions are not the only models available that relate cluster structure to electron count. The superatom concept suggests that the stability of spherical clusters reflects the relationship between the nodal structures of their frontier orbitals and those of atomic orbitals. This perspective, based on the jellium model,[116,117] provides a complementary framework for understanding the electronic structure and stability of such clusters. As a result, atomic orbital labels can be assigned to the molecular orbitals based on nodal characteristics in their isosurface representations. This approach was first applied to $[AlAl_{12}]^-$ and

then extended to other spherical clusters such as fullerenes and Zintl clusters. For example, the theoretically proposed $[CaPb_{12}]^{2-}$ cluster has been interpreted as a superatom with a closed-shell electronic configuration of $1S^2 1P^6 1D^{10} 1F^8$, as revealed by AdNDP analysis.[118] This assignment aligns with the symmetry-adapted irreducible representations of the occupied molecular orbitals — specifically, a_g, t_{1u}, h_g, and g_u. Electron donation from the $[Pb_{12}]^{2-}$ to Ca^{2+} $4s$, $4p$ and $4d$ orbitals is observed.

AdNDP analysis, which localises electrons as far as possible, has also been used with some success to understand cluster structure from the viewpoint of aromaticity.[119] For example, the AdNDP analysis of $[Pb_{12}]^{2-}$ shown in Figure 3.2 (b) suggests that the molecule can be decomposed into three parts, as two capping pentagonal pyramids ($PbPb_5$) fragments and a connecting Pb_{10} pentagon antiprism. Each Pb_6 cap is composed of three six-centre-two-electron bonds, with Occupation Numbers (ONs) in the range of 1.95–1.98, which corresponds to the σ-aromaticity in the capping region. The Pb_{10} moiety is constructed by seven ten-centre-two-electron bonds, which conform to the $4n + 2$ electron count and lead to a σ-aromaticity in this fragment. The isosurface plot of ten-centre-two-electron bonds in the flat pentagon antiprism can be connected with the characteristics of disk aromaticity applied to planar boron clusters.[120] NICS,[121] ring current,[122,123] and shielding cones are complementary indicators for justifying aromaticity. The concept of aromaticity established for the archetype, $[Pb_{12}]^{2-}$, and similar clusters such as $[Pb_{10}]^{2-}$ can be extended to more complicated examples such as $[Ge_{24}]^{4-}$ and $[Mo_2(CO)_6Sn_2Sb_5]^{3-}$.[124,125]

In contrast to the delocalised bonding models that are required for the electron-deficient Group 14 clusters, the structures of Group 15 analogues (which will be the focus in Chapter 4) are rather simpler to rationalise. The additional electron per atom renders them much less electron deficient, and in fact the structures can very often be rationalised in terms of localised two-centre-two-electron bonds along each short interatomic contact. Tetrahedral P_4 is a good example, where the 20 valence electrons can be divided into 4 lone pairs (1 per vertex) and 6 σ bonding pairs, 1 per P-P edge. The Zintl-Klemm concept establishes an equivalence between As and Ge^-, Sb and Sn^-, Bi and Pb^-, and so mixed clusters can, in principle, be interpreted using either framework.[126–129]

In summary, the stability of Zintl clusters can be rationalised through multiple approaches, including electron-counting rules and orbital-based analyses. The essence of these methods lies in the principle of maximising bonding interactions while preserving the orbital degeneracies associated with high symmetry. The selection of an

appropriate analytical framework is essential and should be guided by the structural and electronic characteristics of the specific cluster under investigation.

3.1.3 Open-shell Zintl clusters

Recent synthetic work on intermetallic Zintl clusters has succeeded in incorporating many early- and mid-transition metal atoms inside polyhedral cages. Unlike late transition metals such as Ni, Co, and Cu, whose low-lying and fully-occupied *d*-bands typically contribute to an inert metal core in closed-shell Zintl clusters, early- and mid-transition metals possess relatively higher energy *d* orbitals with unpaired electrons. These *d* electrons become actively involved in bonding, effectively behaving as valence electrons and giving rise to open-shell electronic configurations in the resulting Zintl clusters. Most reported open-shell Zintl clusters to date feature a single encapsulated transition metal atom: notable examples include spin-doublet $[FeGe_{10}]^{3-}$,[18] $[FeSn_{10}]^{3-}$ [17] and spin-triplet $[MnPb_{12}]^{3-}$,[16] $[RuGe_{12}]^{3-}$.[19] These clusters can be broadly categorised based on the distribution of their metal *d* electrons. In the first category, exemplified by $[MnPb_{12}]^{3-}$ and $[FeSn_{10}]^{3-}$, the unpaired electrons are largely retained on the metal centre. These clusters resemble closed-shell analogues in their deltahedral geometry and retain a similar overall electronic structure, though a small degree of structural distortion may arise due to the metal-to-cage back-bonding. In the second category, exemplified by $[RuGe_{12}]^{3-}$ and $[FeGe_{10}]^{3-}$, the metal *d* electrons show a high degree of covalent orbital mixing with the surrounding cage, consistent with their valence-like character. The structures of clusters in this category can be interpreted using the 'jigsaw' model, wherein electron-sharing between the core and shell components shifts electron density onto the cluster, driving the system toward structures that are typical of electron-precise three-connected cases. This greater orbital hybridisation often leads to more pronounced distortions in cage geometry and more complex bonding interactions.

The presence of unpaired electrons in active *d* orbitals also opens up the possibility of metal-metal bonding when multiple transition metals are encapsulated within a cage. The first reported example was $[Fe_2Ge_{16}]^{4-}$,[20] where the two Fe atoms reside within a prolate cage with a very short Fe-Fe distance at 2.636(3) Å. DFT calculations confirm a spin triplet ground state for this system. However, two closely separated states, $^3B_{1g}$ and $^3B_{3u}$, were identified. The two states differ in the occupation of core-related orbitals in the spin-β electron manifold: in the $^3B_{1g}$ an out-of-phase combination of Fe $3d_{z^2}$ orbitals in the minority spin is occupied while for $^3B_{3u}$ the spin-β Fe $3d_{x^2-y^2}$ out-of-phase combination is occupied. The other unpaired electron occupies

an Fe-Fe π^* orbital (d_{xy}) in both states, resulting in an identifiable Fe-Fe bond with π character. A notable and recurring feature is the presence of spin contamination in DFT calculations. As discussed in the previous chapter, spin contamination arises in spin-unrestricted calculations and serves as an indicator of the multi-configurational nature of the cluster, effective as the admixture of higher spin state wavefunctions into the ground state. The presence of two near-degenerate states suggests that MC-SCF approaches may afford a more accurate picture of the electronic structure than DFT, and indeed Generalised Active Space Self-Consistent Field (GASSCF) calculations revealed significant multi-configurational character, reflected in deviations of the natural orbital occupation numbers from the idealised 2/0 pattern. Strong electron correlation was particularly observed in the π^* (Fe $3d_{xz}$) and δ (Fe $3d_{yz}$) orbitals, giving an EBO of 0.66 for the Fe-Fe bond. An even more extreme example of the distortions caused by open d shells comes from the complex Matryoshka-type open-shell clusters such as $[AsCo_{12}As_{10}(As_5)_2]^{4-/5-}$ and $[SbFe_{12}Sb_{10}(Sb_5)_2]^{5-}$,[130] which are open-shell analogues of the closed-shell species $[AsNi_{12}As_{20}]^{3-}$ and $[SnCu_{12}Sn_{20}]^{12-}$, respectively. Replacing Ni and Cu with Co and Fe introduces unpaired electrons on the transition metal centres, and the resulting charge transfer between main-group and transition metal orbitals drives significant geometric distortions from the idealised dodecahedral structures.

The investigations described in the previous paragraphs establish a basic conceptual framework for studying open-shell Zintl clusters. A well-defined closed-shell reference always serves as a valuable starting point for constructing the initial electronic structure, and this idea will be used extensively in the following sections. The synthesis of diamagnetic multi-metal-encapsulated Zintl clusters has now reached a mature stage, and useful references are often available. Open-shell behaviour then arises from partial electron depletion from the spin-β metal d orbitals, often leading to marked changes in electronic properties and geometry distortions. While DFT offers useful insights, it is frequently insufficient for the description of open-shell clusters due to spin contamination and inadequate treatment of static correlation. MC-SCF approaches therefore have an important role, often as complements to DFT, and we can identify common features emerging from the two quite different approaches. The remainder of this chapter will explore three distinct examples of this emerging class of clusters, and will emphasise the interplay between open-shell character, metal-metal bonding, metal-cage interactions and electronic correlation in multi-metal encapsulated Zintl clusters.

3.1.4 Metal-metal bonding in clusters containing Fe and Cr

Over the following three sections, I will describe the structure and bonding of a series of clusters containing two, three, and four transition metal atoms as cores within Zintl cages. In the majority of cases, the metal in question is Fe, although one important case involves Cr. It is useful, therefore, to provide a brief overview of the now quite extensive literature on metal-metal bonding between these first-row transition metal elements. Metal-metal bonding, particularly in paramagnetic clusters, has been extensively studied in coordination chemistry due to promising applications in single-molecule magnets, spintronic devices, and quantum information technologies. Iron clusters are known with a wide variety of nuclearities and geometries, ranging from simple dinuclear complexes to larger species such as the distorted Fe_8 cube core in the Kochi cluster.[131] In dinuclear systems, the oxidation state of iron typically ranges from +1 to +3, and the bridging ligands play a critical role in supporting the Fe-Fe bond and modulating its strength. For example, in $Fe_2(Pipiso)_2$ (Pipiso = $[(DipN)_2C(cis\text{-}2,6\text{-}Me_2NC_5H_8)]$), a short Fe-Fe bond length of 2.127 Å is observed, corresponding to a high-spin state ($S = 3$).[132] By contrast, when bridging ligands are absent, as in $Fe_2(tim)_2$ (tim = 2,3,9,10-tetramethyl-1,4,8,11-tetraazacyclotetradeca-1,3,8,10-tetraene) coordinated in a paddlewheel fashion, the Fe-Fe bond is significantly elongated, reaching 2.687 Å ($S = 1$).[133] Cr-Cr bonds have played an important role in the story of the metal-metal bond, starting from the synthesis of chromium acetate in 1844,[134] a molecule that was subsequently recognised as an example of the quadruple bond. Cr(I), with a d^5 configuration, is remarkable in so much as is can form quintuple bonds, $\sigma^2\pi^4\delta^4$, with ultra-short Cr-Cr bonds ranging from 1.7056 Å in $Cr_2(Ar^{iPr}NC\{dmp\}NAr^{iPr})_2$ to 1.8351(4) Å in $Cr_2Ar'_2$.[6,135–138] Cr(II), with a d^4 configuration, supports quadruple bonding ($\sigma^2\pi^4\delta^2$) in a wide range of compounds, with bond lengths between 1.77 and 2.52 Å, often in paddlewheel type geometries.[139,140] The stability of these clusters relies to a large extent on the relatively diffuse nature of the $3d$ orbitals in the elements in the middle of the first transition series which allows effective overlap to be established.

Both iron and chromium can also form larger high-spin assemblies, and Betley and co-workers have reported polynuclear giant spin clusters such as Cr_3L and $LFe_3(thf)_3$ (triangular arrangements),[141–145] as well as Fe_6L (octahedral geometries),[146–148] where L is a multi-dentate ligand. These clusters often exhibit substantial spin multiplicities, as confirmed by EPR spectroscopy, magnetic susceptibility, and magnetisation measurements. Linear tri-iron clusters, such as $[Fe_3(DpyF)_4]^{2+}$ (DpyF = dipyridylformamide),[149,150] have also been synthesised, with high-spin ground states where the

ferromagnetic coupling rather than formal covalent bonding has been invoked. Many linear tri- and penta-chromium clusters such as $Cr_3(dpa)_4X_2$ (dpa = dipyridylamide, X = axial ligands, including halide and pseudohalide ions), $Cr_5(tpda)_4(NCS)_2$ (tdpa = tripyridyldiamido dianion) and $Cr_5(etpda)_4Cl_2$ (etpda = bis(4-ethyl-2-pyridylamido) pyridine) are also known,[151–154] and have been extensively investigated in the context of 'molecular wires'. The axial ligands X in the tri-chromium cluster, which lie trans to the Cr-Cr bonds, have been shown to exert a significant influence on both the Cr-Cr separations and the magnetic behaviour of these clusters.[155] In this context, Zintl clusters offer an interesting alternative, in so much as the cage structure often prevents a 'ligand' atom from occupying the site immediately *trans* to the M-M bond, allowing stronger M-M bonding to develop. In these systems, electron density can also be transferred from the high-lying M-M antibonding orbitals to the cage, further enhancing both metal-metal and metal-cage bonding. It is this complex electronic landscape that has motivated the studies in the next two chapters.

In this chapter, I extend the exploration of open-shell Zintl clusters to the domain of multi-metal encapsulated systems with direct metal-metal bonds. Specifically, I examine three classes of endohedral Zintl clusters with two, three and four Fe centres, using DFT. The focus is on the nature of the covalent metal-metal bonds which significantly influence the magnetic properties, as well as the geometry and the overall stability of the clusters. The presence of unpaired electrons in compact $3d$ orbitals leads to strong electron correlation, and indeed these clusters can exhibit significant multi-configurational character. We have, therefore, also used multi-reference methods such as CASSCF, DMRG and MC-PDFT calculations on the same clusters to provide a different but complementary perspective on the bonding. A central strategy in our analysis involves comparing the open-shell clusters with their known closed-shell counterparts, which are typically easier to interpret with simple electron-counting paradigms and the emergence of metal-metal bonding.

The first section deals with a pair of dimetallic clusters, $[Fe_2Sn_4Bi_8]^{3-}$ and $[Cr_2Sb_{12}]^{3-}$ (Figure 3.3 (a)), both of which have been structurally characterised by our collaborator, Prof. Zhong-Ming Sun and his group. The two clusters have very different structures, but share the same valence electron count. Our exploration of their electronic structure shows how different energetic alignment of orbitals on the transition metal and the main-group cluster can drive charge transfer, which in turn drives structural change. The second section moves on to trimetallic systems, specifically the $[Fe_3Sn_{18}]^{4-}$ cluster with a linear Fe_3 unit (Figure 3.3 (b)). Here, there

is an obvious comparison with related closed-shell species such as $[Cd(NiSn_9)_2]^{6-}$, and the structural differences reflect the emergence of Fe-Fe bonding in the former. Walsh diagrams prove to be particularly powerful here in understanding the evolution of structure as a function of electron count. Finally, we move on to a pair of Fe_4 clusters, $[Fe_4Sn_{18}]^{4-}$ and $[Fe_4Pb_{18}]^{4-}$ (Figure 3.3 (c)), which have the same valence electron count but subtly different structures for the diamond-shaped Fe_4 core. Our results suggest that this difference reflects the presence of two closely-spaced electronic states with different Fe-Fe bonding. Deeper insight into the electronic ground state of $[Fe_4Sn_{18}]^{4-}$ was obtained *via* DMRG/MC-PDFT.

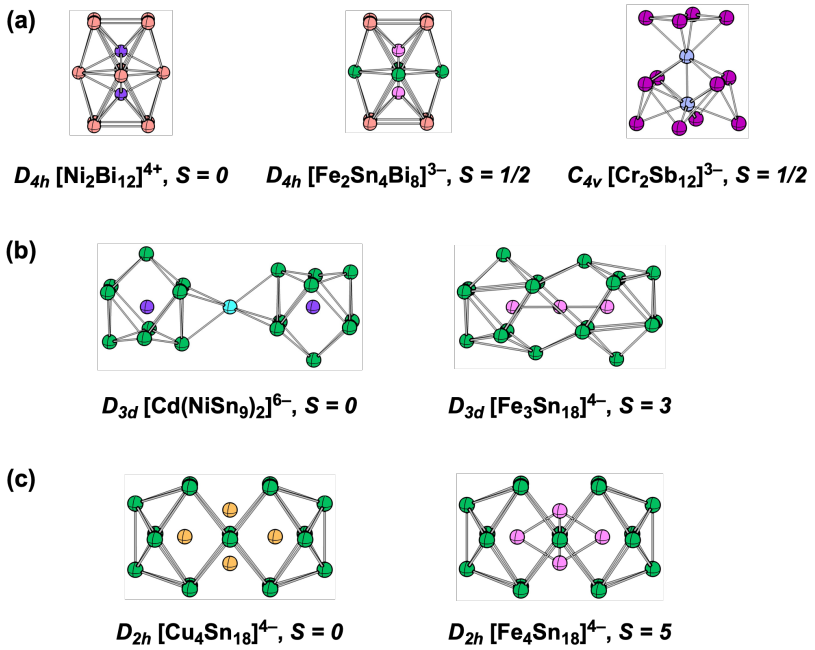

Figure 3.3: Open-shell Zintl clusters discussed in this chapter, along with their closed-shell references.

3.2 Structure and Bonding in $[Cr_2Sb_{12}]^{3-}$ and $[Fe_2Sn_4Bi_8]^{3-}$: isoelectronic but not isostructural

In this section, I compare the electronic structures of a pair of clusters, $[Cr_2Sb_{12}]^{3-}$ and $[Fe_2Sn_4Bi_8]^{3-}$, that share the same valence electron count (75). The compounds were synthesised and characterised by Prof. Zhong-Ming Sun and his group, and all experimental results are theirs. The crystal structures are shown in Figure 3.4. The work was also done in collaboration with another student in the group, Dr. Sourav Mondal. The work has been published in *Chinese Chemical Letters*, 2024, **35**, 109048.

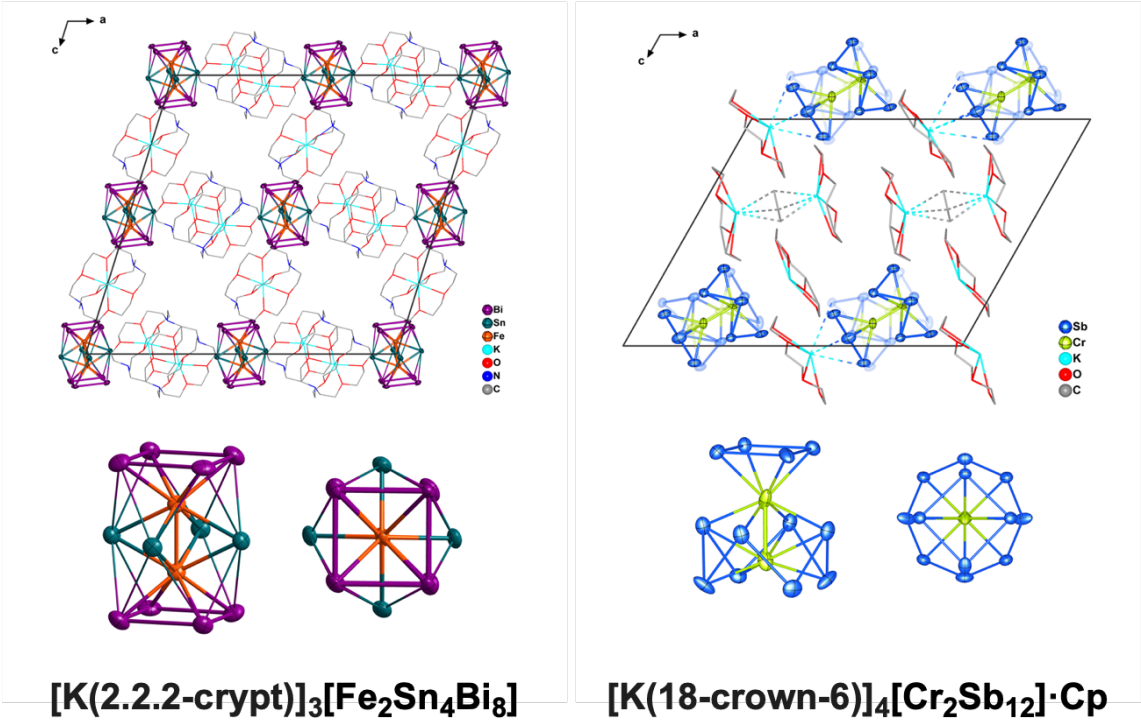

Figure 3.4: Unit cells of (a) $[Fe_2Sn_4Bi_8]^{3-}$ and (b) $[Cr_2Sb_{12}]^{3-}$, including front and top views of the anions. The XRD experiment was performed by Ya-Nan Yang in Prof. Zhong-Ming Sun's group. (Reproduced from our published work as Ref. 1)

3.2.1 Introduction

The icosahedral ME_{12} framework, with a single metal inside a 12-vertex shell, is a common motif in Zintl cluster chemistry, and the earliest examples exhibit a deltahedral shell structure and a metal atom with a d^{10} configuration, such as $[MPb_{12}]^{2-}$

(M = Ni, Pd, Pt).[92] The structures of these clusters can be predicted by the Wade-Mingos rules: there are 60 valence electrons on $[MPb_{12}]^{2-}$, 10 of which fill all five valence d orbitals of the metal centre. The remaining 50 electrons construct the skeleton structure of the cage, which corresponds to the $4n + 2$ ($4 \times 12 + 2 = 50$) electron count required for a *closo* structure in Wade's scheme. These 60-electron clusters have proved to be useful reference points for understanding geometric distortions in related clusters with more or fewer electrons. For example, $[MnPb_{12}]^{3-}$ is a 58-electron cluster and is slightly distorted from I_h to D_{2h}.[16] A more extreme distortion is observed in $[RuGe_{12}]^{3-}$ [19] and $[TaGe_8As_4]^{3-}$,[156] which are in a three-connected fullerene-like structure. The 60-electron $[TaGe_8As_4]^{3-}$ cluster can be considered an electron-precise cage if all the valence electrons on the tantalum centre are considered in the skeletal electron count, where all Ge atoms can mimic a Group 15 atom. In the context of this chapter, the salient point is that whilst $[NiPb_{12}]^{2-}$ and $[TaGe_8As_4]^{3-}$ share the valence electron count, their structures are very different due to differences in the character of the metal d electrons — inert, core-like d electrons in $[NiPb_{12}]^{2-}$ and valence-like d electron in $[TaGe_8As_4]^{3-}$.

The relatively small volume of the 12-vertex pseudo-spherical clusters makes encapsulation of more than one metal challenging. M_2E_{12} (E = Si,[157–159] Ge[160–162]) have been explored using gas-phase spectroscopy and computational analysis, but in these clusters one of the two metal atoms typically occupies a vertex of the cage, rather than exhibiting complete endohedral encapsulation. However, a series of triple-decker clusters in M_2E_{12} have been synthesised by Ruck, Dehnen and co-workers, where a prolate D_{4h}-symmetric E_{12} cage accommodates two transition metals, each sandwiched between two E_4 layers (Figure 3.5). Examples include the binary cluster $[Ni_2Bi_{12}]^{4+}$ [105] and ternaries such as $[Ni_2Sn_7Sb_5]^{3-}$,[106] $[Ni_2Sn_7Bi_5]^{3-}$,[107] $[Ni_2Pb_7Bi_5]^{3-}$ [108] and $[Co_2Sn_5Sb_7]^{3-}$.[106] All clusters are in a similar D_{4h} point group ignoring the necessarily asymmetric distribution of Sn, Sb and Bi in the ternaries, and all have the same valence electron count of 76. The metal-metal distances presented in Table 3.1 are all approximately 2.45 Å, and the transition metals are all in d^{10} configuration. There is, therefore, no possibility of direct M-M bonding, despite the short distance that is clearly imposed by the confining effects of the cage. In this section, we compare these 76-electron prolate clusters to two new open-shell cases, $[Fe_2Sn_4Bi_8]^{3-}$ and $[Cr_2Sb_{12}]^{3-}$, both of which have 75 rather than 76 electrons. The $[Fe_2Sn_4Bi_8]^{3-}$ retains the D_{4h} structure adopted by the 76-electron Ni and Co family, but $[Cr_2Sb_{12}]^{3-}$ is very different: it distorts to a C_{4v} geometry, with separated Sb_4 and crown-like Sb_8 units. The Cr-Cr bond length in $[Cr_2Sb_{12}]^{3-}$ is also much shorter

than the Fe-Fe bond in $[Fe_2Sn_4Bi_8]^{3-}$. The situation is reminiscent of the transition from icosahedral $[NiPb_{12}]^{2-}$ [92] to the fullerene-like $[RuGe_{12}]^{3-}$, [19] and my purpose is to establish how the geometry change and the emergence of metal-metal bonding are linked to the changes in orbital energies on the transition metal and main-group fragments. The initial calculations were done using DFT, but I then extended this to the DMRG method to explore their multi-configurational character.

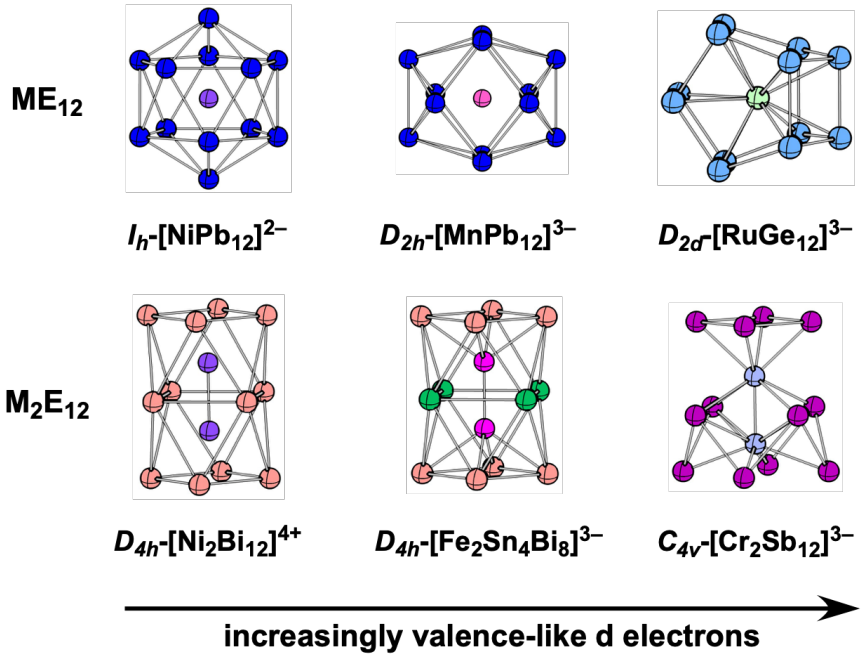

Figure 3.5: Structural trends within the ME_{12} and M_2E_{12} families. The two new clusters reported in this section are highlighted in the box.

Table 3.1: Total valence-electron count and crystallographic and DFT-optimised bond lengths for members of the $M_2E_4E'_8$ family (all values in Å).

	VE		M-M	M-E	M-E′	E-E	E′-E′	E-E′	ref
$[Fe_2Sn_4Bi_8]^{3-}$	75	X-ray	2.396(4)	2.670	2.698	3.374	3.095	3.290	This work
		DFT (D_{4h})	2.37	2.68	2.71	3.40	3.10	3.30	
$[Cr_2Sb_{12}]^{3-}$	75	X-ray	2.319(17)	2.782 2.831	2.757 2.740	3.614	2.755 3.725	3.549 2.801	This work
		DFT (D_{4h})	2.16	2.79	2.64	3.64	3.19	3.09	
		DFT (C_{4v})	2.29	2.78 2.83	2.77 2.73	3.62	2.85 3.65	3.51 2.87	
$[Ni_2Bi_{12}]^{4+}$	76	X-ray	2.429	2.678	2.741	3.371	3.045	3.393	105
		DFT (D_{4h})	2.45	2.69	2.75	3.39	3.06	3.416	
$[Ni_2Sn_7Bi_5]^{3-}$	76	X-ray	2.444	2.631	2.665	3.290	3.009	3.307	107
$[Ni_2Pb_7Bi_5]^{3-}$	76	X-ray	2.499	2.710	2.710	3.401	3.066	3.355	108
$[Ni_2Sn_7Sb_5]^{3-}$	76	X-ray	2.432	2.609	2.595	3.264	2.897	3.275	106
$[Co_2Sn_5Sb_7]^{3-}$	76	X-ray	2.411	2.626	2.575	3.298	2.885	3.253	106

3.2.2 Computational details

All DFT calculations in this section were performed with the ADF package, version 2021.104.[69] The exchange-correlation functional proposed by Perdew, Burke and Ernzerhof (PBE) was used throughout,[47] and scalar relativistic effects were introduced using the scalar Zeroth-Order Regular Approximation (ZORA).[163] For all geometry optimisations, a triple-zeta quality basis set of Slater-type orbitals was used,[164] supplemented by two sets of polarisation functions. All electrons were included in the basis set. The Conductor-like Screening Model (COSMO)[165] was applied to simulate the confining effects of the crystalline environment with water as the solvent.

The DMRG calculations were performed with the Block 2.0 interface[166] compiled with the OpenMolcas package.[167] The two-electron integrals were approximated by Cholesky decomposition at the threshold of 10^{-6}, and the integration grid was tuned to 'ultrafine'. Atomic Natural Orbital for Scalar-Relativistic Core-Correlated (ANO-RCC) basis sets were applied at the level of double-zeta plus one polarisation function.[168] Symmetry was treated using the Abelian point group. In all DMRG calculations, the bond dimension m was set to 1500. The default convergence criteria were used, where the energy, orbital rotation matrix and energy gradient thresholds are 10^{-8}, 10^{-4}, 10^{-4} respectively. Orbital entropies and mutual information were calculated with the PySCF package[169–171] from the FCIDUMP file generated by OpenMolcas.

3.2.3 Electronic structure analysis

3.2.3.1 DFT analysis

Just as closed-shell $[NiPb_{12}]^{2-}$ serves as a reference point for the ME_{12} family, the 76-electron $[Ni_2Bi_{12}]^{4+}$ is a logical starting point for analysing the electron-deficient pairs. DFT optimisation confirms its ground spin state to be a singlet, and its geometry is consistent with the X-ray result shown in Table 3.1. A large HOMO-LUMO gap of 1.77 eV implies its electronic stability, which is close to 1.80 eV in $[NiPb_{12}]^{2-}$ that was identified as stable. To explore the electronic structure in more detail, the Kohn-Sham orbital arrays are presented in Figure 3.6 (a), and the Projected Density of States (PDOS) to Ni 3*d*, Bi 6*s*, Bi 6*p* along with the Ni-Ni OPDOS, is in Figure 3.6 (b). The midpoint of the HOMO and LUMO is set as the energetic zero for both plots. The PDOS projects the total Density of States (DOS) onto the appointed basis χ_μ, to exhibit the importance of individual orbitals in the DOS. The OPDOS is weighted

by the overlap between χ_μ and χ_ν, with positive values associated with bonding interactions and negative values with antibonding interactions. The magnitude of the OPDOS peak is proportional to the product of the atomic orbital coefficients as $C_{\mu i} \cdot C_{\nu i}$. Isosurfaces of significant Kohn-Sham orbitals are also included. In the PDOS, almost all the Ni $3d$ character is located below the Fermi level, ranging from π bonding orbitals at -3.3 eV to σ^* orbital near the HOMO. The full occupation of Ni $3d$ indicates that both Ni atoms are in d^{10} configurations, just as in the icosahedral $[NiPb_{12}]^{2-}$ cluster. Even though the Ni-Ni distance is as close as 2.45 Å due to a confined space, the Ni-Ni formal bond order is 0, resulting in the absence of significant Ni-Ni bonding. The OPDOS plot also confirms that the occupied bands contain almost all bonding and antibonding character. The charge distribution of $[Ni_2Bi_{12}]^{4+}$ can then be described as $[Ni_2]^0$ + $[Bi_{12}]^{4+}$, and so the skeletal electron count for the empty triple-decker $[Bi_{12}]^{4+}$ cage is 56. The precise reasons why the triple-decker geometry is favoured are not easy to discern. Dehnen failed to rationalise the structure of $[Ni_2Pb_7Bi_5]^{3-}$, which is isoelectronic and isostructural to $[Ni_2Bi_{12}]^{4+}$, with either the localised Zintl-Klemm-Busmann model or the Wade-Mingos rules, because there is a large deviation from a spherical reference. Alternatively, the more general Jemmis '*mno*' rules provide a rationale: in the case of $[Ni_2Bi_{12}]^{4+}$, its structure can be regarded as two anti-prismatic Bi_8 fused by sharing a Bi_4 face ($m = 2$). The top and bottom Bi_4 square can be considered as two open faces ($p = 2$). According to Jemmis' rules, its SEP corresponds to $m+n+o+p-q = 2+12+0+2-0 = 16$. Counting an extra s electron pair for each vertex, the aggregate SEP is 28, which corresponds to the electron count of 56 in $[Ni_2Bi_{12}]^{4+}$. Based on the analysis above, the $[Ni_2Bi_{12}]^{4+}$ can perform as an electron-precise reference like $[NiPb_{12}]^{2-}$ for the other two open-shell cases in this section.

The 75-electron $[Fe_2Sn_4Bi_8]^{3-}$ cluster possesses a similar D_{4h} structure to $[Ni_2Bi_{12}]^{4+}$, but is more electron deficient, and the metal-metal distance contracts to 2.396(4) Å compared to 2.429 Å in the nickel analogue. Our DFT calculations confirm the ground state to be a doublet, $^2A_{2u}$, a conclusion that is independent of the functional choice (PBE, M06-L and PBE0 were tested). The geometry optimised by the PBE functional aligns best with the experimental data, and forms the foundation of the subsequent analysis. In comparing 76-electron $[Ni_2Bi_{12}]^{4+}$ to 75-electron $[Fe_2Sn_4Bi_8]^{3-}$, it is crucial to identify which orbital hosts the missing electron. Intuitively, the decreasing metal-metal distance and conserved cage structure suggest that the radical could be localised on the metal centres, and indeed the total Mulliken spin density of 1.67 on Fe_2 fragment supports this conclusion. A deeper

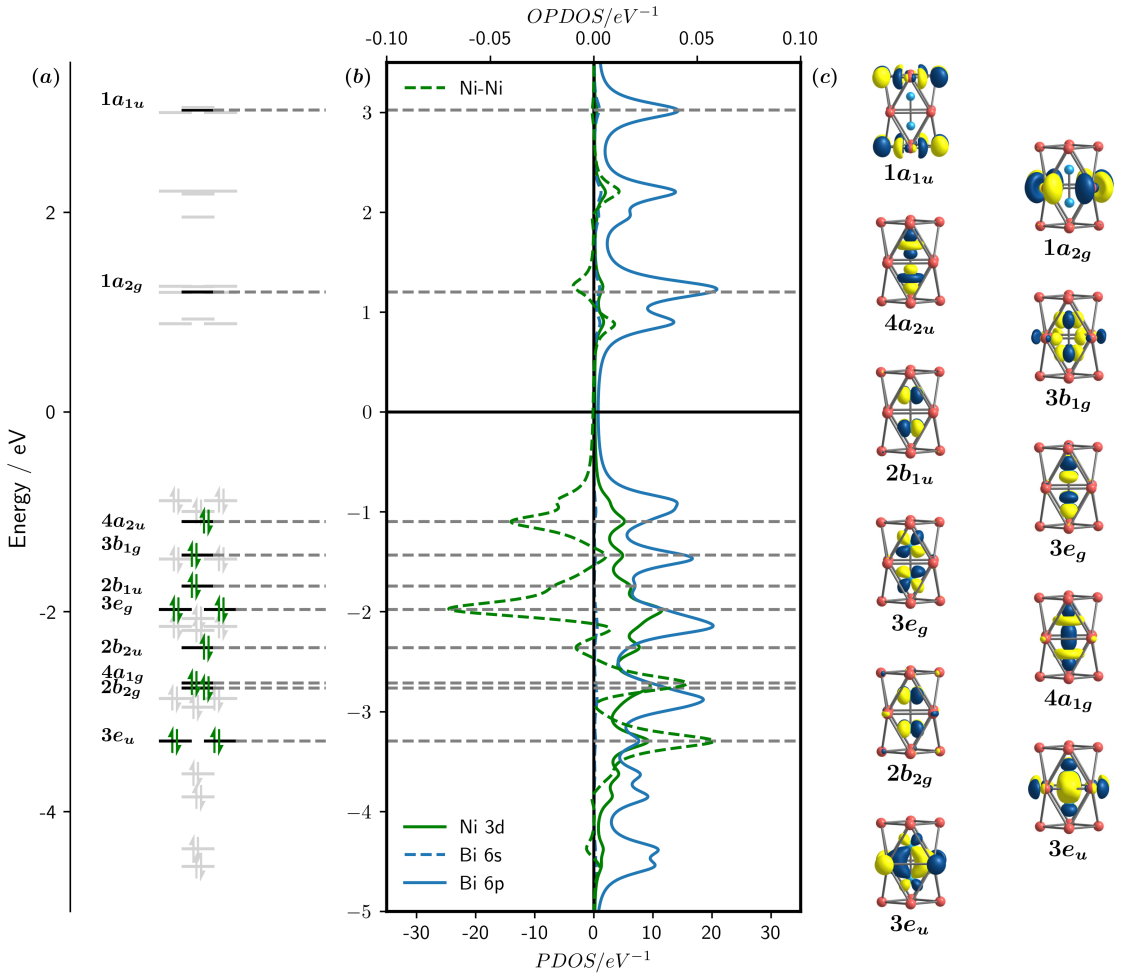

Figure 3.6: (a) Kohn-Sham orbital array of D_{4h}-$[Ni_2Bi_{12}]^{4+}$; (b) PDOS plot of Ni 3d, Bi 6s, Bi 6p and OPDOS plot of the Ni-Ni bond. The orbital levels are broadened with Lorentzian functions with the width of 0.1 eV; (c) Kohn-Sham orbital isosurface plots for significant orbitals, including all orbitals contributed by Ni 3d as well as $1a_{1u}$ and $1a_{2g}$ located on the cage. The isovalue for the orbitals is 0.05 e/Bohr^3.

analysis can be performed with the help of the Kohn-Sham orbital array in Figure 3.7 (a), the PDOS on the spin-β valence shell of Sn, Bi, Fe, and the Fe-Fe OPDOS of the minority spin manifold in Figure 3.7 (b). The Fe 3d orbitals in the majority spin manifold remain occupied, just as in the nickel reference, but in the spin-β channel, the σ^* orbital is unoccupied ($\sim$0.3 eV), while the rest of the Fe 3d-based bands lie below the Fermi level. The singly-occupied σ^* orbital and its corresponding low-lying σ bonding orbital at -1.6 eV generate a formal Fe-Fe bond order of 0.5, but the calculated Mayer bond order analysis gives a slightly higher value of 0.92. This difference can be attributed to the interactions between the metal core and the

Zintl shell. By analogy to the $[Ni_2Bi_{12}]^{4+}$ reference ($[Ni_2]^0$, $[Bi_{12}]^{4+}$), we could assert a charge distribution of $[Fe_2]^{3-}$ and $[Sn_4Bi_8]^0$, where the cage retains both 56 valence electrons and D_{4h} symmetry. However, the highly negatively charged metal fragment can interact strongly with the cage (back-bonding from $[Fe_2]^{3-}$ to $[Sn_4Bi_8]^0$). This mechanism can be identified in the $4e_g/5e_g$ pair in the Kohn-Sham array, which are highlighted in blue and red boxes respectively in Figure 3.7 (c). There is substantial Fe-Fe π^* character in the vacant $5e_g$ orbital, which serves to increase the Fe-Fe bond order above the formal value of 0.5. Also, it results in the slight elongation of the Bi-Bi bond length from 3.06 Å in $[Ni_2Bi_{12}]^{4+}$ to 3.10 Å in $[Fe_2Sn_4Bi_8]^{3-}$. The back-bonding is more pronounced in the spin-β manifold, where the metal d orbitals are less stable, and this asymmetry results in spin contamination, a deviation of the spin operator eigenvalue, $\hat{S}^2$, from the expected value of 0.75 to 0.88. The key differences between $[Ni_2Bi_{12}]^{4+}$ and $[Fe_2Sn_4Bi_8]^{3-}$ are captured in the Electron Density Difference (EDD) plots shown in Figure 3.8. The EDD is generated by subtracting the sum of the fragment electron densities ($\sum D_{frag}$) from the total electron density (D_{tot}) (The fragments were $[Ni_2]^0$ and $[Bi_{12}]^{4+}$ and $[Fe_2]^{3-}$ and $[Sn_4Bi_8]^0$, and the electronic configurations of the fragments are adjusted to be consistent with those in the encapsulated cluster).

$$D_{diff} = D_{tot} - \sum D_{frag} \tag{3.2.1}$$

The EDD is projected onto the Bi_2-M_2-Bi_2 plane. The red area in the plot corresponds to electron concentration, and the blue area indicates electron depletion, relative to the respective fragments. In $[Ni_2Bi_{12}]^{4+}$, redistribution of electron density is largely restricted to the $3d$ and $4s$ orbitals of Ni_2, while charge transfer between core and shell is less obvious. In $[Fe_2Sn_4Bi_8]^{3-}$, in addition to the redistribution between the metal orbitals, there is an accumulation of density on the Bi corners, at the cost of density depletion on Fe_2, a consequence of the back-bonding noted above. This density redistribution carries the fingerprint of the $4e_g/5e_g$ orbitals.

Turning to $[Cr_2Sb_{12}]^{3-}$, I emphasise that it has the same electron count as $[Fe_2Sn_4Bi_8]^{3-}$, but the structure is distorted to a combination of a square pyramid $CrSb_4$ and a crown-like $CrSb_8$ with C_{4v} symmetry, and the connecting Cr-Cr bond is contracted to 2.319(17) Å. Its ground state is also confirmed to be a doublet, but now with $^2B_2$ spatial symmetry. DFT computations were again performed with a range of functionals (GGA (PBE), meta-GGA (M06-L) and hybrid (PBE0)) with PBE exhibiting the closest match to the XRD data. The Kohn-Sham orbital arrays, spin-β-PDOS and spin-β-OPDOS of the C_{4v}-symmetric ground state are shown in

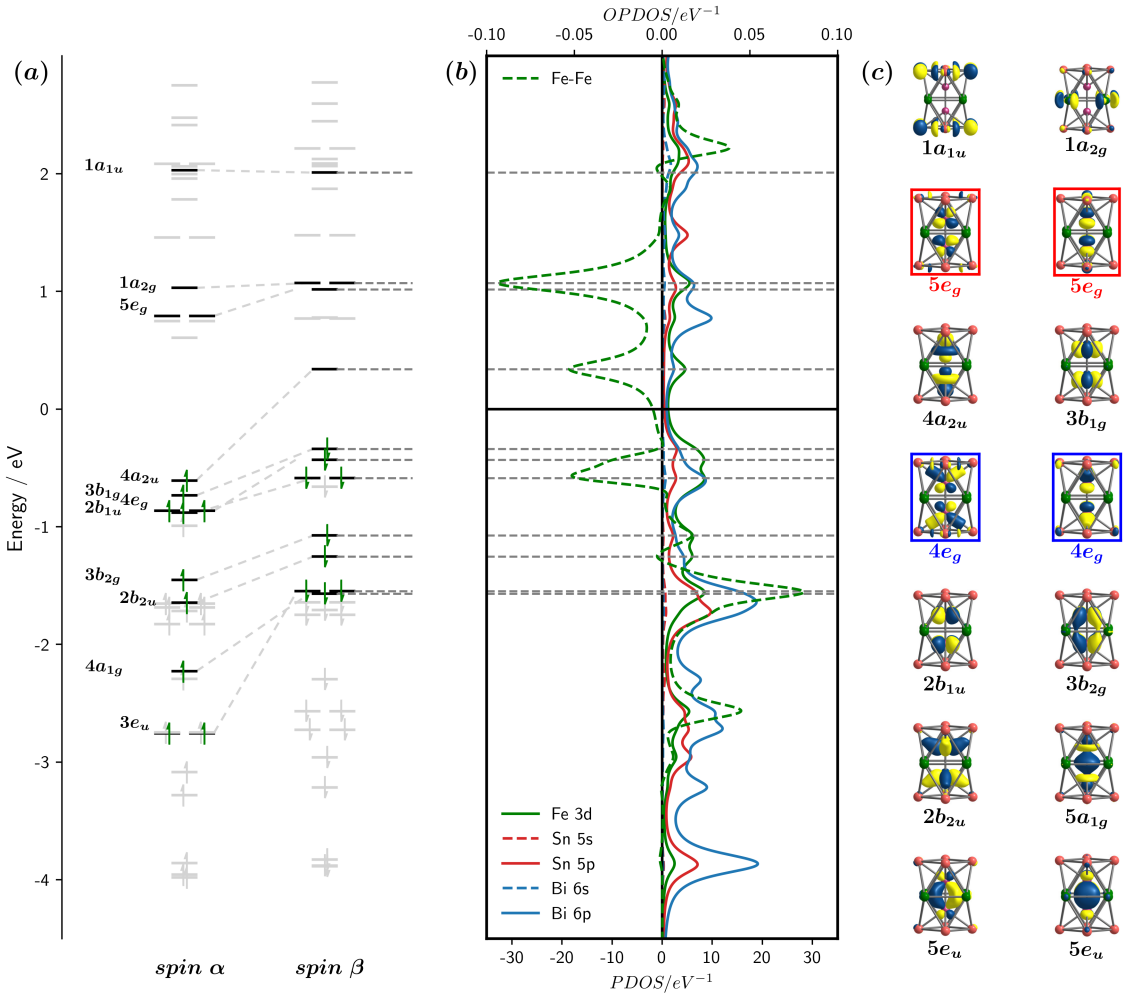

Figure 3.7: (a) Spin-α and spin-β Kohn-Sham orbital arrays of ${}^2A_{2u}$-$[Fe_2Sn_4Bi_8]^{3-}$; (b) PDOS plot of Fe $3d$, Sn $5s/5p$, Bi $6s/6p$ and the OPDOS of the Fe-Fe bond of the minority spin. The orbital levels are broadened with Lorentzian functions at the width of 0.1 eV; (c) Kohn-Sham orbital isosurface plots for significant orbitals, including all orbitals contributed by Fe $3d$ as well as $1a_{1u}$ and $1a_{2g}$ located on the cage in the spin-β array. The orbital isovalue is 0.05 e/Bohr^3.

Figure 3.9, and there are immediately obvious differences in the distribution of $3d$ character compared to $[Fe_2Sn_4Bi_8]^{3-}$. There is now much more $3d$ character in the vacant manifold, above the Fermi level, and the OPDOS confirms that it has dominant Cr-Cr antibonding character (negative OPDOS). Both components of the Cr-Cr σ^* orbital ($10a_1$) are empty, as are $12e$, which have significant Cr-Cr π^* character. $9e$, in contrast, are largely localised on the Sb_{12} cage, indicating that the back-bonding noted in the case of $[Fe_2Sn_4Bi_8]^{3-}$ has now developed into a more complete oxidation of Cr with concomitant reduction of Sb. The total Mulliken spin density on Cr_2 is

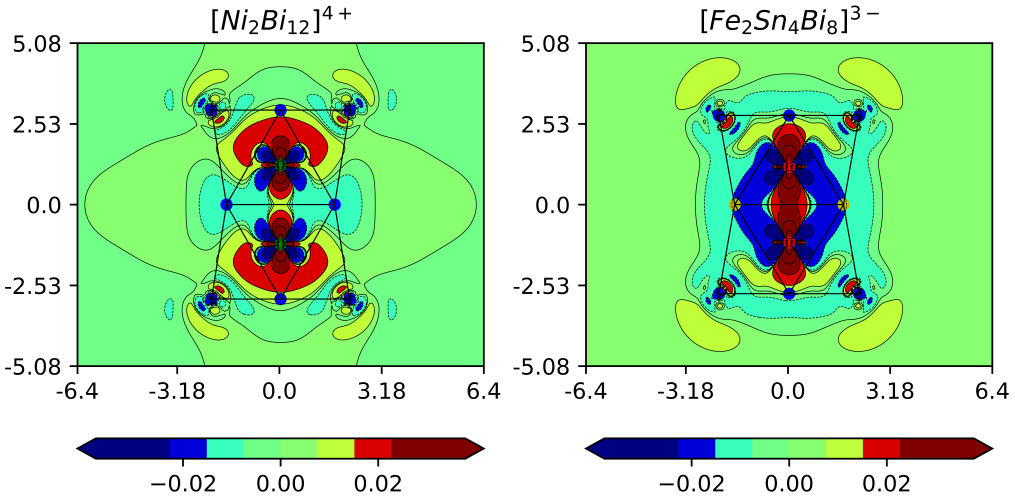

Figure 3.8: Electron Density Difference plots for $[Ni_2Bi_{12}]^{4+}$ and $[Fe_2Sn_4Bi_8]^{3-}$, showing the difference in electron density between the self-consistent solution and the sum of two separated fragments ($[Ni_2]^0$ + $[Bi_{12}]^{4+}$ or $[Fe_2]^{3-}$ + $[Sn_4Bi_8]^0$, respectively). Contours range from -3×10^{-3} to 3×10^{-3} e/Bohr^3, and values on the x- and y- axes are in Å. (Reproduced from our published work as Ref. 1)

1.44, showing increased spin contamination compared to $[Fe_2Sn_4Bi_8]^{3-}$. There is also a δ component to the Cr-Cr bond, by virtue of the singly-occupied Cr-Cr δ^* $5b_2$ orbital. The calculated Mayer bond order for the Cr-Cr bond is 1.38 compared to 0.92 in $[Fe_2Sn_4Bi_8]^{3-}$, reflecting the enhanced back-donation.

The link between the greater transfer of charge from Cr to Sb and the distortion of the Sb_{12} unit can be established by imposing a symmetry constraint, forcing the $[Cr_2Sb_{12}]^{3-}$ cluster to remain D_{4h}-symmetric, and then relaxing the constraint. The D_{4h}-constrained calculation optimises to a stationary point which is 0.86 eV more unstable than the C_{4v} isomer, indicating that the driving force for distortion is substantial. Spin-β PDOS plots for both isomers are presented in Figure 3.10, and a Walsh diagram connects the two sides. The Walsh diagram was generated by performing single point calculations on 20 structures generated by interpolation between the optimised D_{4h} and C_{4v} stationary points. Orbital energies from single point calculations were read and connected to construct the Walsh diagram. In the distortion process, only orbitals with the same irreducible representation can interact with each other. The PDOS for the D_{4h} isomer is significantly different from the $[Fe_2Sn_4Bi_8]^{3-}$ in Figure 3.7, in that the $1a_{2g}$ orbital is now occupied and the $2b_{1u}$ is empty. These orbitals are localised on the Sb_4 square and on the Cr_2 unit, respectively, so even in the D_{4h} limit, the more extreme charge transfer from metal to cage is apparent. In

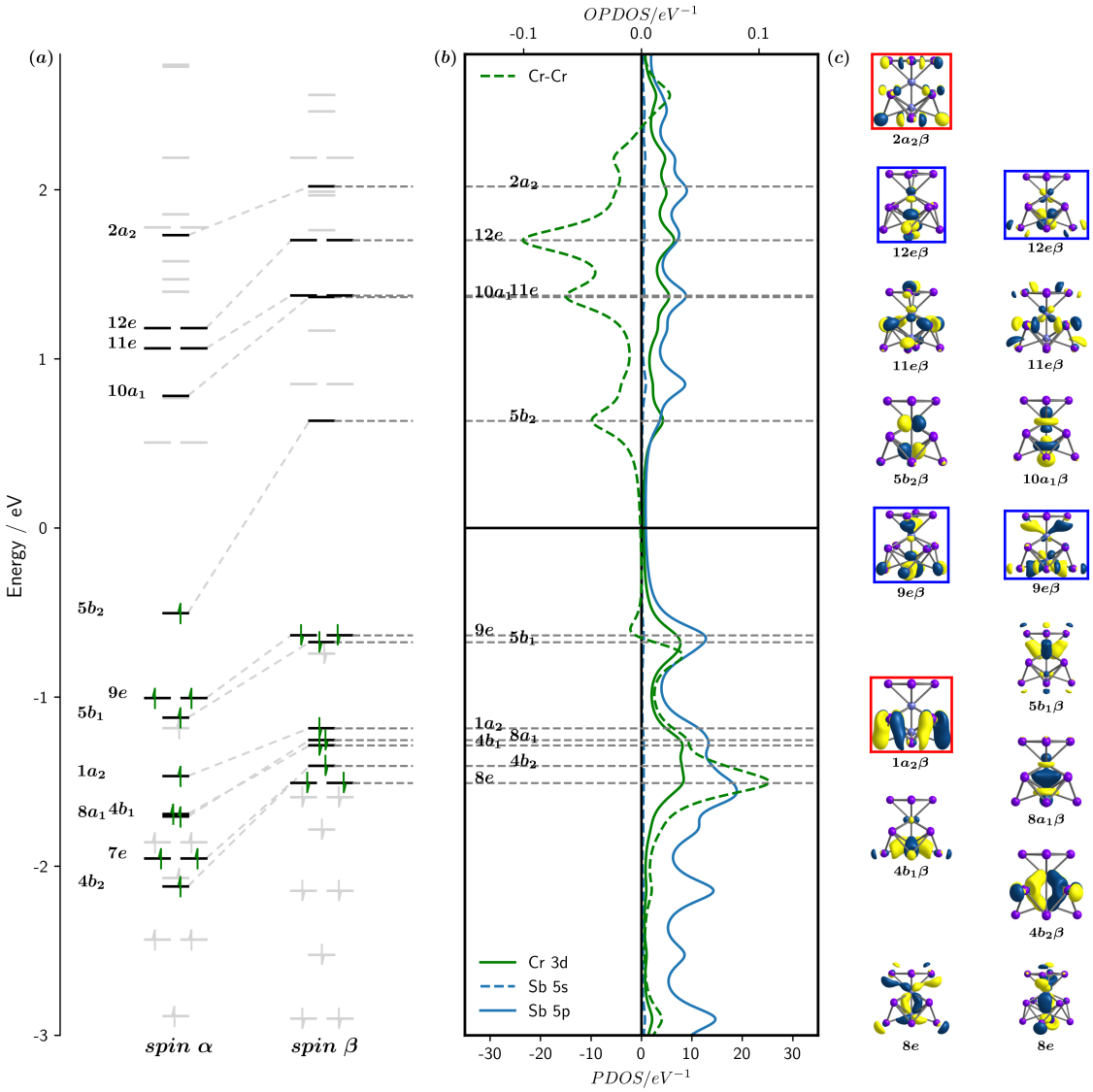

Figure 3.9: (a) Spin-α and spin-β Kohn-Sham orbital arrays of $^2B_2$-$[Cr_2Sb_{12}]^{3-}$; (b) PDOS plot of Cr $3d$, Sb $5s/5p$ and OPDOS plot of the Cr-Cr bond in the minority spin. Orbital levels are broadened with Lorentzian functions at the width of 0.1 eV; (c) Kohn-Sham orbital isosurface plots for significant orbitals, including all orbitals contributed by Cr $3d$. The $1a_2$ and $2a_2$ pair located on the cage in the spin-β array is also presented, which triggers the second-order Jahn-Teller distortion. The orbital isovalue is 0.05 e/Bohr^3.

terms of formal electron counting, the count at the Sb_{12} cage is increased by 2 to 58, while the count on the Cr_2 unit is reduced to 17.

As the structure relaxes from D_{4h} to C_{4v}, the filled $1a_{2g}$ and vacant $1a_{1u}$ orbitals in D_{4h} symmetry both transform as a_2 in C_{4v}, and so mixing between the two drives the distortion (a second-order Jahn-Teller distortion). This is highlighted by the

divergence of the two levels shown in blue in the Walsh diagram. Physically, this interaction corresponds to the transfer of electron density from the equatorial Sb_4 unit to one of the Sb_4 poles, fragmenting the triple-decker Sb_{12} unit into separate Sb_4 and Sb_8 units.

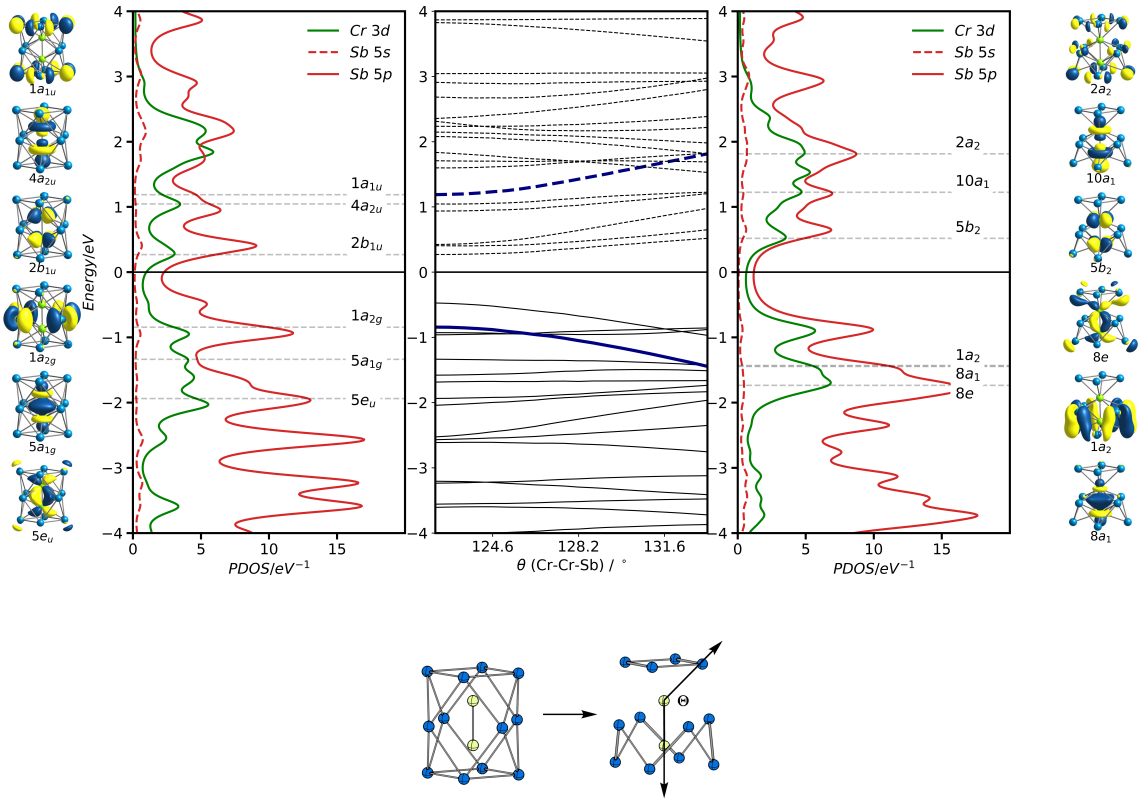

Figure 3.10: The Walsh diagram connects the D_{4h}- and C_{4v}-symmetric limits in $[Cr_2Sb_{12}]^{3-}$. 18 intermediate structures were generated by interpolating between the two optimised structures in Table 3.1. The orbitals and PDOS plots shown correspond to the spin-β set: Occupied levels are shown as solid lines, virtual levels as dashed lines and the $1a_2/2a_2$ pair is shown in blue.

3.2.3.2 DMRG analysis

The significant spin contamination that emerges from the DFT calculations on the open-shell cluster pair — $[Fe_2Sn_4Bi_8]^{3-}$ and $[Cr_2Sb_{12}]^{3-}$ implies that they have significant multi-configurational nature. This issue arises from the inherent limitation of unrestricted DFT, which employs different spatial distributions for the spin-α and spin-β orbitals. The increase of the expectation value of the spin operator $\hat{S}^2$ above the value implied by the number of unpaired electrons present is a direct consequence of the difference between the spin-α and spin-β manifolds. In such circumstances,

multi-configurational approaches offer an alternative means of capturing the electron correlation. The active space of the MC-SCF calculation should incorporate all $3d$ orbitals of both transition metal cores and their correlated orbitals (*i.e.* bonding-antibonding pairs), which requires an active space close to, or equal to, (20e, 20o) (20 electrons in 20 orbitals), a dimension that is at the limit of conventional (exact) CASSCF. We have therefore chosen to adopt the DMRG approach, which is a computationally efficient approach to multi-configurational calculations.

Mirroring our approach to the DFT work, the DMRG approach was first applied to the closed-shell reference $[Ni_2Bi_{12}]^{4+}$. DFT calculations assigned its electronic structure as $[Ni_2]^0$ + $[Bi_{12}]^{4+}$, where both nickel atoms are in core-like d^{10} configurations, giving 20 electrons in 10 occupied $3d$ orbitals. Each $3d$ orbital is then correlated with an empty orbital, giving an active space of DMRG(20e, 20o). The symmetry was set to D_{2h}, the highest Abelian sub-point group implemented in OpenMolcas. The isosurface of the natural orbitals and their occupation numbers are shown in Figure 3.11. The ONs of Ni $3d$ orbitals are predominantly over 1.95, along with their correlated orbitals holding less than 0.06 electrons, indicating the Ni $3d^{10}$ configuration dominates the total wavefunction. The correlated orbitals (those with low ONs) can be divided into two groups according to their distribution. In the first group, orbitals in b_{2u} and b_{3u} symmetry have Ni-Ni π character, and the correlated orbitals are primarily located on Bi $6p$ with Ni-Bi antibonding character. The underlying cause here is the slight back-bonding within the Ni-Ni π orbitals noted in the PDOS in the context of the DFT calculations. Likewise, in b_{1g}, the correlated orbitals are localised on the equatorial Bi_4 unit. The correlation in these symmetry groups can be viewed as 'in-out' correlation between the metals and the cage.

In the second group, a_g, b_{2g}, b_{3g}, b_{1u} and a_u, the $3d$ orbitals correlate with their $4d$ counterparts, which is known as the 'double-d-shell' effect. The difference arises because there are no vacant orbitals on the Bi_{12} cage that can engage in back-bonding with these metal orbitals, so the only available correlated orbitals are d orbitals with larger radial amplitudes. The 'double-d-shell' effect highlights the necessity to incorporate excitations from metal $3d$ to $4d$ orbitals in the wavefunction when metal-cage interactions are weak.

We can extract further insight from the single-orbital entropy $s(1)_i$ and mutual information $I_{i,j}$, which serve as criteria for distinguishing different types of electron correlation. Their values are generated from the one-orbital and two-orbital reduced density matrix (1o-RDM and 2o-RDM) introduced by Boguslawski et al.[172]

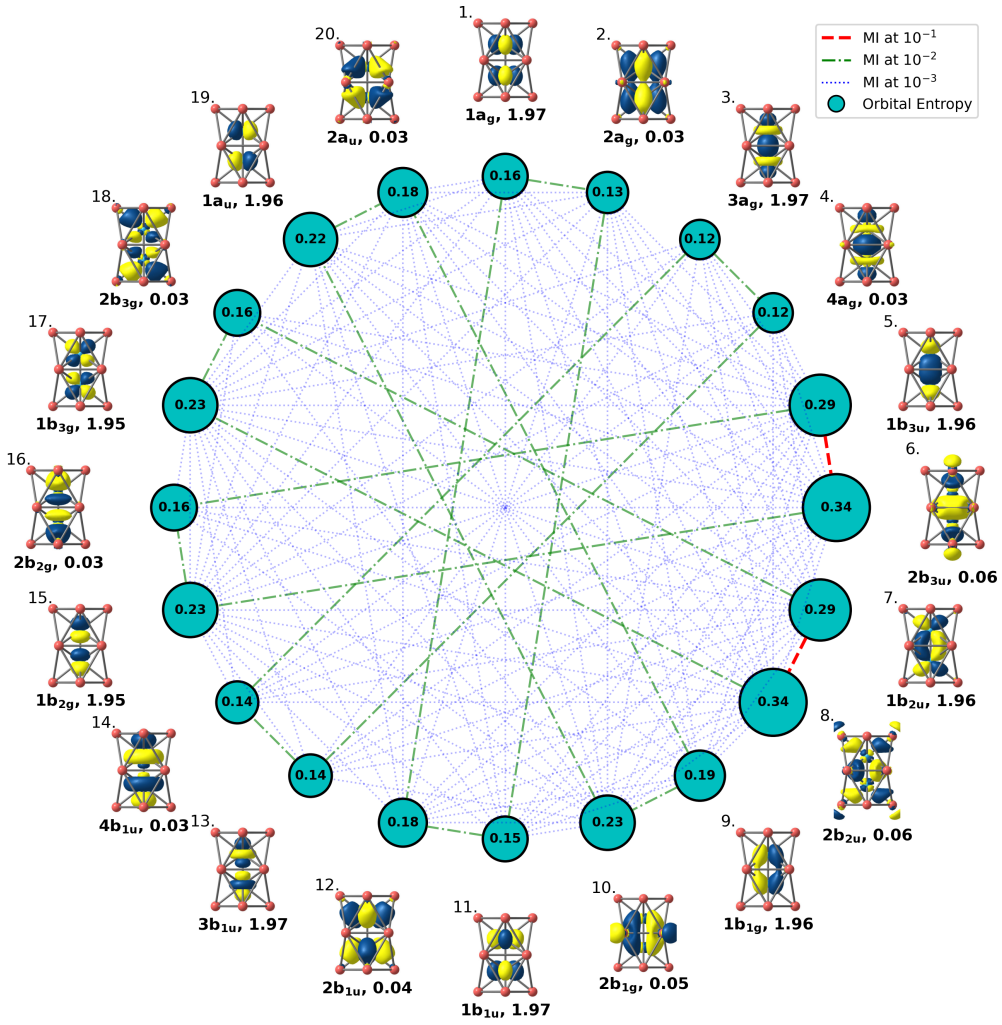

Figure 3.11: Isosurface plots of natural orbitals and their ONs in the active space of a DMRG(20e, 20o) calculation on $[Ni_2Bi_{12}]^{4+}$. D_{2h} symmetry in the Abelian point group was imposed. Single orbital entropies correspond to the size of a circle on each site, and mutual information is represented by the line connecting sites. Different line styles reflect the strength of entanglement.

$s(1)_i$ can be obtained from the eigenvalues of the 1o-RDM

$$s(1)_i = -\sum_{\alpha=1}^{4} w_{\alpha,i}\ ln\ w_{\alpha,i} \tag{3.2.2}$$

Two-orbital entropies can also be represented by the eigenvalues of 2o-RDM

$$s(2)_i = -\sum_{\alpha=1}^{16} w_{\alpha,ij}\ ln\ w_{\alpha,ij} \tag{3.2.3}$$

and the mutual information is obtained from single-orbital and two-orbital entropies

according to:

$$I_{i,j} = \frac{1}{2}(s(2)_{i,j} - s(1)_i - s(1)_j)(1 - \delta_{ij}) \tag{3.2.4}$$

According to Reiher et al.,[173] orbitals with $s(1)_i > 0.5$ and $I_{i,j} \sim 10^{-1}$ are crucial for the non-dynamic correlation, while those with $0.1 < s(1)_i < 0.5$ and $I_{i,j} \sim 10^{-2}$ contribute primarily to static correlation. In contrast, orbitals characterised by negligible $s(1)_i$ and $I_{i,j}$ are associated with dynamic correlation. Non-dynamic correlation refers to maintaining the correct charge distribution upon bond dissociation. Static correlation is important for obtaining a balanced description of several near-degenerate states and dynamic correlation accounts for the instantaneous movement of electrons, which is always related to electron excitations. The single-orbital entropies and mutual information for $[Ni_2Bi_{12}]^{4+}$ were also plotted in Figure 3.11. The orbitals are arranged in a circular layout, where the size of each circle at a given orbital site reflects its single-orbital entropy value. Mutual information between orbitals is represented by lines connecting the sites. Red dashed lines indicate pairs with $I_{i,j} \sim 10^{-1}$, corresponding to non-dynamic correlation; green dash-dotted lines match $I_{i,j} \sim 10^{-2}$, associated with static correlation; and blue dotted lines demonstrate $I_{i,j} \sim 10^{-3}$, as a contribution to dynamic correlation. All active orbitals show moderate single-orbital entropies ranging from 0.1 to 0.4, indicating their importance on describing static correlation. Orbitals 5–8, which correspond to the degenerate π bonding orbitals and their correlated partners related to the 'in-out' correlation, exhibit $s(1)_i$ values over 0.3. This value is marginally higher than those of other active orbitals, where their $s(1)_i$ values are around 0.2. The mutual information between these π correlated pairs, $I_{5,6}$ and $I_{7,8}$, is also high at 0.16, even reaching the non-dynamic range. Significant mutual information values are found within each symmetric group, and also observed between orbitals belonging to different irreducible representations, especially for the entanglement between Ni-Ni bonding orbitals and the correlated orbitals of their corresponding antibonding ones (for example $I_{5,16}$) or Ni-Ni antibonding orbitals and the correlated orbitals of their bonding ones (for example $I_{8,17}$). This analysis suggests that the 'in-out' correlation orbitals exhibit a stronger static correlation than those associated with the 'double-d-shell' effect. The correlations between different irreducible representation groups are also predominantly dynamic in nature. In summary, DMRG calculations on $[Ni_2Bi_{12}]^{4+}$ provide a perspective that is complementary to the DFT picture captured in Figure 3.6. The encapsulated Ni atoms possess relatively contracted, core-like $3d$ orbitals that do not interact strongly with the cage, resulting in 'double-d-shell' correlation rather than 'in-out' correlation with the $[Bi_{12}]^{4+}$ shell in many cases. The intermediate values of

$s(1)_i$ and $I_{i,j}$ indicate the presence of static correlation in the active space, with the 'in-out' correlation stronger than the 'double-d-shell' one.

In the case of 75-electron $[Fe_2Sn_4Bi_8]^{3-}$, DFT calculations indicate that the ground state of the cluster is $^2A_{2u}$, with the unpaired electron located in the Fe-Fe σ^* orbital. The electron distribution was characterised as $[Fe_2]^{3-} + [Sn_4Bi_8]^0$, albeit with substantial back-bonding from the Fe_2 unit. The active space was initialised as DMRG(19e, 20o), where every 3d orbital is paired with a correlated orbital. After optimising for all state symmetries, the $^2B_{1u}$ state was confirmed to be the ground state, which lies at least 0.54 eV below the others. In the active space of $^2B_{1u}$, the σ^* orbital has an ON close to 1, while its correlated orbital has an ON of less than 0.01, indicating that this correlated orbital remains vacant in almost every configuration, and has little influence on the correlation energy. As a result, the active space was then truncated to DMRG(19e, 19o) without significant loss of accuracy. Natural orbitals and their ONs for the DMRG(19e, 19o) active space are shown in Figure 3.12. Compared to the high occupancy of ∼1.95 of the Ni 3d orbitals in $[Ni_2Bi_{12}]^{4+}$, the ONs of the occupied Fe 3d orbitals are substantially lower, in the range of 1.80-1.92, and the correlated orbital ONs rise to approximately 0.15. These much greater deviations from 2/0 indicate that the Fe-based orbitals show increased valence character compared to the Ni 3d orbitals. The isosurface plots of the natural orbitals also confirm stronger interactions between Fe 3d and the p orbitals on the surrounding cage contrary to $[Ni_2Bi_{12}]^{4+}$, consistent with more pronounced 'in-out' correlation effects. The correlated orbitals are mostly the corresponding p-d antibonding interactions, made up predominantly by p orbitals from the cage. Among these active orbitals, the degenerate Fe-Fe π^* orbitals in b_{2g} (orbital 14) and b_{3g} (orbital 16) symmetry groups have the lowest ONs (1.81) within the Fe 3d manifold and their correlators (orbitals 15 and 17) have the highest ONs (0.19) and the largest contribution from Fe d_{xz}/d_{yz} orbitals, accounting for 47.0 % of the total composition. The single-orbital entropy values, $s(1)_i$, of most active orbitals in $[Fe_2Sn_4Bi_8]^{3-}$ also increase compared to $[Ni_2Bi_{12}]^{4+}$, and only orbitals 4 and 19 (those with ON below 0.05) now fall below 0.2. $s(1)_i$ values of orbital 1 and 12 as Fe-Fe σ/σ^* pair and orbitals 14–17 with Fe-Fe π^* character, are over 0.5, implying strong correlation. The orbital entanglement, captured in the mutual information indices, is most pronounced for the Fe-cage bonding/antibonding pairs ($I_{1,2}$, $I_{5,6}$, $I_{7,8}$, $I_{11,12}$, $I_{14,15}$, $I_{16,17}$), although correlation between Fe-Fe bonding/antibonding pairs is also apparent, for example in $I_{3,13}$ (Fe-Fe σ/σ^*). This picture is again fully consistent with the back-bonding that emerged from the DFT framework from the same $4e_g/5e_g$ pairs, highlighted by blue and red boxes in Figure 3.12. The wavefunction

and DFT approaches are therefore consistent with each other, although the relevant information emerges in a rather different context (spin contamination in DFT and ON, mutual information in DMRG). Both DMRG and DFT calculations reveal a greater tendency for the Fe 3*d* orbitals to engage in back-bonding compared to the more core-like Ni 3*d* orbitals.

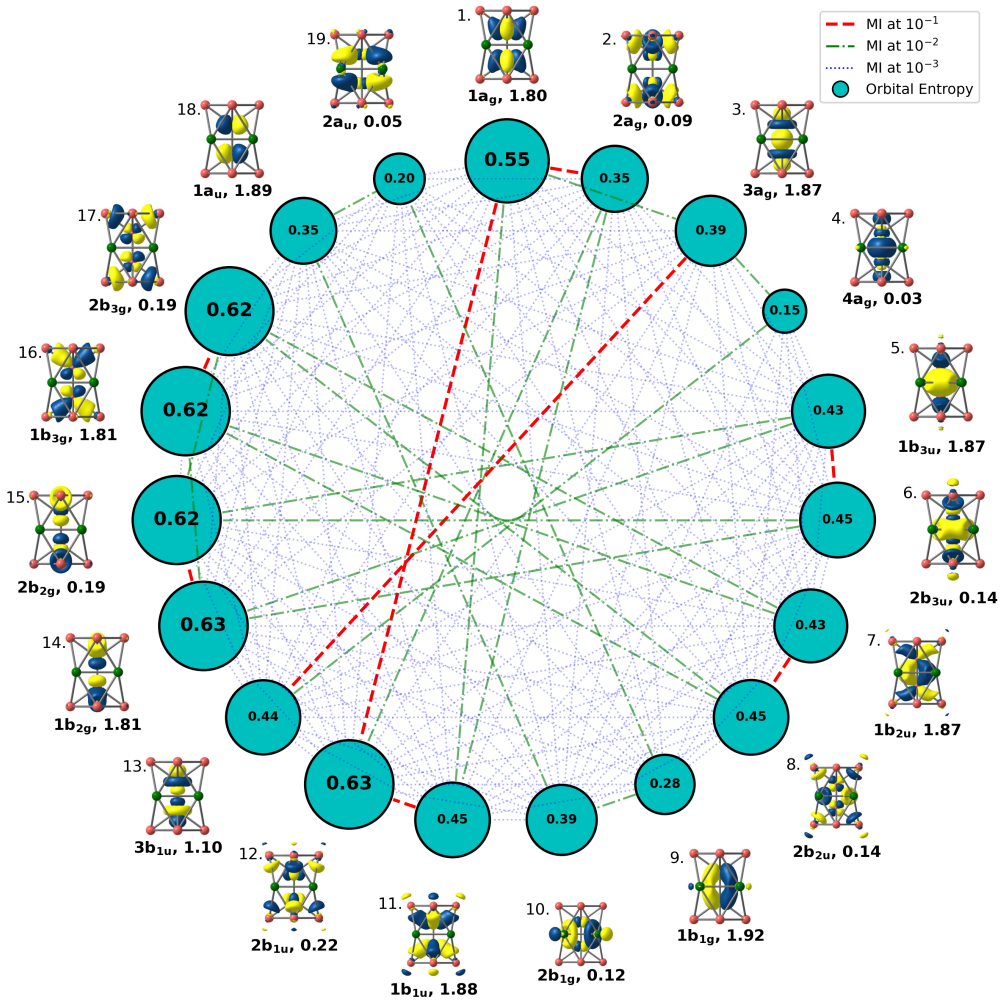

Figure 3.12: Isosurface plots of natural orbitals and their ONs in the active space of a DMRG(19e, 19o) calculation on $[Fe_2Sn_4Bi_8]^{3-}$. D_{2h} symmetry in the Abelian point group was used. Single orbital entropies correspond to the size of a circle on each site, and mutual information is represented by the line connecting sites. Different line styles reflect the strength of entanglement.

The C_{4v}-$[Cr_2Sb_{12}]^{3-}$ was deduced to have a charge distribution of $[Cr_2]^{5-}$ + $[Sb_{12}]^{2+}$. Following a similar DMRG initialisation approach used in $[Fe_2Sn_4Bi_8]^{3-}$, all Cr 3*d* orbitals and their correlated orbitals are selected to be in the active space, establishing a preliminary calculation framework as DMRG(17e, 20o) under a re-

laxed C_{2v} symmetry. The introductory results confirm that the spatial symmetry of the ground state is $^2A_2$, matching the result from DFT. The wavefunction analysis further reveals three active orbitals with ONs lower than 0.01, which correlate to the Cr-Cr σ, σ^* and δ^* orbitals. Among these orbitals, the δ^* one hosts the unpaired electron, and does not exhibit strong correlation with any other orbital. The unoccupied Cr-Cr σ^* now shows correlation with the σ orbital, demonstrating a 'left-right' correlation between two Cr atoms. According to these findings, the following calculations were then performed with an active space of (17e, 17o) in $^2A_2$ spatial symmetry for further detailed investigations. The computational result is presented in Figure 3.13. The occupation numbers of Cr 3d orbitals are comparable to those of Fe 3d orbitals in $[Fe_2Sn_4Bi_8]^{3-}$ in most active orbitals, which also deviate significantly from uncorrelated pair as 2/0. However, their isosurface plots exhibit a stronger mixing between Cr 3d and Sb 5p orbitals. Due to the symmetry reduction from D_{4h}, the δ/δ^* orbital pair is decomposed into two separate d_{xy} orbitals, each of which localises on one Cr atom. These orbitals exhibit correlations with the upper and lower Sb_4 units, respectively. The 'in-out' correlation can be captured in most pairs, with approximate ONs of 1.85/0.15. The most significant orbital mixing between Cr 3d and Sb 5p still occurs on two Cr-Cr π^* orbitals, labelled as $3b_2/4b_2$ (orbital 16 and 17) and $3b_1/4b_1$ (orbital 9 and 10), which should be degenerate under C_{4v} symmetry. Natural orbital isosurface plots suggest that the occupied orbitals now clearly represent back-bonding interactions from the Cr 3d to the bottom and top Sb_4 decks. Their corresponding correlated orbitals exhibit a substantial contribution from the Cr 3d orbitals, consistent with Cr-Cr π^* interactions. Their ONs also exhibit the largest discrepancy to 2/0 as 1.90/0.18. In addition to the prominent 'in-out' correlation, there are exceptions in the electronic structure of $[Cr_2Sb_{12}]^{3-}$. As briefly mentioned above, the σ^* orbital (orbital 6) remains unoccupied, which can accept electrons excited from σ orbital (orbital 5), giving rise to the 'left-right' correlation. The ONs for this correlation pair deviate significantly from 2/0, as 1.72/0.29. This indicates substantial interactions between the Cr-Cr σ/σ^* orbitals. Furthermore, the δ^* orbital, primarily contributed by the d_{xy} orbital in the a_2 symmetry array, possesses an ON of 0.99, which can be identified as a singly-occupied orbital. Even though there is negligible change on the ONs from $[Fe_2Sn_4Bi_8]^{3-}$ to $[Cr_2Sb_{12}]^{3-}$, the increased $s(1)_i$ can demonstrate stronger non-dynamic correlation for the chromium cluster. In the active space of $[Cr_2Sb_{12}]^{3-}$, $s(1)_i$ values of more than half orbitals are greater than 0.5. The most prominent $s(1)_i$ values occur on orbital 5 and 6 at over 0.7, which corresponds to the Cr-Cr σ/σ^* orbital pair. The $I_{5,6} = 0.36$ also supports the strong non-dynamic correlation between

these orbitals. For orbitals with δ character by Cr $3d_{xy}$, the non-dynamic correlation is contributed mostly by the interactions between the Cr-Cr δ bonding orbital (orbital 11) and its correlated orbital (orbital 12). The unpaired electron on Cr-Cr δ^* orbital (orbital 13) mainly donates to the static correlation, through its interactions with the other two δ orbitals in a_2 symmetry. Cr $3d_{yz}$ and $3d_{xz}$ are involved in the π interactions between two chromium atoms. The π bonding orbitals (orbital 7 and 14) show non-dynamic correlation with the empty π^* correlated orbitals (Orbital 10 and 17) proven by both $I_{7,10}$ and $I_{14,17}$ reaching 0.15. This observation can be explained by strong electron density back-donation from Cr-Cr π^* to the cage on the occupied orbital 9 and 16, leading to most Cr $3d$ contributions left on the mostly vacant ones as orbital 10 and 17. The obvious exceeding mutual information value of $I_{14,17}$ over $I_{14,16}$, plus the ON summation of orbital 14 and 17 close to 2, can be evidence for direct π/π^* correlation. There are still two orbitals that possess $s(1)_i$ close to 0.1 as orbital 1 and 2, which present the 'in-out' correlation based on the $d_{x^2-y^2}$ orbital on Cr2. Their mutual information with other orbitals is at the magnitude of 10^{-3} and 10^{-2}, exhibiting their contribution to both dynamic and static correlation. The dynamic correlation can be captured between orbitals in different symmetry groups, as the blue dashed lines crossing the orbital site circle in the mutual information plot. Based on the results of DMRG calculations, Cr $3d$ orbitals now show pronounced valence character, especially for the Cr-Cr π^* orbitals. This valence character can be explained through both spin contamination and back-bonding in the spin-β manifold by DFT calculations, and through its multi-configurational nature as robust 'in-out' correlation by ONs and mutual information from DMRG calculations. Either way finally induces the electron accumulation on the cage and a second-order Jahn-Teller distortion from the D_{4h} structure.

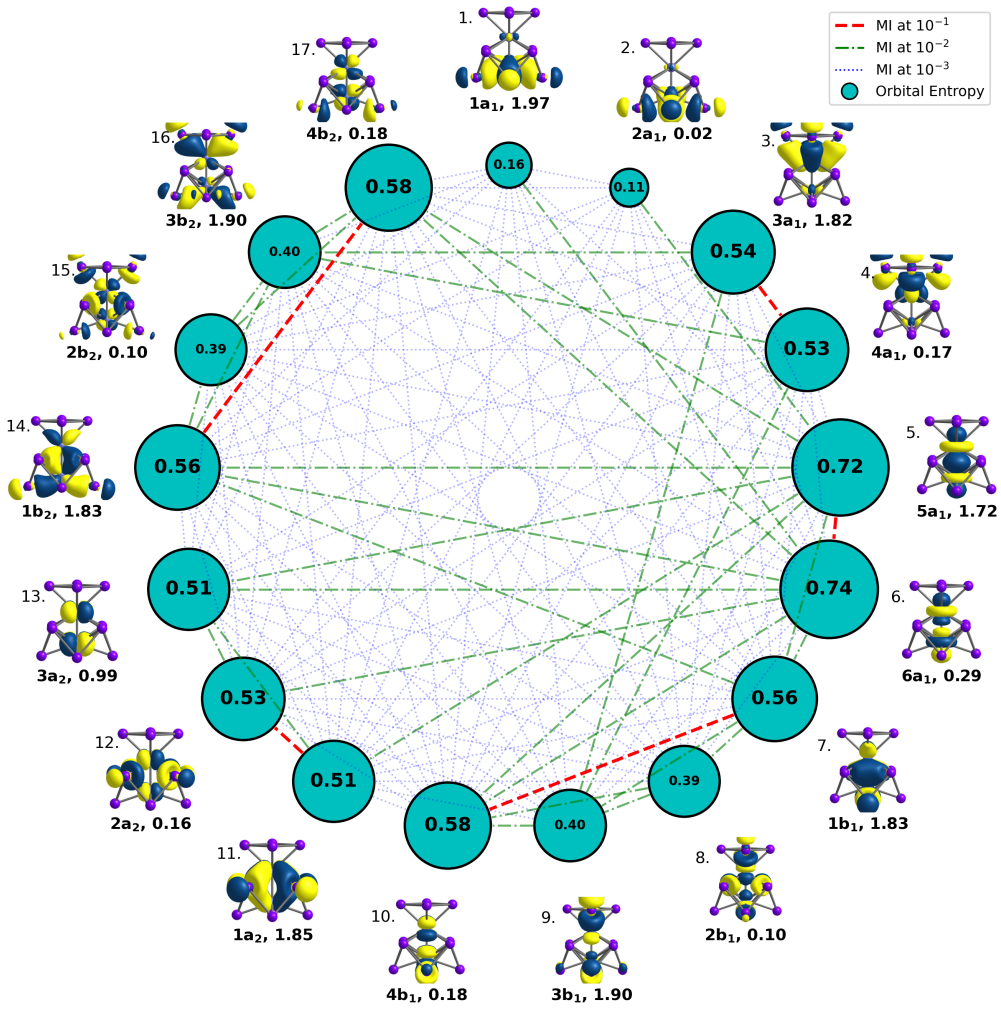

Figure 3.13: Isosurface plots of natural orbitals and their ONs in the active space of a DMRG(17e, 17o) calculation on $[Cr_2Sb_{12}]^{3-}$. C_{2v} symmetry in the Abelian point group was applied. Single orbital entropies correspond to the size of a circle on each site, and mutual information is represented by the line connecting sites. Different line styles reflect the strength of entanglement.

3.2.4 Conclusion

In this section, we perform both DFT and DMRG calculations to investigate the electronic configurations of $[Ni_2Bi_{12}]^{4+}$, $[Fe_2Sn_4Bi_8]^{3-}$ and $[Cr_2Sb_{12}]^{3-}$. The 76-electron $[Ni_2Bi_{12}]^{4+}$ is as a closed-shell reference point, confirming that 56 skeletal electrons are required to support a D_{4h} cage without the help of core-like nickel atoms. Two 75-electron clusters exhibit different geometries. $[Fe_2Sn_4Bi_8]^{3-}$ has a similar D_{4h} structure as $[Ni_2Bi_{12}]^{4+}$, but a stronger back-donation from metal to the cage. The singly-occupied electron locates on the Fe-Fe σ^* orbital and helps build up the Fe-Fe bond. In the meantime, the electronic structure of the cage is largely retained. From

Fe to Cr, the metal d-band is shifted upwards, creating two more electron holes at the Cr-Cr $\sigma^*\alpha$ and $\delta^*\beta$ orbitals. These holes are compensated by the occupation of $1a_2$ orbital leading to the second-order Jahn-Teller distortion on the cage, downgrading the geometry symmetry to C_{4v}. The charge distribution can be regarded as lying between two extreme ends as $[Cr_2]^{5-}$+$[Sb_{12}]^{2+}$ and $[Cr_2]^{-}$+$[Sb_{12}]^{2-}$. The progressive upward shift in the energy of the d orbitals shows more valence-like d orbitals, which strengthens the back-bonding and finally triggers the geometry distortion. The back-bonding appears as spin contamination in the unrestricted DFT, and as orbital isosurface plots with ON deviation from 2/0 and mutual information change in DMRG. This distortion pathway from $[Ni_2Bi_{12}]^{4+}$ to $[Cr_2Sb_{12}]^{3-}$ shown in Figure 3.14 is a replication to the change from $[NiPb_{12}]^{2-}$ to $[RuGe_{12}]^{3-}$ with the existence of the metal-metal bond. $[Ni_2Bi_{12}]^{4+}$ matches $[NiPb_{12}]^{2-}$ as a reference. The slightly distorted case is covered by $[Fe_2Sn_4Bi_8]^{3-}$ and $[MnPb_{12}]^{3-}$, and d electrons become valence-like in $[Cr_2Sb_{12}]^{3-}$ and $[RuGe_{12}]^{3-}$, finally rearranging the cage geometry.

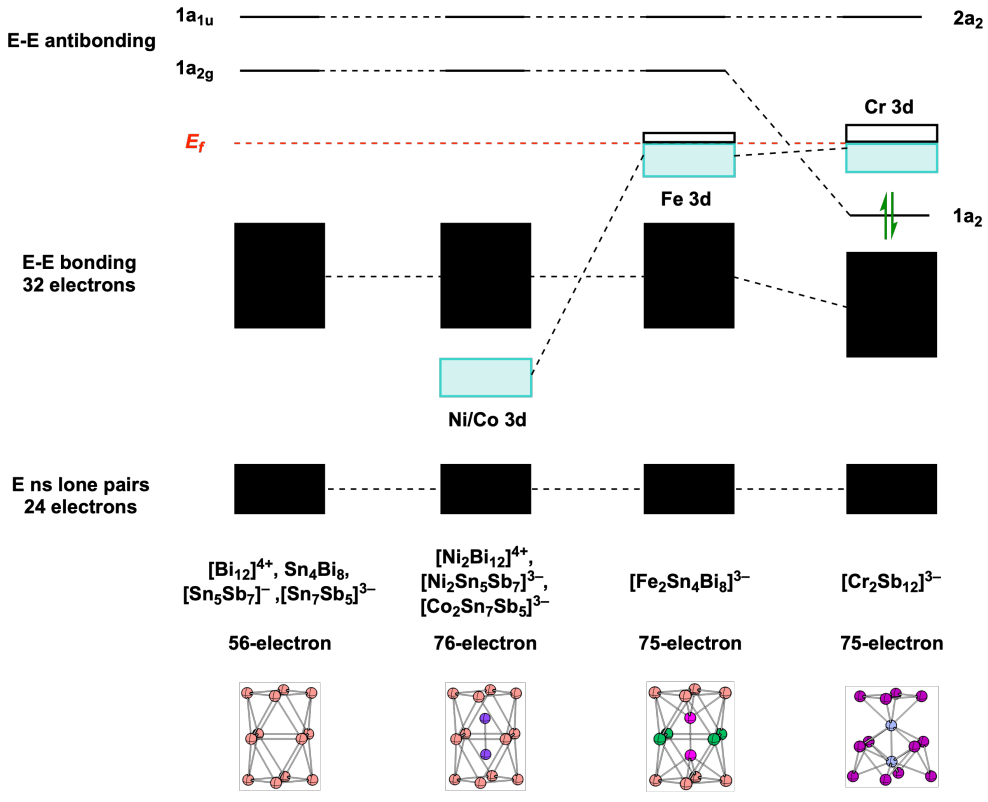

Figure 3.14: Overview of the trends in electronic structure across the 75- and 76-electron M_2E_{12} series.

3.3 Fe-Fe bonding and its role in the cluster formation in $[Fe_3Sn_{18}]^{4-}$

This section focuses on the tri-iron cluster, $[Fe_3Sn_{18}]^{4-}$, which was synthesised by Prof. Zhong-Ming Sun and co-workers. All experimental work referenced here, including the X-ray structure, is theirs. The unit cell and structure of $[Fe_3Sn_{18}]^{4-}$ are presented in Figure 3.15. The motivation for the work was to understand how the presence of Fe-Fe bonding, made possible by the open-shell nature of the Fe centres, impacts on the cluster. The work has been published in *Chemical Science*, 2024, **15**, 1018–1026.

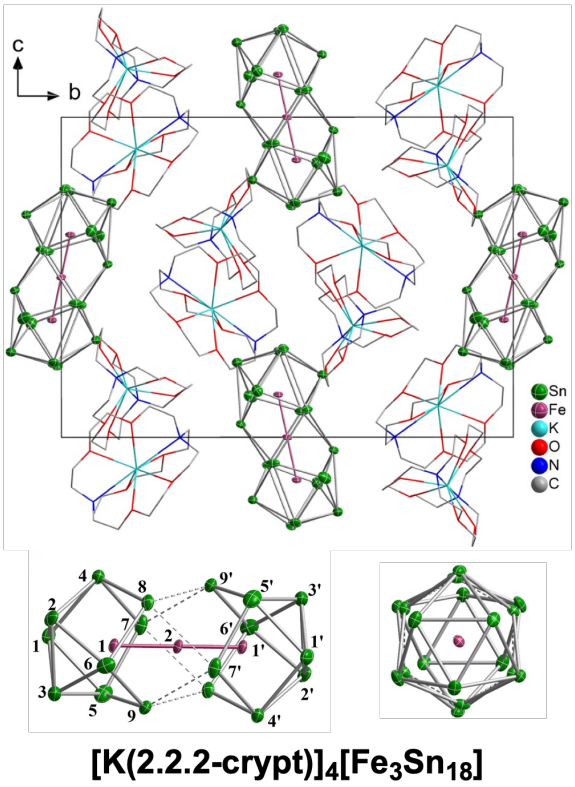

Figure 3.15: Unit cell of $[K(2.2.2\text{-crypt})]_4[Fe_3Sn_{18}]$, including front and side views of the anions. The XRD experiment was performed by Dr. Wei-Xing Chen in Prof. Zhong-Ming Sun's group. (Reproduced from our published work as Ref. 2)

3.3.1 Introduction

Moving beyond the encapsulated M_2E_{12} clusters discussed in the previous section, I now consider further expansion of the Zintl cluster to incorporate three transition metal atoms. The cluster in question, $[Fe_3Sn_{18}]^{4-}$, is a high-spin Fe_3 system composed of a linear tri-iron core encapsulated inside a D_{3d}-symmetric E_{18} cage. X-ray

crystallography shows that the length of the cluster is 9.74 Å approximately 1.5 times as large as $[Fe_2Sn_4Bi_8]^{3-}$ (5.59 Å). The Fe-Fe distances of 2.4300(9) Å indicate the existence of metal-metal bonds, which will be discussed in detail below. Intuitively, the E_{18} cluster can be regarded as two fused E_9 fragments, joined by two triangular faces. The relatively small E_9 cluster is common in endohedral Zintl cluster chemistry, and is known to adopt two isomeric structures. $[CoSn_9]^{5-}$,[98] $[RuSn_9]^{6-}$,[95] $[RhSn_9]^{4-}$,[174] $[NiSn_9]^{4-}$[96] and $[PdSn_9]^{4-}$[174] are C_{4v}-symmetric Monocapped Square Antiprism (MSA) while $[CuE_9]^{3-}$ (E = Sn, Pb) is a Tricapped Trigonal Prism (TTP) with D_{3h} point symmetry.[97] The MSA is formally a *nido* cluster, while the TTP is *closo*. The two isomers are, in fact, relatively similar in energy. The $[E_9]^{4-}$ cage (with a *nido* electron count) can be derived by adding two electrons to the LUMO of *closo*-$[E_9]^{2-}$, which causes an elongation along the principal axis. The stability of both $[E_9]^{2-}$ and $[E_9]^{4-}$ has been explained in terms of aromaticity through Ad-NDP analysis.[175] The square faces in MSA and a triangle face in TTP geometries of E_9 or ME_9 clusters, are loci for functionalisation by metal complexes. For example, the square base of the MSA isomer can act as an η^4 ligand (shown in Figure 3.16 (a)) in $[E_9M(CO)_3]^{4-}$ (E = Sn, Pb; M = Cr, Mo, W),[176–180] $[Sn_9Ir(cod)]^{3-}$,[94] $[Cu(Ge_9)R]^{3-}$ (R = PCy_3, P*i*-Pr_3),[181] $[E_9ZnR]^{3-}$ (E = Ge, Sn, Pb; R = Mes, *i*Pr, Ph),[182] $[Ge_9PdPPh_3]^{3-}$,[183] $[NiSn_9Ni(CO)]^{3-}$,[184] $[CoSn_9NiL]^{3-}$ (L = CO, C_2H_4).[185] A triangular face of the TTP isomer can also act as an η^3 ligand (shown in Figure 3.16 (b)) in $[Ge_9Ni(CO)]^{3-}$,[186] $[Ni(Ge_9NiL)]^{x-}$ (x = 2, L = CO; x = 3, L = CCPh),[186] $[Ni(Ge_9PdPPh_3)]^{2-}$,[183] $[PtSn_9Pt(PPh_3)]^{2-}$,[184] $[PdSn_9Pd(SnCy_3)]^{3-}$,[187] $[CoSn_9Pt(PPh_3)]^{3-}$, and $[CoSn_9AuPh]^{3-}$.[185] In addition to functionalisation by metal ligands, self-functionalisation, in the form of fusion or oligomerisation, can also occur through the formation of localised *exo* or delocalised bonds connecting triangular faces. Unlike the Coulomb attraction between a negatively-charged Zintl ion and a transition metal cation, the challenge in dimerisation arises because both components typically carry negative charges, leading to strong Coulomb barriers. In examples with *exo* bonds, the repulsion can be compensated by sharing electron pairs between fragments, as for example in $[(Ge_9)_3]^{6-}$[188] and $[(Sn_9)_4]^{8-}$.[189] In cases with only a single direct bond between E_9 units, the introduction of the positively charged transition metal can also reduce the Coulomb repulsion, as in $[AgSn_{18}]^{5-}$[190] and $[AuSn_{18}]^{5-}$.[191] The bonding between two units can also be highly delocalised, with a transition metal cation again playing a role in balancing the negative charges, such as in $[Cd(NiSn_9)_2]^{6-}$,[102] $[In(NiGe_9)_2]^{5-}$,[103] $[NbCp_2(Ge_9)_2]^{5-}$, $[(NbCp_2)_2(Ge_9)_2]^{5-}$.[191] The formation of the metal-metal bonds can also favour cluster fusion, as in the case

of $[Ni_3Ge_{18}]^{4-}$ [112] and $[Pd_2E_{18}]^{4-}$ (E = Ge,[110] Sn[111]). In this series, the germanium fragment Ge_{18} shows a progressive fusion from the separated-limit $[In(NiGe_9)_2]^{5-}$ [103] to an intermediate stage in $[Ni_3Ge_{18}]^{4-}$ [112] and finally to the completely fused-limit $[Pd_2Ge_{18}]^{4-}$.[110] In the analogous Sn chemistry, only the fully separated and fully-fused limits were known, in $[Cd(NiSn_9)_2]^{6-}$ [102] and $[Pd_2Sn_{18}]^{4-}$,[111] respectively. The new $[Fe_3Sn_{18}]^{4-}$ represents the missing intermediate in the Sn_{18} cluster fusion process, having structural properties intermediate between $[Cd(NiSn_9)_2]^{6-}$ and $[Pd_2Sn_{18}]^{4-}$. After discussing the electronic structure of the new cluster, we will consider how it fits amongst the known structural chemistry of this class, and what information it provides about possible cluster growth mechanisms.

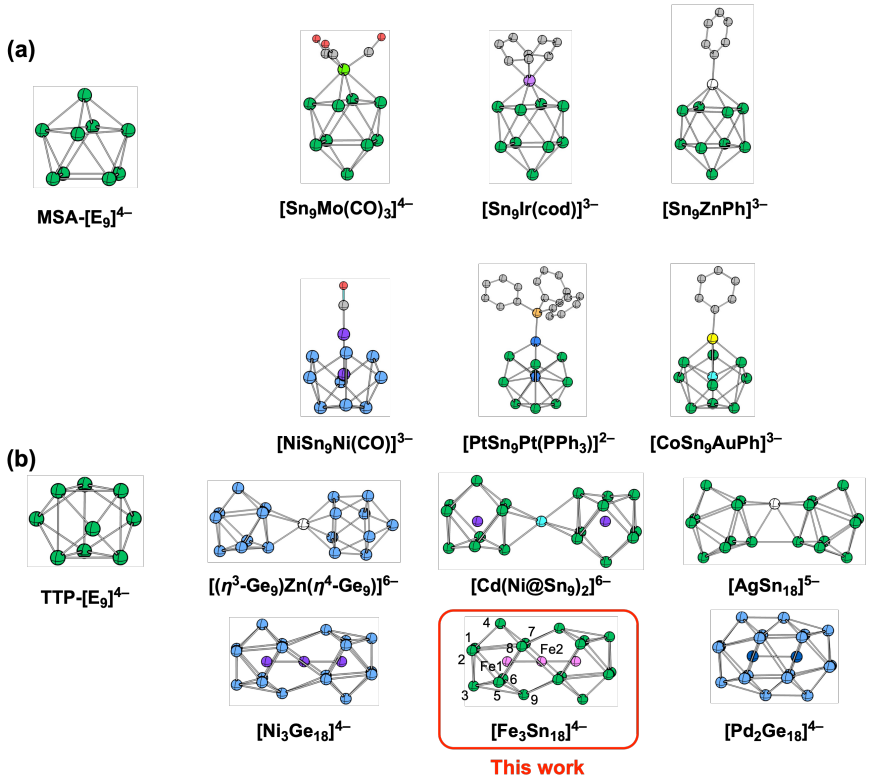

Figure 3.16: Geometries of MSA and TTP $[E_9]^{4-}$ and their coordinated derivatives. (H atoms were omitted for clarity)

3.3.2 Computational details

All computational work in this section was performed by the ADF 2021.104 package.[69] The PBE,[47] M06-L[53,54] and PBE0[57,192] functionals were used to benchmark, and the results with the former were applied for further analysis. Slater-type TZ2P basis sets were used.[164] All electrons were incorporated in the basis sets. Relativistic effects were

considered by the scalar-ZORA.[163] The numerical grid was tuned to 'verygood'.[193] The COSMO[165] was included using water as the solvent (equals to the dielectric constant of 78.39) to produce a confined space mimicking the crystalline environment. EHT calculations were performed by Gaussian16,[194] where the Hoffmann parameters were applied.

3.3.3 Electronic structure analysis

DFT calculations confirm the high-spin nature of D_{3d}-$[Fe_3Sn_{18}]^{4-}$: it has a $^7A_{2g}$ ground state, which lies 0.1 eV below the $M_s = 1$ broken-symmetric state (PBE functional). Through benchmarking using PBE, M06-L and PBE0 functionals, the results from the PBE functional show the best agreement with the geometry in experiment as shown in Table 3.2, and these geometric parameters were applied for further electronic structure analysis. Its structure is very similar to D_{3d}-symmetric $[Ni_3Ge_{18}]^{4-}$. Both clusters show a large difference between the E4-E9′ and E8-E9′ distances (4.05 Å vs. 3.47 Å in $[Ni_3Ge_{18}]^{4-}$ and 4.10 Å vs. 3.460 Å in $[Fe_3Sn_{18}]^{4-}$), and the ratio of E4-E9′ to E8-E9′ is similar for both clusters (1.17 in $[Ni_3Ge_{18}]^{4-}$ and 1.18 in $[Fe_3Sn_{18}]^{4-}$) (see Figure 3.15 for atom numbers): the E7-E8-E9 face expands as the two E_9 fragments fuse. The electronic structure of $[Ni_3Ge_{18}]^{4-}$ is first reinvestigated here as a precursor to our study of $[Fe_3Sn_{18}]^{4-}$. The ground state of $[Ni_3Ge_{18}]^{4-}$ is a singlet, and Figure 3.17 shows (a) the Kohn-Sham eigenvalue array, (b) the PDOS plus OPDOS and isosurface plots of significant orbitals of $[Ni_3Ge_{18}]^{4-}$. The orbital levels dominated by Ni 3*d* character are highlighted in the Kohn-Sham array, and those with Ni-Ni-Ni σ character are connected by the red dashed line. From the PDOS, it is evident that there is a small Ni 3*d* band above the Fermi level, at +0.4 eV, which corresponds to antibonding interactions according to the negative OPDOS. This band corresponds to the $9a_{1g}$ orbital, the isosurface plot of which confirms it to be the Ni-Ni σ^* orbital of the Ni_3 core. Other orbitals with σ character include $7a_{1g}$ and $5a_{2u}$, with bonding and nonbonding character, respectively. Therefore, the configurations of the σ framework can be represented as $\sigma^2\sigma^{nb\ 2}\sigma^{*0}$. The remaining Ni 3*d*-based orbitals are all in the occupied manifold: $4e_g$, $5e_u$, $7e_g$ have Ni-Ni π character and $5e_g$, $4e_u$, $6e_g$ are Ni-Ni δ set. Their net contribution to the Ni-Ni bonds is 0, as all bonding, nonbonding and antibonding combinations are filled. The formal Ni-Ni bond order is therefore 0.5 (half of a σ bond), consistent with the computed Mayer bond order of 0.45. The electron distribution of $[Ni_3Ge_{18}]^{4-}$ can be summarised as follows: there are 28 valence electrons located on the $[Ni_3]^{2+}$ chain, with the remaining 78 valence electrons forming a $[Ge_{18}]^{6-}$ cage.

Table 3.2: Selected bond lengths from crystallographic and DFT-optimised structures for the $[M_3E_{18}]^{4-}$ family (all distances in Å). See Figure 3.15 for atom numbering.

		M1-M2	E2-E8	E6-E9	E8-E9′	E4-E9′	ref
$\mathbf{[Fe_3Sn_{18}]^{4-}}$	X-ray (100 K)	2.4300(9)	3.690	3.004	3.460	4.10	This work
	DFT ($^7A_{2g}$)	2.45	3.64	3.04	3.50	4.22	
$\mathbf{[Ni_3Ge_{18}]^{4-}}$	X-ray (100 K)	2.395(1)	3.016	2.612	3.47	4.05	112
	DFT ($^1A_{1g}$)	2.43	3.09	2.66	3.29	4.01	
$\mathbf{[Cd(NiSn_9)_2]^{6-}}$	X-ray (100 K)	4.201	3.549	2.981	5.24	6.71	102
	DFT ($^1A_{1g}$)	4.26	3.71	3.02	5.32	6.81	
$\mathbf{[Pd_2Sn_{18}]^{4-}}$	X-ray (100 K)	-	3.303	3.145	3.426	3.096	111
	DFT ($^1A_{1g}$)	-	3.31	3.13	3.33	3.10	

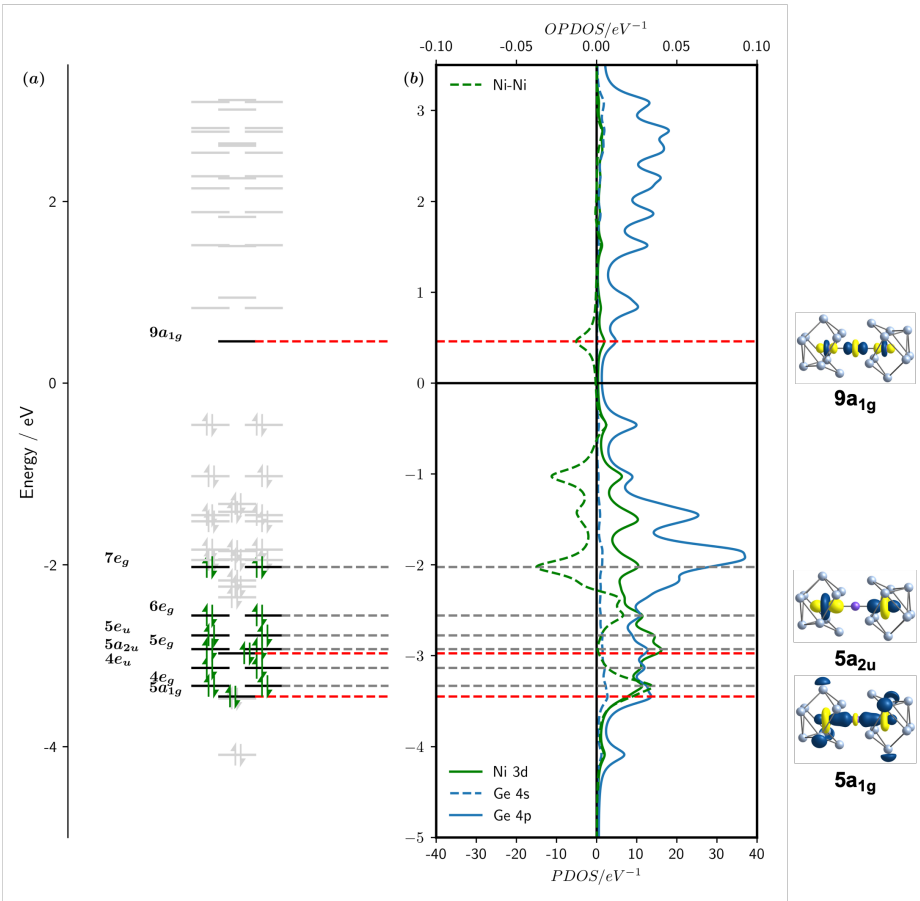

Figure 3.17: (a) Kohn-Sham orbitals of $[Ni_3Ge_{18}]^{4-}$ (b) PDOS of Ni 3*d*, Ge 4*s* and Ge 4*p* along with OPDOS of the Ni-Ni bond. The Lorentzian broadening parameter was set to 0.1 eV. Levels with Ni-Ni-Ni σ character are labelled by red dashed lines and their orbital isosurfaces are shown along the right side of the PDOS/OPDOS plot.

Based on the analysis of $[Ni_3Ge_{18}]^{4-}$ and the structural similarity between the Sn_{18} and Ge_{18} cages, we can assign the charge distribution of $[Fe_3Sn_{18}]^{4-}$ as $[Sn_{18}]^{6-}$ (78 electrons), and therefore $[Fe_3]^{2+}$ (22 electrons). The frontier Kohn-Sham energy

arrays and orbital isosurface plots (for both spins), along with the DOS for the spin-β manifold, are presented in Figure 3.18. The eigenfunctions with dominant Fe $3d$ contribution are highlighted by black lines and green arrows. As was the case in $[Ni_3Ge_{18}]^{4-}$, the Fe-Fe-Fe σ^* orbital, $9a_{1g}$, is unoccupied in both spin manifolds. Both spin components of the corresponding σ and σ^{nb} orbitals are again occupied ($7a_{1g}$ and $7a_{2u}$ in the spin-β array, $5a_{1g}$ and $5a_{2u}$ in spin-α). The configuration of the Fe-Fe σ framework is therefore $\sigma^2\sigma^{nb\ 2}\sigma^{*0}$, giving a net bond order of 0.5 for each Fe-Fe bond, precisely as we saw in the Ni_3 case. The multiplicity of the ground state as septet indicates the presence of six unpaired electrons, which are found in $8e_g\alpha$, $7e_g\alpha$ and $5e_u\alpha$ — the corresponding vacant spin-β components are $10e_g\beta$, $9e_g\beta$ and $8e_u\beta$. Both Fe-Fe π and δ orbitals belong to the e symmetry and so a clean separation on symmetry grounds is not possible. However, the isosurfaces show dominant π character in $4e_g\alpha/5e_g\beta$, π^{nb} character in $4e_u\alpha/7e_u\beta$ and π^* in $8e_g\alpha/10e_g\beta$. The latter is vacant, so the π bonding manifold of the Fe-Fe-Fe chain is $\pi^4\pi^{nb\ 4}\pi^{*2}$, giving a formal π bond order of 0.5 per Fe-Fe bond. The δ bonding and nonbonding orbitals are also singly occupied (unoccupied in $8e_u\beta$ and $9e_g\beta$), but as δ overlap is weak, these orbitals make little contribution to the overall bond strength. Therefore, each Fe-Fe bond can be regarded as $1/2\sigma+1/2\pi$ and the total bond order is 1, also in accordance with the calculated Mayer bond order of 0.95. Compared to $[Ni_3Ge_{18}]^{4-}$, the electron count on the linear tri-metal core is reduced from 28 to 22, which creates an additional π component of the bond.

After clarifying the nature of Fe-Fe interactions in $[Fe_3Sn_{18}]^{4-}$ in the previous paragraph, we now turn to its relationship to the other known clusters in the E_{18} family. As noted in the introduction, the three clusters $[In(NiGe_9)_2]^{5-}$, $[Ni_3Ge_{18}]^{4-}$ and $[Pd_2Ge_{18}]^{4-}$ map out a progressive fusion of the two Ge_9 units, and so the electronic changes associated with fusion can be analysed by decreasing the distance between two Ge_9 fragments. Bond formation is usually associated with removal of electrons from antibonding orbitals, so we anticipate that the charge state of the cluster will change along the pathway. The charge state of the cluster during the fusion process can be determined by the oxidation state of the encapsulated metal atoms, with the remaining electrons assigned to the cage. In $[In(NiGe_9)_2]^{5-}$, the nickel is in the Ni^0 oxidation state while indium is +3, leading to a net charge of −8 on the $[Ge_{18}]^{8-}$ cage. For $[Ni_3Ge_{18}]^{4-}$, we have established a charge of +2 on the $[Ni_3]^{2+}$ fragment, and therefore a $[Ge_{18}]^{6-}$ cage. Finally, in $[Pd_2Ge_{18}]^{4-}$ the metals are also in the Pd^0 oxidation state giving a $[Ge_{18}]^{4-}$ cage. The fusion of Sn_{18} units follows a similar pattern across the series $[Cd(NiSn_9)_2]^{6-}$, $[Fe_3Sn_{18}]^{4-}$ and $[Pd_2Sn_{18}]^{4-}$, where

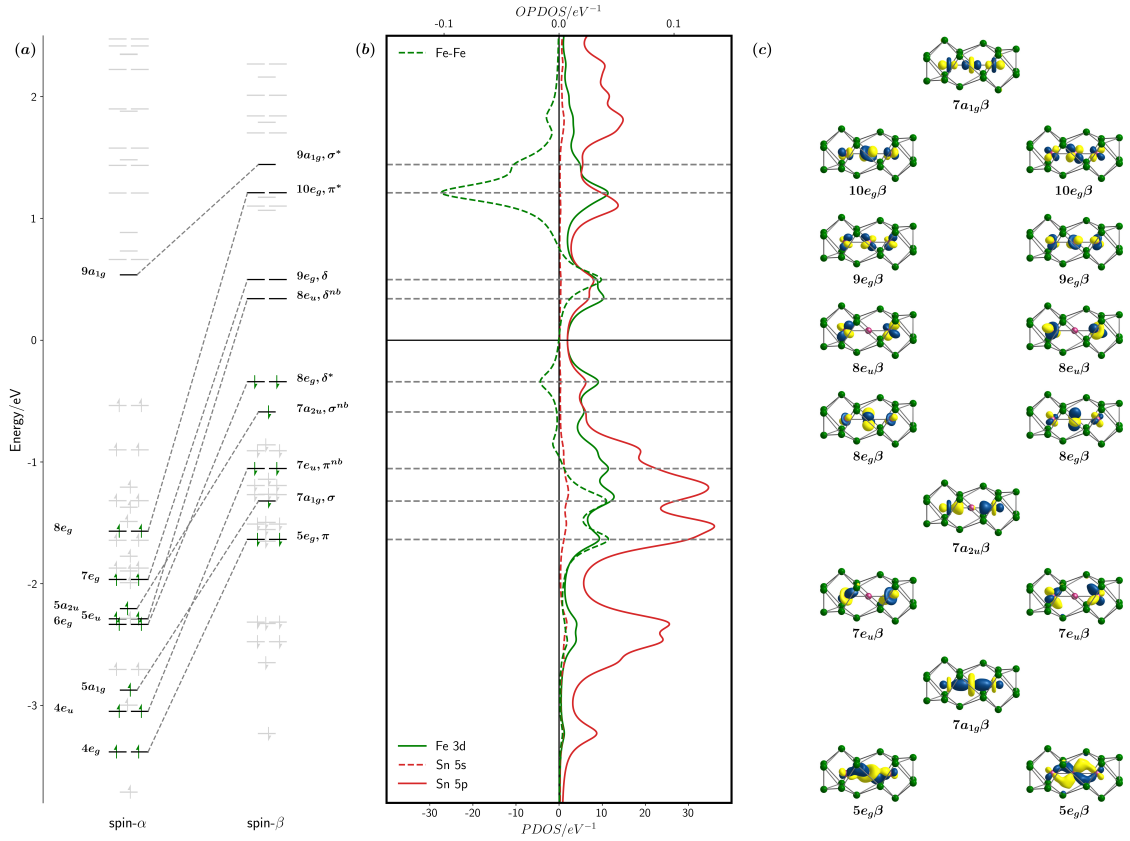

Figure 3.18: (a) Kohn-Sham frontier orbital arrays of both spin-α and spin-β. Orbitals with dominant Fe 3d contributions are highlighted with green arrows and black lines. (b) PDOS projected to Fe 3d and Sn 5p atomic orbital, along with OPDOS of Fe-Fe bond in the minority spin. The Lorentzian broadening parameter was set to 0.1 eV. (c) The isosurface plots of the Fe 3d based Kohn-Sham orbitals, and their irreducible representations were denoted below the figure. The isovalue for the orbitals is 0.04 e/Bohr^3.

again the charge on the Sn_{18} unit decreases $-8 \rightarrow -6 \rightarrow -4$ during the fusion procedure. With this preliminary hypothesis on the charge states in different stages of Sn_{18} fusion, we then need to determine the orbitals involved in the redox events. Because the three endohedral clusters encapsulate different numbers of transition metal atoms, it is not straightforward to compare them, especially in the case of an open-shell species as $[Fe_3Sn_{18}]^{4-}$. An alternative approach is to consider only the Sn_{18} cage structures. The cage geometries are extracted from the geometries of the optimised endohedral clusters, and a series of 8 intermediate geometries were generated by interpolation between either two consecutive structures among these three points. The Walsh diagram shown in Figure 3.19 connects the frontier levels of isolated $[Sn_{18}]^{8-}$, $[Sn_{18}]^{6-}$ and $[Sn_{18}]^{4-}$ in the geometries of $[Cd(NiSn_9)_2]^{6-}$, $[Fe_3Sn_{18}]^{4-}$ and $[Pd_2Sn_{18}]^{4-}$.

As the charge state changes across this coordinate, we have chosen to use a simple non-self-consistent electronic structure model, namely Extended Hückel Theory, to avoid discontinuities at points where the charge changes. Moreover, the relatively small electron-electron repulsions in the valence orbitals of the heavier main-group elements reduce the demand for highly accurate computational methods. From Table 3.2, we can identify two geometric parameters, Sn4-Sn9′ and Sn8-Sn9′, as the ones that differ most across the series of three clusters. These can then be used to define the reaction coordinate for Sn_{18} fusion. The Sn4-Sn9′ distance contracts continuously from the separated limit to the fused limit. The Sn8-Sn9′ distance, in contrast, decreases rapidly in the first stage from $[Sn_{18}]^{8-}$ to $[Sn_{18}]^{6-}$, while having little change in the second step to the fused limit. Both structural parameters are incorporated along the x-axis in the Walsh diagram to give a comprehensive picture of the geometry changes involved in cluster fusion.

From the separated-limit to the intermediate state, the $[Sn_{18}]$ unit is oxidised by 2 electrons. From the Walsh diagram, it can be recognised that the energy of the $7a_{2u}$ level increases steeply in the first section of the coordinate, and it is from this orbital that the first pair of electrons is removed. This orbital, shown in Figure 3.19, has antibonding character between the six atoms at the interface of the two Sn_9 fragments — Sn8-Sn9′ as well as five other equivalent bonds. The removal of two electrons from this orbital therefore contributes to the formation of the red bonds shown in the schematic plot below the Walsh diagram. In the second step, the major geometric change is in the Sn4-Sn9′ bond, which contracts rapidly. In this second section of the reaction coordinate the $7a_{1g}$ orbital is raised in energy from the low-lying orbital arrays, and its depopulation leads to further oxidation from -6 to -4 to reach the fused-limit. The corresponding isosurface shows antibonding character across the Sn4-Sn9′ bond, as well as five other equivalent bonds according to D_{3d} symmetry. It also contains some bonding character between Sn4-Sn8 as well as in two capping Sn_3 triangle surfaces. Therefore, from the intermediate to the fused-limit, the Sn4-Sn9′ distance, which is highlighted as blue bonds in the schematic plot, shrinks from 4.10 Å to 3.10 Å while at the same time the Sn4-Sn8 and Sn1-Sn2 distances expand, increasing the radius at the waist of the cluster.

The detailed electronic changes involved in the stepwise cluster fusion highlighted by the Walsh diagram provide a framework to rationalise the number of SEPs required to construct the $[Sn_{18}]^{n-}$ cage. The Wade-Mingos rules and the jellium model are most suitable for the pseudo-spherical structure, but the prolate Sn_{18} cluster represents a significant deviation from a sphere. We therefore turn to the more general Jemmis

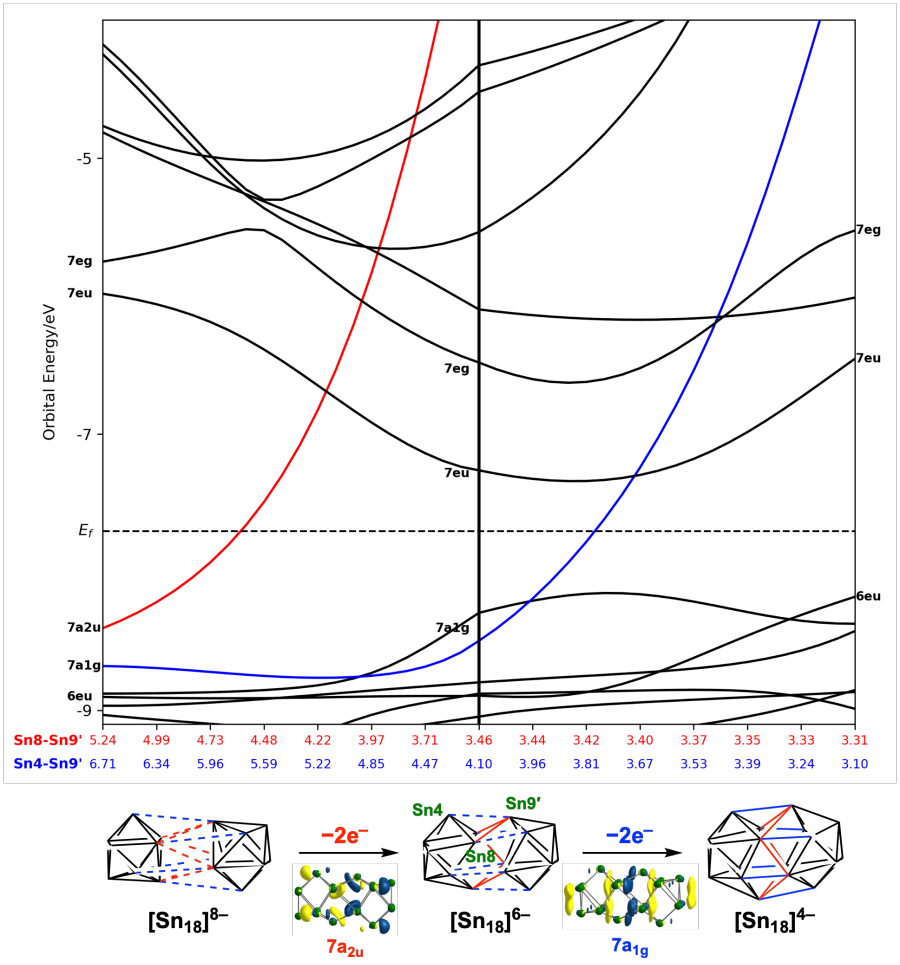

Figure 3.19: Walsh diagram showing the coalescence of the two Sn_9 polyhedra to a single ellipsoidal Sn_{18} unit. The figure is generated by interpolating between the optimised structures of the Sn_{18} unit as it is found in the optimised geometries of $[Cd(NiSn_9)_2]^{6-}$, $[Fe_3Sn_{18}]^{4-}$ and $[Pd_2Sn_{18}]^{4-}$.

mno rule,[115] which can be applied to clusters made up of fused monomers. At the fused limit, we have no single connecting vertices, no open faces and no capping atoms, so $o = p = q = 0$ and the number of SEPs predicted is $m + n + o + p - q = 2 + 18 + 0 + 0 - 0 = 20$. Along with the 18 lone pairs at the vertices, this corresponds to the electron count of 76, *i.e.* $[Sn_{18}]^{4-}$ as in $[Pd_2Sn_{18}]^{4-}$. At the separated limit, the two connecting faces can be regarded as 'open-face' (Sn8-Sn9 = 3.30 Å compared to 3.11 Å for Sn1-Sn2). Hence the number of SEPs increases to $m + n + o + p - q = 2 + 18 + 0 + 2 - 0 = 22$ which, along with the lone pairs at each vertex, corresponds to the $[Sn_{18}]^{8-}$ at the separated-limit. For the intermediate $[Sn_{18}]^{6-}$, we can regard the connecting trigonal antiprism as a pseudo-'open-face', as two triangle faces are only partially fused. Therefore, the SEP count is $m+n+o+p-q = 2+18+0+1-0 = 21$,

which matches skeletal electron count of $[Sn_{18}]^{6-}$.

It is striking that the first pair of electrons in the Walsh diagram in Figure 3.19 results in the formation of six bonds across the waist of the cluster (Sn8-Sn9′ and symmetry-related bonds). Clearly, then, these cannot be two-centre-two-electron bonds, but rather highly delocalised bonds. The alternative would be to form a single, stronger, two-centre-two-electron σ bond between two atoms for each pair of electrons removed: this is referred to as oligomerisation as opposed to fusion. Oligomerisation is known to occur in the closely-related $[AgSn_{18}]^{5-}$ and also in $Sn_{36}{}^{8-}$ in Figure 3.20 (b), where four Sn_9 units are linked by two localised bonds. The oxidation level of the Sn_{18} cage in $[AgSn_{18}]^{5-}$ is clearly -6 (Ag is $+1$), exactly the same as in $[Fe_3Sn_{18}]^{4-}$, yet the two Sn_9 units in the former are linked by a single two-centre-two-electron bond, where only a single Sn-Sn bond exists. To analyse the different outcomes of two-electron oxidation, the Sn_{18} structures were extracted from the optimised geometries of $[AgSn_{18}]^{5-}$ and $[Sn_{36}]^{8-}$, and the changes in frontier orbitals are compared to those of the $[Cd(NiSn_9)_2]^{6-}$, $[Fe_3Sn_{18}]^{4-}$, $[Pd_2Sn_{18}]^{4-}$ series in Figure 3.20 (a). The oligomerisation process was initiated from D_{3h}-$[Sn_{18}]^{8-}$, which is generated from a 180° rotation of a Sn_9 fragment from its D_{3d} isomer. The energy difference between two isomers is as negligible as 0.02 eV, since the weak interaction between fragments creates a small energy barrier for the rotation of Sn_9. The important frontier orbitals in the oligomerisation process are highlighted in Figure 3.20 (b). In the first step, the electrons are oxidised from the $7a_2''$ orbital, which is an out-of-phase combination between the connecting faces. This orbital is the direct counterpart of the $7a_{2u}$ orbital in D_{3d}-$[Sn_{18}]^{8-}$. This orbital correlates with the $13b_1$ orbital in $[Sn_{18}]^{6-}$, where the antibonding interaction is mostly localised along the Sn9-Sn9′ bond with σ character. This process generates a localised two-centre-two-electron *exo* bond between the two Sn_9 fragments. In the second step, the $12b_1$ orbital in C_{2v}-$[Sn_{18}]^{6-}$ is destabilised and becomes vacant, correlating with the $7b_g$ orbital in C_{2h}-$[Sn_{18}]^{4-}$. Going back to the D_{3h} limit of $[Sn_{18}]^{8-}$, this orbital is derived from one component of the $6e''$. Its antibonding component is localised primarily to Sn9-Sn9′ and Sn7-Sn8′ bonds, forming a four-centre-two-electron localised bond. Comparing the two oxidation processes, fusion across a face versus oligomerisation by forming isolated *exo* bonds, it is clear that the electronic processes are very similar: both are driven by depopulation of antibonding orbitals. If these orbitals are localised *exo* bonds, the coalescence will proceed *via* oligomerisation, while if delocalised bonds prevail, fusion to form larger clusters will occur. The existence of metal-metal bonds in $[Fe_3Sn_{18}]^{4-}$ resists

the bending at the central metal atom that is essential to oligomerisation and so directs the process to formation of delocalised six-centre-two-electron bonds instead of a localised Sn9-Sn9′ bond. The Fe_3 has an important role to play in templating the formation of a continuous Sn_{18} cluster rather than two Sn_9 units linked by a localised *exo* bond.

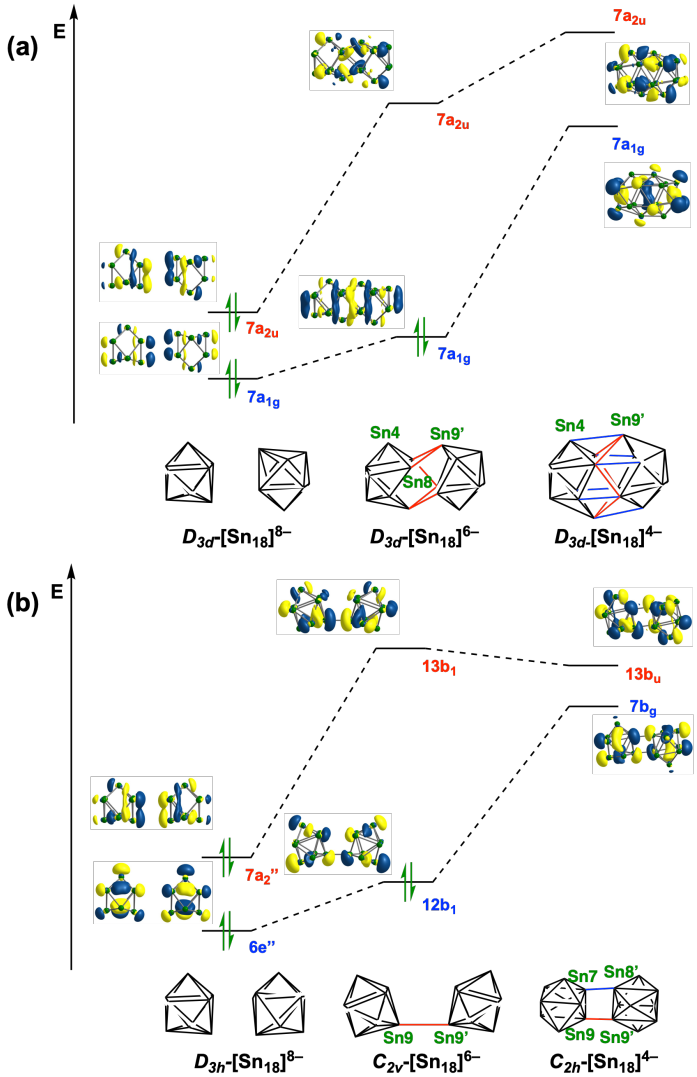

Figure 3.20: Schematic plot of significant frontier orbitals for (a) cluster fusion process from D_{3d}-$[Sn_{18}]^{8-}$ to D_{3d}-$[Sn_{18}]^{6-}$ and finally reaching D_{3d}-$[Sn_{18}]^{4-}$. Three cage structures were obtained from the optimised endohedral clusters as $[Cd(NiSn_9)_2]^{6-}$, $[Fe_3Sn_{18}]^{4-}$ and $[Pd_2Sn_{18}]^{4-}$, respectively; (b) cluster oligomerisation process from D_{3h}-$[Sn_{18}]^{8-}$, C_{2v}-$[Sn_{18}]^{6-}$ and C_{2h}-$[Sn_{18}]^{4-}$. The first two structures were obtained from the optimised D_{3h}-$[Cd(NiSn_9)_2]^{6-}$, $[AgSn_{18}]^{5-}$ respectively, and C_{2h}-$[Sn_{18}]^{4-}$ was individually optimised.

3.3.4 Conclusion

In this section, an endohedral Zintl cluster $[Fe_3Sn_{18}]^{4-}$ composed of a linear tri-iron core and a semi-fused Sn_{18} cage was investigated using DFT and EHT. The Fe-Fe bond length of 2.4300(9) Å observed in XRD indicates significant Fe-Fe bonding, with a formal bond order of $1/2\sigma$ and $1/2\pi$. Both the architecture and the charge state of the $[Sn_{18}]^{6-}$ cage are intermediate between the separated-limit, $[Sn_{18}]^{8-}$, as observed in $[Cd(NiSn_9)_2]^{6-}$ and the fused-limit, $[Sn_{18}]^{4-}$, found in $[Pd_2Sn_{18}]^{4-}$. In that sense, the $[Fe_3Sn_{18}]^{4-}$ cluster is the analogue of the $[Ni_3Ge_{18}]^{4-}$ cluster in germanium chemistry, where the charge state is also -6. Cluster fusion is accompanied by a stepwise electron oxidation from the delocalised antibonding orbitals, from the separate-limit to the fused-limit. Along the reaction coordinate for fusion, the strong repulsion between two $[Sn_9]^{4-}$ units is reduced through the transfer of electron density to the transition metal fragments. The competition between fusion and oligomerisation (presented in Figure 3.21) equates to a contest between delocalised and localised bonding, and the presence of Fe-Fe bonding in the Fe_3 chain resists the bending that is essential to oligomerisation, thereby directing the reaction towards fusion instead.

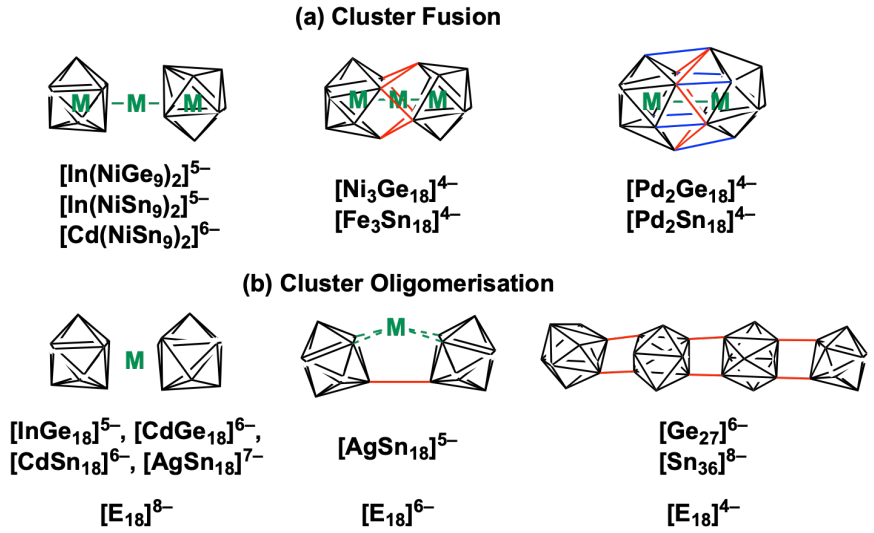

Figure 3.21: Cluster fusion vs. cluster oligomerisation of E_9 polyhedra (E = Ge, Sn). (Reproduced from our published work as Ref. 2)

3.4 Isomerisation of the Fe_4 core in $[Fe_4E_{18}]^{4-}$ (E = Sn, Pb)

In this section, I explore the electronic structure of a pair of Fe_4 clusters, $[Fe_4Sn_{18}]^{4-}$ and $[Fe_4Pb_{18}]^{4-}$, each of which has 108 valence electrons. Both DFT and DMRG approaches are employed. The cluster pair has similar structures, but subtle differences in the geometry of the rhombic Fe_4 core suggest different electronic structures. The isostructural copper analogues, 120-electron $[Cu_4Sn_{18}]^{4-}$ and $[Cu_4Pb_{18}]^{4-}$,[109] are known and, following the pattern established in previous sections, these are used as a closed-shell reference. This work was done in collaboration with Prof. Zhong-Ming Sun and co-workers, who carried out all the experimental work including the X-ray crystallography (unit cells are shown in Figure 3.22). It has been published in *Chemical Science*, 2024, **15**, 4981–4988.

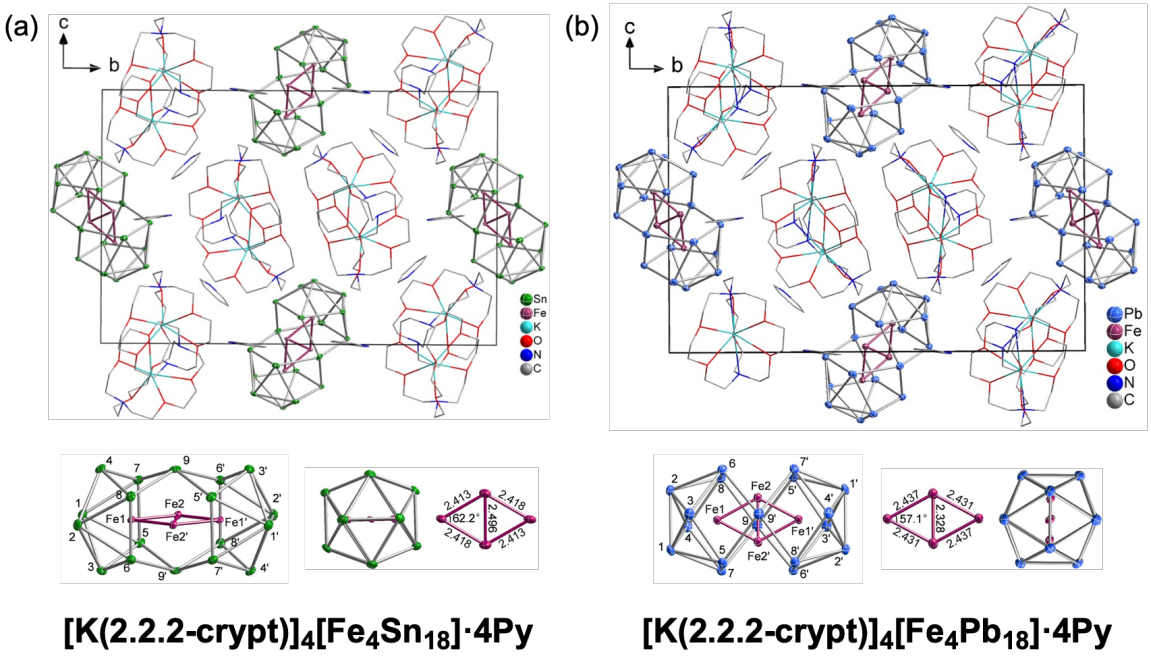

Figure 3.22: Unit cells of (a) $[K(2.2.2\text{-crypt})]_4[Fe_4Sn_{18}]\cdot 4Py$ and (b) $[K(2.2.2\text{-crypt})]_4[Fe_4Pb_{18}]\cdot 4Py$, including front and side views of the anions. XRD experiment was performed by Dr Wei-Xing Chen in Prof. Zhong-Ming Sun's group. The Fe_4 structures are highlighted. (Reproduced from our published work as Ref. 3)

3.4.1 Introduction

The investigation of intermetallic Zintl clusters containing heavy tetrel elements started in 2006 with the identification of $[MPb_{10}]^{2-}$ and $[MPb_{12}]^{2-}$ (M = Ni, Pd, Pt),[92] and numerous other clusters have emerged in the following decades.[10,11] Examples of mono-metallic Zintl cages include $[CoSn_9]^{5-}$,[98] $[CuE_9]^{3-}$ (E = Sn, Pb),[97] $[NiSn_9]^{4-}$,[96] $[AgPb_{11}]^{3-}$,[86] $[IrSn_{12}]^{3-}$,[94] $[RhSn_{12}]^{3-}$,[85] where in all cases the transition metal is in a closed-shell d^{10} configuration and the geometry of the cage is consistent with the predictions of Wade's rules. A smaller number of open-shell cases have also been studied, including C_{2v}-$[FeSn_{10}]^{3-}$[17] and D_{2h}-$[MnPb_{12}]^{3-}$,[16] both of which have distorted structures compared to the ideal Wade-Mingos model. These monomeric fragments can, at least conceptually, be used as building elements for constructing larger fused clusters. For example, $[Ni_2Sn_{17}]^{4-}$ can be regarded as being constructed from two $[NiSn_9]^{4-}$ units by fusing a Sn vertex.[99] Co, Pt and Rh can also form the $[M_2Sn_{17}]^{n-}$ geometry, albeit with stronger interactions between the fused monomers.[85,100,101] $[NiSn_9]^{4-}$ can also be connected by a third metal cation, leading to the $[In(NiSn_9)_2]^{5-}$[195] and $[Cd(NiSn_9)_2]^{6-}$[102] clusters introduced in the previous section. The presence of two Sn_9 cages in close proximity can be viewed as a precursor to stepwise fusion, as seen in $[Fe_3Sn_{18}]^{4-}$[2] and $[Pd_2Sn_{18}]^{4-}$,[111] or oligomerisation, as in $[AgSn_{18}]^{5-}$.[190] The 18-vertex cage in $[Fe_3Sn_{18}]^{4-}$ could, in principle, also rearrange into the D_{2h}-symmetric geometry that has been reported for the pair of copper clusters, $[Cu_4E_{18}]^{4-}$ (E = Sn, Pb),[109] which are the closed-shell analogues of $[Fe_4E_{18}]^{4-}$. An even larger cluster, $[Rh_3Sn_{24}]^{5-}$, has also been investigated — it can be regarded as D_{2h}-$[Sn_{18}]$ capped by a $[SnSn_5]$ fragment.[85] The $[Cu_4Pb_{22}]^{4-}$ cluster is also known, but in this binary cluster two of the copper atoms form part of the icosahedral cage rather than remaining encapsulated.[113] This cluster can also be considered as a link between $[AgPb_{11}]^{3-}$ and the trimeric and tetrameric binary clusters $[Au_8Pb_{33}]^{6-}$ and $[Au_{12}Pb_{44}]^{8-}$.[86] In these coinage metal clusters, and indeed the majority of other cases, the transition metal in the fused cage has a fully occupied valence *d*-band. Geometries of the above-mentioned intermetallic clusters are shown in Figure 3.23.

In this section, I present a pair of iron/tetrel binary clusters, $[Fe_4Sn_{18}]^{4-}$ and $[Fe_4Pb_{18}]^{4-}$, where open shells generate a magnetic moment. The two clusters have very similar geometries to their copper analogues, with a D_{2h}-symmetric E_{18} cage made up of two E_9 units fused *via* a common E-E edge, rather than a face as in $[Fe_3Sn_{18}]^{4-}$. Two of the Fe atoms are endohedral, sitting at the approximate centres of the E_9 cages, while the remaining two are exohedral, sitting on either side of the shared edge. The four Fe atoms form a rhombus, with short Fe-Fe distances suggestive

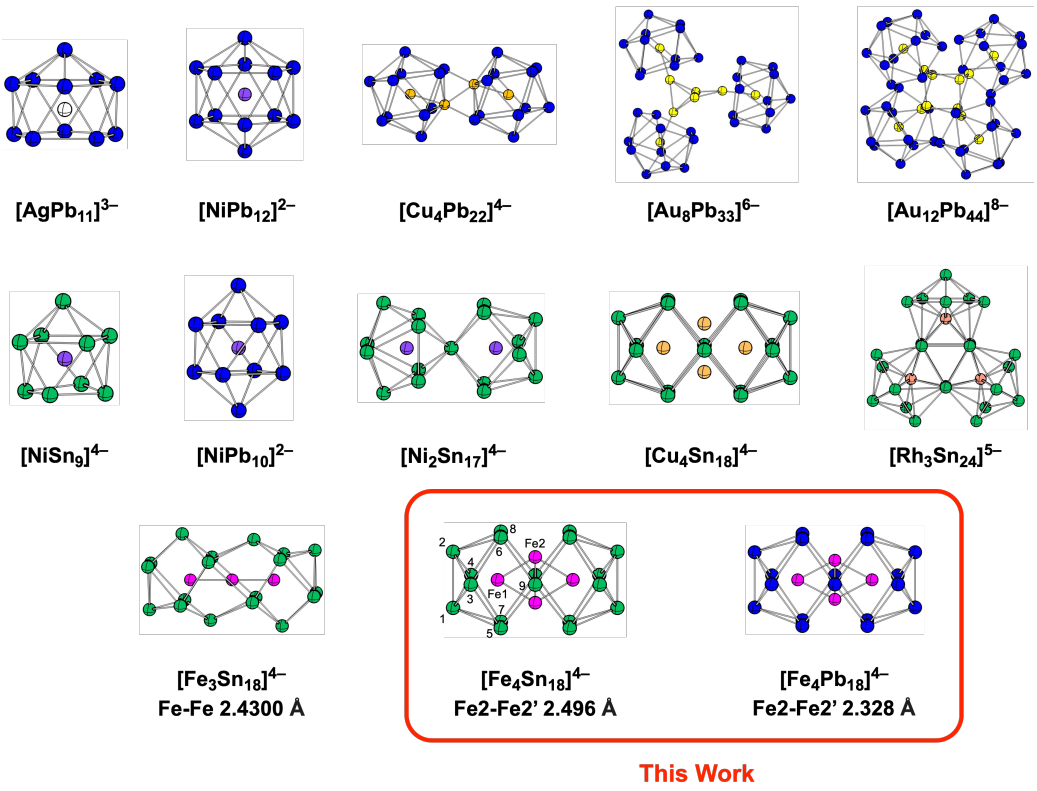

Figure 3.23: Representative Zintl cluster geometries composed of Sn and Pb.

of direct Fe-Fe bonding. The Sn and Pb clusters are grossly isostructural, but the Fe_4 rhombus is subtly different in different cages. Specifically, the Fe2-Fe2′ bond length is 2.496 Å in the Sn_{18} cluster, but only 2.328 Å in the Pb_{18} analogue (Figure 3.23, red box). The electronic configurations that drive this change will be discussed, and the D_{2h} cage architecture will also be compared with the isomeric D_{3d}-$[Sn_{18}]^{n-}$ family discussed in the previous section. The high-spin electronic structure based on 4×5 highly degenerate Fe $3d$ orbitals generates a complex electronic landscape with many close-lying states, so a detailed study of $[Fe_4Sn_{18}]^{4-}$ using DMRG is also presented as a complement to the DFT in search of the ground state configuration.

3.4.2 Computational details

All DFT work in the section was done using ADF 2021.104 package.[69] The PBE,[47] M06-L[53,54] and PBE0[56,57,192] functionals were used to benchmark, and the results of the PBE functional are adopted for further analysis. Slater-type TZ2P basis sets were used throughout[164] and all electrons were incorporated in the basis sets. Relativistic effects were considered by the scalar-ZORA,[163] and the numerical grid was 'very-good'.[193] The COSMO[165] was included with the dielectric constant of 78.39 as water

to produce a confined space simulating the crystalline environment. The Extended Hückel Theory calculations were performed with Gaussian16,[194] using the Hoffmann parameter set.

The DMRG calculations were done using the Block 2.0 interface[166] compiled with the OpenMolcas package.[167] The two-electron integrals were approximated by Cholesky decomposition at the threshold of 10^{-6}, and the grid was tuned to 'ultra-fine'. ANO-RCC basis sets were used at the level of double-zeta plus one polarisation function.[196] Symmetry was considered with the Abelian point group. The details of the bond dimension setting (m) will be specified for different calculations. The convergence criteria were the defaults, where the energy, orbital rotation matrix and energy gradient thresholds are 10^{-6}, 10^{-3}, 10^{-3} respectively.

3.4.3 Electronic structure analysis

3.4.3.1 DFT analysis

$[Fe_4E_{18}]^{4-}$ can be regarded as an open-shell counterpart of $[Cu_4E_{18}]^{4-}$.[109] Both clusters possess similar D_{2h} structures with a rhombic M_4 core, and the charge distribution of the iron analogues can be assumed, as a first approximation, to be similar to $[Cu_4E_{18}]^{4-}$, where the E_{18} cage carries 8 negative charges, leaving each metal atom in the +1 oxidation state. The electron count of the cage can be rationalised using Jemmis *mno* rule.[115] The E_{18} cage can be regarded as composed of two E_9 shells, leading to a monomer count of 2, and straightforwardly the vertex count is 18. There is no single-vertex connecting two segments ($o = 0$), and the number of open-faces is two (Sn5-Sn8-Sn6′-Sn7′ and its symmetry-related square face) considering the case of $[Rh_3Sn_{24}]^{5-}$. Therefore, the SEP count according to the *mno* rule is $m+n+o+p-q = 2 + 18 + 0 + 2 - 0 = 22$. Adding the 18 $5s^2$ lone-pair electrons on each vertex gives 40 pairs in total, consistent with the total electron count of 80 for $[Sn_{18}]^{8-}$.

We start the discussion of the electronic structures of $[Fe_4Sn_{18}]^{4-}$ and $[Fe_4Pb_{18}]^{4-}$ using DFT. As the clusters have 28 electrons in $4 \times 5 = 20$ $3d$ orbitals, we anticipate a complex and flat potential energy surface around the global minimum, with many near-degenerate states. Both clusters are optimised with M06-L, PBE and PBE0 functional using different multiplicities to avoid functional bias. Due to the very inefficient treatment of two-electron integrals in ADF, the hybrid PBE0 functional was only used for the two $S = 5$ states of $[Fe_4Sn_{18}]^{4-}$. Experimental measurements of $[Fe_4Sn_{18}]^{4-}$ show a magnetic moment of 9.37 μ_B at 300 K, which equates to 8.42 unpaired electrons if the spin-only formula is applied. The fact that the magnetic

moment is not converged at low temperature also indicates the possibility of a higher multiplicity ground state. We have therefore also considered states with $S = 4$ as well as higher spin states, $S = 5$ and $S = 6$. In order to identify the true ground state, potential energy surfaces were carefully explored by perturbing the starting electronic configurations and by initialising calculations for Sn using optimised structures for Pb and *vice versa*. The lowest energy state of both clusters has $^{11}B_{1g}$ symmetry, with 10 unpaired electrons. For $[Fe_4Sn_{18}]^{4-}$, the $^{11}B_{3g}$ state lies only 0.05 eV above using M06-L, and only 0.02 eV at PBE. With PBE0 the order is reversed with the $^{11}B_{3g}$ is 0.07 eV more stable than $^{11}B_{1g}$. For $[Fe_4Pb_{18}]^{4-}$, PBE and M06-L functionals have the $^{11}B_{3g}$ state over 0.15 eV above $^{11}B_{1g}$. The $S = 6$ state, $^{13}B_{2g}$, which is the maximum multiplicity possible for 28 electrons in 20 orbitals, also lies more than 0.15 eV above the ground state: the gain in exchange energy is clearly not enough to offset population of the most antibonding orbitals in the Fe_4 array. The very small energy gap and the strong functional dependency between the $^{11}B_{1g}$ and $^{11}B_{3g}$ of $[Fe_4Sn_{18}]^{4-}$ means that we cannot determine the ground state with confidence using only the DFT energies. Therefore, we turn to a comparison of the optimised geometries with the known XRD structure. As noted above, the Fe2-Fe2′ bond length across the diagonal of the Fe_4 rhombus is the most obvious distinction between the Sn and Pb clusters, and it is on this that we will focus. The computational results using M06-L summarised in Table 3.3 show that the Fe2-Fe2′ bond length is approximately 0.2 Å shorter in the $^{11}B_{1g}$ state compared to $^{11}B_{3g}$, in both tin and lead clusters. The XRD value of 2.496 Å in $[Fe_4Sn_{18}]^{4-}$ is a strong match for the value of 2.52 Å in the $^{11}B_{3g}$ state, while the distance of 2.328 Å in $[Fe_4Pb_{18}]^{4-}$ is a better match to 2.28 Å for $^{11}B_{1g}$. This comparison suggests that we can assign $^{11}B_{1g}$ as the ground state for $[Fe_4Pb_{18}]^{4-}$, and $^{11}B_{3g}$ as the electronic state for $[Fe_4Sn_{18}]^{4-}$, despite the fact that $^{11}B_{3g}$ is 0.05 eV less stable than $^{11}B_{1g}$ for the latter.

As we noted above, the Fe/Sn binary cluster is an open-shell analogue of $[Cu_4Sn_{18}]^{4-}$, and a comparison between Cu and Fe analogues can be made by plotting PDOS and OPDOS, as well as the projected density plot on the M_4 plane shown in Figure 3.24. The DOS is projected onto Cu $3d/4s$, Sn $5s/5p$ for $[Cu_4Sn_{18}]^{4-}$ and Fe $3d/4s$, Sn $5s/5p$ of the minority spin for $[Fe_4Sn_{18}]^{4-}$. The OPDOS, shown as dashed lines, is weighted by the overlap integral of M1-M2 (sky blue) and M2-M2′ (maroon), and highlights the bonding/antibonding properties of the bands. The projected density plots shown in Figure 3.24 (b) highlight the concentration of electron density on M_4 plane, where the electron density increases with the colour from blue to red.

Table 3.3: Selected bond lengths from crystallographic and DFT-optimised structures (M06-L functional) for the $[M_4E_{18}]^{4-}$ family (all energies in eV and distances in Å).

		E_{rel}	**M1-M2**	**M2-M2′**	**E2-E6**	**E5-E9′**	**E7-E8′**	**ref**
$\mathbf{[Fe_4Sn_{18}]^{4-}}$	X-ray (100 K)		2.413	2.496	3.142	3.225	4.898	This
	DFT (^9A_g)	0.59	2.41	2.47	3.17	3.18	4.89	work
	DFT ($^{11}B_{1g}$)	0.0	2.42	2.31	3.20	3.19	4.88	
	DFT ($^{11}B_{3g}$)	0.05	2.41	2.52	3.17	3.24	4.86	
	DFT ($^{13}B_{2g}$)	0.25	2.43	2.63	3.14	3.27	5.06	
$\mathbf{[Fe_4Pb_{18}]^{4-}}$	X-ray (100 K)		2.437	2.328	3.247	3.287	4.941	This
	DFT ($^9B_{1u}$)	0.79	2.41	2.46	3.32	3.37	4.99	work
	DFT ($^{11}B_{1g}$)	0.0	2.44	2.28	3.35	3.32	4.99	
	DFT ($^{11}B_{3g}$)	0.17	2.43	2.48	3.32	3.36	4.98	
	DFT ($^{13}B_{3g}$)	0.18	2.46	2.35	3.34	3.37	5.05	
$\mathbf{[Cu_4Sn_{18}]^{4-}}$	X-ray (100 K)		2.525	2.631	2.842	3.219	4.915	[109]
	DFT (^1A_g)		2.52	2.58	3.14	3.24	4.91	
$\mathbf{[Cu_4Pb_{18}]^{4-}}$	X-ray (100 K)		2.547	2.561	3.224	3.299	5.012	[109]
	DFT (^1A_g)		2.55	2.52	3.30	3.35	5.02	

The DOS and OPDOS for the Cu clusters confirm that the Cu 3d bands lie well below the Fermi level, between −4.5 eV and −2.5 eV. Bands with dominant Sn 5p character are well separated from Cu 3d, lying above −2.5 eV, indicating largely ionic interactions between $[Cu_4]^{4+}$ and $[Sn_{18}]^{8-}$. All bonding and antibonding orbitals generated by linear combinations of Cu 3d atomic orbitals are below the Fermi level, resulting in a total bond order of 0 between any two neighbouring copper atoms. The Cu-Cu distances are 2.631 Å for Cu2-Cu2′ and 2.525 Å for Cu1-Cu2, which can be taken as a measure of nonbonding distances in this family of clusters. The density plots in Figure 3.24 (b) also show blue in between Cu atoms, which reinforces our result.

In contrast to the inert 3d electrons in $[Cu_4Sn_{18}]^{4-}$, some of the spin-β orbitals of the Fe 3d bands are raised up above the Fermi level, indicating open-shell character. All of the majority (spin-α) orbitals are occupied and the DOS/PDOS plot (not shown here) is qualitatively very similar to the Cu cluster. The distribution of spin-β Fe 3d is broader than the Cu case, in the energy range between −2 eV and 2 eV. The overlap between the Fe 3d and Sn 5p bands also implies the existence of covalent character in the Fe-Sn bonds. From the OPDOS, it can be seen that the occupied levels have positive OP values on both Fe2-Fe2′ and Fe1-Fe2 bond, indicating their bonding character. Conversely, the unoccupied bands have mostly negative OP values, indicating antibonding character. It is clear, therefore, that net Fe-Fe bonding is present in the $[Fe_4]^{4+}$ unit. The same feature can be seen in the electron density plots, where the yellow and green regions emerge between the Fe atoms. The Fe-Fe

bond distances are also ∼0.2 Å smaller, at 2.413 Å and 2.496 Å for Fe1-Fe2 and Fe2-Fe2′ respectively, compared to the Cu-Cu distances.

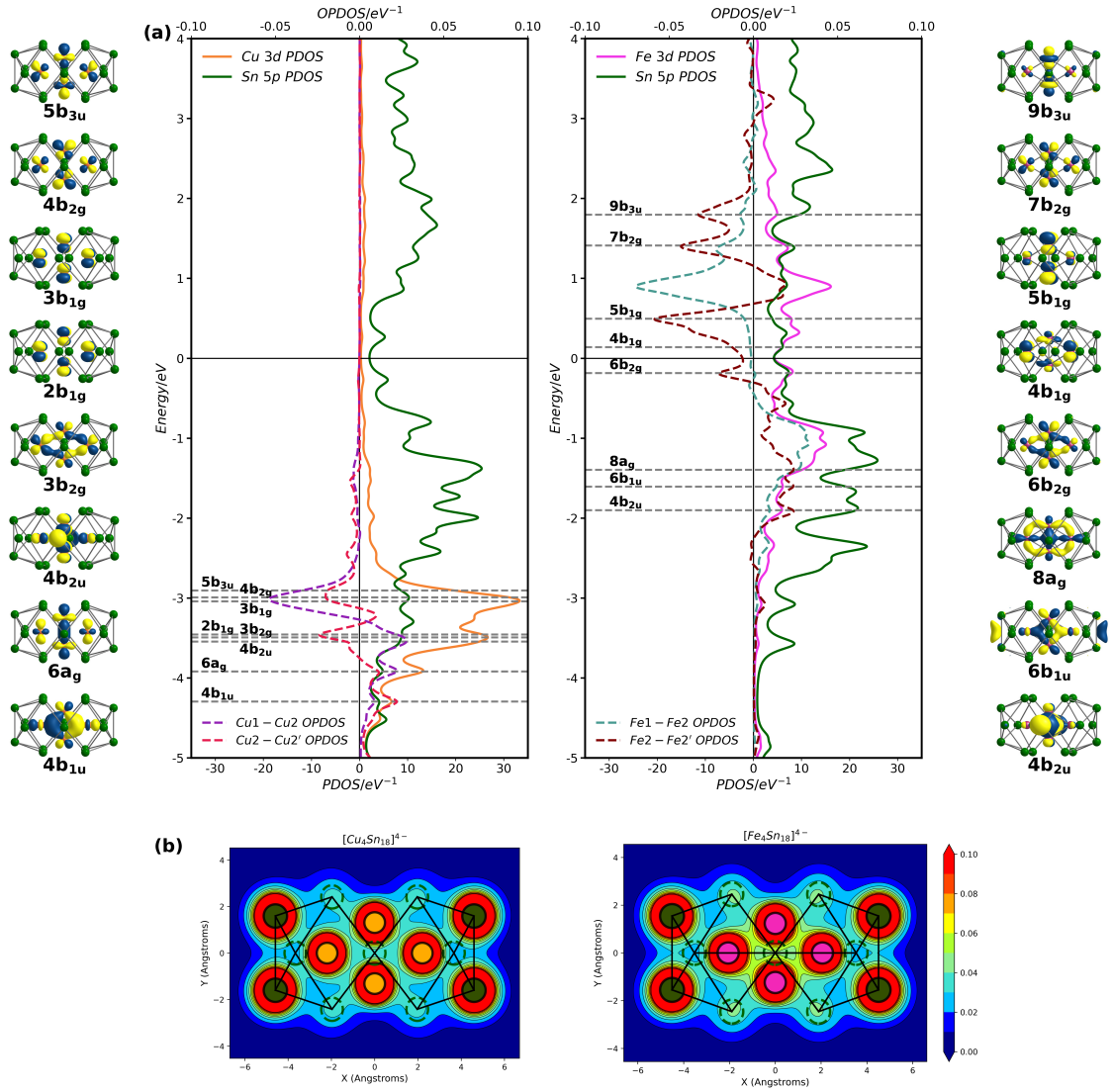

Figure 3.24: (a) PDOS projected to Cu 3*d* and Sn 5*p* for $[Cu_4Sn_{18}]^{4-}$, Fe 3*d* and Sn 5*p* for $[Fe_4Sn_{18}]^{4-}$. OPDOS was plotted for the M1-M2 and M2-M2′. The isosurface plots for significant orbitals $[Cu_4Sn_{18}]^{4-}$ and $[Fe_4Sn_{18}]^{4-}$. The isovalue for the orbitals was set to be 0.04 e/Bohr^3. (b) Projected density plot in the M_4 plane for $[Cu_4Sn_{18}]^{4-}$ and $[Fe_4Sn_{18}]^{4-}$.

The comparison of measured and computed Fe-Fe bond lengths suggests that $[Fe_4Sn_{18}]^{4-}$ and $[Fe_4Pb_{18}]^{4-}$ have $^{11}B_{3g}$ and $^{11}B_{1g}$ ground states, respectively. A schematic Kohn-Sham plot for these two states is shown in Figure 3.25 (the spin-β eigenvalues are shown). The orbital isosurface plots are shown on the right. We

can classify the Fe-based orbitals into in-plane and out-of-plane groups. The in-plane orbitals are linear combinations of Fe $3d_{xy}$, $3d_{x^2-y^2}$ and $3d_{z^2}$, giving irreducible representations of a_g, b_{1g}, b_{2u}, b_{3u} symmetry. These correspond to Fe-Fe σ, π_{ip}, δ interactions. The out-of-plane orbitals are generated from linear combinations of $3d_{xz}$ and $3d_{yz}$ with a_u, b_{1u}, b_{2g}, b_{3g} symmetry, and local π_{op} and δ symmetry with respect to the Fe-Fe bonds. The majority of the orbital manifold is identical for the two different states. In both $^{11}B_{1g}$ and $^{11}B_{3g}$ states, the $7b_{1g}$ orbital remains unoccupied. This orbital is Fe2-Fe2′ π_{ip} antibonding, and is generated by a linear combination of the Fe $3d_{xy}$ orbitals. An Fe2-Fe2′ σ interaction is present in doubly-occupied $8a_g$ while σ^* character is present in the singly-occupied $8b_{2u}$ orbital, giving a net configuration of $\sigma^2\sigma^{*1}$. The Fe2-Fe2′ π_{op} interactions in $4b_{1u}$ and $5b_{3g}$ form a bonding/antibonding pair, giving rise to a common $\pi_{op}^2\pi_{op}^{*\,1}$ contribution to the Fe-Fe bonding.

The major difference between the $^{11}B_{3g}$ and $^{11}B_{1g}$ comes in the occupation of $6b_{1g}$ and $4b_{3g}$ orbitals. In the $^{11}B_{3g}$-$[Fe_4Sn_{18}]^{4-}$, the $6b_{1g}$ is doubly occupied and an unpaired electron is present in $4b_{3g}$, while in $^{11}B_{1g}$-$[Fe_4Pb_{18}]^{4-}$, $4b_{3g}$ is doubly occupied and $6b_{1g}$ singly occupied. The isosurface plot for the $6b_{1g}$ orbital, highlighted by a red box, has π_{ip}^* character between Fe2-Fe2′ and σ character on Fe1-Fe2. The $4b_{3g}$ orbital, however, is concentrated on Fe1 and Fe1′, and is essentially a nonbonding orbital between Fe2 and Fe2′. Therefore, in the $^{11}B_{3g}$ state, the double occupation of the $6b_{1g}$ orbital increases the Fe2-Fe2′ antibonding character, leading to the longer Fe-Fe bond. The Mayer bond order[33] of Fe2-Fe2′ also decreases from 0.91 to 0.51 when replacing in the respective ground states of $[Fe_4Pb_{18}]^{4-}$ and $[Fe_4Sn_{18}]^{4-}$. At the same time, the enhanced σ contribution to Fe1-Fe2 increases its bond order slightly from 0.69 to 0.85.

Another separate point of interest for us to investigate is the relationship between the Sn_{18} cases in $[Fe_4Sn_{18}]^{4-}$ and $[Fe_3Sn_{18}]^{4-}$. Both clusters are Fe/Sn binary clusters with an 18-vertex cage but $[Fe_3Sn_{18}]^{4-}$ is in D_{3d} symmetry with two Sn_9 cages fused across two trigonal faces while $[Fe_4Sn_{18}]^{4-}$ has D_{2h} symmetry with the two units sharing a common edge. Also, the arrangement of the Fe_n core is linear in $[Fe_3Sn_{18}]^{4-}$ but rhombic in $[Fe_4Sn_{18}]^{4-}$. In the synthetic procedure, both clusters rely on K_4Sn_9 as the source of tin, but the source of iron differs, as does the reaction temperature: $FeCp_2$ at 60°C for the synthesis of $[Fe_4Sn_{18}]^{4-}$ and $[K(thf)Fe(O\mathit{t}Bu)_3]_2$ at room temperature for the synthesis of $[Fe_3Sn_{18}]^{4-}$. From the DFT electronic structure analysis, both $[Fe_3Sn_{18}]^{4-}$ and $[Fe_4Sn_{18}]^{4-}$ have a completely unoccupied Fe_n σ^* orbital, $9a_{1g}$ and $7b_{1g}$ in $[Fe_3Sn_{18}]^{4-}$ and $[Fe_4Sn_{18}]^{4-}$, respectively. The Fe-Fe overlap is clearly sufficient in both cases to prevent unpairing of an additional electron on the antibonding

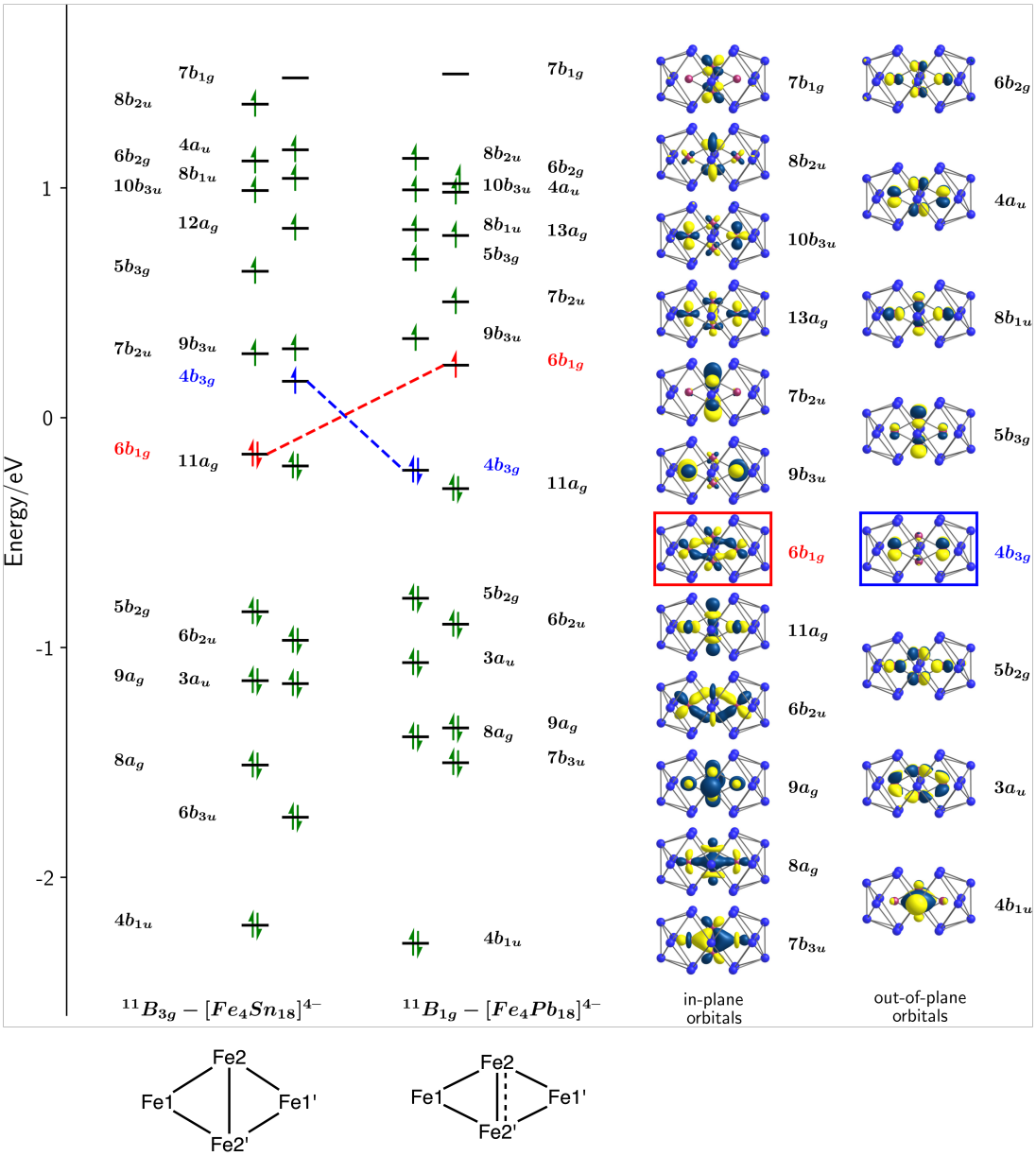

Figure 3.25: Kohn-Sham molecular orbitals for the $^{11}B_{3g}$ state of $[Fe_4Sn_{18}]^{4-}$ and the $^{11}B_{1g}$ state of $[Fe_4Pb_{18}]^{4-}$. The eigenvalues correspond to the spin-β manifold in both cases, and they are shifted such that $E = 0$ is defined as the midpoint between the eigenvalues of HOMO and LUMO. The orbitals highlighted in red and blue are those whose occupations differ in the $^{11}B_{3g}$ and $^{11}B_{1g}$ states. The isosurfaces shown correspond to the spin-β set of $[Fe_4Pb_{18}]^{4-}$.

orbital to generate the maximum possible spin multiplicity. The $[Cr_2Sb_{12}]^{3-}$ cluster discussed previously also shows a similar preference as its $^2B_2$ state leaves the σ^* orbital vacant in both spin manifolds.

The electronic changes that occur as the cluster rearranges from the D_{3d} to D_{2h} are

summarised in the Walsh diagram in Figure 3.26. The first step is the reverse of the fusion process discussed in the previous section: an increase in the distance between the two Sn_9 units leads to stabilisation of one orbital, $7a_{2u}$, and hence a two-electron reduction of the cluster to $[Sn_{18}]^{8-}$. From this intermediate point, a rotation of the two Sn_9 units, such that two atoms move into positions that bridge the two clusters, is associated with the stabilisation of one orbital (from $7e_g$ to $5b_{1g}$) while destabilising another (from $7a_{1g}$ to $5b_{2g}$). The final conclusion, then, is that the 'natural' charge (the charge that maximally occupies the bonding orbitals) for the D_{2h} isomer of the Sn_{18} cluster is -8, whereas it is -6 for the D_{3d} form. The additional Fe centre in $[Fe_4Sn_{18}]^{4-}$ therefore delivers an extra pair of electrons to the cluster, driving it into the geometry that is characteristic of its more negative charge state.

3.4.3.2 DMRG analysis

The DFT calculations summarised in the previous section show that the two distinct geometries of $[Fe_4Sn_{18}]^{4-}$ and $[Fe_4Pb_{18}]^{4-}$ correspond to two different electronic states, $^{11}B_{3g}$ and $^{11}B_{1g}$. Both states correspond to local minima with nearly identical total energies using both PBE and M06-L functionals. The structural differences are subtle: the Fe2-Fe2′ bond length in the Fe_4 core, and the geometry in the $^{11}B_{3g}$ resembles the crystal structure of $[Fe_4Sn_{18}]^{4-}$ while the optimised structure of the $^{11}B_{1g}$ resembles the X-ray structure of $[Fe_4Pb_{18}]^{4-}$. In the remainder of this section, we will refer to the structure with a long Fe2-Fe2′ bond (as in $[Fe_4Sn_{18}]^{4-}$) as isomer 1 and the structure with the short Fe2-Fe2′ bond (as in $[Fe_4Pb_{18}]^{4-}$) as isomer 2.

In trying to identify the ground state of these clusters, we are left frustrated by the very small energy differences, of the order of 0.05 eV, between them at the DFT level. Given the known sensitivity of spin states to functional choice, the differences are below the level that we could confidently treat as significant. The presence of these two energetically comparable states as well as the close-lying frontier orbitals highlights the strongly correlated nature of the wavefunction, and this has prompted us to turn to multi-configurational methods for an alternative perspective on the identities of the ground states. Traditional multi-configurational approaches such as CASSCF are limited by the size of the active space they can handle: for example, an active space comprising 18 electrons in 18 orbitals generates over 448 million CSFs for a singlet state, exceeding the capabilities of most high-performance computers. In this cluster, the presence of four Fe^+ centres requires a minimum active space that includes at least all their $3d$ shells, 28 electrons and 20 orbitals, rendering a full CASSCF treatment

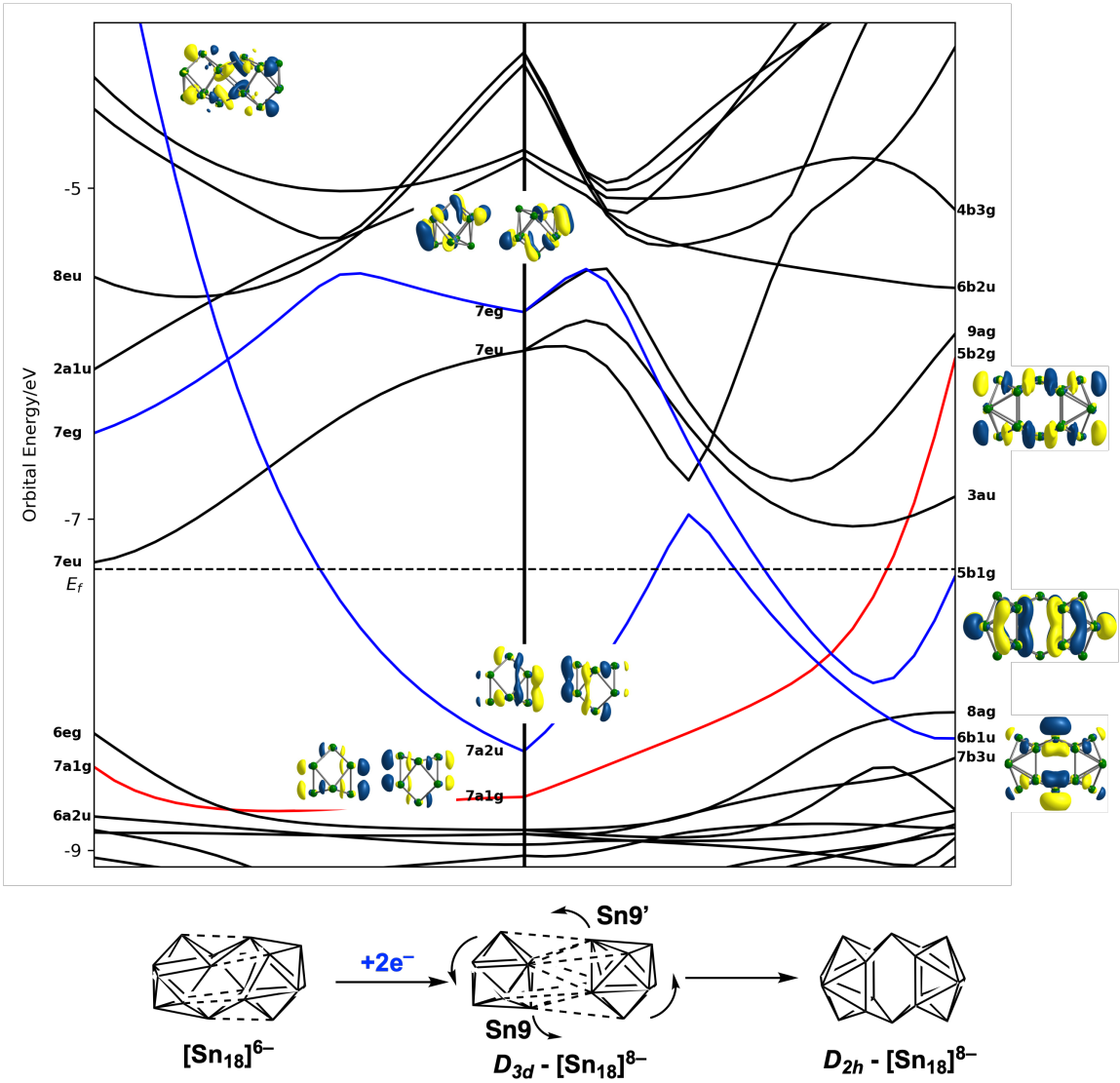

Figure 3.26: Walsh diagram showing the geometry rearrangement of the Sn_{18} cage from D_{3d}-$[Fe_3Sn_{18}]^{4-}$ to D_{2h}-$[Fe_4Sn_{18}]^{4-}$. An intermediate state of the D_{3d}-$[Sn_{18}]^{8-}$ was generated from $[Cd(NiSn_9)_2]^{6-}$. 18 interpolated structures connect two optimised structures.

impractical without significant truncations. To overcome this limitation, various approximation methods have been developed, including Configuration Interaction using a Perturbative Selection made Iteratively (CIPSI),[197] heat-bath CI,[198] and DMRG. In our work, DMRG[62,64,199] is chosen due to its ability to handle very large active spaces (up to approximately 100 orbitals and 100 electrons) and its implementation in software packages such as Molcas. Whilst multi-configurational methods can effectively account for static correlation arising from near-degenerate states, dynamic correlation associated with instantaneous electron movement requires post-DMRG

treatment. It is likely here that a significant contribution to the relative energies of isomers 1 and 2 will come from rearrangement of the Sn or Pb atoms, rather than the change within the Fe_4 core, so dynamic correlation is an important element of the calculation. Methods for capturing dynamic correlation include CASPT2, MRCI, and MC-PDFT. As mentioned in Chapter 2, CASPT2 is often hindered by the presence of intruder states, which, although partially mitigated by level shifting, can still lead to arbitrary and unreliable results. MRCI, on the other hand, is severely constrained by memory requirements in practical computation. In contrast, MC-PDFT offers an efficient and accurate means of recovering dynamic correlation, with the added benefit of avoiding double counting of correlation already captured by DMRG. In the remainder of this section, we explore the extent to which MC-PDFT can be applied to the Sn cluster, $[Fe_4Sn_{18}]^{4-}$, of this size, and the extent to which the choice of active space and the on-top functional matters.

For both isomers of $[Fe_4Sn_{18}]^{4-}$, our initial work involved a minimum active space, DMRG(28e, 20o), incorporating only a single Fe $3d$ shell. According to the DFT calculations reported previously, the two states with $S = 5$ are almost degenerate, but the gap to states with $S = 6$ is also within 0.2 eV. DMRG calculations were therefore performed for all possible spatial symmetry states (A_g, B_{3u}, B_{2u}, B_{1g}, B_{1u}, B_{2g}, B_{3g} and A_u) under both $S = 5$ and $S = 6$ spin multiplicities. The calculations were single-point ones, using the geometries of $[Fe_4Sn_{18}]^{4-}$ optimised in the $^{11}B_{3g}$ state (labelled isomer 1) and in the $^{11}B_{1g}$ state (labelled isomer 2) by the M06-L functional. To ensure a balanced description of active orbitals and avoid convergence to a local minimum, a state-averaged DMRG calculation was first carried out over the three lowest-lying electronic states in each specific spin and state symmetry. The ground-state candidates identified from these calculations were subsequently re-optimised in a state-specific calculation to refine the energy. A bond dimension of 1500 was selected for all calculations.

The optimised energies of the various states are summarised in Table 3.4. The results from the DMRG calculations are quite different from the DFT values, in so much as it is now a state with $S = 6$, $^{13}B_{2g}$ of isomer 1, which has the lowest energy among the 32 examined states (2 multiplicities $\times$ 2 isomers $\times$ 8 spatial symmetries in D_{2h}). The tendency of CASSCF and similar methods to over-stabilise high-spin states is well known, and our results here reflect that trend. The $^{11}B_{3u}$ and $^{11}B_{1u}$ states of isomer 1, as well as $^{13}B_{2g}$, $^{11}B_{1u}$ and $^{11}B_{2g}$ states of isomer 2, lie within 0.1 eV of the global minimum.

Table 3.4: Relative energy of $[Fe_4Sn_{18}]^{4-}$ isomer 1 and isomer 2 in all spatial symmetry states with $S = 5$ and $S = 6$ by DMRG(28e, 20o). All energies are reported relative to the $^{13}B_{2g}$ of isomer 1.

Energy/eV	isomer 1	isomer 2		isomer 1	isomer 2
$^{13}A_g$	0.19	0.18	$^{11}A_g$	0.17	0.20
$^{13}B_{3u}$	0.26	0.39	$^{11}B_{3u}$	0.05	0.19
$^{13}B_{2u}$	0.32	0.26	$^{11}B_{2u}$	0.15	0.19
$^{13}B_{1g}$	0.11	0.42	$^{11}B_{1g}$	0.18	0.23
$^{13}B_{1u}$	0.22	0.39	$^{11}B_{1u}$	0.06	0.09
$^{13}B_{2g}$	0.00	0.10	$^{11}B_{2g}$	0.11	0.10
$^{13}B_{3g}$	0.20	0.43	$^{11}B_{3g}$	0.18	0.30
$^{13}A_u$	0.21	0.44	$^{11}A_u$	0.11	0.20

For a more detailed analysis of the static correlation, we have chosen to focus on the $^{13}B_{2g}$ and $^{11}B_{1u}$ states of the two isomers, because these states are no more than 0.1 eV above the ground state for each isomer. The results of the DMRG calculation are summarised in the cycle plot in Figures 3.27 for $^{13}B_{2g}$ and 3.28 for $^{11}B_{1u}$. The 20 active orbitals are arranged on the circumference of a circle, and are numbered 1–20, starting at 12 o'clock and going clockwise. The isosurface of the natural orbital and its occupation number are shown alongside the orbital index. The number inside the blue circle indicates the single orbital entropy, and the size of the circle is proportional to the number. The occupation numbers and single-orbital entropies give an indication of the participation of a given orbital in static correlation: occupation numbers that deviate from 2, 1 or 0, and orbital entropies above 0.5 indicate strong correlation. Finally, the mutual information, or entanglement, is shown by the lines connecting the circles: the red lines correspond to the most strongly correlating pairs.

For the $^{13}B_{2g}$ state shown in Figure 3.27, the isosurfaces of the natural orbitals of isomer 1 are generally more localised than those of isomer 2. This is most evident in orbitals 11 and 12 (b_{1g} symmetry) and orbitals 15 and 16 (b_{2g} symmetry). In isomer 1, $1b_{1g}/1b_{2g}$ are localised on Fe1/Fe1′ while $2b_{1g}/2b_{2g}$ are localised on Fe2/Fe2′. In contrast, in isomer 2, the corresponding orbitals within the same irreducible representation display significant mixing over all Fe1 and Fe2 $3d$ orbitals, specifically in $3d_{xy}$ for b_{1g} and $3d_{xz}$ for b_{2g}. In the isosurface of isomer 2, an Fe1-Fe2 σ/σ^* pair is apparent in b_{1g} and Fe1-Fe2 π_{op}/π^*_{op} in b_{2g}. In the $^{13}B_{2g}$ state for both isomers, the majority of orbitals possess occupation numbers close to 1 or 2, conforming to either a formal singly or doubly-occupied state. The exceptions are the σ and π_{op} bonding and antibonding orbitals associated with the Fe2-Fe2′ interactions. The bonding part has ONs of approximately 1.7, while their antibonding components have ONs around

1.3. This deviation is a measure of the inherent correlation and entanglement between these orbitals. Also, the excessive ON on the bonding orbital rather than antibonding ones indicates a net bonding interaction between the Fe2 and Fe2′ centres in both isomers. A comparison of the single orbital entropies and the mutual information shows that the $s(1)_i$ values of isomer 1 are generally larger than the corresponding orbitals of isomer 2, indicating a stronger degree of orbital correlation in isomer 1. The strong static correlation in both isomers can be attributed to interactions between either two of Fe2-Fe2′ σ, σ^*, π_{op}, π^*_{op} orbitals, which corresponds to the orbitals with ONs deviating from 1 or 2. The six largest values of the mutual information (those with a magnitude of $> 10^{-1}$, shown in red), correspond to interactions between these orbitals. The two isomers show a similar number of orbital pairs with mutual information values $I_{i,j}$ of the order of 10^{-2}, usually associated with static correlation. However, isomer 1 displays more than twice as many dynamic correlated pairs (characterised by $I_{i,j}$ values of $\sim 10^{-3}$) as isomer 2. The cumulative effect of these numerous weakly correlated pairs contributes significantly to the higher single-orbital entropy values observed in isomer 1.

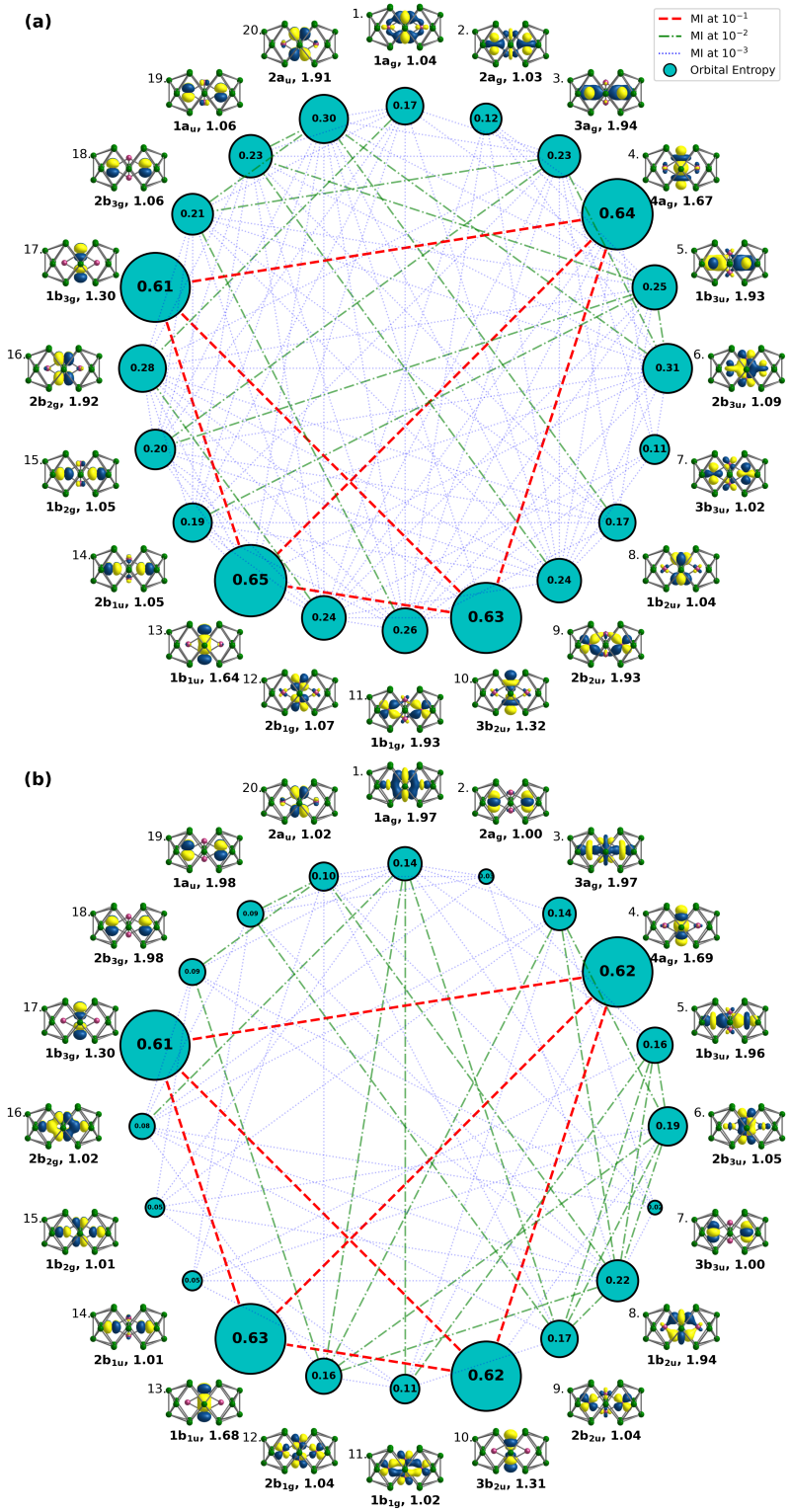

Figure 3.27: Single orbital entropies and mutual information plot of the wavefunction of $^{13}B_{2g}$-$[Fe_4Sn_{18}]^{4-}$ on both (a) isomer 1 and (b) isomer 2. The corresponding isosurfaces are shown adjacent to the respective orbital vertices.

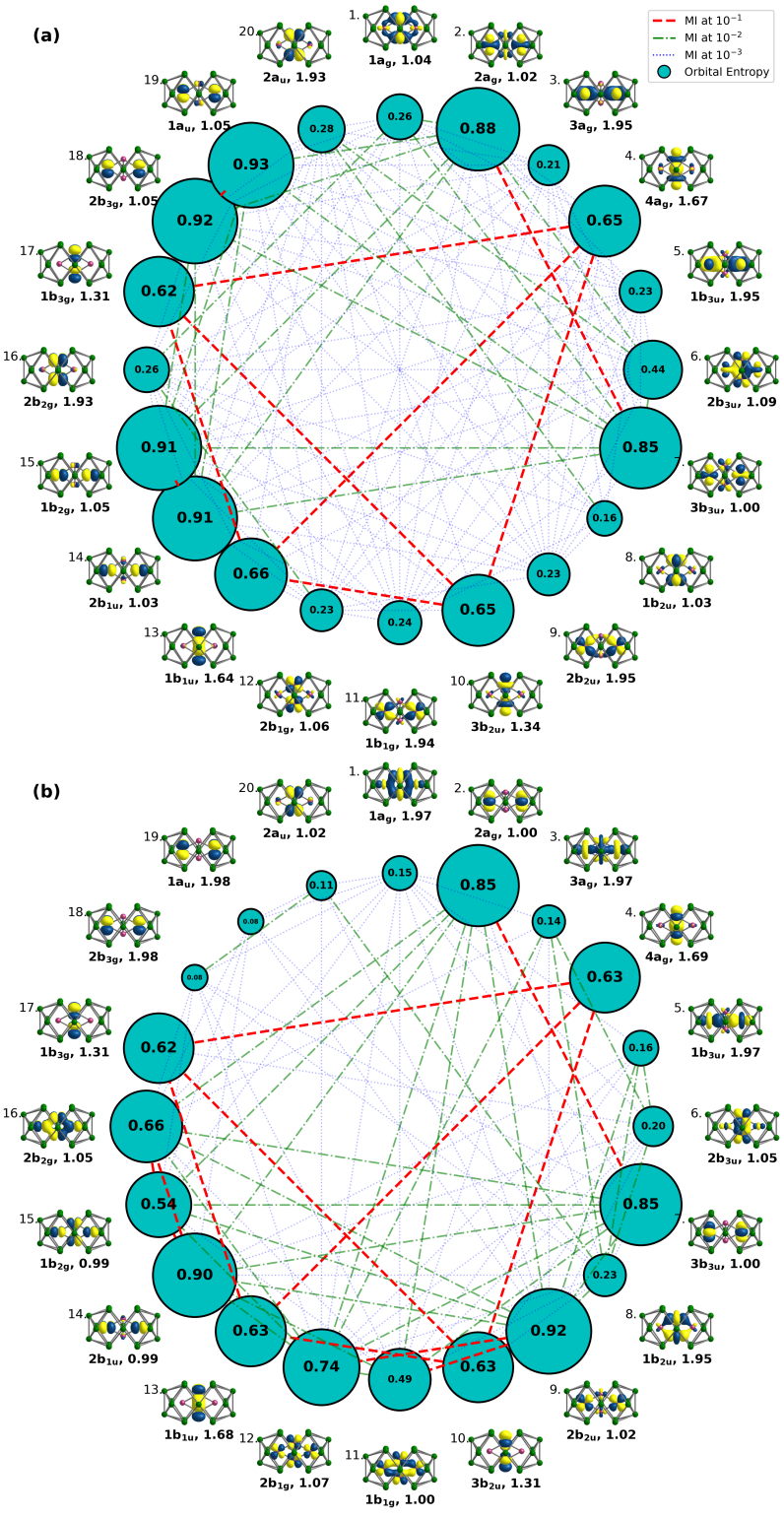

Figure 3.28: Single orbital entropies and mutual information plot of the wavefunction of $^{11}B_{1u}$-$[Fe_4Sn_{18}]^{4-}$ on both (a) isomer 1 and (b) isomer 2. The corresponding isosurfaces are shown adjacent to the respective orbital vertices.

In the $^{11}B_{1u}$ configuration, the electron correlation is more prominent due to the greater number of CSFs, and no single dominant configuration can be identified in the wavefunction. The values of $s(1)_i$ and $I_{i,j}$ for $^{11}B_{1u}$ in Figure 3.28 are therefore generally larger in both isomers compared to $^{13}B_{2g}$ state. This is indicative of stronger entanglement between orbitals. The dominant contributions to the static correlation come from the Fe2-Fe2′ σ/σ^* and π_{op}/π^*_{op} orbitals, just as in $^{13}B_{2g}$. Additionally, a significant static correlation also emerges between the in-phase and out-of-phase combinations of Fe1/Fe1′ $3d_{x^2-y^2}$ and $3d_{yz}$ orbitals in both isomers. In isomer 2, orbitals with b_{1g} and b_{2g} symmetry also show orbital mixing between Fe1 and Fe2, generating bonding/antibonding pairs among four Fe atoms. Stronger static correlation contributions are observed in isomer 2, as indicated by mutual information values ($I_{i,j}$) on the order of 10^{-1}. In particular, significant static correlation arises between the in-phase and out-of-phase combinations of the Fe1/Fe1′ $3d_{xz}$ and $3d_{xy}$ orbitals. As the out-of-phase combinations of these orbitals show mixing with the corresponding $3d$ orbitals on Fe2/Fe2′, the in-phase orbital shows strong static correlation with both orbitals after mixing. Furthermore, the mutual information between orbitals 15 and 16 ($I_{15,16}$) is also in the strong static correlation regime. These orbitals correspond to the π_{op} and π^*_{op} interactions between the Fe1 and Fe2 centres. Even though in isomer 2, there are more orbital pairs contributing to non-dynamic and static correlations, the sum of single-orbital entropy values of orbitals in isomer 1 is still higher than that in isomer 2, which can be ascribed to the complex and numerous dynamic contributions between orbitals in isomer 1.

Overall, in both the $^{11}B_{1u}$ and $^{13}B_{2g}$ states, the single-orbital entropies of isomer 1 are consistently higher than those of isomer 2, indicating stronger orbital entanglement associated with the elongation of the Fe2-Fe2′ bond. However, the static correlation is more pronounced in isomer 2. The increased $s(1)_i$ values in isomer 1 are assigned to the presence of growing dynamically correlated orbital pairs.

The energy separations calculated by DMRG are different from those obtained by DFT, but the differences remain small, underscoring the necessity of including dynamic correlation effects, which are not adequately captured by the multi-configurational method itself. To address this, MC-PDFT calculations were performed using eight on-top functionals, either translated or fully-translated, t-LSDA, t-PBE, t-BLYP, t-revPBE and ft-LSDA, ft-PBE, ft-BLYP, ft-revPBE. These functionals were selected to benchmark their performance in the absence of established DMRG/MC-PDFT protocols for Zintl clusters, particularly those involving multiple Fe-Fe interactions. The results are presented in Figure 3.29 in the form of a heat

map. The left-hand column shows results for $S = 5$ (isomer 1 and isomer 2) while the right-hand column shows $S = 6$. Areas shaded dark blue are those with lowest energy, varying to red for the highest energies (+1.2 eV). With the inclusion of dynamic correlation *via* MC-PDFT, the energy separations between electronic states increase significantly, from less than 0.5 eV in the DMRG results to over 1 eV. The plot clearly shows that the MC-PDFT approach, irrespective of functional, stabilises isomer 2 over isomer 1, and $S = 5$ over $S = 6$, with the result that the three lowest-lying states, $^{13}B_{2g}$, $^{11}B_{1u}$, and $^{11}B_{2g}$, are almost degenerate in the geometry of isomer 2. These states also exhibit almost identical natural orbital occupation numbers. Among them, the $^{11}B_{1u}$ state is slightly favoured by all translated functionals and ft-LSDA, while $^{11}B_{2g}$ is preferred by all GGA-based fully-translated functionals. Benchmarking reveals that the relative energy differences between translated and fully-translated functionals derived from the same GGA root remain fairly consistent, with LSDA-based functionals being the exception. In most cases, fully-translated functionals yield larger energy gaps between electronic states compared to their translated counterparts. Based on these observations, t-PBE and ft-PBE were selected as representative on-top functionals for MC-PDFT calculations to compute on-top energies in the subsequent analysis.

The strong energetic preference for isomer 2 for $[Fe_4Sn_{18}]^{4-}$ shown by the MC-PDFT calculations contrasts with experimental observations, which show it to adopt the isomer 1 structure. A number of possible factors may account for this discrepancy. First, we have selected geometries optimised at the DFT level to be representative of isomers 1 and 2, but of course these are not necessarily the minima on the full MC-PDFT surface. Second, the partitioning of static and dynamic correlation between DMRG and MC-PDFT may lead to an overestimation of the latter by MC-PDFT, compromising the accuracy of the results. This issue could potentially be resolved by expanding the active space to include the Fe 4*d* shell, accounting for the 'double-*d*-shell' effect, or by capturing 'in-out' correlation between the Fe_4 core and the Sn_{18} shell, as has been demonstrated previously for M_2E_{12} clusters.

To address the first of these challenges, we conducted a wider exploration of the MC-PDFT potential energy surfaces by elongating the Fe2-Fe2′ bond. We have performed a series of constrained geometry optimisations with $S = 5$ where the Fe2-Fe2′ bond is constrained in the range of 2.1 to 2.8 Å in 0.1 Å increments and all other parameters are allowed to vary freely (M06-L functional in ADF 2019.304). Throughout the constraint optimisation, the molecular symmetry was restricted to D_{2h}. The Potential Energy Surface (PES) profiles of the $^{11}B_{1g}$ and $^{11}B_{3g}$ states computed using

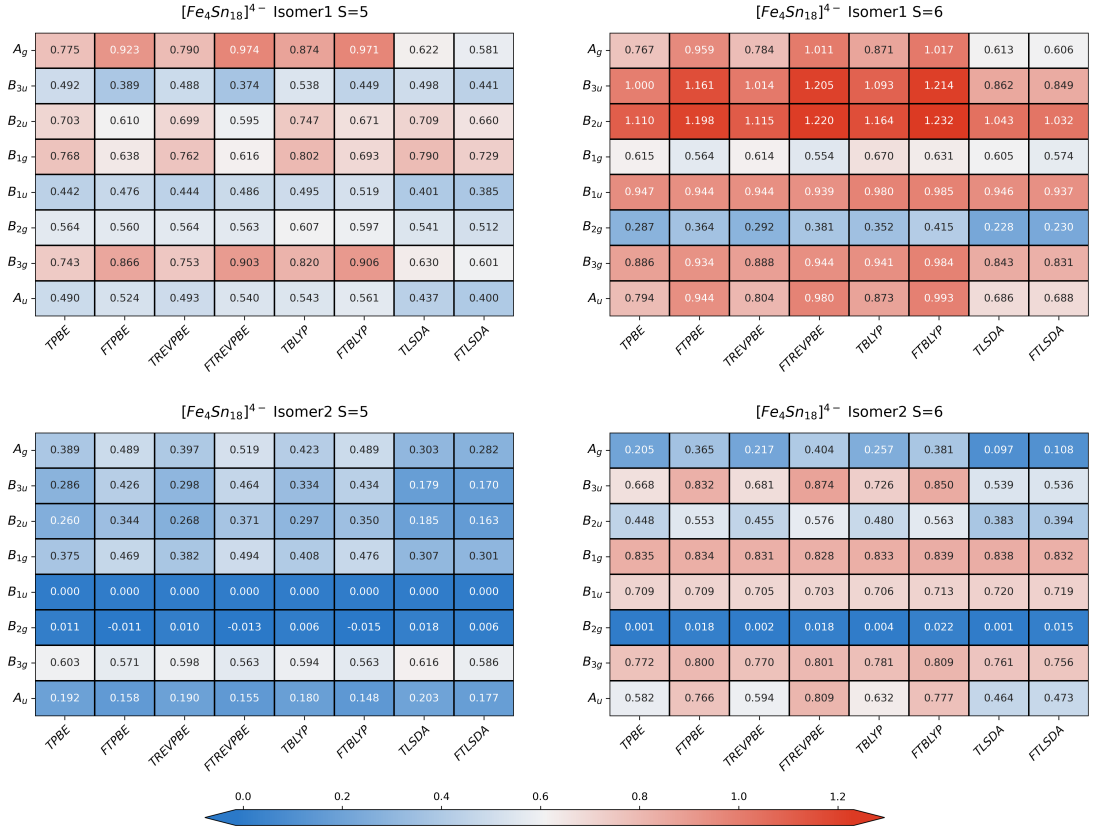

Figure 3.29: Heatmap plot of the MC-PDFT energies for all spatial symmetries of both isomers in $S = 5$ and $S = 6$. All energies are relative to $^{11}B_{1u}$-$[Fe_4Sn_{18}]^{4-}$ of isomer 2. The colour scale varies from blue to red with the increment of the energy. Functionals were benchmarked with eight approximations, as t-PBE, ft-PBE, t-BLYP, ft-BLYP, t-revPBE, ft-revPBE, t-LSDA, ft-LSDA.

DFT are shown in Figure 3.30 (a). The PES clearly shows the two local minima referred to previously: one at 2.3 Å and the other at 2.5 Å, corresponding to two distinct electronic configurations, $^{11}B_{1g}$ and $^{11}B_{3g}$ states, respectively. A conical intersection of these two states is located around 2.4 Å.

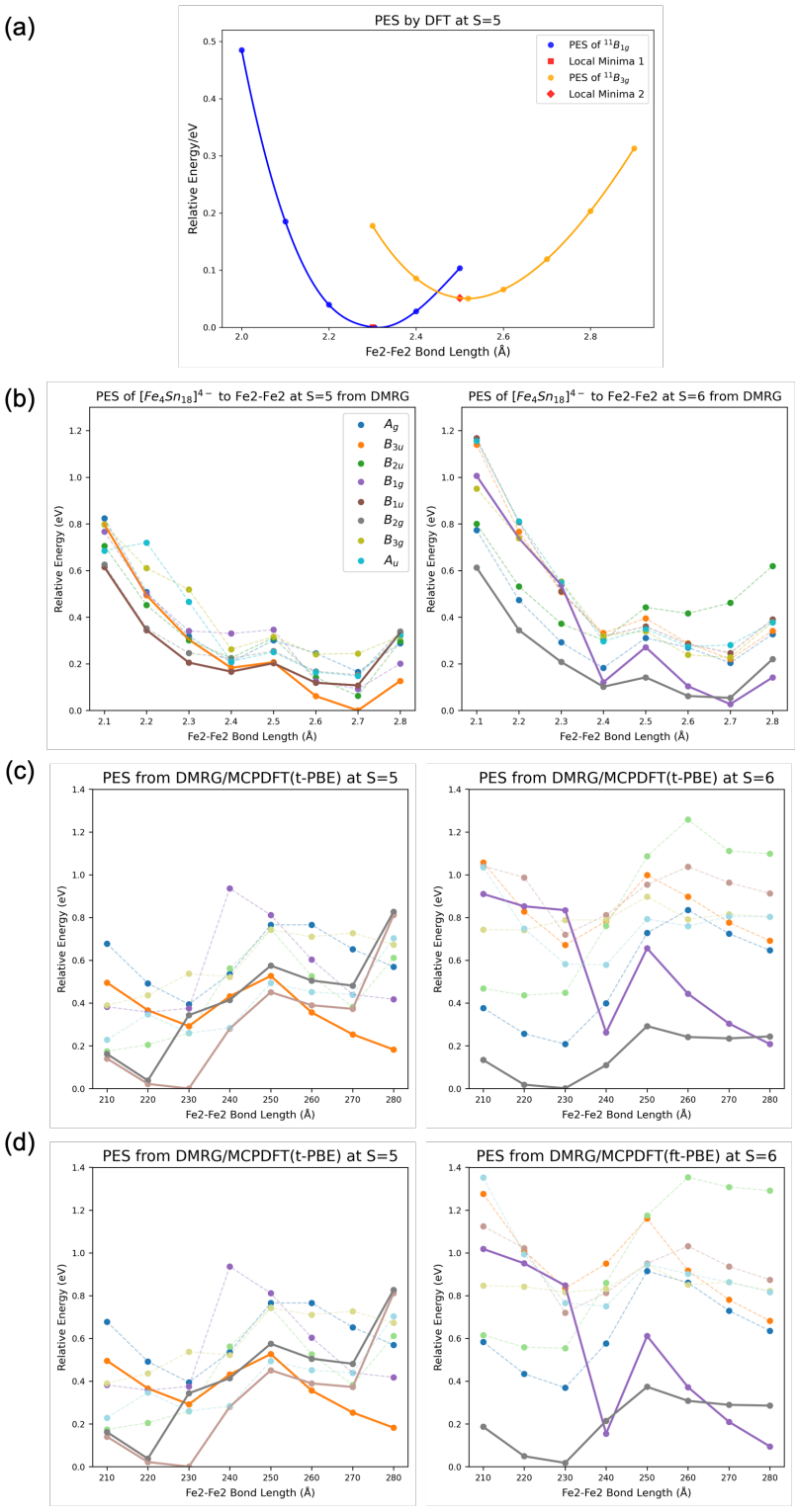

Figure 3.30: PES generated from (a) DFT calculations on $S = 5$ state; (b) DMRG calculations on $S = 5$ and $S = 6$ states; (c) DMRG/MC-PDFT calculations using t-PBE functional on $S = 5$ and $S = 6$ states; (d) DMRG/MC-PDFT calculations using ft-PBE functional on $S = 5$ and $S = 6$ states.

The geometries obtained from each point of this PES scan were then used as input to compute the DMRG energies for all spatial symmetries, for both $S = 5$ and $S = 6$ spin states. A total of sixteen PES curves obtained are shown in Figure 3.30 (b), divided into two subplots according to the spin state. Generally, all PES profiles from DMRG exhibit the same two local minima upon the elongation of the Fe2-Fe2′ bond, one centred around 2.4 Å and the other near 2.7 Å. In most cases, the second minimum is slightly lower in energy, but no lower than 0.27 eV. The exception includes the $^{13}A_g$ (blue line) and $^{13}B_{2u}$ (green line), which favour the minimum with shorter Fe2-Fe2′ bond length. This trend suggests a spin- or spatial symmetry-driven energy reordering of electronic configurations along the Fe2-Fe2′ elongation. Among these PES plots, the $^{13}B_{1g}$ state (purple line) notably shows a particularly deep and sharp minimum at 2.4 Å, with discontinuous jumps to its adjacent geometries (Fe2-Fe2′ at 2.3 Å and 2.5 Å) on the PES. This behaviour points to the existence of a narrow but deep potential well. The global minimum on the DMRG PES is located at 2.7 Å for the $^{11}B_{3u}$ state (orange line). Several near-degenerate states such as $^{13}B_{1g}$, $^{11}B_{2u}$, and $^{11}B_{1g}$ are also found at this bond length, lying within 0.1 eV above the ground state.

Dynamic correlation was then incorporated into the PES using the MC-PDFT with the t-PBE (Figure 3.30 (c)) and ft-PBE (Figure 3.30 (d)) functionals. The two local minima persist even after inclusion of dynamic correlation: one at 2.3 Å and the other beyond 2.8 Å. Again, within the investigated range, we see a systematic stabilisation of isomer 2 (2.3 Å) over isomer 1 (2.7 Å) and, with the t-PBE functional, the global minimum shifts to the $^{11}B_{1u}$ state (brown line) at 2.3 Å, closely followed by the $^{13}B_{2g}$ state (gray line) at the same Fe2-Fe2′ distance, only 0.01 eV higher in energy. The ft-PBE functional generates a very similar PES topology, with again a negligible energy separation of 0.02 eV between $^{11}B_{1u}$ and $^{13}B_{2g}$.

The stabilisation of the first minimum at the shorter Fe-Fe bond length can be attributed to the fact that dynamic correlation energy is more prominent in the bonding region at reduced Fe2-Fe2′ distances, where the electron density becomes more concentrated between the metal centres. This configuration is also characterised by a single dominant CSF, reducing the role of static correlation. In contrast, the stabilisation of the second minimum at the elongated bond length can be understood as a consequence of Fe-Fe bond cleavage, resulting in electron localisation on the individual Fe atoms. While this reduces electron density in the bonding region, it enhances electron localisation on the Fe2/Fe2′ centres, thereby increasing the relative contribution of dynamic correlation to the total energy.

This wider analysis of the PES does not alter the conclusion from MC-PDFT that isomer 2 is the most stable, contrary to the experimental evidence. The second possibility that we wish to explore is that the discrepancy between the experiment and theory arises from the limited size of the active space used in the multi-configurational calculations. In particular, the single-d-shell active space may omit orbitals involving strong static correlation that are essential for an accurate static correlation description. To overcome the limitations imposed by the small active space, we extended our approach to include the 'double-d-shell' effect, which facilitates radial correlation by introducing more diffuse orbitals into the active space, often referred to as the $4d$ orbitals. Due to the computational resource constraints and convergence issues, these calculations were performed only for electronic states lying within 0.4 eV above the ground state at the DMRG/MC-PDFT(ft-PBE) in the single-shell calculations. D_{2h} symmetry is still retained. To keep adequate information in the reduced density matrix, the bond dimension was increased to 2000. Furthermore, state-averaged DMRG-SCF calculations were performed over the three lowest-lying states to obtain a consistent and optimally balanced set of active orbitals across the calculated electronic states.

The relative energies of the electronic states are presented in Table 3.5, from which it is clear that the larger active space has resulted in an energy reordering among these configurations. The ground state is now identified as the $^{13}B_{2g}$ of isomer 1, which is at least 0.23 eV more stable than any of the electronic states of isomer 2. Upon inclusion of dynamic correlation, the energy separation changes, the $^{13}B_{2g}$ is preferred by 0.01 eV with the ft-PBE functional compared to $^{11}B_{2u}$ and this preference even reaches 0.22 eV with the t-PBE functional. These results provide a clear energy separation between states after incorporating Fe $4d$ orbitals to the energy. The absolute increase in correlation energy in the DMRG calculation resulting from the addition of the $4d$ shell is large (15 eV) but this is compensated by a reduction in the dynamic part captured by MC-PDFT, and the total correlation energy increases by only about 1.0 eV. The redistribution between the static and dynamic correlation indicates a more complete description of static correlation effects by providing correlated partners for the Fe $3d$ orbitals.

A comparison between the single- and double-d-shell calculations for the $^{13}B_{2g}$ state of $[Fe_4Sn_{18}]^{4-}$ shows some notable differences in the occupation numbers of orbitals involved in the 'double-d-shell' correlation, as illustrated in Figure 3.31. In this figure, the second d shell of each orbital (numbered 21–40) is shown directly outside the corresponding $3d$ orbital in the second concentric circle. The differences

Table 3.5: Relative energies for the DMRG(28e, 40o) and DMRG(28e, 40o)/MC-PDFT calculations for the low-lying states determined from single-shell calculations. Root 1 of $^{13}A_g$ in isomer 2 is the reference point.

	Isomer 1				Isomer 2			
Method	$^{11}B_{3u}$	$^{13}B_{2g}$	$^{11}B_{2u}$	$^{11}B_{1u}$	$^{11}B_{2g}$	$^{11}A_u$	$^{13}A_g$	$^{13}B_{2g}$
DMRG Root1	1.61	-0.23	0.46	1.50	1.32	2.03	0.00	1.12
DMRG Root2	1.96	0.43	0.85	1.69	1.60	2.06	0.56	1.23
DMRG Root3	1.99	1.32	1.44	2.26	2.07	2.36	1.34	1.83
t-PBE Root1	2.24	-0.40	-0.18	1.09	0.72	1.22	0.00	1.20
t-PBE Root2	2.39	0.13	0.13	1.29	1.20	1.23	0.45	1.54
t-PBE Root3	2.38	1.36	0.75	1.49	1.40	1.41	1.31	1.50
ft-PBE Root1	1.81	-0.29	-0.28	0.76	0.42	1.23	0.00	1.08
ft-PBE Root2	2.10	0.18	0.03	1.10	0.96	1.20	0.46	1.31
ft-PBE Root3	2.10	1.26	0.63	1.11	1.14	1.28	1.31	1.48

arise from the enhanced delocalisation of the Fe 3d-based orbitals upon inclusion of the 4d shell. For example, the 4a_g orbital (orbital 4), which is fully localised on Fe2 and Fe2′ and acts as its σ-bonding orbital in the single-shell description, exhibits significant mixing with the out-of-phase combination d_{z^2} orbitals on Fe1 and Fe1′ when the 'double-d-shell' effect is included. The occupation numbers from the double-d-shell DMRG calculations also differ from the single-shell ones, which deviate strongly from 1 or 2. In contrast, ONs of the Fe 3d orbitals in the double-d-shell calculations are typically close to 1 or 2. In cases where the 3d orbitals have occupancies close to 2, their 4d counterparts have ONs exceeding 0.05. In contrast, 4d correlated orbitals paired with singly-occupied 3d orbitals (occupation close to 1) typically exhibit very low ONs below 0.01. For this reason, three decimal places on the occupation number were retained in Figure 3.31 to highlight their negligible difference. This behaviour is attributable to the limited need for correlation in singly-occupied orbitals. Although the contribution of such weakly occupied orbitals to the total correlation energy and wavefunction is minimal, their inclusion in the active space is essential for maintaining a consistent active space across different electronic states. This consistency ensures a balanced treatment of orbital correlations when comparing states in different state symmetries.

The orbital entanglement analysis presented in Figure 3.31 shows that the previously strong static correlation contributed by the Fe 3d orbitals is significantly relaxed upon inclusion of the Fe 4d shell. The most prominent mutual information values in the single-shell calculations, associated with Fe2-Fe2′ π_{op}, π^*_{op}, σ and σ^* orbitals are now reduced, and lie in the range typically associated with static rather than non-dynamic correlation. In contrast, the non-dynamic correlation now concentrates along

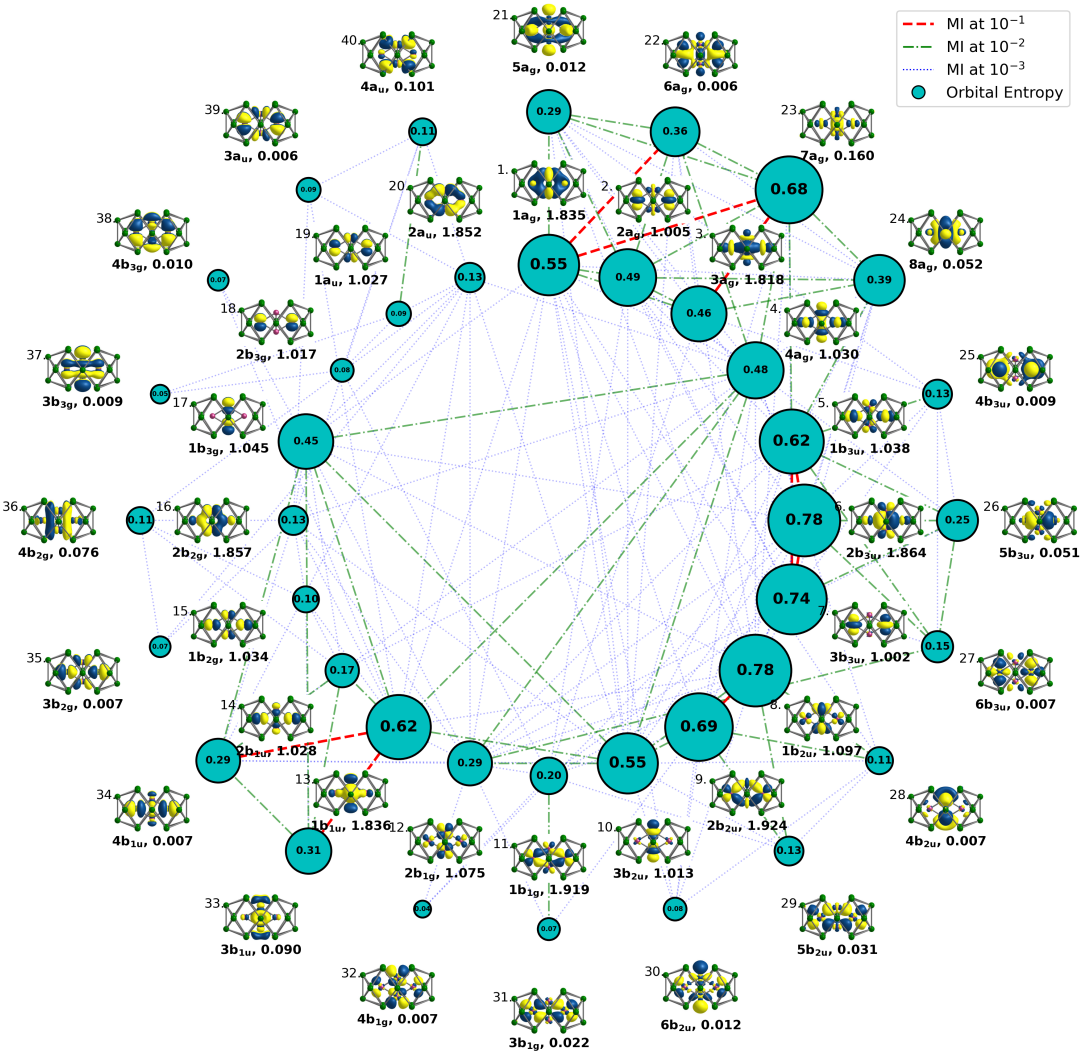

Figure 3.31: Single orbital entropies and mutual information plot for the $^{13}B_{2g}$-$[Fe_4Sn_{18}]^{4-}$ of isomer 1 at an active space of DMRG(28e, 40o) including the 'double-d-shell' effect. The isosurfaces are shown adjacent to the respective orbital vertices.

the Fe1-Fe2 bond. This is reflected in the σ-bonding and antibonding interactions between Fe1 $3d_{xy}$ and Fe2 $3d_{x^2-y^2}$ orbitals in the b_{2u} set, as well as in π interactions constructed by the in-phase combination of Fe2 $3d_{xy}$ and the out-of-phase combination of Fe1 $3d_{x^2-y^2}$ orbitals in $1b_{3u}$ and $2b_{3u}$, complemented by another in-phase Fe1 $3d_{x^2-y^2}$ orbital in $3b_{3u}$. The $3d$-$4d$ correlation is dynamic in nature. However, static and even non-dynamic correlation also exist. A significant portion of both static and non-dynamic correlations involve the Fe $4d$ orbitals, with notable $3d$-$4d$ orbital pairs contributing. Fe $4d$ orbitals with relatively high single-orbital entropy values are primarily located within the a_g and b_{1u} subgroup, with $s(1)_i > 0.29$. These orbitals are responsible for several non-dynamic correlations with their $3d$ counterparts. For

example, the in-phase combination of Fe1 and Fe2 $3d_{x^2-y^2}$ orbitals forms a bonding interaction across the central rhombus of Fe atoms in $3a_g$ orbital. Additionally, the in-phase combination of Fe1 and Fe2 $3d_{z^2}$ orbitals constitutes another bonding orbital along the Fe1-Fe2 axis in the $1a_g$ orbital. These orbitals show non-dynamic correlations with their corresponding $4d_{x^2-y^2}$ orbitals in the $7a_g$ representation. Furthermore, the $1a_g$ orbital also exhibits non-dynamic correlation with the correlated orbital of out-of-phase combination of Fe1 and Fe2 $3d_{x^2-y^2}$ orbitals as $6a_g$. In the b_{1u} subset, the $1b_{1u}$ orbital — an in-phase combination of Fe2 $3d_{yz}$ and Fe1 $3d_{xz}$ — exhibits delocalised π_{op}-bonding character across four Fe atoms and shows non-dynamic correlations with both its $4d$ counterpart as $3b_{1u}$ and the correlated orbital of the corresponding π^*_{op} interactions as $4b_{1u}$. Static correlation effects are observed across the a_g, b_{3u}, b_{2u}, b_{1g}, b_{1u} and a_u subsets and include either $3d$-$4d$ or $4d$-$4d$ interactions.

Since DMRG is particularly adept at capturing static and non-dynamic correlations, the inclusion of the second d shell orbitals appears to be crucial for an accurate description of electron correlation in systems with metal-metal bonding. This shifts the balance between static and non-dynamic correlations that can be distinguished by their single orbital entropies and mutual information. This observation aligns with previous findings for single metal complexes, where the importance of the 'double-d-shell' effect has been demonstrated,[173,200] although the behaviour diverges in exchange-coupled bimetallic systems.[201] In some cases, the 'double-d-shell' effect of transition metals can be less pronounced than that of metal-ligand correlation or correlation with s and p shell of the metal core. We have additionally tested the possibility of including Fe $4s$ and $4p$ orbitals into the active space. However, DMRG-CI calculations reveal that their ONs are much lower than 0.01, indicating negligible contributions to the wavefunction. Subsequent DMRG-SCF calculations rotate these orbitals out of the active space, reaffirming their unoccupied character and their lack of importance to static correlation in this system.

3.4.4 Conclusion

In conclusion, DFT calculations were applied to explain the isomerisation of the Fe_4 rhombus in $[Fe_4Sn_{18}]^{4-}$ and $[Fe_4Pb_{18}]^{4-}$. Both clusters are in an $S = 5$ high-spin configuration, but in different state symmetry, as $^{11}B_{1g}$ for $[Fe_4Pb_{18}]^{4-}$ and $^{11}B_{3g}$ for $[Fe_4Sn_{18}]^{4-}$. The inherent reason is an electron swap between two spin-β orbitals, where the occupation of $6b_{1g}$ orbital in $[Fe_4Sn_{18}]^{4-}$ introduces more in-plane π^* component to the Fe2-Fe2′ bond. However, PBE and M06-L functionals exhibit a negligible energy difference between $^{11}B_{1g}$ and $^{11}B_{3g}$ for $[Fe_4Sn_{18}]^{4-}$, which can be attributed to

its inherent strong correlation that cannot be captured by the exchange-correlation term in DFT. The follow-up DMRG and MC-PDFT calculations based on the DFT optimised geometry and all Fe $3d$ orbitals in the active space, even though incorporating both static and dynamic correlations, fail to reproduce the correct energetic ordering of two isomers either with or without symmetry. A scrutinisation on the PES of $[Fe_4Sn_{18}]^{4-}$ on Fe2-Fe2′ bond was performed, while the minimum was observed at 2.3 Å by DMRG/MC-PDFT. A stronger correlation character was noticed for the isomer possessing longer Fe2-Fe2′ bond. Another effort was made by introducing Fe $4d$ orbitals into the active space, to capture the 'double-d-shell' effect and obtain a correlated orbital for each $3d$ orbital for the low-lying states. The isomer 1 is energetically preferred in this framework. The importance of the $4d$ orbitals incorporation in correlation is highlighted by this method. However, due to the lack of search for all possible state symmetries as well as the exploration on the non-symmetric wavefunction, the identity of the true ground state of $[Fe_4Sn_{18}]^{4-}$ therefore remains uncertain.

3.5 Summary

In this chapter, we have explored five multi-centre, transition metal-encapsulated Zintl clusters featuring open-shell electronic configurations, including $[Fe_2Sn_4Bi_8]^{3-}$, $[Cr_2Sb_{12}]^{3-}$, $[Fe_3Sn_{18}]^{4-}$, $[Fe_4Sn_{18}]^{4-}$, and $[Fe_4Pb_{18}]^{4-}$. Our discussion centres on two primary aspects: (1) the nature of metal-metal bonding between the transition metal centres, and (2) the interactions between these metals and the surrounding Zintl cage. Regarding metal-metal bonding, the spatial confinement inherent to Zintl clusters results in relatively short intermetallic distances, creating an environment favourable for valence-bond formation between transition metal atoms. These metals, as mid-transition elements, exhibit partially filled and energetically near-degenerate d orbitals. Due to the weak ligand field provided by the Zintl cage, which is insufficient to pair all unpaired electrons, unpaired electrons retain in linear combinations of $3d$ orbitals. The balance between exchange energy stabilisation and the increasing anti-bonding character of high-energy orbitals culminates in a characteristic feature of leaving the σ^* orbital along the metal-metal bond axis unoccupied in the clusters. This pattern is consistently observed in open-shell clusters such as $[Cr_2Sb_{12}]^{3-}$, $[Fe_3Sn_{18}]^{4-}$, and $[Fe_4E_{18}]^{4-}$. Given the presence of unpaired electrons and the small energy gaps within the d-manifold, these clusters also have a strong multi-configurational character. This multi-configurational nature manifests as significant spin contamination in UDFT calculations, indicating the necessity of using MC-SCF methods such as CASSCF and DMRG. The DMRG approach provides insights into both metal-metal ('left-right' and 'double-d-shell') and metal-cage ('in-out') electron correlations with a higher computational efficiency compared to CASSCF. Quantitative analysis of these correlations *via* occupation number deviations, single-orbital entropy ($s(1)_i$), and mutual information ($I_{i,j}$) reveals that correlations between metal centres are generally stronger. Nevertheless, core-shell interactions, particularly metal-to-cage back-donation, are also substantial. For instance, the mutual information study reveals that in $[Cr_2Sb_{12}]^{3-}$ occupied π-bonding orbitals of the cage are prominently correlated more strongly with the unoccupied correlated orbitals of π^* than with itself. This indicates the electron density flowing back to the cage in the occupied orbital. This is further supported by isosurface plots of the corresponding molecular orbitals and their occupation numbers. In more complex systems, such as $[Fe_4Sn_{18}]^{4-}$, which contain multi-centre metal-metal bonds, an accurate description of both static and dynamic correlations is crucial, rather than relying solely on the obscure exchange-correlation energy in the DFT framework. There can be energy degenerate states manifested by

DFT calculations, underscoring the need for multi-reference approaches. A minimal active space including only the 3d orbitals may overestimate intra-3d static correlations while neglecting essential 3d-4d correlations that cannot be simply treated by post-MC-SCF calculations. Furthermore, on-top dynamic correlation energy incorporated by MC-PDFT can alter the relative energies of electronic states, highlighting the system's sensitivity to correlation effects. Due to computational constraints, we have limited our treatment to 'double-d-shell' effect in a subset of representative systems; however, the roles of the metal 4s/4p orbitals and valence p orbitals of the cage in correlation energy remain obscure. Moreover, benchmarking against traditional perturbative methods such as CASPT2 and NEVPT2 is still required to validate our results from the MC-PDFT. These limitations point to promising directions for future research on open-shell Zintl clusters.

The skeletal electron counts of the Zintl cages can be anticipated using the Wade-Mingos rules or the more generalised Jemmis *mno* rules. Closed-shell analogues with inert d^{10} metal cores provide additional guidance for deducing electronic structures of the cage, which can be a useful reference for their open-shell analogues. These approaches are complementary and help establish an initial hypothesis for electron distribution of the intermetallic clusters. DFT calculations can corroborate this predefined electron count for the cage. With the incorporation of transition metals, the electron repulsion between main-group cluster fragments is moderated, allowing for cluster expansion. Except for understanding the electron count of the shell, elucidating the cluster-growth pathway also becomes an important topic of investigation. In studying various 18-vertex cage conformations, our analysis reveals the electronic drivers behind the cluster growth from two $[Sn_9]^{4-}$ fragments to a fused D_{3d}-$[Sn_{18}]^{4-}$ cluster, which proceeds *via* stepwise electron oxidation from antibonding orbitals located between two fragments with the help of transition metals. Besides, the existence of the metal-metal bonds can inhibit cluster oligomerisation and favour fusion. The transformation pathway from D_{3d} to D_{2h}-$[Sn_{18}]^{8-}$ is also clarified through Walsh diagram analysis. Geometrically, D_{2h}-$[Fe_4Sn_{18}]^{4-}$ can be viewed as a D_{3h}-$[Sn_9]^{4-}$ unit where two $FeSnSn_5$ caps replace the Sn atom in the middle deck, while the remaining Sn is removed and replaced by two Fe atoms to reduce steric strain and charge repulsion. A structurally analogous species, $[Sn_{24}]^{8-}$ in $[Rh_3Sn_{24}]^{5-}$, can be interpreted as the replacement of a third central Sn atom with a $RhSnSn_5$ fragment. This structure also supports a growth model where Sn_{18} is capped by $SnSn_5$ units on its open faces. Notably, $[Sn_9]^{4-}$ can function either as a trigonal prismatic Sn_6 centre or as a substitutional ligand as $SnSn_5$ for the transition metal. However, further experimental

evidence and computational studies are still required to support this geometrically derived growth hypothesis.

The incorporation of transition metals with an active d-band into Zintl cages promotes valence-like behaviour of these orbitals. As shown in Figure 3.32, based on the present work and previous studies, Mn (Group 7) appears to be a borderline case between core-like and valence-like d orbital behaviour when incorporated into heavy main-group Zintl frameworks. While in Ge-based clusters, size mismatches between the cage and the encapsulated metal often preclude the formation of deltahedral structures. Open-shell clusters such as $[MnPb_{12}]^{3-}$, $[FeSn_{10}]^{3-}$, $[Fe_2Sn_4Bi_8]^{3-}$, $[Fe_3Sn_{18}]^{4-}$ and $[Fe_4E_{18}]^{4-}$ exhibit only minor geometry distortions on the cage relative to their closed-shell analogues, with moderate metal-cage back-bonding. In $[MnPb_{12}]^{3-}$, strong spin contamination and a D_{2h} symmetry that deviates from ideal icosahedral geometry can be rationalised by resonance between $Mn^{2+}@Pb_{12}{}^{5-}$ and $Mn^{-}@Pb_{12}{}^{2-}$ configurations. As for the latter four iron binary/trinary clusters, their shell structures largely retain the symmetry and shape of their closed-shell counterparts. The reduced electrons are depleted from the metal core and promote metal-metal bonding. In contrast, $[Cr_2Sb_{12}]^{3-}$ shows stronger back-bonding than $[Fe_2Sn_4Bi_8]^{3-}$ with the same electron count, inducing noticeable cage distortion.

Group 6 Cr, Mo, W	Group 7 Mn, Tc, Re Borderline	Group 8 Fe, Ru, Os	Group 9 Co, Rh, Ir	Group 10 Ni, Pd, Pt	Reference Geometries
		C_{2v}-$[FeSn_{10}]^{2-}$		D_{4d}-$[NiPb_{10}]^{2-}$	
	D_{2h}-$[MnPb_{12}]^{3-}$		I_h-$[CoPb_{12}]^{3-}$	I_h-$[NiPb_{12}]^{2-}$	
C_{4v}-$[Cr_2Sb_{12}]^{3-}$		D_{4h}-$[Fe_2Sn_4Bi_8]^{3-}$	$[Co_2Sn_5Bi_7]^{3-}$	D_{4h}-$[Ni_2Bi_{12}]^{4+}$	
		D_{3d}-$[Fe_3Sn_{18}]^{4-}$		D_{3d}-$[Ni_3Ge_{18}]^{4-}$	
		D_{2h}-$[Fe_4Sn_{18}]^{4-}$		D_{2h}-$[Cu_4Sn_{18}]^{4-}$	
valence-like *d* orbital		core-like *d* orbital			

Figure 3.32: Representative intermetallic deltahedral Zintl cluster structures and their geometries. The borderline between valence and core-like d orbitals is located at Group 7.

Chapter 4

Metal-Metal Bonding and Structural Modulation in Iron-Pnictogen Clusters

4.1 Introduction

In the previous chapter, our focus was on Zintl clusters with core-shell architectures mainly composed of Group 14 elements. In this chapter, we extend our research to functionalised clusters composed of iron and Group 15 (Pn) elements. In contrast to the delocalised bonding discussed in the previous chapter, localised bonding becomes more prevalent in electron-precise pnictogen-based clusters. Homonuclear pnictogen anion clusters, such as $[Pn_4]^{2-}$, $[Pn_7]^{3-}$, and $[Pn_{11}]^{3-}$, are fundamental building blocks for transition-metal-containing intermetallic clusters. These homonuclear clusters can also act as flexible electron donors, enabling the coordinated transition metal to satisfy the 18-electron rule by varying its coordination mode from one-atom (η^1) to four-atom coordination (η^4).[202] Studies on $[Pn_7]^{3-}$-based clusters show bonding modes from two-connected $[(\eta^2\text{-}Pn_7)Pt(PPh_3)]^{2-}$ (Pn = P, As)[203] to four-connected $[(\eta^4\text{-}Pn_7)M(CO)_3]^{3-}$ (M = Cr, Mo, W and Pn = P, As, Sb),[204] $[(\eta^4\text{-}P_7)Ni(CO)]^{3-}$ (Figure 4.1 (a)),[205] $[(\eta^4\text{-}P_4)Fe(\eta^4\text{-}P_7)]^{-}$.[206] In general, early and mid-transition metals with fewer d electrons tend to bind to a larger number of pnictogen atoms than their late-transition-metal analogues. Clusters incorporating multiple transition metals bound to a single Pn_7 unit have also been investigated, examples include the homometallic $[Sb_7Ni_3(CO)_3]^{3-}$,[207] $[Bi_7M_3(CO)_3]^{2-}$ (M = Co, Rh) (Figure 4.1 (b))[208] and heterometallic $[(Cp''_2Sm)_2As_7(Cp^*Fe)]$ (Cp''=1,3-tBu$_2$C$_5$H$_3$),[209] where each metal centre is coordinated by four pnictogen atoms from the Pn_7. Additionally, dimerisation of Pn_7 units can occur *via* one or two transition metal atoms

acting as a bridge. For example, in the single-metal case $[M(\eta^2\text{-}Pn_7)_2]^{4-}$ (M = Zn, Cd; Pn = P, As) (Figure 4.1 (c)),[210] the transition metal is coordinated by two pnictogen atoms from each Pn_7 fragment, and two Pn_7 are aligned in a staggered fashion. In $[Fe(\eta^4\text{-}HP_7)_2]^{2-}$,[211] a bonding rearrangement occurs in each HP_7 fragment to form an open rectangle motif coordinated to the iron centre. The copper atoms act as electron acceptors in $[Cu_2(\eta^4\text{-}As_7)_2]^{4-}$ (Figure 4.1 (d)),[212] where Cu is coordinated by four atoms of one As_7 fragment, but bound only to one As atom on the other As_7 to form a donor-acceptor pair. Dimerisation mediated by an M_2 bridge is also seen in $[Ag_2(\eta^1,\eta^1\text{-}As_7)_2]^{4-}$,[213] $[Au_2(\eta^1,\eta^1\text{-}As_7)_2]^{4-}$,[214] and $[Pd_2(\eta^2,\eta^2\text{-}As_7)_2]^{4-}$.[215,216] In these cases, each metal is coordinated to atoms from both As_7 units. Metal-metal bonding is also observed between the transition metal atoms, for example, in the Hg-Hg bond in $[Hg_2(\eta^2\text{-}As_7)_2]^{4-}$ (Figure 4.1 (e)).[210]

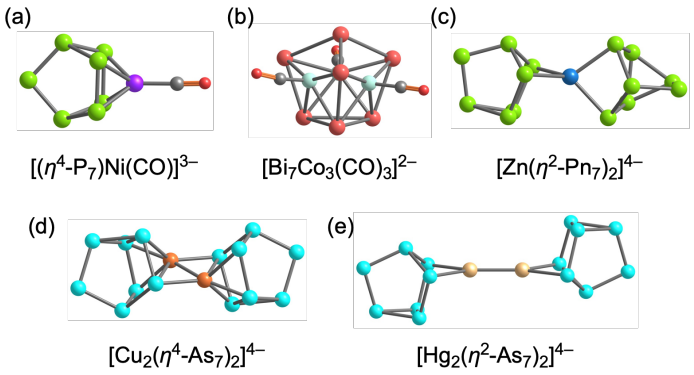

Figure 4.1: Representative structures of Pn_7-based clusters.

Another category of clusters arises from the isolobal relationship between Pn and CH. The geometries of Pn_n species often resemble those of their isoelectronic organic molecules. For instance, $(P_2)^{2-}$ can be regarded as an inorganic counterpart of ethylene (C_2H_4), and P_6 can adopt a hexagonal structure similar to that of benzene. Such planar Pn_n units can function either as end-blocks or bridging ligands in transition metal complexes. As end-blocks, Pn_n rings can substitute for cyclopentadienyl (Cp) ligands in sandwich compounds, with ring sizes ranging from Pn_3 to Pn_6. Examples illustrating this role include $[(Cp^RNi)(P_3)]$ (Cp^R = Cp‴ (1,2,4-tBu$_3$C$_5$H$_2$)[217] or Cp* (C_5Me_5)[218]), $[(Cp'''Co)(P_3)]^-$ (Figure 4.2 (a)),[219] $[(Cp'''Co)(P_4)]$ (Figure 4.2 (b)),[220] $[(C_5Ph_5Fe)(P_4)]^-$,[221] and $[(Cp^*M)(Pn_5)]$ (M = Fe (Figure 4.2 (c)),[222] Ru,[223] Pn = P; M = Fe, Pn = As;[224] $Cp^* = C_5Me_5$). There are also cases where both Cp rings are replaced by Pn_n rings to yield inorganic ferrocene analogues such as $[Fe(P_4)_2]^{2-}$ (Figure 4.2 (d))[206] and $[Ti(P_5)_2]^{2-}$.[225] In these clusters, both Pn_n and Cp ligands act as electron-donating ligands, again helping the transition metal centre to adopt an

18-electron configuration. A general trend is that smaller Pn_n ligands bind to later transition metal centres. When Pn_n ligands act as bridging moieties, dinuclear or double-sandwich structures can be constructed. For example, a small bridging unit such as Pn_3 appears in $[(Cp'''Ni)_2(P_3)]$ (Figure 4.2 (e)),[226] while larger rings such as Pn_5 have been observed in $[(Cp^R M)_2(P_5)]$ (M = Cr, Mn), $[(Cp^*Mo)_2(Pn_5)]^-$ (Pn = P, As), and $[(CpV)_2(Pn_5)]$ (Pn = Sb, Bi) (Figure 4.2 (g)).[227] Pn_6 rings have been synthesised as bridging ligands in compounds such as $[(Cp^R M)_2(P_6)]$ (M = Ti,[228] V,[229] Nb,[230] Mo,[231] W[232]) (Figure 4.2 (h)). The wider ring size also facilitates metal-metal bonding across the pnictogen ring, which was analysed in $[(CpV)_2(Pn_5)]$.[227] In clusters with smaller rings such as Pn_4, the *cyclo* ring can be cleaved with concomitant formation of a metal-metal bond, as in $[(Cp^*M)_2(P_2)_2]$ (M = Fe, Co) (Figure 4.2 (f)).[233] Planar Pn_n rings can also replace Cp-type ligands in coordination complexes bound by multidentate ligands, such as $[({}^{Ph}PP_2{}^{Cy}Fe)(P_4)]$,[234] and $[(PHDICo)(P_4)]^-$ (PHDI = bis(2,6-diisopropylphenyl)phenanthrene-9,10-diimine).[235] Rings ranging from Pn_3 to Pn_5 are observed as bridges between metal complexes. The smallest example features As_3 in $[(L^3Co)_2(As_3)]$ (L^3 = [{N(2,6-C_6H_3*i*Pr_2)C(Me)}$_2$CH]) (Figure 4.2 (i)).[236] Pn_4 units exhibit various isomers as bridging moieties — from the all-single-bond $[Pn_4]^{4-}$, to aromatic $[Pn_4]^{2-}$, to neutral Pn_4 with alternating single and double bonds. These species are often generated from activation of white phosphorus or yellow arsenic. Ni and Cu show limited ability to activate E_4, typically forming non-planar species like $[(L^3Cu)_2(E_4)]$ (E = P, As)[237] and $[(MeL^{Dipp}Ni)_2(P_4)]$ (L^{Dipp} = CH[CHN(2,6-*i*$Pr_2C_6H_3$)]$_2$).[238] Co and Fe complexes can reduce Pn_4, leading to planar geometries. $[(LFe)_2(Pn_4)]$ complexes will be discussed in detail in Section 4.3. Cobalt analogues including $[(LCo)_2(As_4)]$ (L = β-diiminato) (Figure 4.2 (j)),[236] $[(L^{Dep}Co)_2(P_4)]$ (L^{Dep} = CH[C(Me)N(2,6-$Et_2C_6H_3$)]$_2$),[239] and $[(L^{Dipp}Co)_2(P_4)]$[240] have been widely investigated. Similar clusters have also been isolated for *f*-block elements, such as $[\{(DippForm)_2Sm\}_2(E_4)]$ (E = P, As; DippForm = (2,6-*i*$Pr_2C_6H_3$)NC(H)).[241] A notable example containing a five-membered Pn ring is $[\{(IMes)Co\}_2(Bi_5)]$ (IMes = bis(1,3-(2,4,6-trimethylphenyl))imidazol-2-ylidene) (Figure 4.2 (k)).[242] Clusters containing small Pn_n ligands can serve as precursors for the assembly of extended Pn_n fragments in the cluster, as illustrated by $[(Cp'''Co)_2(P_8)]^{2-}$,[243] $[(Cp'''Co)_4(As_{10})]$,[244] $[(Cp'''Co)_3(As_{12})]$,[244] and $[(LFe)_4(P_8)]$,[245] $[(LFe)_4(As_8)]$ (L stands for the multidentate ligand).[246]

In addition to planar structures, non-planar Pn_n moieties are also observed in clusters, especially those resembling the prismane motif. Representative examples include $[(Cp^*Co)_3(As_6)]^{2+}$ (Figure 4.3 (a)),[247] $[\{CpRu\}_3(Bi_6)]^-$, $[\{(cod)Ir\}_3(Bi_6)]^-$

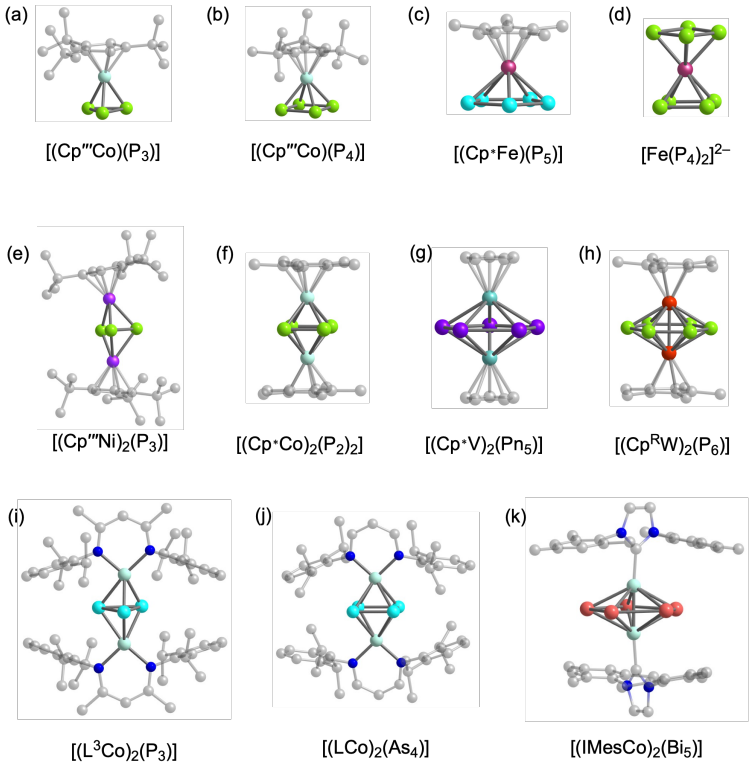

Figure 4.2: Representative clusters containing the Pn_n moiety.

(cod = 1,5-cyclooctadiene)[248] and $[Bi_6\{Mo(CO)_3\}_3]^{4-}$ (Figure 4.3 (b)).[249] In these clusters, Cp rings serve as ligands coordinating the transition metals adjacent to the square faces of the Pn_6 trigonal prism — similar to the η^4 coordination seen in M_3Pn_7 clusters. An alternative non-planar arrangement of Pn_n is found in clusters where an icosahedral skeleton is composed of both transition metals and main-group elements, in which the transition metals are coordinated by CO in $[Ni_{0.3}\{Bi_6\{Ni_3(CO)_4\}_2\}]^{4-}$ [250] and $[Bi_{12}Ni_7(CO)_4]^{4-}$ (Figure 4.3 (c)),[251] or phosphine ligands in $[Co_6As_{12}(PEt_2Ph)_6]$ (Figure 4.3 (d)).[252] These clusters possess a 9-vertex or 12-vertex deltahedral architecture, sharing structural similarities with clusters composed of Group 14 elements.

The examples given above mainly contain late transition metals, but early transition metals (pre-Group 7) tend to donate *d* electrons to the cage framework, consistent with the findings in the previous chapter regarding their valence character, and they can influence cluster rearrangement. This behaviour can be observed in crown-like pnictogen clusters, which are well-documented for arsenic and antimony as $[NbE_8]^{3-}$ (E = As, Sb),[253] $[MoAs_8]^{2-}$,[254] $[MoSb_8]^{3-}$, and $[CrAs_8]^{3-}$ (Figure 4.3 (e)).[255] The active *d* orbitals of early transition metals can contribute their valence electron density to the cage, enabling the formation of eight two-centre-two-electron Pn-Pn bonds. These clusters may exist as discrete species or may be extended into infinite chains,

typically stabilised by potassium cations. Crown-like Pn_8 units can further connect with smaller pnictogen fragments to build larger clusters.[256] Ternary clusters, normally comprising one transition metal and two main-group elements, have also been widely investigated. Representative examples include $[Cr_5Sb_{20}Sn_2]^{4-}$ and its dimer,[257] $[K_2Zn_{20}Bi_{16}]^{6-}$(Figure 4.3 (f)),[258] and $[Pd_3Sn_8Bi_6]^{4-}$ (Figure 4.3 (g)).[259]

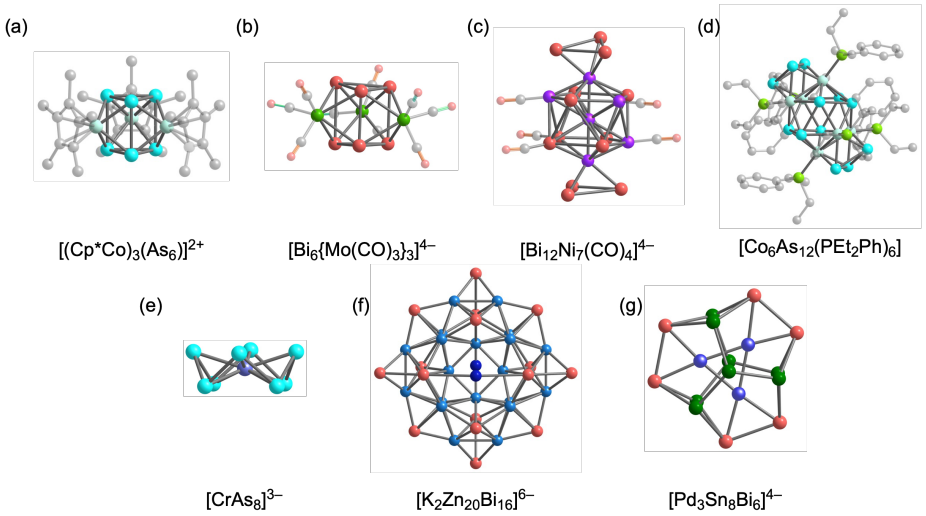

Figure 4.3: Representative pnictogen-based deltahedral clusters ((a) to (d)) and binary/ternary clusters ((e) to (g)).

In this chapter, we present two Fe/Pn-based clusters, analysed through DFT and MC-SCF calculations. The two clusters, one based on an unsymmetrical Fe_3 core, the other on Fe_2, are connected by the presence of a Pn_4 bridging unit: As_4 in the former and P_4 in the latter. We show that they share a common oxidation state, but different structures. We first present an iron/arsenic binary cluster, $[Fe_3As_{13}]^{3-}$ with an iron triangle core.[4] The Fe-Fe bonding in this cluster is discussed, and the origin of the unsymmetrical structure is also explored, shedding some light on the cluster's assembly pathway. In the second case, a series of clusters of the type $[\{(dppe)Fe\}_2(Pn_2)_2]^{2-}$ (dppe = 1,2-Bis(diphenylphosphino)ethane; Pn = P, As, Bi) is analysed. These three clusters adopt similar geometries but exhibit increasing Fe-Fe bond lengths from P to Bi as the bridging element. Both DFT and MC-SCF were applied to understand the similarities and differences on the Fe-Fe bonds, and comparison with related $[(LFe)_2(Pn_4)]$ is presented to explain the difference in the electronic configuration behind the different bridging Pn_4 isomers.

4.2 $[Fe_3As_{13}]^{3-}$ with an unsymmetrical Fe_3 core

In this section, we discuss an iron/arsenic binary cluster as $[Fe_3As_{13}]^{3-}$, in which three iron atoms are arranged in a triangular core, each coordinated by an As_3 fragment. An As_4 chain surrounds the Fe_3 unit and, together with Fe3, constructs a $FeAs_4$ pentagonal ring. All experimental synthesis and characterisation were carried out by Prof. Zhong-Ming Sun's group, including structures determined from XRD (shown in Figure 4.4). In the theoretical work, we aim to elucidate the metal-metal bonding in the Fe_3 core and understand the distorted geometry by introducing a transition state. This work has been published in *Angewandte Chemie International Edition* 2023, **62**, e202217316.

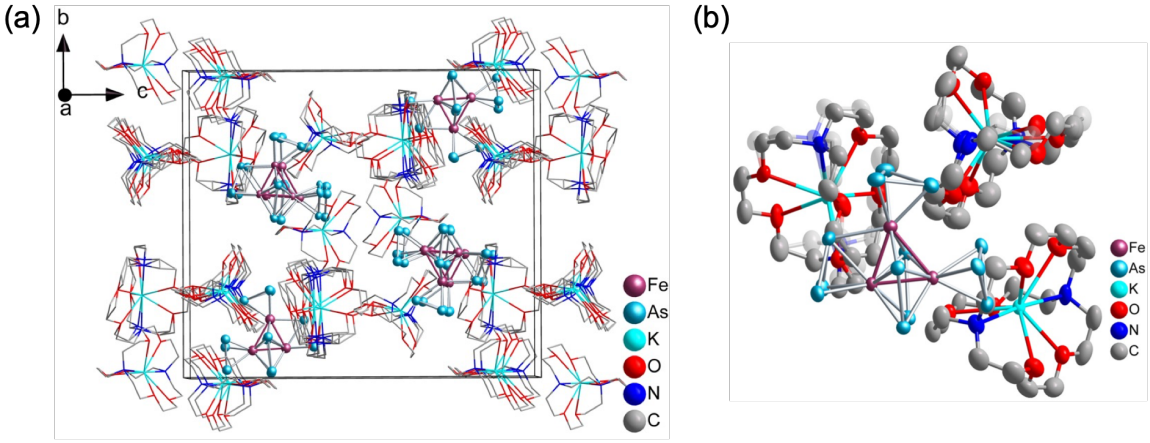

Figure 4.4: (a) Unit cell of $[K(2.2.2\text{-crypt})]_3[Fe_3As_{13}]$ and (b) its asymmetric unit with the cluster fragment. X-ray crystallography was performed by Dr. Wei-Qiang Zhang in Prof. Zhong-Ming Sun's group. (Reproduced from our published work as Ref. 4)

4.2.1 Introduction

As mentioned in the introduction, arsenic is isolobal to the CH fragment, allowing its frameworks to adopt skeletal structures analogous to those of isoelectronic organic molecules. The geometry of the arsenic skeleton can be divided into two categories as planar (Figure 4.5 (a)) and prismatic (Figure 4.5 (b)). Investigations of clusters containing planar As_n began with the sandwich compound $[Cp^*Fe(As_5)]$, which can be regarded as an analogue of ferrocene.[222] This cluster can serve as precursors for synthesising its binary and other large and complex clusters through reduction by potassium and its hydride, as $[(Cp^*Fe)_2(As_{10})]$, $[(Cp^*Fe)_2(As_{14})]$ and $[(Cp^*Fe)_4(As_{18})]$.[260]

The As-based four-membered ring and its derivatives were also investigated, as a pathway to activate yellow arsenic. Scheer and co-workers reported such a pair of isomers as $[(Cp'''Fe)_2(As_4)]$.[261] The Fe-Fe distance decreases from 3.502 Å to 2.693 Å upon ring opening of the As_4 fragment from the *cyclo*-As_4 to *catena*-As_4. DFT calculations also identified two local minima in agreement with the isomer pair, with the energy difference of only 0.18 eV. The electron redistribution from Fe to As_4 also exhibits the flexibility of charge states in the Fe/As clusters. Another example is $[(L^3Fe)_2(As_4)]$ also reported by Scheer's group.[246] The Fe-Fe bond length exhibits as 3.787 Å in the presence of a *cyclo*-As_4 and 2.940(5) Å with a dumbbell $(As_2)_2$ fragment. The other category of iron-arsenic clusters comprises a trigonal prismatic As_6 skeleton structure (a prismane). Early DFT investigations verified that the prismane-like As_6 is the most stable structures over other isomers.[262] Recently, two analogues with the same electron count as $[(Cp^*Fe)_3(As_6)]$ and $[(Cp''Fe)_3(As_6)]$ were synthesised again by Scheer.[263,264] Each iron atom is coordinated by an aromatic ligand, located above the square side faces of the trigonal prism. The Fe-Fe distances are averaged to 3.789 Å in $[(Cp''Fe)_3(As_6)]$ due to the strong repulsion between the aromatic ligands, where the As-As bonds in the trigonal prism largely retain in the bonding range below 2.90 Å. However, one Fe-Fe bond in $[(Cp^*Fe)_3(As_6)]$ becomes apparently shorter than the other two bonds, as 3.2504(4) Å vs. 3.5012(4) Å. Its cation $[(Cp^*Fe)_3(As_6)]^+$ was also synthesised by removing the $FeCp^*$ fragment from $[(Cp^*Fe\{(\eta^3\text{-}As_3)Fe\}(As_6)]$.[265] This cation also possesses uneven Fe-Fe bond lengths. The Fe_3As_6 core in these clusters shows a structure similar to the MSA and TTP $[Sn_9]^{4-}$. A common point among all clusters mentioned above is that the Fe atoms are always coordinated by an aromatic ring. The only exception is $[(Cp^*Fe)_3\{(\eta^3\text{-}As_3)Fe\}(As_6)]$, in which one of the iron atoms is coordinated by As_3. In $[Fe_3As_{13}]^{3-}$, all Fe atoms are coordinated by an As_3 fragment, as a final destination to pure inorganic clusters.

4.2.2 Computational details

All computational work on $[Fe_3As_{13}]^{3-}$ was performed by ADF 2021.104.[69] PBE[47] and M06-L[53,54] functionals were applied. Triple-zeta all-electron basis sets were used with two polarisation functions.[164] The grid was tuned to 'verygood' in numerical integration quality setting.[193] All geometries were optimised to stationary points. Scalar-ZORA was used to incorporate relativistic effects.[163] The COSMO was included with the dielectric constant of 78.39 to provide a confined space for optimising the anion.[165]

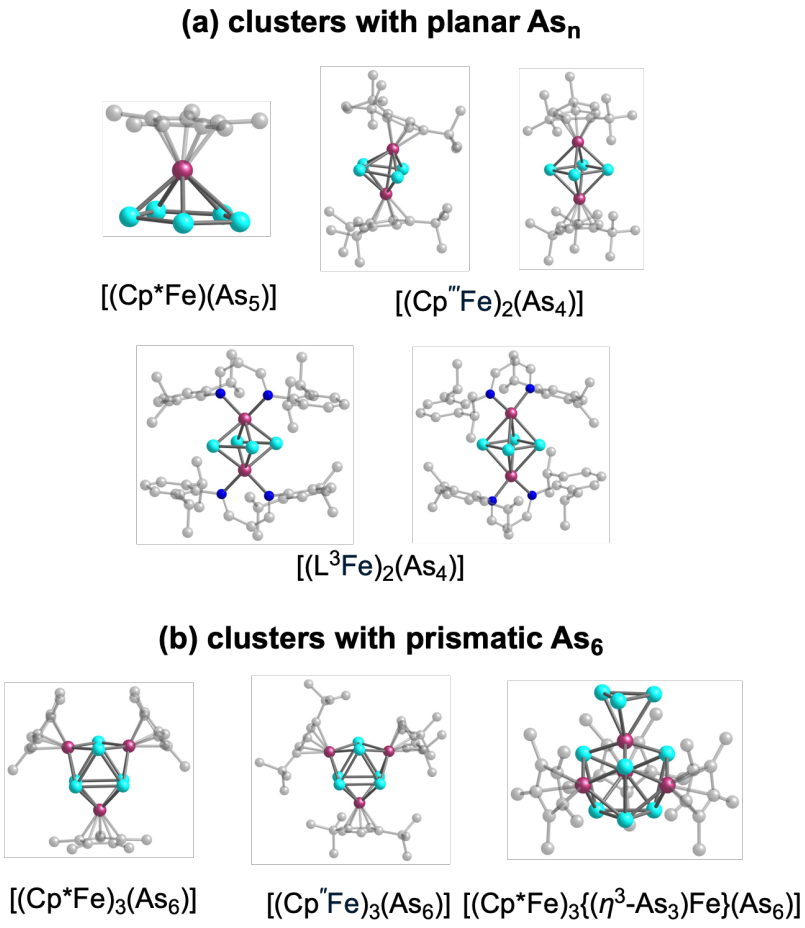

Figure 4.5: Representative iron-arsenic clusters, including (a) a planar As_n fragment and (b) a trigonal prismatic As_6 fragment.

4.2.3 Electronic structure analysis

Because each As_3 fragment is bound to Fe with considerable rotational freedom, the local minimum exploration was conducted by rotating the As_3 fragments. During this process, three spin-triplet stationary points are denoted as T1, T2 and T3, as shown in Figure 4.6. T1 and T2 were examined as local minima by the absence of any imaginary frequency. The two local minima differ only in the orientation of the As_3 connected to Fe3 without perturbing the structure of Fe_3 too much. In T1, the Fe-Fe bond lengths are 2.66 Å for Fe1-Fe3, 2.44 Å for Fe1-Fe2 and 2.46 Å for Fe2-Fe3, and in T2, the Fe1-Fe3 bond length becomes 2.70 Å, as well as 2.43 Å for Fe1-Fe2 and 2.55 Å for Fe2-Fe3. DFT calculations manifest that the energy difference between the two local minima is within 0.01 eV by both PBE and M06-L functionals, where the PBE prefers T1 while M06-L prefers T2. The functional sensitivity as well as negligible energy difference does not allow an unambiguous ground state assignment between

two close-lying isomers. These results indicate that this cluster possesses a very flat potential energy surface due to the loosely bound As_3. The XRD data also exhibit a slight disorder between T1 and T2. In this section, T1 will be discussed primarily, and the results of the PBE functional will be our reference for further investigations.

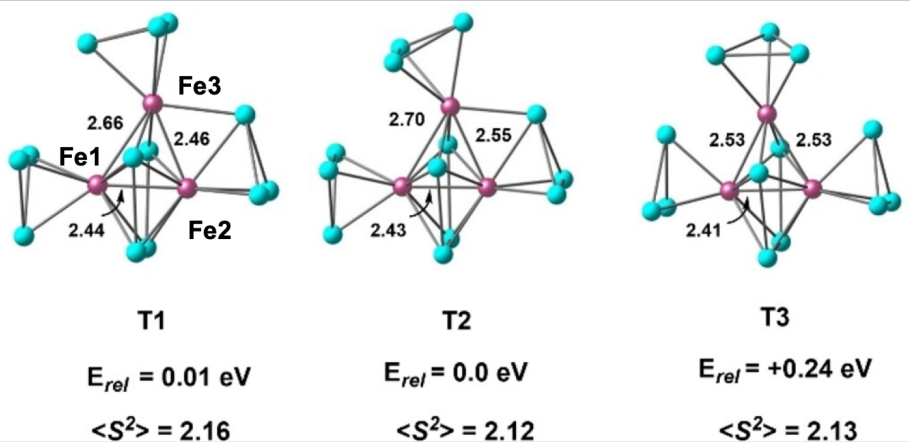

Figure 4.6: Stationary points T1, T2 and T3, on the triplet potential energy surface of $[Fe_3As_{13}]^{3-}$.

An important characteristic of this cluster is the distorted Fe_3 triangle core, where the unequal Fe-Fe bond lengths motivate an investigation into the origin of the distortion. In our survey on the potential energy surface, a structure with isosceles Fe_3, denoted T3, was constructed. It possesses C_s symmetry, and the mirror plane is perpendicular to the Fe_3 triangular plane crossing the Fe3 atom. All Fe-Fe distances are within the bonding range, as 2.53 Å for the isosceles Fe-Fe bonds, and 2.41 Å for the Fe1-Fe2 bond. The structure is optimised to a stationary point 0.24 eV above a local minimum as T2, with one imaginary frequency of $i120\ cm^{-1}$. Perturbing along the imaginary frequency mode, we can reach a local minimum as T1. Therefore, T3 can be regarded as a transition state connecting two mirror-related T1 minima.

The electronic structure change along this pathway needs to be further clarified by an in-depth orbital analysis on both T1 and T3. For the transition state T3, the spin eigenvalue is 2.13. Mulliken spin density analysis manifests that the unpaired electrons concentrate on Fe3, with spin density of +1.88. Fe1 and Fe2 only carry +0.30 spin density. The minority spin PDOS of Fe 3*d* and OPDOS of three Fe-Fe bonds shown in Figure 4.7 can be applied to explain the bonding properties of Fe-Fe bonds as well as the distribution of orbitals with dominant Fe 3*d* character. The Mulliken charge distribution analysis assigns two positive charges to the Fe_3

fragments, leaving 20 electrons distributed among 3×5 $3d$ orbitals. For the Fe1-Fe2 bond shown as black dotted lines in OPDOS, two low-lying Fe1-Fe2 π bonding orbitals can be identified at -3.6 eV. However, the π bonding contributions are offset by their corresponding antibonding orbitals located close to the Fermi level. Its σ bonding orbital can be found at -1.3 eV, while the σ^* remains vacant as LUMO+2 at 0.9 eV, creating a net σ interaction between Fe1 and Fe2. As for the two equivalent bonds as Fe1-Fe3 and Fe2-Fe3, their OPDOS are shown as red dash-dotted line and green dotted line, respectively. The two OPDOS curves overlap with each other due to symmetry. An obvious character is that the overlap integral between Fe3 and Fe1/Fe2 is smaller than Fe1-Fe2. The bonding interactions between Fe3 and the two other iron are generated mainly by the bonding orbital at -3.3 eV. The two unpaired electrons are mostly distributed over the d_{xy} and d_{z^2} orbitals of Fe3 as shown in the isosurface plots of LUMO and LUMO+1, consistent with the spin density analysis. Therefore, T3 can be regarded as a closed-shell Fe_2As_{10} capped with a triplet $FeAs_3$. From T3 to T1, the spin density now not only locates on Fe3, but also generates +0.92 on Fe2. There is still negligible spin density detected on Fe1. We again look into the PDOS and OPDOS plots of T1. The OPDOS shape of the Fe1-Fe2 bond in T1 is mostly identical to T3. The Fe1-Fe2 π bonding and antibonding pairs remain in the occupied levels, and the positions of σ/σ^* bands are at -1.3 eV and +1.0 eV, respectively, keeping a net σ interaction along the Fe1-Fe2 bond. The corresponding bond distance also has little change, as 2.41 Å in T3 and 2.44 Å in T1. However, the bond lengths have drastically changed for Fe1-Fe3 and Fe2-Fe3. This is due to the polarisation of the σ interactions to the Fe2-Fe3 bond. The HOMO originally in T3 now becomes a σ bonding orbital localised on the Fe2-Fe3 bond in T1 at -0.9 eV. The corresponding antibonding orbital is generated on the LUMO at +0.8 eV. The bond order of Fe2-Fe3 increases from 0.47 to 0.55 after the distortion. Therefore, the structure of $[Fe_3As_{13}]^{3-}$ can be regarded as a diamagnetic Fe_2As_{10} capped with a triplet $FeAs_3$, creating a first-order geometry as T3, and further distorts to T1 through the orbital interactions between HOMO and LUMO.

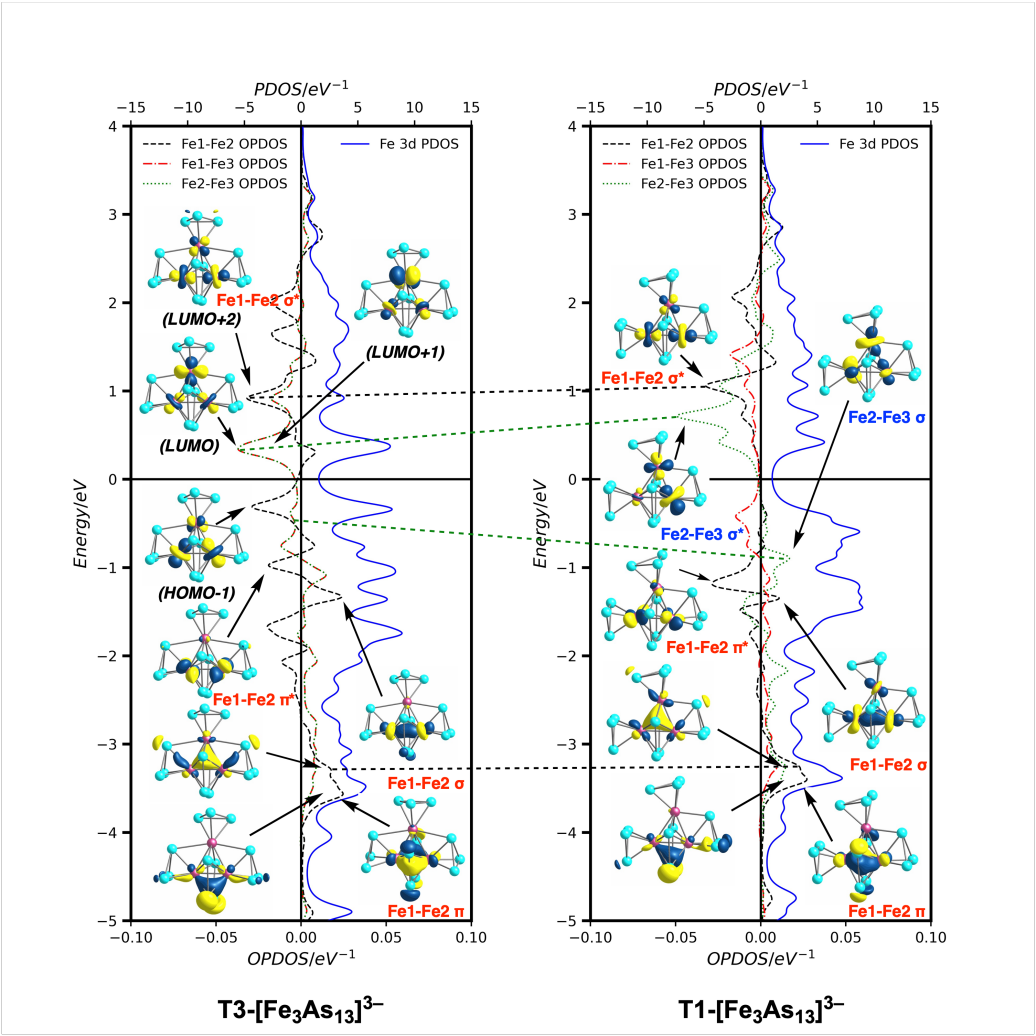

Figure 4.7: OPDOS for the three Fe-Fe bonds, Fe1-Fe2 (black), Fe1-Fe3 (red) and Fe2-Fe3 (green). T3 is shown on the left and T1 on the right. Positive values of the OPDOS indicate that states are making a net bonding contribution to the particular bond, while negative values indicate a net antibonding interaction. Plots are shown for the transition structure (left) and the equilibrium structure (right). Kohn-Sham orbitals that contribute to the most significant peaks in the OPDOS plots are also shown. All plots are for the spin-β eigenstates.

4.2.4 Conclusion

In this section, we introduced an iron-arsenic binary cluster $[Fe_3As_{13}]^{3-}$ with an unsymmetrical iron triangle, where the Fe-Fe bond lengths are 2.66 Å, 2.44 Å and 2.46 Å. DFT calculations confirm two local minima, T1 and T2, separated by a small energy difference below 0.02 eV. The geometries of the two isomers can be distinguished by the orientation of the capping $FeAs_3$. The unsymmetrical Fe_3 core can be understood by considering the higher-symmetry transition state T3. A second-order Jahn-Teller

distortion generates a σ bond on Fe2-Fe3, leading to unequal bond lengths for Fe1-Fe3 and Fe2-Fe3. The cluster can be elucidated as a diamagnetic Fe_2As_{10} fragment capped by a triplet $FeAs_3$ fragment, following a second-order Jahn-Teller distortion.

4.3 Electronic structures of the Fe_2Pn_4 (Pn = P, As, Bi) core in $[\{(dppe)Fe\}_2(Pn_2)_2]^{2-}$

In this section, I focus on an aspect of the structural chemistry of the pnictide ligands that is closely related to that discussed in the context of $[Fe_3As_{13}]^{3-}$. The motivation for this work comes from a series of iron complexes with general formula $[\{(dppe)Fe\}_2Pn_4]^{2-}$ (Pn = P, As and Bi) that have been synthesised by Prof. Zhong-Ming Sun and co-workers. The last of these is the first bismuth cluster of this type. The work is as yet unpublished.

4.3.1 Introduction

The structure of the central Fe_2Pn_4 unit is the focus of attention here, because the Fe-Fe bond length elongates from 2.574 Å for Pn = P to 2.820 Å for Pn = Bi. The Pn_4 unit is split into two separate 'dumbbell' units, with the closest separation between the atoms (of phosphorus) being more than 3.2 Å. There is, therefore, a direct comparison to Scheer's $[(L^3Fe)_2(As_4)]$ cluster (shown in Figure 4.8 (b)),[246] which has been isolated in two distinct forms. In one isomer, the As_4 unit is split into two distinct As_2 dumbbell units, and the Fe-Fe bond length is 2.940(5) Å. In the other isomer, the Fe-Fe bond length is 3.787 Å and the As_4 ligand is in the *cyclo*-As_4 form. The structural chemistry also resembles that for the $[(CpFe)_2(As_4)]$ cluster discussed in the previous section,[261] except that in the isomer with the short Fe-Fe bond length (2.6927(6) Å), the E_4 unit splits into two E_2 dimers rather than a butadienyl-like E_4.

The clusters described here are part of a wider family with bridging ligands of various sizes from Pn_3, Pn_4, Pn_5, Pn_8, Pn_{11}, Pn_{14} as summarised in reviews.[266–269] Among these, the Pn_4 members exhibit great structural flexibility, as was emphasised in the previous section in the specific context of As_4. The dumbbell-type motif was first reported in $[\{Cp(CO)Mo\}_2(P_2)_2]$ by Scherer,[231] but a number of related examples quickly followed, including $[(Cp^*M)_2(P_2)_2]$ (M = Fe, Co)[233] (left in Figure 4.8 (a)). The dumbbell-like $(P_2)_2$ architecture is typically associated with short M-M distances, as in $[(L^{Dipp}Co)_2(P_2)_2]$, $[(L^{Dipp}Fe)_2(P_2)_2]$ and its anion. In the latter case, one-electron reduction elongates the Fe-Fe bond from 2.777 Å to 2.871 Å (middle in Figure 4.8 (a)).[240] The *cyclo*-P_4 is also well established, and is found in different isomers noted in the introduction to this chapter including $[(LCo)_2(P_4)]$,[239] $[(L^3Fe)_2(P_4)]$ (right in Figure 4.8 (a)),[245] $[\{(BIAN)Co\}_2(P_4)]^{2-}$ (BIAN=1,2-bis(2,6-diisopropylphenylimino)acenaphthene)[270] and $[\{(P_2N_2)Zr\}_2(P_4)]$ (P_2N_2=

$PhP(CH_2SiMe_2NSiMe_2CH_2)_2PPh$).[271] White phosphorus can also be slightly activated to a non-planar P_4 moiety with late transition metals such as Ni and Cu in $[(Cp^{iPr4}Ni)_2(E_4)]$ (E = P, As),[272] $[(L^3Cu)_2(E_4)]$ (E = P, As).[237] Whilst there are many examples of P_4 and As_4 clusters, the synthesis of heavier analogues containing Sb and Bi has been less well explored, and $[Sb_4\{Mo(CO)_3\}_2]^{4-}$ is the only antimony example so far.[273] A Bi_4 butterfly structure bridging two Ga centres has been reported,[274] but planar bismuth-bridged dinuclear transition metal complexes are unknown. The $(Bi_2)_2$ dumbbell reported here in the (dppe)Fe is the first example of its kind.

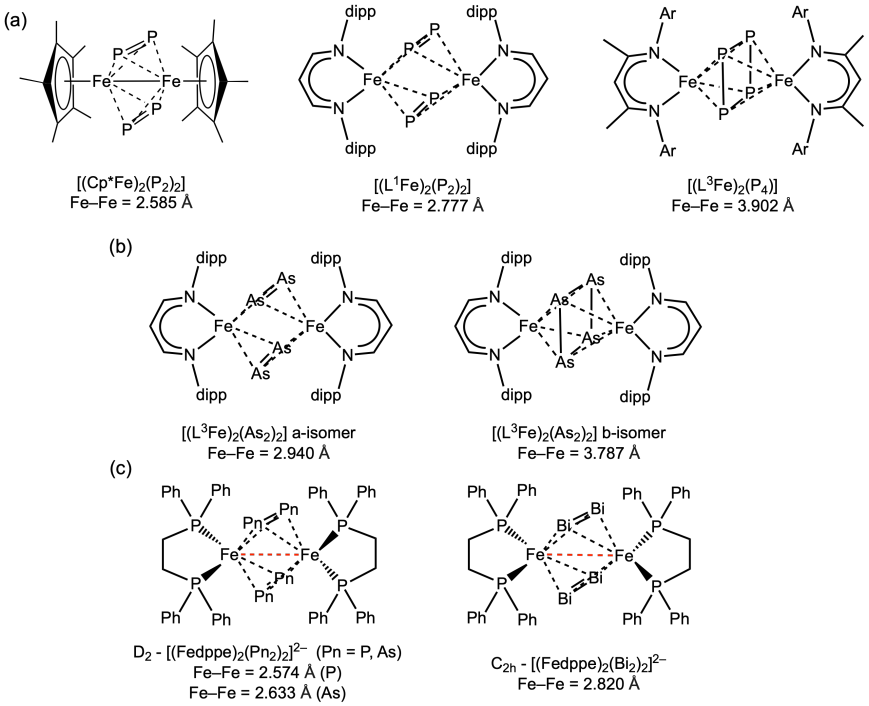

Figure 4.8: Schematic plots of representative $[(LFe)_2(Pn_4)]$ (Pn = P, As, Bi) complexes.

4.3.2 Computational details

The computational details of the DFT calculations follow precisely on the calculations on $[Fe_3As_{13}]^{3-}$, except the dielectric constant set to 100.0 in COSMO. The results from the PBE functional were chosen for further analysis. Restricted Active Space Self-Consistent Field (RASSCF) calculations were performed with OpenMolcas using pymolcas v2.01.[275] ANO-RCC basis sets were used at the level of double-zeta plus one polarisation function. Cholesky decomposition was applied to accelerate the two-electron integral calculations, where the threshold is 10^{-6}. The RASSCF convergence

criteria were set as 10^{-8} for energy, 10^{-4} for orbital rotation matrix, and 10^{-4} for the energy gradient.

4.3.3 Electronic structure analysis

4.3.3.1 DFT analysis

The XRD analysis of the three clusters indicates that although they are isostructural, their precise symmetries are slightly different, as shown in Figure 4.9. The phosphorus- and arsenic-containing species have D_2 symmetry while the bismuth analogue is C_{2h}-symmetric. The structural differences between the anions are, however, small, and the low-symmetry distortion in the bismuth case is probably a consequence of structural correlations induced by the packing cations. Specifically, the $[K(18\text{-crown-}6)]^+$ cation stabilises the D_2-symmetric structures of $[\{(dppe)Fe\}_2(P_2)_2]^{2-}$ and
$[\{(dppe)Fe\}_2(As_2)_2]^{2-}$, whereas the use of $[K(2.2.2\text{-crypt})]^+$ in $[\{(dppe)Fe\}_2(Bi_2)_2]^{2-}$ favours the C_{2h} symmetry. To probe this structural preference, geometry optimisations were performed using the PBE functional for all three clusters. The results confirm that both symmetry-adapted structures are local minima on the singlet potential energy surface, as indicated by the absence of imaginary frequencies. While the D_2-symmetric structure is slightly lower in energy in all cases, the energy differences are marginal, less than 0.1 eV in each case. These findings highlight the role of cation-mediated packing effects in small distortions. As in other parts of this thesis, we use a high-dielectric continuum solvent to mimic the effects of the crystalline environment, but this inevitably fails to replicate subtle cation-anion contacts.

Table 4.1: Selected bond lengths of the $[(LM)_2(Pn)_4]$ clusters.

		M1-M2	M1-Pn1	M1-Pn2	Pn1-Pn2	Pn1-Pn2′	Ref
$[\{(dppe)Fe\}_2(P_2)_2]^{2-}$	X-ray	2.5742(9)	2.2903(14)	2.3583(13)	2.0851(1)	3.265	This
	DFT	2.55	2.27	2.35	2.10	3.24	work
$[\{(dppe)Fe\}_2(As_2)_2]^{2-}$	X-ray	2.6331(18)	2.3922(15)	2.5000(16)	2.3119(13)	3.416	
	DFT	2.62	2.38	2.48	2.34	3.37	
$[\{(dppe)Fe\}_2(Bi_2)_2]^{2-}$	X-ray	2.8202(13)	2.7354(7)	2.7282(7)	2.8189(3)	3.738	
	DFT	2.81	2.74	2.72	2.86	3.69	
Cs_2P_4	X-ray	-	-	-	2.146(1)	2.1484(9)	[276]
	DFT	-	-	-	2.16	2.16	
$[(L^3Fe)_2(P_4)]$	X-ray	3.902	2.4376(6)	2.5064(6)	2.178(1)	2.207(1)	[245]
	DFT	3.70	2.42	2.43	2.19	2.24	
$[\{(P_2N_2)Zr\}_2(P_4)]$	X-ray	4.441	2.7202(10)	2.7355(10)	2.2407(13)	2.2407(13)	[271]
	DFT	4.50	2.77	2.74	2.25	2.25	

The energy difference between the D_2 and C_{2h} symmetric structures is negligible in all three clusters, so the D_2 structure is adopted for subsequent analyses. The cleaved Pn_4 fragment contains two short Pn-Pn bonds, each within the typical range of double

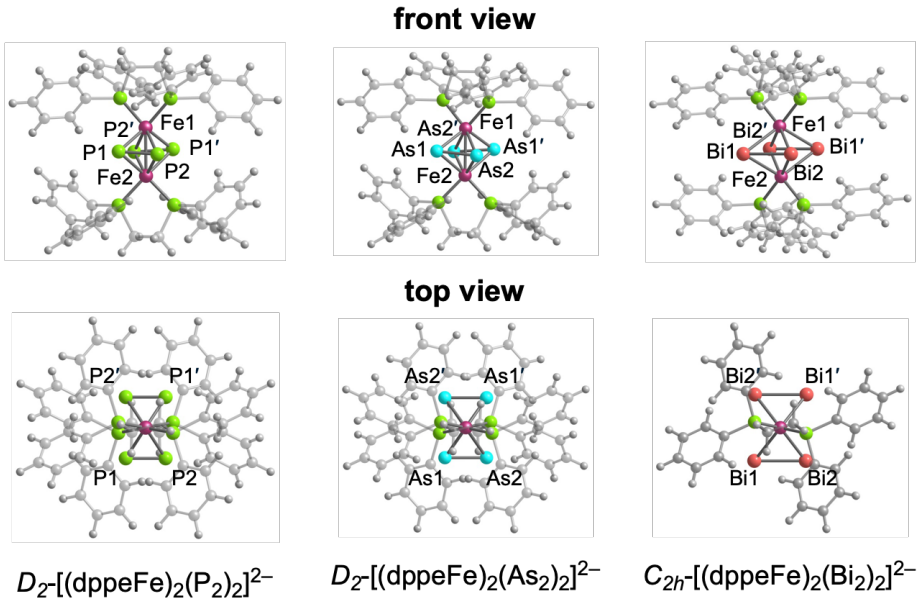

Figure 4.9: Front and top views of $[\{(\text{dppe})\text{Fe}\}_2(\text{Pn}_2)_2]^{2-}$ (Pn = P, As, Bi).

bonds. Based on the octet rule, the Pn_4 fragment can be considered to carry a -4 charge and, as the dppe ligands are neutral, the oxidation state of each iron centre is assigned as $+1$. The Fe-Fe bond distances increase systematically with the heavier bridging pnictogen ligands: from 2.5742(9) Å in $[\{(\text{dppe})\text{Fe}\}_2(\text{P}_2)_2]^{2-}$, to 2.6331(18) Å in $[\{(\text{dppe})\text{Fe}\}_2(\text{As}_2)_2]^{2-}$, and finally to 2.8202(13) Å in $[\{(\text{dppe})\text{Fe}\}_2(\text{Bi}_2)_2]^{2-}$. To gain deeper insight into the electronic configurations of these three clusters, we have examined the isosurface plots of Fe-dominated molecular orbitals, as well as the PDOS on Fe $3d$ and Pn np orbitals and the OPDOS for the Fe-Fe bond, as shown in Figure 4.10.

The PDOS and OPDOS reveal that Fe-Fe interactions are qualitatively consistent across all three complexes. Using $[\{(\text{dppe})\text{Fe}\}_2(\text{P}_2)_2]^{2-}$ as a representative example, the Fe-Fe σ bonding band is located at approximately -2.0 eV as $40a$, while the corresponding σ^* antibonding orbital appears above the Fermi level at around $+0.6$ eV as $40b_1$. This supports the presence of a σ bonding interaction between the Fe centres. Orbitals with π character are oriented either in the dppe-Fe-Fe-dppe plane (Fe $3d_{xz}$) or perpendicular to it (Fe $3d_{yz}$) (the xy-plane is perpendicular to the Fe-Fe bond). The out-of-plane π orbital (π_{op}), $39b_3$, is located at -0.7 eV and its antibonding π^*_{op} counterpart, $38b_2$, is at -1.3 eV. Both are in the occupied manifold, resulting in no net π_{op} bonding. In the orthogonal orientation, the π_{ip} and π^*_{ip} orbitals derived from the Fe $3d_{xz}$ orbitals are strongly mixed with the P $3p$ orbitals of the dppe ligands, forming molecular orbitals $43b_2$ and $44b_3$, respectively. Both orbitals lie above

the Fermi level and therefore do not contribute to the Fe-Fe bonding interaction. We conclude, therefore, that there is a single Fe-Fe σ bond linking the two metals.

Similar electronic features are apparent in the arsenic and bismuth analogues, and the Fe-Fe Mayer bond orders are almost constant at ∼0.54 across the series. The increase in Fe-Fe bond length is therefore primarily driven by the larger atomic radius of the pnictogen atoms, which results in steric expansion and elongation of the Fe-Fe distance, rather than any substantial change in the nature of the Fe-Fe bond. However, the Fe 3*d* band does become slightly more compressed as the Fe-Fe distance increases from P_4 to Bi_4: the vacant Fe-Fe σ^* orbital shifts down in energy to +0.5 eV in $[\{(\text{dppe})\text{Fe}\}_2(\text{Bi}_2)_2]^{2-}$, while the occupied σ bonding orbital shifts up to −1.6 eV. The variations in the σ/σ^* gap, whilst small, suggest the potential for increased multi-configurational character in the Bi system, which we now explore using MC-SCF calculations.

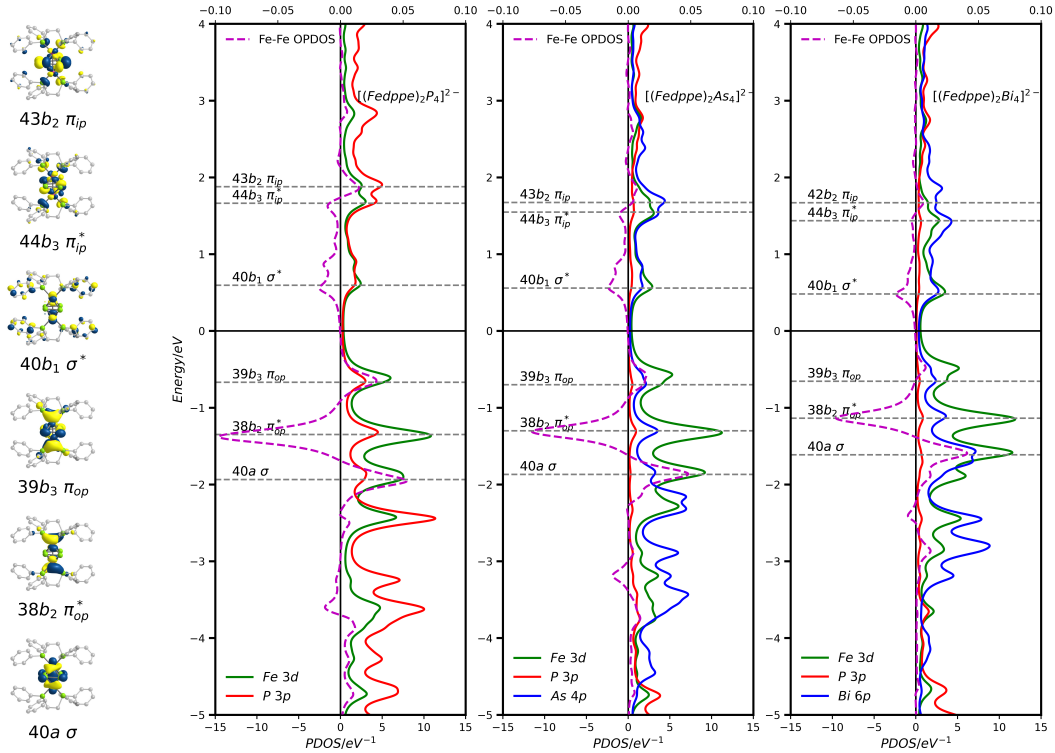

Figure 4.10: PDOS on Fe 3*d*, P 3*p*, and Pn *np* orbitals, along with the OPDOS for the Fe-Fe bond in $[\{(\text{dppe})\text{Fe}\}_2(\text{Pn}_2)_2]^{2-}$ (Pn = P, As, Bi). The isosurface plots of Fe-Fe σ and π bonding orbitals are shown on the left, with their corresponding bands marked by grey horizontal lines in the PDOS plots.

4.3.3.2 MC-SCF analysis

Given the relatively modest size of these spin-singlet systems, with only two active metal centres, we have chosen to perform direct RASSCF, rather than DMRG, calculations to investigate their detailed electronic structures. While the three systems exhibit broadly similar bonding motifs, the discrepancies in Fe-Fe bond lengths may reflect underlying configurational differences. The natural orbitals and their occupation numbers are shown in Figure 4.11. Based on their crystallographic structures, the D_2 and C_{2h} point groups were employed for the phosphorus/arsenic and bismuth systems, respectively. The active space included all Fe $3d$ orbitals along with their correlating partners, amounting to 18 electrons in 18 orbitals (18e, 18o). In the RASSCF protocol, orbitals with strong correlation (as measured by occupation numbers between 0.1 and 1.9) are assigned to RAS2, and all possible excitations within these orbitals are included in the CI expansion. Orbitals with occupation numbers greater than 1.9 were assigned to RAS1, and those below 0.1 to RAS3. Only one- and two-electron excitations are allowed from RAS1 into RAS2, and from RAS2 into RAS3. In this way, the number of configurations is kept to a manageable level. The active orbitals can be divided into two subgroups: one involving correlation with the dppe and Pn_4 fragments, evident in in-phase and out-of-phase combinations of Fe d_{xy} and d_{yz} orbitals; while the other reflects the metal-metal correlation. The occupied orbitals of d_{yz} have occupation numbers above 1.94, while the associated correlating orbitals located on dppe fall below 0.06, indicating limited electron excitation into these orbitals. The Fe d_{xy} orbital is correlated with orbitals on the Pn_4 moiety, especially a π^*_{op} orbital formed from p_z for the out-of-phase combination and a σ^* orbital from p_x in b_1 symmetry for the in-phase combination. These orbitals display slightly stronger correlation than the dppe-related orbitals, with occupation numbers around 1.90 (occupied) and 0.10 (virtual), respectively. As previously discussed, electron donation from the dppe ligands to Fe d_{xz} orbitals results in Fe $3d$-dominated unoccupied orbitals in b_2 and b_3 symmetry, further supporting the assignment of Fe in the +1 oxidation state. The Fe $3d_{x^2-y^2}$ orbitals, however, correlate with their $4d$ counterparts in RAS1 and RAS3, through the 'double-d-shell' effect. Their occupation numbers are 1.97/0.03. The strongest correlation is also observed between the two Fe centres through the σ/σ^* orbital pair, the occupation numbers of which deviate substantially from the values of 2 and 0 for single-determinant methods. This reflects a significant contribution from the $\sigma^0\sigma^{*2}$ configuration to the multi-configurational wavefunction. On replacing the bridging P_4 ligand with As_4, the bonding orbital occupation decreases from 1.69 to 1.64 as the weight of the $\sigma^2\sigma^{*0}$ CSF drops from

68.0% to 65.3%, while the weight of the doubly excited $\sigma^0\sigma^{*2}$ configuration rises from 9.4% to 11.1%. Upon further substitution of the bridging element with Bi, the symmetry changes to C_{2h}, but the general orbital and correlation characteristics of the active space remain largely conserved. The weak 'in-out' correlation between Fe and dppe persists, while Fe-Pn_4 correlation becomes slightly stronger. The most notable change lies in the 'left-right' correlation between Fe atoms. Although still dominated by the σ/σ^* pair, the weight of the $\sigma^2\sigma^{*0}$ configuration is reduced to 59.1%, while the contribution from the $\sigma^0\sigma^{*2}$ configuration increases to 15.6%. The occupation number of the bonding orbital therefore drops to 1.48 and the antibonding one rises to 0.52, indicating stronger correlation than in the P and As analogues. As a result of these rather subtle changes, the effective Fe-Fe bond orders derived from the RASSCF calculations decrease along the series from 0.68 for P_4 to 0.64 for As_4 and 0.46 for Bi_4, in line with the observed trend of Fe-Fe bond elongation. The effective bond orders arising from RASSCF calculations appear, therefore, to be more sensitive to structural change than are the Mayer bond orders from DFT calculations.

4.3.3.3 Comparison to $[(LFe)_2(Pn_4)]$

We have noted in previous sections that the P_4 moiety can adopt various isomeric forms when acting as a bridging ligand in dinuclear complexes, one of which is the dumbbell-like $(P_2)_2$ form present in the new clusters described here. However, several examples of isomerism are known, where the P_4 or As_4 units adopt quite different geometries. In this section, we explore how the electronic configuration of P_4 evolves in response to changes in structure. A convenient reference point for this discussion is the $[P_4]^{2-}$ ring, which has an aromatic electron count characterised by six π electrons, and has uniform P-P bond lengths. This six-π-electron aromatic P_4 fragment has been observed both as an isolated anion in Cs_2P_4 and also as a bridging ligand in the dinuclear complex $[(L^3Fe)_2(P_4)]$. The electronic structure of *cyclo*-$[P_4]^{2-}$ is shown at the left end of Figure 4.12. The orbital energies of all structures were normalised with respect to the midpoint between the HOMO and LUMO energies. For spin-unrestricted calculations, the spin-β manifold was selected as the reference zero point. Frontier orbitals that are localised primarily on the P_4 fragment and are relevant to the geometry changes are highlighted with black lines and green arrows. The HOMO of ${P_4}^{2-}$, $1e_g$, is a pair of degenerate out-of-plane π orbitals (denoted as π_{op}) localised on opposite sides of the square P_4 ring. The LUMO, $1b_{1u}$, corresponds to the fully π^*_{op} orbital, composed of an out-of-phase combination of four p_z orbitals. The fully bonding, in-phase combination of p_z orbitals, not shown in the diagram, completes

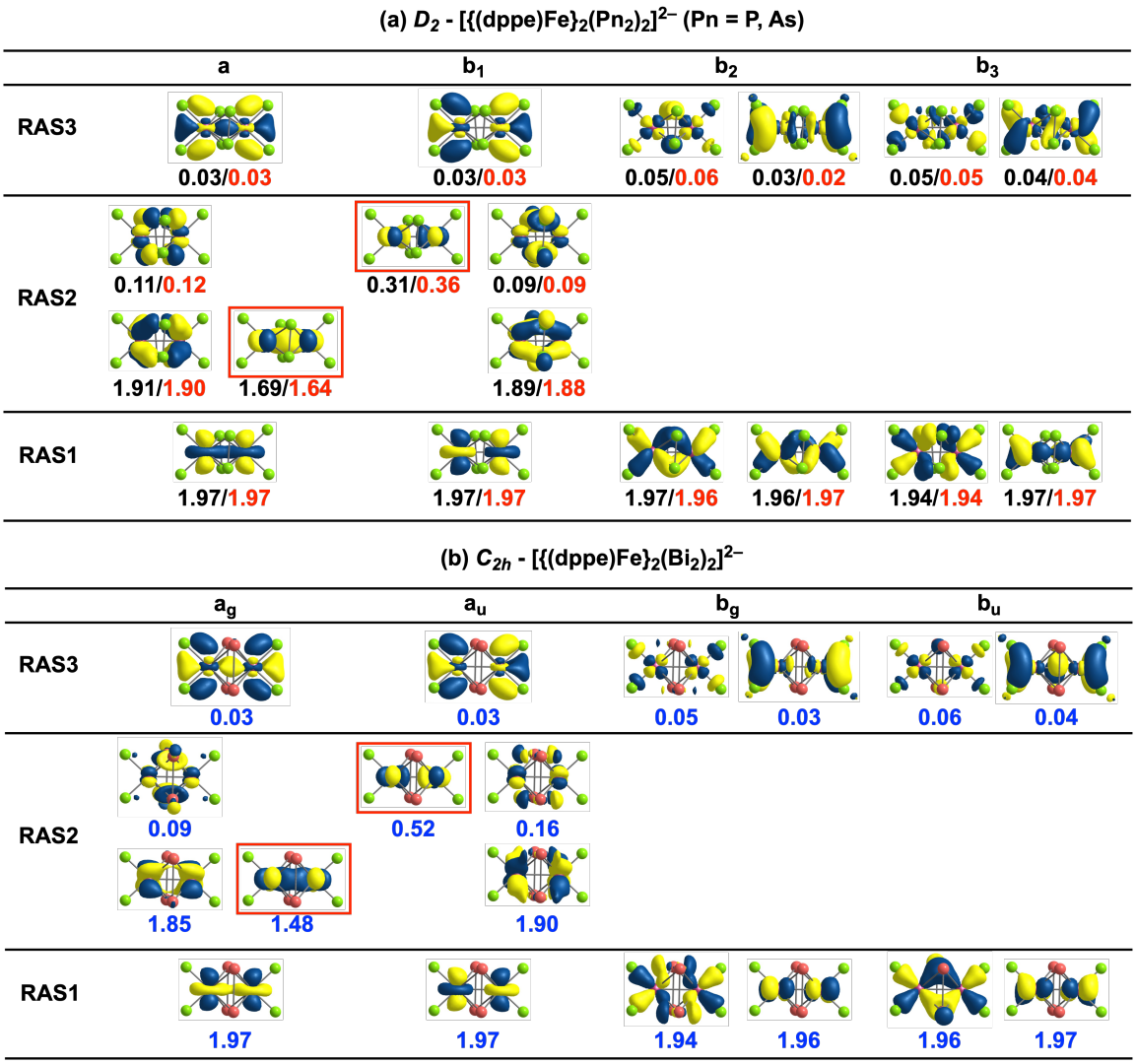

Figure 4.11: Isosurfaces and occupation numbers of the active orbitals from RASSCF calculations on (a) D_2-$[\{(dppe)Fe\}_2(Pn_2)_2]^{2-}$ (Pn = P (ONs in black), As (ONs in red)) and (b) C_{2h}-$[\{(dppe)Fe\}_2(Bi_2)_2]^{2-}$ (ONs in blue).

the aromatic π_{op} electron count of 6. Only 0.4 eV above the LUMO is a degenerate pair of orbitals, $3e_u$, with mixed P-P σ^* and π character.

In clusters where the charge state on the Pn_4 unit is -4, two-electron further reduced than $P_4{}^{2-}$, the structural characteristics are determined by which orbital the extra electrons occupy. In $[\{(P_2N_2)Zr\}_2(P_4)]$, the charge on the P_4 unit is unambiguously -4 (the P_2N_2 ligand carries a -2 charge, each Zr is $+4$) and the additional pair of electrons occupies the π^* orbital locates at $94a$ shown in the second column of Figure 4.12. The P_4 unit therefore remains approximately square, with P-P bond lengths of 2.25 Å, considerably longer than those in Cs_2P_4.

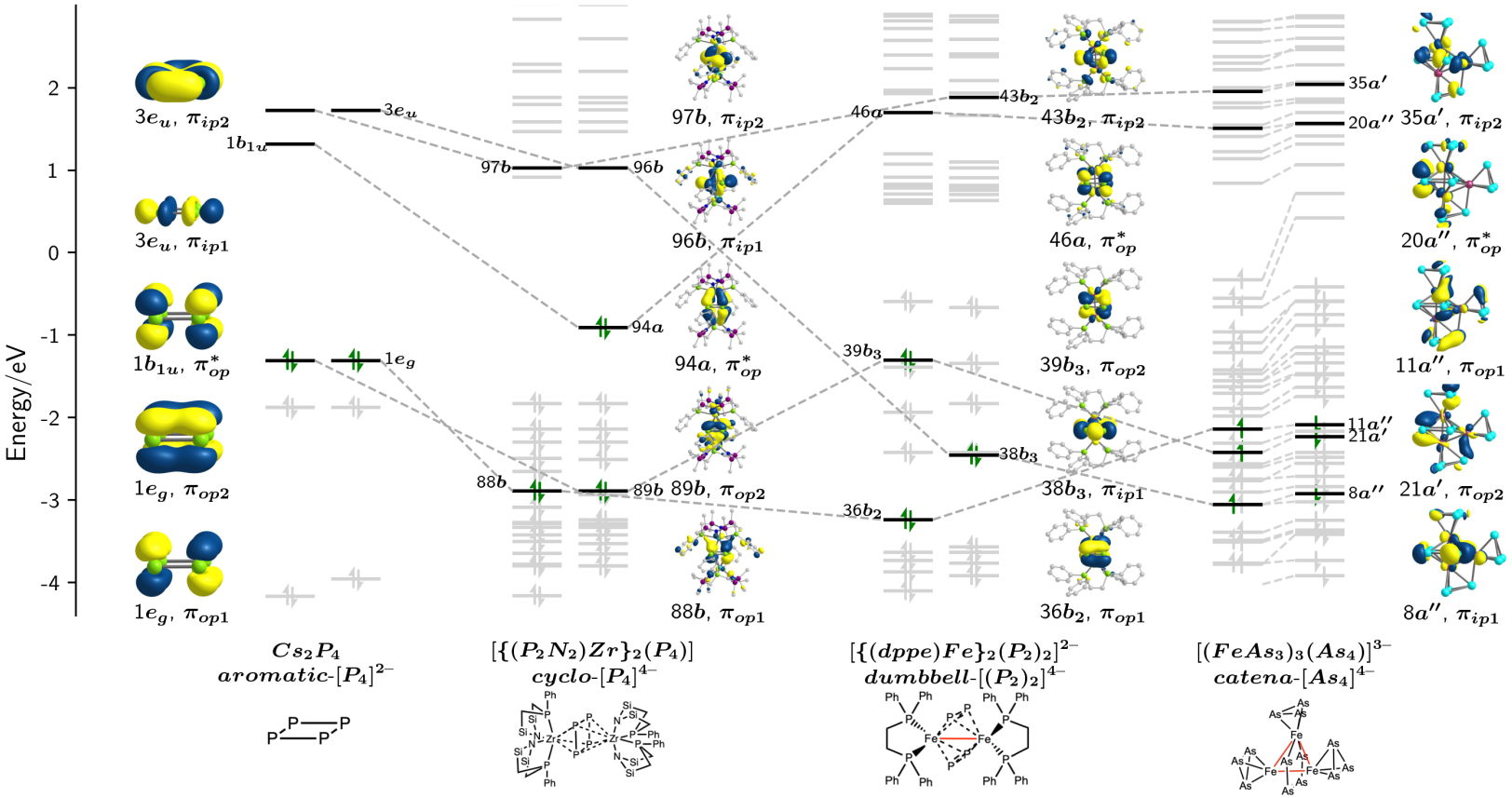

Figure 4.12: Frontier molecular orbitals of representative complexes containing the isomers of the Pn_4 moiety. Geometry change related orbitals are highlighted with black lines and green arrows, and are connected across clusters to illustrate the transformation pathways. The geometry evolution includes a transition from aromatic $[P_4]^{2-}$ in Cs_2P_4 to *cyclo*-$P_4{}^{4-}$ in $[(\{P_2N_2\}Zr)_2(P_4)]$, then to $[(P_2)_2]^{4-}$ dumbbell in $[\{(dppe)Fe\}_2(P_2)_2]^{2-}$, and finally reaches a 'U-shaped' $[As_4]^{4-}$ in $[Fe_3As_{13}]^{3-}$.

The correlation of orbitals is also traced from Cs_2P_4 to $[\{(dppe)Fe\}_2(P_2)_2]^{2-}$ in Figure 4.12. The picture here is rather different, because it is not the P-P π^* orbital that is filled, but rather one of the components of the $3e_u$ LUMO+1 of Cs_2P_4. The occupation of one component of the degenerate pair drives a first-order Jahn-Teller distortion, leading to the dumbbell structure with P-P distances of 2.10 Å and 3.24 Å. The effect of the distortion is to stabilise the occupied component, $38b_3$, and destabilise the vacant one ($43b_2$). The P-P π^* orbital, $46a$, remains unoccupied. It is significant that the $45b_1$ orbital, with P_2-P_2 σ^* character, remains vacant (not labelled in the figure). This means that there is residual P-P σ bonding character (a formal bond order of 1.0) between the two P_2 fragments, which are not, therefore, entirely separated despite the separation of 3.24 Å. Likewise, three of the four π symmetry orbitals are occupied, so there is a net π bond order of 1, distributed over the two P_2 units. It is not, therefore, correct to view these as entirely separated $(P{=}P)^{2-}$ units.

What is it, then, that makes the Zr complex favour the *cyclo* form whereas the $[\{(dppe)Fe\}_2(P_2)_2]^{2-}$ complex adopts the dumbbell geometry, given that the two arrangements of the P_4 unit are isoelectronic. The Kohn-Sham orbitals of the latter show that the P-P π^*_{op} orbital, $46a$, has significant Fe d character: it is engaged in π-back-bonding, which destabilises it. This then favours the P-P σ^* $3e_u$ orbital to accommodate additional electrons, as this can be done without compromising the back-bonding. In complexes of Zr^{4+}, there are no d electrons to participate in back-bonding, so the P-P π^*_{op} orbital is more readily available to accommodate the additional electrons, preserving the *cyclo* structure.

A further comparison can be made with $[Fe_3As_{13}]^{3-}$ at the right end of Figure 4.12, which features a 'U-shaped' As_4 ring. In this As_4 fragment, the two outer As-As bonds are at 2.65 Å, whereas the central As-As bond measures at 2.43 Å in the double-bond range. This bonding arrangement suggests an As1-As2=As3-As4 motif. According to the octet rule, each terminal arsenic atom (As1 and As4) carries a -2 charge and arsenic atoms in the middle retain neutral, leading to a charge assignment of $[As_4]^{4-}$. The reduced symmetry of the ring can be understood from a second-order Jahn-Teller distortion from the dumbbell prototype. Specifically, the mixing between π^*_{op} and π_{op1} results in enhancement of the π^*_{op} component onto As2-As3 bond, locating above the Fermi level as $20a''$. Meanwhile, the out-of-phase combination of p_z orbitals on As1 and As4 stays occupied at $11a''$, as a counterpart of $20a''$. On the other hand, the low-lying out-of-plane π orbital mixes with the π_{op2} orbital, and creates a π_{op} bonding orbital along As2-As3 on $21a'$, leading to a second bond order on As2-As3 bond except for the σ bond. In contrast, the π_{ip1} bonding orbital interacts with the

unoccupied π^*_{ip1} orbital and shows significant localisation on As1 and As4 in $8a''$, rather than contributing to in-plane π bonding on As1-As2 and As3-As4 bonds in the dumbbell.

4.3.4 Conclusion

In conclusion, we have introduced here a series of dinuclear complexes of the type $[\{(\text{dppe})\text{Fe}\}_2(\text{Pn}_2)_2]^{2-}$ (Pn = P, As, Bi), where the Pn_4 unit is split into two Pn_2 dumbbells. The Bi_4-bridged species is the first of its type to be reported. The Fe-Fe bond length increases systematically from approximately 2.57 Å to 2.82 Å as the bridging pnictogen changes from P to As and then to Bi. DFT calculations reveal that an Fe-Fe σ bond persists across the entire series, with a constant Mayer bond order of 0.54, despite the 0.25 Å increase in bond length. RASSCF calculations, in contrast, indicate that the EBO of the Fe-Fe bond decreases progressively from P_4 to Bi_4, as a result of a small reduction in the contribution of the $\sigma^2\sigma^{*0}$ CSF to the total wavefunction. This trend is attributed to the increasing steric repulsion associated with the larger atomic radii of heavier pnictogens, which leads to elongation of the Fe-Fe bond.

The geometry of the ${\text{P}_4}^{4-}$ unit, split into two P_2 dumbbells, is a common motif in bimetallic complexes, but it contrasts with the structure of ${\text{P}_4}^{4-}$ in the Zr complex $[(\{\text{P}_2\text{N}_2\}\text{Zr})_2(\text{P}_4)]$. The different structural chemistry arises from the energetic proximity of P-P π^*_{op} and σ^* orbitals, and the possibility that either can accommodate the highest-lying electrons. In the $[(\{\text{P}_2\text{N}_2\}\text{Zr})_2(\text{P}_4)]$ case, the highest-energy electrons occupy the P-P π^*_{op} orbital, leading to an expansion of the ring compared to Cs_2P_4. In $[\{(\text{dppe})\text{Fe}\}_2(\text{Pn}_2)_2]^{2-}$, in contrast, the electrons occupy one component of the degenerate P-P σ^* LUMO+1 of Cs_2P_4, and a first-order Jahn-Teller instability then drives the distortion to the dumbbell structure. A further second-order distortion from the $[(\text{Pn}_2)_2]^{4-}$ dumbbell to the 'U-shaped' $[\text{As}_4]^{4-}$ in $[\text{Fe}_3\text{As}_{13}]^{3-}$ produces another π_{op} bond on As2-As3. The in-plane double bond collapses with the polarisation of π_{ip} to As1 and As4. This closes up the relationship between $[\{(\text{dppe})\text{Fe}\}_2(\text{Pn}_2)_2]^{2-}$ and $[\text{Fe}_3\text{As}_{13}]^{3-}$ in this chapter.

4.4 Summary

In this chapter, we investigate two classes of Fe/Pn-based clusters that feature low-valent Fe cores using DFT and RASSCF calculations. The metal-metal interactions and the structural correlation between the Fe_n units and Pn_n ligands have been analysed using DOS and frontier orbital analysis. Although apparently rather different, the $[Fe_3As_{13}]^{3-}$ and $[\{(dppe)Fe\}_2(Pn_2)_2]^{2-}$ (Pn = P, As, Bi) systems share many features. This becomes most apparent if we view the $[Fe_3As_{13}]^{3-}$ cluster as an Fe_2As_{10} dimer unit, capped by an additional $FeAs_3$ fragment. The Fe_2As_{10} contains two Fe centres bridged by an As_4 unit, and in that sense is very similar to the $[\{(dppe)Fe\}_2(As_2)_2]^{2-}$ cluster described in the second section. Furthermore, our analysis shows that the oxidation level of the two As_4 fragments is the same: -4 in both clusters, and the dumbbell and 'U-shaped' geometries can both be considered as resonance structures of ${As_4}^{4-}$. Indeed, the similarity even extends to the σ and π bond orders: in both cases, the net π bond order, summed over all bonds, is one, while the net σ bond order is 3. Despite the rather different geometries, the As_4 units in $[Fe_3As_{13}]^{3-}$ and $[\{(dppe)Fe\}_2(As_2)_2]^{2-}$ share many common features, and differ only in the subtle distribution of electrons among the same set of orbitals, understood in terms of a second-order Jahn-Teller distortion.

Chapter 5

Summary

This thesis explores the electronic structure of intermetallic Zintl clusters containing transition metal ions coordinated by main-group element ligands, either as encapsulating shells or as direct bonding partners. Specifically, I focus on systems with two or more metal atoms, where open-shell character is the norm and metal-metal bonding emerges in various forms. Much of the fundamental work was carried out with dinuclear models, before I extend to more complex systems such as the linear tri-metallic $[Fe_3Sn_{18}]^{4-}$, triangular $[Fe_3As_{13}]^{3-}$, and rhombic $[Fe_4Sn_{18}]^{4-}$ clusters. DFT is used throughout the thesis and, when combined with techniques such as PDOS, OPDOS, and frontier molecular orbital analysis, this combination proves to be a powerful tool set for assessing the character and strength of the metal-metal bond. Across the systems studied here, the presence of a high-lying and vacant or partially occupied σ^* antibonding orbital is a common factor, and so net σ bonding underpins the integrity of all clusters. In some cases, including M_2E_{12} and $[\{(dppe)Fe\}_2(P_2)_2]^{2-}$, where multiconfigurational character is significant, I have also turned to MC-SCF methods for a complementary perspective on electron correlation. In the case of $[Fe_4Sn_{18}]^{4-}$, where a precise identification of the ground state is the goal, I have used the DMRG approach to access large active spaces, along with the MC-PDFT approach to capture dynamic correlation. These post-HF methods confirm the importance of including Fe $4d$ orbitals in the active space to capture sufficient static and nondynamic correlation effects in the active space and achieve an accurate ground-state description.

A second theme that runs through the thesis is a focus on the correlations between electron count and geometry. The field is rich in structural detail, and identifying links between apparently unrelated molecules is perhaps one of the most important roles for a computational chemist. In many cases, isostructural systems with closed-shell electron counts (d^{10} configurations at the metals) are available (typically with

the late transition metals), and these provide a valuable reference point for their open-shell counterparts. The structure of the ligand cage depends heavily on the valence properties of the transition metal d orbitals, particularly for early transition metals where the d orbitals are high in energy and relatively diffuse. Across the series of clusters explored here, it seems that the transition from active to inert, in a structural sense, occurs around Groups 6 and 7.

The triple-decker M_2E_{12} clusters that form the first results section capture most of the important themes in this thesis: back-bonding increases for the earlier transition metals (Fe, Cr), culminating in a symmetry reduction from D_{4h} to C_{4v} in $[Cr_2Sb_{12}]^{3-}$ that is associated directly with the transfer of two electrons from the metal to the cage. The picture that emerges from DMRG calculations allows us to quantify the effects of so-called 'in-out' correlation (metal-to-ligand back-donation) and 'left-right' correlation between the metals. The first logical increase in complexity is then the $[Fe_3Sn_{18}]^{4-}$ cluster, where the metal chain remains linear. The presence of Fe-Fe bonding here is essential for maintaining the D_{3d} symmetry, preventing collapse to a bent structure with a localised *exo*-bond, as seen in isoelectronic $[AgSn_{18}]^{5-}$. In coordinated clusters, such as $[Fe_3As_{13}]^{3-}$ and $[\{(dppe)Fe\}_2(P_2)_2]^{2-}$, the electron distribution governs the geometry, and first- and second-order Jahn-Teller distortions provide a powerful framework for understanding structure. A deeper understanding of the electron density distribution in the bridging Pn_4 units in these two quite distinct clusters highlights the fact that they share much in common, most notably the oxidation level ($[Pn_4]^{4-}$) and the net σ and π bond orders. In fact, they differ only in the distribution of the frontier orbitals over the Pn_4 framework.

In summary, this thesis extends the theoretical understanding of Zintl chemistry to open-shell species with multiple transition metal centres by applying a range of electronic structure methods, from EHT, through DFT, to post-HF approaches, to study electronic structures, bonding interactions, and geometric distortions in these intermetallic clusters. The findings not only enhance our comprehension of bonding and structure in Zintl systems but also provide a valuable computational reference for future studies, including those targeting magnetic properties and machine-learning-based structural prediction in main-group cluster chemistry.

References

[1] Y.-N. Yang, Z.-S. Li, S. Mondal, L. Qiao, C.-C. Wang, W.-J. Tian, Z.-M. Sun and J. E. McGrady, *Chinese Chemical Letters*, 2024, **35**, 109048.

[2] Z.-S. Li, W.-X. Chen, H. W. T. Morgan, C.-C. Shu, J. E. McGrady and Z.-M. Sun, *Chemical Science*, 2024, **15**, 1018–1026.

[3] W.-X. Chen, Z.-S. Li, H. W. T. Morgan, C.-C. Shu, Z.-M. Sun and J. E. McGrady, *Chemical Science*, 2024, **15**, 4981–4988.

[4] W.-Q. Zhang, Z.-S. Li, J. E. McGrady and Z.-M. Sun, *Angewandte Chemie International Edition*, 2023, **62**, e202217316.

[5] F. A. Cotton and C. B. Harris, *Inorganic Chemistry*, 1965, **4**, 330–333.

[6] T. Nguyen, A. D. Sutton, M. Brynda, J. C. Fettinger, G. J. Long and P. P. Power, *Science*, 2005, **310**, 844–847.

[7] A. Joannis, *Comptes Rendus Hebdomadaires des Séances de l'Académie des Sciences*, 1891, **113**, 795.

[8] C. A. Kraus, *Journal of the American Chemical Society*, 1907, **29**, 1557–1571.

[9] E. Zintl, J. Goubeau and W. Dullenkopf, *Zeitschrift für Physikalische Chemie, Abteilung A*, 1931, **154**, 1–46.

[10] J. E. McGrady, F. Weigend and S. Dehnen, *Chemical Society Reviews*, 2022, **51**, 628–649.

[11] R. J. Wilson, B. Weinert and S. Dehnen, *Dalton Transactions*, 2018, **47**, 14861–14869.

[12] K. Wade, *Journal of the Chemical Society D: Chemical Communications*, 1971, 792–793.

[13] D. M. P. Mingos, *Nature: Physical Science*, 1972, **236**, 99–102.

[14] K. Wade, in *K. Wade*, ed. H. Emeléus and A. Sharpe, Academic Press, 1976, vol. 18 of Advances in Inorganic Chemistry and Radiochemistry, pp. 1–66.

[15] W. N. Lipscomb, *Science*, 1977, **196**, 1047–1055.

[16] B. Zhou, T. Krämer, A. L. Thompson, J. E. McGrady and J. M. Goicoechea, *Inorganic Chemistry*, 2011, **50**, 8028–8037.

[17] T. Krämer, J. C. A. Duckworth, M. D. Ingram, B. Zhou, J. E. McGrady and J. M. Goicoechea, *Dalton Transactions*, 2013, **42**, 12120–12129.

[18] B. Zhou, M. S. Denning, D. L. Kays and J. M. Goicoechea, *Journal of the American Chemical Society*, 2009, **131**, 2802–2803.

[19] G. Espinoza-Quintero, J. C. A. Duckworth, W. K. Myers, J. E. McGrady and J. M. Goicoechea, *Journal of the American Chemical Society*, 2014, **136**, 1210–1213.

[20] H. W. T. Morgan, K.-S. Csizi, Y.-S. Huang, Z.-M. Sun and J. E. McGrady, *The Journal of Physical Chemistry A*, 2021, **125**, 4578–4588.

[21] K. Andersson, P. Malmqvist and B. O. Roos, *The Journal of Chemical Physics*, 1992, **96**, 1218–1226.

[22] C. Angeli, R. Cimiraglia, S. Evangelisti, T. Leininger and J.-P. Malrieu, *The Journal of Chemical Physics*, 2001, **114**, 10252–10264.

[23] G. Li Manni, R. K. Carlson, S. Luo, D. Ma, J. Olsen, D. G. Truhlar and L. Gagliardi, *Journal of Chemical Theory and Computation*, 2014, **10**, 3669–3680.

[24] R. K. Carlson, D. G. Truhlar and L. Gagliardi, *Journal of Chemical Theory and Computation*, 2015, **11**, 4077–4085.

[25] J. P. Foster and F. Weinhold, *Journal of the American Chemical Society*, 1980, **102**, 7211–7218.

[26] A. E. Reed, L. A. Curtiss and F. Weinhold, *Chemical Reviews*, 1988, **88**, 899–926.

[27] D. Y. Zubarev and A. I. Boldyrev, *Physical Chemistry Chemical Physics*, 2008, **10**, 5207–5217.

[28] J.-X. Zhang, F. K. Sheong and Z. Lin, *Chemistry – A European Journal*, 2018, **24**, 9639–9650.

[29] J.-X. Zhang, F. K. Sheong and Z. Lin, *WIREs Computational Molecular Science*, 2020, **10**, e1469.

[30] M. P. Mitoraj, A. Michalak and T. Ziegler, *Journal of Chemical Theory and Computation*, 2009, **5**, 962–975.

[31] A. Michalak, M. Mitoraj and T. Ziegler, *The Journal of Physical Chemistry A*, 2008, **112**, 1933–1939.

[32] K. Wiberg, *Tetrahedron*, 1968, **24**, 1083–1096.

[33] I. Mayer, *Chemical Physics Letters*, 1983, **97**, 270–274.

[34] R. F. W. Bader, *Chemical Reviews*, 1991, **91**, 893–928.

[35] A. Savin, O. Jepsen, J. Flad, O. K. Andersen, H. Preuss and H. G. von Schnering, *Angewandte Chemie International Edition*, 1992, **31**, 187–188.

[36] D. R. Hartree, *Mathematical Proceedings of the Cambridge Philosophical Society*, 1928, **24**, 89–110.

[37] V. Fock, *Zeitschrift für Physik*, 1930, **61**, 126–148.

[38] C. C. J. Roothaan, *Reviews of Modern Physics*, 1951, **23**, 69–89.

[39] G. G. Hall and J. E. Lennard-Jones, *Proceedings of the Royal Society of London. Series A. Mathematical and Physical Sciences*, 1951, **205**, 541–552.

[40] R. Hoffmann, *The Journal of Chemical Physics*, 1963, **39**, 1397–1412.

[41] L. H. Thomas, *Mathematical Proceedings of the Cambridge Philosophical Society*, 1927, **23**, 542–548.

[42] E. Fermi, *Rendiconti: Accademia Nazionale dei Lincei*, 1927, **6**, 32.

[43] P. Hohenberg and W. Kohn, *Physical Review*, 1964, **136**, B864–B871.

[44] W. Kohn and L. J. Sham, *Physical Review*, 1965, **140**, A1133–A1138.

[45] R. Stowasser and R. Hoffmann, *Journal of the American Chemical Society*, 1999, **121**, 3414–3420.

[46] S. H. Vosko, L. Wilk and M. Nusair, *Canadian Journal of Physics*, 1980, **58**, 1200–1211.

[47] J. P. Perdew, K. Burke and M. Ernzerhof, *Physical Review Letters*, 1996, **77**, 3865–3868.

[48] A. D. Becke, *Physical Review A*, 1988, **38**, 3098–3100.

[49] J. P. Perdew, *Physical Review B*, 1986, **33**, 8822–8824.

[50] J. P. Perdew and Y. Wang, *Physical Review B*, 1992, **46**, 12947–12954.

[51] C. Lee, W. Yang and R. G. Parr, *Physical Review B*, 1988, **37**, 785–789.

[52] J. Tao, J. P. Perdew, V. N. Staroverov and G. E. Scuseria, *Physical Review Letters*, 2003, **91**, 146401.

[53] Y. Zhao and D. G. Truhlar, *The Journal of Chemical Physics*, 2006, **125**, 194101.

[54] Y. Zhao and D. G. Truhlar, *Theoretical Chemistry Accounts*, 2008, **120**, 215–241.

[55] P. J. Stephens, F. J. Devlin, C. F. Chabalowski and M. J. Frisch, *The Journal of Physical Chemistry*, 1994, **98**, 11623–11627.

[56] J. P. Perdew, M. Ernzerhof and K. Burke, *The Journal of Chemical Physics*, 1996, **105**, 9982–9985.

[57] C. Adamo and V. Barone, *The Journal of Chemical Physics*, 1999, **110**, 6158–6170.

[58] B. O. Roos, P. R. Taylor and P. E. Sigbahn, *Chemical Physics*, 1980, **48**, 157–173.

[59] C. Møller and M. S. Plesset, *Physical Review*, 1934, **46**, 618–622.

[60] P. A. Malmqvist, A. Rendell and B. O. Roos, *The Journal of Physical Chemistry*, 1990, **94**, 5477–5482.

[61] D. Ma, G. Li Manni and L. Gagliardi, *The Journal of Chemical Physics*, 2011, **135**, 044128.

[62] S. R. White, *Physical Review Letters*, 1992, **69**, 2863–2866.

[63] S. R. White, *Physical Review B*, 1993, **48**, 10345–10356.

[64] S. Östlund and S. Rommer, *Physical Review Letters*, 1995, **75**, 3537–3540.

[65] S. Rommer and S. Östlund, *Physical Review B*, 1997, **55**, 2164–2181.

[66] J. C. Slater, *Physical Review*, 1930, **36**, 57–64.

[67] S. F. Boys and A. C. Egerton, *Proceedings of the Royal Society of London. Series A. Mathematical and Physical Sciences*, 1950, **200**, 542–554.

[68] W. J. Hehre, R. F. Stewart and J. A. Pople, *The Journal of Chemical Physics*, 1969, **51**, 2657–2664.

[69] G. te Velde, F. M. Bickelhaupt, E. J. Baerends, C. Fonseca Guerra, S. J. A. van Gisbergen, J. G. Snijders and T. Ziegler, *Journal of Computational Chemistry*, 2001, **22**, 931–967.

[70] J. Zhao, Q. Du, S. Zhou and V. Kumar, *Chemical Reviews*, 2020, **120**, 9021–9163.

[71] J. Heath, S. O'brien, Q. Zhang, Y. Liu, R. Curl, F. Tittel and R. Smalley, *Journal of the American Chemical Society*, 1985, **107**, 7779–7780.

[72] A. A. Popov, S. Yang and L. Dunsch, *Chemical Reviews*, 2013, **113**, 5989–6113.

[73] S. Yang, T. Wei and F. Jin, *Chemical Society Reviews*, 2017, **46**, 5005–5058.

[74] Z. Slanina, S.-L. Lee, L. Adamowicz, F. Uhlík and S. Nagase, *International Journal of Quantum Chemistry*, 2005, **104**, 272–277.

[75] M. M. Olmstead, A. de Bettencourt-Dias, S. Stevenson, H. C. Dorn and A. L. Balch, *Journal of the American Chemical Society*, 2002, **124**, 4172–4173.

[76] M. Krause and L. Dunsch, *ChemPhysChem*, 2004, **5**, 1445–1449.

[77] D. E. Bergeron, A. W. Castleman, T. Morisato and S. N. Khanna, *Science*, 2004, **304**, 84–87.

[78] H. Tsunoyama, H. Akatsuka, M. Shibuta, T. Iwasa, Y. Mizuhata, N. Tokitoh and A. Nakajima, *The Journal of Physical Chemistry C*, 2017, **121**, 20507–20516.

[79] V. T. Ngan, E. Janssens, P. Claes, J. T. Lyon, A. Fielicke, M. T. Nguyen and P. Lievens, *Chemistry – A European Journal*, 2012, **18**, 15788–15793.

[80] B. Molina, J. R. Soto and J. J. Castro, *The Journal of Physical Chemistry C*, 2012, **116**, 9290–9299.

[81] X. G. Gong and V. Kumar, *Physical Review Letters*, 1993, **70**, 2078–2081.

[82] V. Kumar, in *Nanosilicon*, ed. V. Kumar, Elsevier, Amsterdam, 2008, pp. 114–148.

[83] E. N. Esenturk, J. Fettinger and B. Eichhorn, *Chemical Communications*, 2005, 247–249.

[84] C. Liu, I. A. Popov, L.-J. Li, N. Li, A. I. Boldyrev and Z.-M. Sun, *Chemistry – A European Journal*, 2018, **24**, 699–705.

[85] C. Liu, X. Jin, L.-J. Li, J. Xu, J. E. McGrady and Z.-M. Sun, *Chemical Science*, 2019, **10**, 4394–4401.

[86] C. Shu, H. Morgan, L. Qiao, J. McGrady and Z. Sun, *Nature Communications*, 2020, **11**, 3477.

[87] M. J. Moses, J. C. Fettinger and B. W. Eichhorn, *Science*, 2003, **300**, 778–780.

[88] S. Stegmaier and T. F. Fässler, *Journal of the American Chemical Society*, 2011, **133**, 19758–19768.

[89] Y.-H. Xu, W.-J. Tian, A. Muñoz-Castro, G. Frenking and Z.-M. Sun, *Science*, 2023, **382**, 840–843.

[90] L.-F. Cui, X. Huang, L.-M. Wang, J. Li and L.-S. Wang, *The Journal of Physical Chemistry A*, 2006, **110**, 10169–10172.

[91] A. Spiekermann, S. D. Hoffmann and T. F. Fässler, *Angewandte Chemie International Edition*, 2006, **45**, 3459–3462.

[92] E. N. Esenturk, J. Fettinger and B. Eichhorn, *Journal of the American Chemical Society*, 2006, **128**, 9178–9186.

[93] A.-M. Li, Y. Wang, D. O. Downing, F. Chen, P. Zavalij, A. Muñoz-Castro and B. W. Eichhorn, *Chemistry – A European Journal*, 2020, **26**, 5824–5833.

[94] J.-Q. Wang, S. Stegmaier, B. Wahl and T. Fässler, *Chemistry – A European Journal*, 2010, **16**, 1793–1798.

[95] B. J. L. Witzel, W. Klein, J. V. Dums, M. Boyko and T. F. Fässler, *Angewandte Chemie International Edition*, 2019, **58**, 12908–12913.

[96] M. M. Gillett-Kunnath, J. I. Paik, S. M. Jensen, J. D. Taylor and S. C. Sevov, *Inorganic Chemistry*, 2011, **50**, 11695–11701.

[97] S. Scharfe, T. Fässler, S. Stegmaier, S. Hoffmann and K. Ruhland, *Chemistry – A European Journal*, 2008, **14**, 4479–4483.

[98] V. Hlukhyy, S. Stegmaier, L. vanWüllen and T. F. Fässler, *Chemistry – A European Journal*, 2014, **20**, 12157–12164.

[99] E. N. Esenturk, J. C. Fettinger and B. W. Eichhorn, *Journal of the American Chemical Society*, 2006, **128**, 12–13.

[100] B. Kesanli, J. E. Halsig, P. Zavalij, J. C. Fettinger, Y.-F. Lam and B. W. Eichhorn, *Journal of the American Chemical Society*, 2007, **129**, 4567–4574.

[101] V. Hlukhyy, H. He, L.-A. Jantke and T. F. Fässler, *Chemistry – A European Journal*, 2012, **18**, 12000–12007.

[102] Y.-N. Yang, L. Qiao and Z.-M. Sun, *Chinese Chemical Letters*, 2023, **34**, 107207.

[103] H.-L. Xu, L. Qiao and Z.-M. Sun, *Chinese Journal of Chemistry*, 2023, **41**, 2432–2438.

[104] L.-J. Li, F.-X. Pan, F.-Y. Li, Z.-F. Chen and Z.-M. Sun, *Inorganic Chemistry Frontiers*, 2017, **4**, 1393–1396.

[105] M. F. Groh, U. Müller, A. Isaeva and M. Ruck, *Zeitschrift für anorganische und allgemeine Chemie*, 2019, **645**, 161–169.

[106] R. J. Wilson, F. Hastreiter, K. Reiter, P. Büschelberger, R. Wolf, R. M. Gschwind, F. Weigend and S. Dehnen, *Angewandte Chemie International Edition*, 2018, **57**, 15359–15363.

[107] F. Lips and S. Dehnen, *Angewandte Chemie International Edition*, 2011, **50**, 955–959.

[108] R. Ababei, J. Heine, M. Hołyńska, G. Thiele, B. Weinert, X. Xie, F. Weigend and S. Dehnen, *Chemical Communications*, 2012, **48**, 11295–11297.

[109] L. Qiao, C. Zhang, C.-C. Shu, H. W. T. Morgan, J. E. McGrady and Z.-M. Sun, *Journal of the American Chemical Society*, 2020, **142**, 13288–13293.

[110] J. M. Goicoechea and S. C. Sevov, *Journal of the American Chemical Society*, 2005, **127**, 7676–7677.

[111] Z.-M. Sun, H. Xiao, J. Li and L.-S. Wang, *Journal of the American Chemical Society*, 2007, **129**, 9560–9561.

[112] J. M. Goicoechea and S. C. Sevov, *Angewandte Chemie International Edition*, 2005, **44**, 4026–4028.

[113] H. W. T. Morgan, C.-C. Shu, Z.-M. Sun and J. E. McGrady, *Journal of the American Chemical Society*, 2022, **144**, 8007–8017.

[114] M. Bühl and A. Hirsch, *Chemical Reviews*, 2001, **101**, 1153–1184.

[115] E. D. Jemmis, M. M. Balakrishnarajan and P. D. Pancharatna, *Journal of the American Chemical Society*, 2001, **123**, 4313–4323.

[116] M. Brack, *Reviews of Modern Physics*, 1993, **65**, 677–732.

[117] Z. Lin, T. Slee and D. Mingos, *Chemical Physics*, 1990, **142**, 321–334.

[118] B. Huo, X.-L. Guan, C. Yuan and Y.-B. Wu, *Inorganic Chemistry*, 2025, **64**, 3000–3007.

[119] C. Liu, I. A. Popov, Z. Chen, A. I. Boldyrev and Z.-M. Sun, *Chemistry – A European Journal*, 2018, **24**, 14583–14597.

[120] S. orević, M. Solà and S. Radenković, *Inorganic Chemistry*, 2022, **61**, 10116–10125.

[121] Z. Chen, C. S. Wannere, C. Corminboeuf, R. Puchta and P. v. R. Schleyer, *Chemical Reviews*, 2005, **105**, 3842–3888.

[122] H. Fliegl, S. Taubert, O. Lehtonen and D. Sundholm, *Physical Chemistry Chemical Physics*, 2011, **13**, 20500–20518.

[123] D. Sundholm, H. Fliegl and R. J. Berger, *WIREs Computational Molecular Science*, 2016, **6**, 639–678.

[124] H.-L. Xu, N. V. Tkachenko, D. W. Szczepanik, I. A. Popov, A. Muñoz-Castro, A. I. Boldyrev and Z.-M. Sun, *Nature Communications*, 2022, **13**, 2149.

[125] Y.-H. Xu, N. V. Tkachenko, I. A. Popov, L. Qiao, A. Muñoz-Castro, A. I. Boldyrev and Z.-M. Sun, *Nature Communications*, 2021, **12**, 4465.

[126] E. Zintl, *Angewandte Chemie*, 1939, **52**, 1–6.

[127] W. Klemm, *Proceedings of the Chemical Society*, 1958, 329–364.

[128] E. Busmann, *Naturwissenschaften*, 1960, **47**, 82–82.

[129] W. Klemm and E. Busmann, *Zeitschrift für anorganische und allgemeine Chemie*, 1963, **319**, 297–311.

[130] X.-H. Yue, W.-X. Chen, T. Yang, A. Muñoz-Castro, G. Frenking and Z.-M. Sun, *Nature Synthesis*, 2023, **2**, 423–429.

[131] C. L. Kwan and J. K. Kochi, *Journal of the American Chemical Society*, 1976, **98**, 4903–4912.

[132] L. Fohlmeister, S. Liu, C. Schulten, B. Moubaraki, A. Stasch, J. D. Cashion, K. S. Murray, L. Gagliardi and C. Jones, *Angewandte Chemie International Edition*, 2012, **51**, 8294–8298.

[133] C. Hess, T. Weyhermüller, E. Bill and K. Wieghardt, *Angewandte Chemie International Edition*, 2009, **48**, 3703–3706.

[134] E. Peligot, *Comptes Rendus Hebdomadaires des Séances de l'Académie des Sciences*, 1844, **19**, 609–618.

[135] A. Noor, T. Bauer, T. K. Todorova, B. Weber, L. Gagliardi and R. Kempe, *Chemistry – A European Journal*, 2013, **19**, 9825–9832.

[136] K. A. Kreisel, G. P. A. Yap, O. Dmitrenko, C. R. Landis and K. H. Theopold, *Journal of the American Chemical Society*, 2007, **129**, 14162–14163.

[137] F. R. Wagner, A. Noor and R. Kempe, *Nature Chemistry*, 2009, **1**, 529–536.

[138] A. Noor, E. Sobgwi Tamne, S. Qayyum, T. Bauer and R. Kempe, *Chemistry – A European Journal*, 2011, **17**, 6900–6903.

[139] S. Horvath, S. Gorelsky, S. Gambarotta and I. Korobkov, *Angewandte Chemie International Edition*, 2008, **47**, 9937–9940.

[140] M. Ardon, A. Bino, S. Cohen and T. R. Felthouse, *Inorganic Chemistry*, 1984, **23**, 3450–3455.

[141] A. K. Bartholomew, R. A. Musgrave, K. J. Anderton, C. E. Juda, Y. Dong, W. Bu, S.-Y. Wang, Y.-S. Chen and T. A. Betley, *Chemical Science*, 2021, **12**, 15739–15749.

[142] E. V. Eames, T. D. Harris and T. A. Betley, *Chemical Science*, 2012, **3**, 407–415.

[143] E. V. Eames and T. A. Betley, *Inorganic Chemistry*, 2012, **51**, 10274–10278.

[144] R. Hernández Sánchez, A. K. Bartholomew, T. M. Powers, G. Ménard and T. A. Betley, *Journal of the American Chemical Society*, 2016, **138**, 2235–2243.

[145] T. P. Latendresse, N. P. Litak, J. S. Zeng, S.-L. Zheng and T. A. Betley, *Journal of the American Chemical Society*, 2024, **146**, 25578–25588.

[146] Q. Zhao, T. D. Harris and T. A. Betley, *Journal of the American Chemical Society*, 2011, **133**, 8293–8306.

[147] R. Hernández Sánchez and T. A. Betley, *Journal of the American Chemical Society*, 2015, **137**, 13949–13956.

[148] R. H. Sánchez and T. A. Betley, *Journal of the American Chemical Society*, 2018, **140**, 16792–16806.

[149] A. Srinivasan, R. A. Musgrave, M. Rouzières, R. Clérac, J. E. McGrady and E. A. Hillard, *Chemical Communications*, 2021, **57**, 13357–13360.

[150] F. Cotton, C. A. Murillo and X. Wang, *Inorganic Chemistry Communications*, 1998, **1**, 281–283.

[151] J. F. Berry, F. A. Cotton, C. A. Murillo and B. K. Roberts, *Inorganic Chemistry*, 2004, **43**, 2277–2283.

[152] J. F. Berry, F. A. Cotton, T. Lu, C. A. Murillo, B. K. Roberts and X. Wang, *Journal of the American Chemical Society*, 2004, **126**, 7082–7096.

[153] H.-C. Chang, J.-T. Li, C.-C. Wang, T.-W. Lin, H.-C. Lee, G.-H. Lee and S.-M. Peng, *European Journal of Inorganic Chemistry*, 1999, **1999**, 1243–1251.

[154] J. F. Berry, F. A. Cotton, C. S. Fewox, T. Lu, C. A. Murillo and X. Wang, *Dalton Transactions*, 2004, 2297–2302.

[155] J. F. Berry, in *Metal–Metal Bonds in Chains of Three or More Metal Atoms: From Homometallic to Heterometallic Chains*, ed. G. Parkin, Springer Berlin Heidelberg, Berlin, Heidelberg, 2010, pp. 1–28.

[156] S. Mitzinger, L. Broeckaert, W. Massa, F. Weigend and S. Dehnen, *Nature Communications*, 2016, **7**, 10480.

[157] H. T. Pham, D. Majumdar, J. Leszczynski and M. T. Nguyen, *Physical Chemistry Chemical Physics*, 2017, **19**, 3115–3124.

[158] V. Khanna, R. Singh, P. Claes, M. T. Nguyen, A. Fielicke, E. Janssens, P. Lievens and J. E. McGrady, *The Journal of Physical Chemistry A*, 2022, **126**, 1617–1626.

[159] N. T. Mai, N. T. Tung, P. T. Thuy, N. T. Minh Hue and N. T. Cuong, *Computational and Theoretical Chemistry*, 2017, **1117**, 124–129.

[160] X.-Q. Liang, X.-J. Deng, S.-J. Lu, X.-M. Huang, J.-J. Zhao, H.-G. Xu, W.-J. Zheng and X. C. Zeng, *The Journal of Physical Chemistry C*, 2017, **121**, 7037–7046.

[161] X. Liang, X. Kong, S.-J. Lu, Y. Huang, J. Zhao, H.-G. Xu, W. Zheng and X. C. Zeng, *Journal of Physics: Condensed Matter*, 2018, **30**, 335501.

[162] L.-J. Zhao, X.-L. Xu, W.-J. Zheng and H.-G. Xu, *Inorganic Chemistry*, 2025, **64**, 13617–13622.

[163] E. van Lenthe, A. Ehlers and E.-J. Baerends, *The Journal of Chemical Physics*, 1999, **110**, 8943–8953.

[164] E. Van Lenthe and E. J. Baerends, *Journal of Computational Chemistry*, 2003, **24**, 1142–1156.

[165] C. C. Pye and T. Ziegler, *Theoretical Chemistry Accounts*, 1999, **101**, 396–408.

[166] H. Zhai, H. R. Larsson, S. Lee, Z.-H. Cui, T. Zhu, C. Sun, L. Peng, R. Peng, K. Liao, J. Tölle, J. Yang, S. Li and G. K.-L. Chan, *The Journal of Chemical Physics*, 2023, **159**, 234801.

[167] F. Aquilante, J. Autschbach, R. K. Carlson, L. F. Chibotaru, M. G. Delcey, L. De Vico, I. Fdez. Galván, N. Ferré, L. M. Frutos, L. Gagliardi, M. Garavelli, A. Giussani, C. E. Hoyer, G. Li Manni, H. Lischka, D. Ma, P. Malmqvist, T. Müller, A. Nenov, M. Olivucci, T. B. Pedersen, D. Peng, F. Plasser, B. Pritchard, M. Reiher, I. Rivalta, I. Schapiro, J. Segarra-Martí, M. Stenrup, D. G. Truhlar, L. Ungur, A. Valentini, S. Vancoillie, V. Veryazov, V. P. Vysotskiy, O. Weingart, F. Zapata and R. Lindh, *Journal of Computational Chemistry*, 2016, **37**, 506–541.

[168] K. Pierloot, B. Dumez, P. Widmark and B. Roos, *Theoretica Chimica Acta*, 1995, **90**, 87–114.

[169] Q. Sun, X. Zhang, S. Banerjee, P. Bao, M. Barbry, N. S. Blunt, N. A. Bogdanov, G. H. Booth, J. Chen, Z.-H. Cui, J. J. Eriksen, Y. Gao, S. Guo, J. Hermann, M. R. Hermes, K. Koh, P. Koval, S. Lehtola, Z. Li, J. Liu, N. Mardirossian, J. D. McClain, M. Motta, B. Mussard, H. Q. Pham, A. Pulkin, W. Purwanto, P. J. Robinson, E. Ronca, E. R. Sayfutyarova, M. Scheurer, H. F. Schurkus, J. E. T. Smith, C. Sun, S.-N. Sun, S. Upadhyay, L. K. Wagner, X. Wang, A. White, J. D. Whitfield, M. J. Williamson, S. Wouters, J. Yang, J. M. Yu, T. Zhu, T. C. Berkelbach, S. Sharma, A. Y. Sokolov and G. K.-L. Chan, *The Journal of Chemical Physics*, 2020, **153**, 024109.

[170] Q. Sun, T. C. Berkelbach, N. S. Blunt, G. H. Booth, S. Guo, Z. Li, J. Liu, J. D. McClain, E. R. Sayfutyarova, S. Sharma, S. Wouters and G. K.-L. Chan, *WIREs Computational Molecular Science*, 2018, **8**, e1340.

[171] Q. Sun, *Journal of Computational Chemistry*, 2015, **36**, 1664–1671.

[172] K. Boguslawski and P. Tecmer, *International Journal of Quantum Chemistry*, 2015, **115**, 1289–1295.

[173] K. Boguslawski, P. Tecmer, Ö. Legeza and M. Reiher, *The Journal of Physical Chemistry Letters*, 2012, **3**, 3129–3135.

[174] M. Boyko, V. Hlukhyy, H. Jin, J. Dums and T. F. Fässler, *Zeitschrift für anorganische und allgemeine Chemie*, 2020, **646**, 1575–1582.

[175] N. V. Tkachenko, *The Concept of Multicenter Bonds in Chemistry and Materials Science*, 2023.

[176] B. W. Eichhorn, R. C. Haushalter and W. T. Pennington, *Journal of the American Chemical Society*, 1988, **110**, 8704–8706.

[177] B. W. Eichhorn and R. C. Haushalter, *Journal of the Chemical Society, Chemical Communications*, 1990, 937–938.

[178] B. Kesanli, J. Fettinger and B. Eichhorn, *Chemistry – A European Journal*, 2001, **7**, 5277–5285.

[179] J. Campbell, H. P. A. Mercier, H. Franke, D. P. Santry, D. A. Dixon and G. J. Schrobilgen, *Inorganic Chemistry*, 2002, **41**, 86–107.

[180] L. Yong, S. D. Hoffmann and T. F. Fässler, *European Journal of Inorganic Chemistry*, 2005, **2005**, 3663–3669.

[181] S. Scharfe and T. F. Fässler, *European Journal of Inorganic Chemistry*, 2010, **2010**, 1207–1213.

[182] B. Zhou, M. S. Denning, C. Jones and J. M. Goicoechea, *Dalton Transactions*, 2009, 1571–1578.

[183] Z.-M. Sun, Y.-F. Zhao, J. Li and L.-S. Wang, *Journal of Cluster Science*, 2009, **20**, 601–609.

[184] B. Kesanli, J. Fettinger, D. R. Gardner and B. Eichhorn, *Journal of the American Chemical Society*, 2002, **124**, 4779–4786.

[185] C. Liu, L.-J. Li, X. Jin, J. E. McGrady and Z.-M. Sun, *Inorganic Chemistry*, 2018, **57**, 3025–3034.

[186] J. M. Goicoechea and S. C. Sevov, *Journal of the American Chemical Society*, 2006, **128**, 4155–4161.

[187] F. S. Kocak, P. Zavalij and B. Eichhorn, *Chemistry – A European Journal*, 2011, **17**, 4858–4863.

[188] A. Ugrinov and S. C. Sevov, *Journal of the American Chemical Society*, 2002, **124**, 10990–10991.

[189] N. V. Tkachenko, W.-X. Chen, H. W. T. Morgan, A. Muñoz-Castro, A. I. Boldyrev and Z.-M. Sun, *Chemical Communications*, 2022, **58**, 6223–6226.

[190] J.-Q. Wang, B. Wahl and T. Fässler, *Angewandte Chemie International Edition*, 2010, **49**, 6592–6595.

[191] Y.-S. Huang, W.-J. Tian, J.-X. Zhang and Z.-M. Sun, *Chinese Chemical Letters*, 2025, 110827.

[192] M. Ernzerhof and G. E. Scuseria, *The Journal of Chemical Physics*, 1999, **110**, 5029–5036.

[193] M. Franchini, P. H. T. Philipsen and L. Visscher, *Journal of Computational Chemistry*, 2013, **34**, 1819–1827.

[194] M. J. Frisch, G. W. Trucks, H. B. Schlegel, G. E. Scuseria, M. A. Robb, J. R. Cheeseman, G. Scalmani, V. Barone, G. A. Petersson, H. Nakatsuji, X. Li, M. Caricato, A. V. Marenich, J. Bloino, B. G. Janesko, R. Gomperts, B. Mennucci, H. P. Hratchian, J. V. Ortiz, A. F. Izmaylov, J. L. Sonnenberg, D. Williams-Young, F. Ding, F. Lipparini, F. Egidi, J. Goings, B. Peng, A. Petrone, T. Henderson, D. Ranasinghe, V. G. Zakrzewski, J. Gao, N. Rega, G. Zheng, W. Liang, M. Hada, M. Ehara, K. Toyota, R. Fukuda, J. Hasegawa, M. Ishida, T. Nakajima, Y. Honda, O. Kitao, H. Nakai, T. Vreven, K. Throssell, J. A. Montgomery, Jr., J. E. Peralta, F. Ogliaro, M. J. Bearpark, J. J. Heyd, E. N. Brothers, K. N. Kudin, V. N. Staroverov, T. A. Keith, R. Kobayashi, J. Normand, K. Raghavachari, A. P. Rendell, J. C. Burant, S. S. Iyengar, J. Tomasi, M. Cossi, J. M. Millam, M. Klene, C. Adamo, R. Cammi, J. W. Ochterski, R. L. Martin, K. Morokuma, O. Farkas, J. B. Foresman and D. J. Fox, *Gaussian˜16 Revision C.01*, 2016, Gaussian Inc. Wallingford CT.

[195] C. Zhang, H. W. T. Morgan, Z.-C. Wang, C. Liu, Z.-M. Sun and J. E. McGrady, *Dalton Transactions*, 2019, **48**, 15888–15895.

[196] B. O. Roos, R. Lindh, P.- Malmqvist, V. Veryazov and P.-O. Widmark, *The Journal of Physical Chemistry A*, 2005, **109**, 6575–6579.

[197] B. Huron, J. P. Malrieu and P. Rancurel, *The Journal of Chemical Physics*, 1973, **58**, 5745–5759.

[198] A. A. Holmes, N. M. Tubman and C. J. Umrigar, *Journal of Chemical Theory and Computation*, 2016, **12**, 3674–3680.

[199] J. Dukelsky, M. Martín-Delgado, T. Nishino and G. Sierra, *Europhysics Letters*, 1998, **43**, 457–462.

[200] L. Freitag, S. Knecht, S. F. Keller, M. G. Delcey, F. Aquilante, T. Bondo Pedersen, R. Lindh, M. Reiher and L. González, *Physical Chemistry Chemical Physics*, 2015, **17**, 14383–14392.

[201] C. J. Stein, D. A. Pantazis and V. Krewald, *The Journal of Physical Chemistry Letters*, 2019, **10**, 6762–6770.

[202] R. S. P. Turbervill and J. M. Goicoechea, *Chemical Reviews*, 2014, **114**, 10807–10828.

[203] B. Kesanli, S. Charles, Y.-F. Lam, S. G. Bott, J. Fettinger and B. Eichhorn, *Journal of the American Chemical Society*, 2000, **122**, 11101–11107.

[204] S. Charles, B. W. Eichhorn, A. L. Rheingold and S. G. Bott, *Journal of the American Chemical Society*, 1994, **116**, 8077–8086.

[205] S. Charles, J. C. Fettinger, S. G. Bott and B. W. Eichhorn, *Journal of the American Chemical Society*, 1996, **118**, 4713–4714.

[206] Z.-C. Wang, L. Qiao, Z.-M. Sun and M. Scheer, *Journal of the American Chemical Society*, 2022, **144**, 6698–6702.

[207] S. Charles, B. W. Eichhorn and S. G. Bott, *Journal of the American Chemical Society*, 1993, **115**, 5837–5838.

[208] Z. Li, D. Ouyang and L. Xu, *Chemical Communications*, 2019, **55**, 6783–6786.

[209] N. Arleth, M. T. Gamer, R. Köppe, S. N. Konchenko, M. Fleischmann, M. Scheer and P. W. Roesky, *Angewandte Chemie International Edition*, 2016, **55**, 1557–1560.

[210] S. Mandal, A. C. Reber, M. Qian, R. Liu, H. M. Saavedra, S. Sen, P. S. Weiss, S. N. Khanna and A. Sen, *Dalton Transactions*, 2012, **41**, 12365–12377.

[211] C. M. Knapp, J. S. Large, N. H. Rees and J. M. Goicoechea, *Chemical Communications*, 2011, **47**, 4111–4113.

[212] C. Knapp, B. Zhou, M. S. Denning, N. H. Rees and J. M. Goicoechea, *Dalton Transactions*, 2010, **39**, 426–436.

[213] W.-Q. Zhang, N. V. Tkachenko, L. Qiao, A. I. Boldyrev and Z.-M. Sun, *Chinese Journal of Chemistry*, 2022, **40**, 65–70.

[214] N. K. Chaki, S. Mandal, A. C. Reber, M. Qian, H. M. Saavedra, P. S. Weiss, S. N. Khanna and A. Sen, *ACS Nano*, 2010, **4**, 5813–5818.

[215] M. J. Moses, J. Fettinger and B. Eichhorn, *Journal of the American Chemical Society*, 2002, **124**, 5944–5945.

[216] A. C. Reber, S. Mandal, M. Qian, H. M. Saavedra, P. S. Weiss, S. N. Khanna and A. Sen, *The Journal of Physical Chemistry C*, 2012, **116**, 10207–10214.

[217] V. Heinl, M. Schmidt, M. Eckhardt, M. Eberl, A. E. Seitz, G. Balázs, M. Seidl and M. Scheer, *Chemistry – A European Journal*, 2021, **27**, 11649–11655.

[218] O. J. Scherer, J. Braun and G. Wolmershäuser, *Chemische Berichte*, 1990, **123**, 471–475.

[219] M. Piesch, S. Reichl, M. Seidl, G. Balázs and M. Scheer, *Angewandte Chemie International Edition*, 2019, **58**, 16563–16568.

[220] F. Dielmann, A. Timoshkin, M. Piesch, G. Balázs and M. Scheer, *Angewandte Chemie International Edition*, 2017, **56**, 1671–1675.

[221] U. Chakraborty, J. Leitl, B. Mühldorf, M. Bodensteiner, S. Pelties and R. Wolf, *Dalton Transactions*, 2018, **47**, 3693–3697.

[222] O. J. Scherer and T. Brück, *Angewandte Chemie*, 1987, **99**, 59–59.

[223] O. J. Scherer, T. Brück and G. Wolmershäuser, *Chemische Berichte*, 1988, **121**, 935–938.

[224] O. Scherer, C. Blath and G. Wolmershäuser, *Journal of Organometallic Chemistry*, 1990, **387**, C21–C24.

[225] E. Urne˙žius, W. W. Brennessel, C. J. Cramer, J. E. Ellis and P. von Ragué Schleyer, *Science*, 2002, **295**, 832–834.

[226] E. Mädl, G. Balázs, E. V. Peresypkina and M. Scheer, *Angewandte Chemie International Edition*, 2016, **55**, 7702–7707.

[227] Y.-H. Xu, X. Yang, Y.-N. Yang, L. Zhao, G. Frenking and Z.-M. Sun, *Nature chemistry*, 2025, 1–8.

[228] O. J. Scherer, H. Swarowsky, G. Wolmershäuser, W. Kaim and S. Kohlmann, *Angewandte Chemie International Edition in English*, 1987, **26**, 1153–1155.

[229] M. Herberhold, G. Frohmader and W. Milius, *Journal of Organometallic Chemistry*, 1996, **522**, 185–196.

[230] A. C. Reddy, E. D. Jemmis, O. J. Scherer, R. Winter, G. Heckmann and G. Wolmershaeuser, *Organometallics*, 1992, **11**, 3894–3900.

[231] O. J. Scherer, H. Sitzmann and G. Wolmershäuser, *Angewandte Chemie International Edition in English*, 1985, **24**, 351–353.

[232] O. J. Scherer, J. Schwalb, H. Swarowsky, G. Wolmershäuser, W. Kaim and R. Gross, *Chemische Berichte*, 1988, **121**, 443–449.

[233] M. E. Barr and L. F. Dahl, *Organometallics*, 1991, **10**, 3991–3996.

[234] A. Cavaillé, N. Saffon-Merceron, N. Nebra, M. Fustier-Boutignon and N. Mézailles, *Angewandte Chemie International Edition*, 2018, **57**, 1874–1878.

[235] C. M. Hoidn, T. M. Maier, K. Trabitsch, J. J. Weigand and R. Wolf, *Angewandte Chemie International Edition*, 2019, **58**, 18931–18936.

[236] F. Spitzer, G. Balázs, C. Graßl, M. Keilwerth, K. Meyer and M. Scheer, *Angewandte Chemie International Edition*, 2018, **57**, 8760–8764.

[237] F. Spitzer, M. Sierka, M. Latronico, P. Mastrorilli, A. V. Virovets and M. Scheer, *Angewandte Chemie International Edition*, 2015, **54**, 4392–4396.

[238] S. Yao, Y. Xiong, C. Milsmann, E. Bill, S. Pfirrmann, C. Limberg and M. Driess, *Chemistry – A European Journal*, 2010, **16**, 436–439.

[239] S. Yao, N. Lindenmaier, Y. Xiong, S. Inoue, T. Szilvási, M. Adelhardt, J. Sutter, K. Meyer and M. Driess, *Angewandte Chemie International Edition*, 2015, **54**, 1250–1254.

[240] S. Yao, T. Szilvási, N. Lindenmaier, Y. Xiong, S. Inoue, M. Adelhardt, J. Sutter, K. Meyer and M. Driess, *Chemical Communications*, 2015, **51**, 6153–6156.

[241] C. Schoo, S. Bestgen, R. Köppe, S. N. Konchenko and P. W. Roesky, *Chemical Communications*, 2018, **54**, 4770–4773.

[242] J. Rienmüller, B. Peerless, S. Paul, F. Bruder, W. Wernsdorfer, F. Weigend and S. Dehnen, *Nature Chemistry*, 2025, **17**, 547–555.

[243] C. Riesinger, F. Dielmann, R. Szlosek, A. V. Virovets and M. Scheer, *Angewandte Chemie International Edition*, 2023, **62**, e202218828.

[244] C. Graßl, M. Bodensteiner, M. Zabel and M. Scheer, *Chemical Science*, 2015, **6**, 1379–1382.

[245] F. Spitzer, C. Graßl, G. Balázs, E. M. Zolnhofer, K. Meyer and M. Scheer, *Angewandte Chemie International Edition*, 2016, **55**, 4340–4344.

[246] F. Spitzer, G. Balázs, C. Graßl and M. Scheer, *Chemical Communications*, 2020, **56**, 13209–13212.

[247] C. von Hänisch, D. Fenske, F. Weigend and R. Ahlrichs, *Chemistry – A European Journal*, 1997, **3**, 1494–1498.

[248] B. Peerless, A. Schmidt, Y. J. Franzke and S. Dehnen, *Nature Chemistry*, 2023, **15**, 347–356.

[249] L. Qiao, D. Chen, J. Zhu, A. Muñoz-Castro and Z.-M. Sun, *Chemical Communications*, 2021, **57**, 3656–3659.

[250] J. M. Goicoechea, M. W. Hull and S. C. Sevov, *Journal of the American Chemical Society*, 2007, **129**, 7885–7893.

[251] L. G. Perla and S. C. Sevov, *Inorganic Chemistry*, 2015, **54**, 8401–8405.

[252] R. Ahlrichs, D. Fenske, K. Fromm, H. Krautscheid, U. Krautscheid and O. Treutler, *Chemistry – A European Journal*, 1996, **2**, 238–244.

[253] B. Kesanli, J. Fettinger, B. Scott and B. Eichhorn, *Inorganic Chemistry*, 2004, **43**, 3840–3846.

[254] B. W. Eichhorn, S. P. Mattamana, D. R. Gardner and J. C. Fettinger, *Journal of the American Chemical Society*, 1998, **120**, 9708–9709.

[255] B. Kesanli, J. Fettinger and B. Eichhorn, *Journal of the American Chemical Society*, 2003, **125**, 7367–7376.

[256] W.-Q. Zhang, H. W. T. Morgan, C.-C. Shu, J. E. McGrady and Z.-M. Sun, *Inorganic Chemistry*, 2022, **61**, 4421–4427.

[257] W.-X. Chen, W.-J. Tian, Z.-S. Li, J.-J. Wang, A. Muñoz-Castro, G. Frenking and Z.-M. Sun, *Nature Synthesis*, 2025, 1–8.

[258] A. R. Eulenstein, Y. J. Franzke, P. Bügel, W. Massa, F. Weigend and S. Dehnen, *Nature Communications*, 2020, **11**, 5122.

[259] F. Lips, R. Clérac and S. Dehnen, *Journal of the American Chemical Society*, 2011, **133**, 14168–14171.

[260] M. Schmidt, D. Konieczny, E. V. Peresypkina, A. V. Virovets, G. Balázs, M. Bodensteiner, F. Riedlberger, H. Krauss and M. Scheer, *Angewandte Chemie International Edition*, 2017, **56**, 7307–7311.

[261] M. Schmidt, A. E. Seitz, M. Eckhardt, G. Balázs, E. V. Peresypkina, A. V. Virovets, F. Riedlberger, M. Bodensteiner, E. M. Zolnhofer, K. Meyer and M. Scheer, *Journal of the American Chemical Society*, 2017, **139**, 13981–13984.

[262] D. S. Warren, B. M. Gimarc and M. Zhao, *Inorganic Chemistry*, 1994, **33**, 710–715.

[263] H. Krauss, G. Balázs, M. Seidl and M. Scheer, *Mendeleev Communications*, 2022, **32**, 42–45.

[264] C. Riesinger, L. Dütsch and M. Scheer, *Zeitschrift für anorganische und allgemeine Chemie*, 2022, **648**, e202200102.

[265] C. von Hänisch and D. Fenske, *Zeitschrift für anorganische und allgemeine Chemie*, 1998, **624**, 367–369.

[266] L. Giusti, V. R. Landaeta, M. Vanni, J. A. Kelly, R. Wolf and M. Caporali, *Coordination Chemistry Reviews*, 2021, **441**, 213927.

[267] C. M. Hoidn, D. J. Scott and R. Wolf, *Chemistry – A European Journal*, 2021, **27**, 1886–1902.

[268] M. Seidl, G. Balázs and M. Scheer, *Chemical Reviews*, 2019, **119**, 8406–8434.

[269] F. Pan, B. Peerless and S. Dehnen, *Accounts of Chemical Research*, 2023, **56**, 1018–1030.

[270] S. Pelties, T. Maier, D. Herrmann, B. deBruin, C. Rebreyend, S. Gärtner, I. G. Shenderovich and R. Wolf, *Chemistry – A European Journal*, 2017, **23**, 6094–6102.

[271] W. Seidel, O. Summerscales, B. Patrick and M. Fryzuk, *Angewandte Chemie International Edition*, 2009, **48**, 115–117.

[272] O. J. Scherer, J. Braun, P. Walther and G. Wolmershäuser, *Chemische Berichte*, 1992, **125**, 2661–2665.

[273] H. Ruan, L. Wang, Z. Li and L. Xu, *Dalton Transactions*, 2017, **46**, 7219–7222.

[274] J. Krüger, C. Wölper and S. Schulz, *Inorganic Chemistry*, 2020, **59**, 11142–11151.

[275] G. Li Manni, I. Fdez. Galván, A. Alavi, F. Aleotti, F. Aquilante, J. Autschbach, D. Avagliano, A. Baiardi, J. J. Bao, S. Battaglia, L. Birnoschi, A. Blanco-González, S. I. Bokarev, R. Broer, R. Cacciari, P. B. Calio, R. K. Carlson, R. Carvalho Couto, L. Cerdán, L. F. Chibotaru, N. F. Chilton, J. R. Church, I. Conti, S. Coriani, J. Cuéllar-Zuquin, R. E. Daoud, N. Dattani, P. Decleva, C. de Graaf, M. G. Delcey, L. De Vico, W. Dobrautz, S. S. Dong, R. Feng, N. Ferré, M. Filatov(Gulak), L. Gagliardi, M. Garavelli, L. González, Y. Guan, M. Guo, M. R. Hennefarth, M. R. Hermes, C. E. Hoyer, M. Huix-Rotllant, V. K. Jaiswal, A. Kaiser, D. S. Kaliakin, M. Khamesian, D. S. King, V. Kochetov, M. Krośnicki, A. A. Kumaar, E. D. Larsson, S. Lehtola, M.-B. Lepetit, H. Lischka, P. López Ríos, M. Lundberg, D. Ma, S. Mai, P. Marquetand, I. C. D. Merritt, F. Montorsi, M. Mörchen, A. Nenov, V. H. A. Nguyen, Y. Nishimoto, M. S. Oakley, M. Olivucci, M. Oppel, D. Padula, R. Pandharkar, Q. M. Phung, F. Plasser, G. Raggi, E. Rebolini, M. Reiher, I. Rivalta, D. Roca-Sanjuán, T. Romig, A. A. Safari, A. Sánchez-Mansilla, A. M. Sand, I. Schapiro, T. R. Scott, J. Segarra-Martí, F. Segatta, D.-C. Sergentu, P. Sharma, R. Shepard, Y. Shu, J. K. Staab, T. P. Straatsma, L. K. Sørensen, B. N. C. Tenorio, D. G. Truhlar, L. Ungur, M. Vacher, V. Veryazov, T. A. Voß, O. Weser, D. Wu, X. Yang, D. Yarkony, C. Zhou, J. P. Zobel and R. Lindh, *Journal of Chemical Theory and Computation*, 2023, **19**, 6933–6991.

[276] F. Kraus and N. Korber, *Chemistry – A European Journal*, 2005, **11**, 5945–5959.